PROTON FORM FACTOR RATIO, $\mu_P G_E^P / G_M^P$ FROM DOUBLE SPIN ASYMMETRY

A Dissertation

By

HABARAKADA LIYANAGE ANUSHA PUSHPAKUMARI

Submitted to the Graduate College of Hampton University in
partial fulfillment of the requirements for the degree of

DOCTOR OF PHILOSOPHY

August 2013

This dissertation submitted by Habarakada Liyanage Anusha Pushpakumari in partial fulfillment of the requirements for the degree of Doctor of Philosophy at Hampton University, Hampton, Virginia is hereby approved by the committee under whom the work has been completed.

Michael Kohl, Ph.D.
Committee Chair

M. Eric Christy, Ph.D.

Jose L. Goity, Ph.D.

Mark Jones, Ph.D.

Patrena N. Benton, Ph.D.
Dean, The Graduate College

Date

Copyright by
HABARAKADA LIYANAGE ANUSHA PUSHPAKUMARI
2013

ABSTRACT

Proton Form Factor Ratio, $\mu_p G_E^p/G_M^p$ from Double Spin Asymmetry. (August 2013)

Habarakada Liyanage Anusha Pushpakumari, B.S., University of Peradeniya;

M.S., Hampton University

Chair of Advisory Committee: Dr. Michael Kohl

The form factors are fundamental properties of the nucleon representing the effect of its structure on its response to electromagnetic probes such as electrons. They are functions of the four-momentum transfer squared Q^2 between the electron and the proton. This thesis reports the results of a new measurement of the ratio of the electric and magnetic form factors of the proton up to $Q^2 = 5.66$ (GeV/c)^2 using the double spin asymmetry with a polarized beam and target.

Experiment E07-003 (SANE, Spin Asymmetries of the Nucleon Experiment) was carried out in Hall C at Jefferson Lab in 2009 to study the proton spin structure functions with a dynamically polarized ammonia target and longitudinally polarized electron beam. By detecting elastically scattered protons in the High-Momentum Spectrometer (HMS) in coincidence with the electrons in the Big Electron Telescope Array (BETA), elastic measurements were carried out in parallel. The elastic double spin asymmetry allows one to extract the proton electric to magnetic form factor ratio G_E^p/G_M^p at high-momentum transfer, $Q^2 = 5.66$ (GeV/c)^2. In addition to the coincidence data, inclusively scattered electrons from the polarized ammonia target were detected by HMS, which allows to measure the beam-target asymmetry in the elastic region with the target spin nearly perpendicular to the momentum transfer, and to extract G_E^p/G_M^p at low $Q^2 = 2.06$ (GeV/c)^2.

This alternative measurement of G_E^p/G_M^p has verified and confirmed the dramatic discrepancy at high Q^2 between the Rosenbluth and the recoil-polarization-transfer

method with a different measurement technique and systematic uncertainties uncorrelated to those of the recoil-polarization measurements. The measurement of the form factor ratio at $Q^2 = 2.06$ (GeV/c)^2 has been determined as $\mu_p G_E^p/G_M^p = 0.605 \pm 0.178_{stat} \pm 0.033_{sys}$ which is in agreement with an earlier measurement with the polarized target technique at similar kinematics. The measurement of the form factor ratio at $Q^2 = 5.66$ (GeV/c)^2 has been determined as $\mu_p G_E^p/G_M^p = 0.672 \pm 0.362_{stat}$ which represents the highest Q^2 reach with the double spin asymmetry to date.

Dedicated to my parents.

ACKNOWLEDGEMENTS

There are so many people who have made it possible for me to finally reach this milestone. First of all, I would like to thank my advisor, Dr. Michael Kohl, for his guidance and support throughout the duration of my thesis research and for revising the manuscript many, many times with patience. Then, of course, I must thank Dr. M. Eric Christy for getting me started on experimental nuclear physics and giving his advice continuously until I reached my final goal. I would also like to acknowledge the assistance provided by the Hampton University Physics Department through out this journey. A very special thanks goes to Dr. Mark Jones who provided me advice, direction and invaluable assistance throughout my data analysis, being patient and answering my endless questions. I would also like to thank Dr. Jose L. Goity for serving on my thesis committee.

I would like to thank Dr. Cynthia Keppel for giving me the chance to come to the United States of America and to continue my graduate studies in the Physics Department at Hampton University.

During my four years at Jefferson Lab, I met many fantastic people who helped me in numerous ways. I would like to thank all the people at Jefferson Lab as well as the UVa polarized target group who made our experiment a success. I also had the pleasure of working with the SANE collaborators, Dr. Oscar Rondon, Dr. Hovannes Baghdasaryan, Dr. Narbe Kalantarians as well as my fellow SANE students Dr. James Maxwell, Dr. Jonathan Mulholland, Whitney Armstrong, Hoyoung Kang and Luwani Ndukun who helped me in many ways. I would like to thank all other hard working fellow students in Jefferson Lab for making my stay at graduate school a pleasant one.

Through this long process, I enjoyed the support of my friends and my husband, Lanka. Throughout all the strange and hard times, he kept me in a positive attitude

and made me feel that I could do this. Without my friends and him, I would have forgotten that there is more to life than physics.

I would like to thank my parents for giving me the freedom to let me choose my own goals and leaving me to fly a long way to here. There are not enough words in the world to thank them and my siblings for their love and support. I would especially like to thank them for always being there on the other side of the phone for me.

TABLE OF CONTENTS

Section Page

LIST OF TABLES

LIST OF FIGURES

Figure Page

SECTION 1

INTRODUCTION

Since Rutherford, Geiger, and Marsden discovered the atomic nucleus by measuring the distribution of alpha particles scattered from gold foils ([1–3]), scientists started to believe that the nucleus consists of a dense center surrounded by a cloud of negatively charged electrons. These electrons are bound to the nucleus by the electromagnetic force which causes the interaction between electrically charged particles.

The nucleus consists of nucleons, *i.e.*, protons and neutrons, which themselves have a substructure. The effort of understanding the nucleonic structure and dynamics has continued for generations up to this day. The first clue that the nucleons themselves are not point-like, elementary particles came from Otto Stern's measurements of the magnetic moment of the proton and the deuteron in 1933 [4]. These measurements showed drastic deviation from the expected value in the Dirac equation for a "point" spin 1/2 particle, implying that protons and neutrons are composite and have internal structure. Since that groundbreaking discovery, a modern understanding of the nucleon has emerged, answering many questions and raising many more.

Elastic electron-nucleon scattering has been an important tool to understand the structure of the nucleon. In one-photon exchange (Born) approximation, the structure of the nucleon is characterized in terms of the electric and magnetic form factors, G_E and G_M, which depend only on the four-momentum transfer squared, Q^2. The form factors, G_E and G_M, are fundamental quantities sensitive to the distribution of charge and magnetization within the nucleon.

The proton form factors, G_E^p and G_M^p, can be extracted individually by measuring the elastic ep scattering cross-sections at constant Q^2, but at different beam energies

and at the different electron scattering angles (Rosenbluth technique). In addition, spin observables in elastic *ep* scattering are sensitive to the ratio of G_E^p/G_M^p, allowing for a direct determination of G_E^p/G_M^p from either the recoil-polarization measurement or the double-spin asymmetry at a single beam energy and a single electron scattering angle. A linear falloff with Q^2 was shown in the polarization-transfer data in contrast to the nearly flat Q^2 dependence of G_E^p/G_M^p measured with the Rosenbluth technique. This discrepancy has been widely considered as due to the significant effects of two-photon exchange. Checking for the possibility of an unknown systematic error in the Rosenbluth or recoil-polarization technique is very important, before physical conclusions can be made. Measurement of the beam-target asymmetry in elastic *ep* scattering offers an independent technique of determining the G_E^p/G_M^p ratio. By measuring G_E^p/G_M^p with the third technique and comparing to previous results, the discovery of unknown or underestimated systematic errors in the previous measurements is possible. This dissertation presents the measurement of G_E^p/G_M^p from double-spin asymmetry for $Q^2 = 2.06$ (GeV/c)^2 and 5.66 (GeV/c)^2.

1.1 Overview of the Experiment

The experiment E07-003 (Spin Asymmetries of the Nucleon Experiment) is a single-arm inclusive-scattering experiment. The goal of SANE was to measure proton spin structure functions $g_1(x, Q^2)$ and $g_2(x, Q^2)$ at four-momentum transfer $2.5<Q^2<6.5$ (GeV/c)^2 and $0.3<x<0.8$ which is an extension of the kinematics of experiment RSS [5] performed in Hall C, Jefferson Lab in 2007.

SANE measured the inclusive spin asymmetries with the target spin aligned parallel and nearly perpendicular (80°) to the beam direction for longitudinally polarized electron scattering from a DNP polarized proton (crystallized NH_3) target. The experiment was carried out in the experimental Hall C at Jefferson Lab from January to March, 2009. A subset of the data was used to measure the elastic beam-target spin

asymmetry from elastic electron-proton scattering. Polarized electrons with energies 4.72 GeV and 5.89 GeV were scattered from the polarized proton target with the spin of the proton aligned nearly perpendicular (80°) to the beam direction. Single-arm electron scattering data were taken by detecting the elastically scattered electrons in the High-Momentum Spectrometer (HMS) for an electron beam energy 5.89 GeV. In addition to that, recoiled protons were detected by the HMS in coincidence with the electrons in Big Electron Telescope Array (BETA) for the two different beam energies 4.72 GeV and 5.89 GeV.

Single-arm data were taken about ∼12 hours in total ($\sim 2 \times 10^4$ elastic events) and the coincidence data were taken about a week for both beam energies, ∼40 hours and ∼155 hours (∼113 elastic events and ∼1200 elastic events) respectively, for the two beam energies 4.72 GeV and 5.89 GeV.

When HMS was at negative polarity, both the HMS Cherenkov detector and the lead-glass calorimeter were used to separate pions and electrons. A relative momentum acceptance cut also was used to extract the elastic events in single-arm data.

For the coincidence data, for HMS is in positive polarity, the relative momentum deviation of the measured proton momentum in HMS from the calculated proton momentum by knowing the recoiled proton angle in HMS, was used to extract the elastic events. The vertical and horizontal positions of the scattered electron on the BETA calorimeter, BigCal was predicted from the proton angle in HMS (X_{HMS}, Y_{HMS}). By taking the horizontal and vertical position differences between the measured electron position on BigCal (X_{clust}, Y_{clust}) and the predicted electron position on BigCal (X_{HMS}, Y_{HMS}) and performing the elliptical cut on them, subtract the inelastic background most effectively.

The following Section 1.2 of the first chapter in this dissertation motivates the use of elastic electron-nucleon scattering to study the structure of the nucleon. Working in both one-photon (Born approximation) and two-photon exchange, the scattering

cross-sections are derived in terms of electric (G_E) and magnetic (G_M) form factors which characterize the effect of the nucleon's electromagnetic structure. Further, the radiative effects on the Born cross-sections is also discussed. The cross-section formula for the inelastic electron-proton scattering is also presented for the completeness of the scattering experiments.

In Chapter 2, the formalism and the methods of measuring the electromagnetic form factor ratio, $\mu G_E/G_M$ from the Rosenbluth separation technique, the polarization-transfer method and the double-spin asymmetry in terms of G_E and G_M are discussed. Existing proton and neutron form factor data from cross-section and polarization experiments are presented and discussed. In addition, possible theoretical interpretations of the nucleon electromagnetic form factors are summarized in Section 2.3.

In Chapter 3, a detailed description of the experiment setup is given, including the polarized electron beam, BETA calorimeter (BigCal), HMS detector package, polarized target, trigger and data-acquisition system.

In the fourth Chapter, the data analysis is reviewed by discussing the HMS event reconstruction through the target magnetic field, HMS and BigCal detector calibrations, elastic event selections, raw and physics asymmetries and hence the proton form factor ratio, $\mu_p G_E^p/G_M^p$ calculation. The results of Montecarlo simulation comparisons of C and NH_3 data to correct the beam-position offsets and correlation corrections are also shown. In addition, the systematic uncertainty determinations for the single-arm data are discussed.

The last Chapter presents the results for the proton form factor ratio from double-spin asymmetry at two Q^2 values, $Q^2 = 2.06$ $(\mathrm{GeV/c})^2$ (with both statistical and systematic uncertainties) and 5.66 $(\mathrm{GeV/c})^2$ (with only statistical uncertainty) highliting the importance of the double-spin asymmetry method. The low HMS drift chamber efficiency of $\sim$40% due to the drift chamber gas leak during the coincidence data-taking decreased the proton yield in HMS, resulting in low statistics for the

coincidence elastic events. Therefore, due to the large error bar on the statistical uncertainty of the form factor measurement from coincidence data, the systematic uncertainty for that measurement was not studied, as it is expected not to dominate the error. Further, the possible improvements of the experiment for future references are also discussed.

1.2 Scattering Experiments

Scattering experiments have been the method of choice of nuclear and particle physicists to examine the microscopic structure of matter. To this day, electron scattering remains one of the most powerful techniques to study nuclear and nucleon structure. The interaction of a beam of electrons with a nuclear target is well understood and precisely calculable within Quantum Electrodynamics (QED). The electromagnetic fine structure constant α, the weak coupling constants g_w and g_z are all sufficiently small at all energies. However, the strong coupling constant α_s is small only at high energy in the limit of asymptotic freedom, leaving the possibility to use perturbation theory to carry out calculations of particle decay rates and scattering cross-sections. At low energies, the probed distance is larger and therefore, the strong force between quarks is stronger; QCD is non-perturbative. At higher energies, the probed distance is small; this is where the quarks are asymptotically free, the force between quarks becomes weak, and perturbative QCD applies. Starting from 'Fermi's Golden Rule', which is a general expression giving the transition rate (number of transmissions per unit time) from an initial state $\mid i\rangle$ of energy E_i to the set of final states $\mid f\rangle$ with energies $E_f = E_i$, the *invariant amplitude* or so-called *Lorentz Invariant Matrix Element*, M and hence the differential cross-section $d\sigma$ for the scattering, is derived in [6] as,

$$d\sigma = \frac{\mid \bar{M} \mid^2}{64\pi^2 M E_1} \frac{d^3p'}{p'^0} \frac{d^3k'}{k'^0} \delta^{(4)}(k + p - k' - p'), \tag{1.2.1}$$

where k, p and k', p' are the initial and final particle four-momenta. The bar over the square of the scattering amplitude indicates that it is to be averaged over the spin states of the initial particles and summed over the spin states of the outgoing particles. Therefore, in other words, the Equation (1.2.1) refers to the *unpolarized* cross-section.

By integrating over all possible outgoing momenta, assuming the two-body scattering process of the form $1 + 2 \rightarrow 3 + 4$, the above Equation (1.2.1) converts to the differential cross-section describing the scattering of a particle into an element of solid angle, $d\Omega$ in the lab frame,

$$\frac{d\sigma}{d\Omega} = \frac{1}{64\pi^2}\left(\frac{E_3}{ME_1}\right)^2 \mid \bar{M} \mid^2, \tag{1.2.2}$$

where E_1 and E_3 are the energies of the incoming and scattered particle, respectively. Note that $d\Omega = 2\pi \mathrm{d}\cos\theta$. The above expression for the differential cross-section depends on the Lorentz-invariant matrix element squared, $\mid \bar{M} \mid^2$, which contains the dynamical information on the process. The matrix element is determined by Feynman diagrams appropriate to that process and applying the Feynman rules (See [7], section 4.8 or [6], table 6.2) to each diagram.

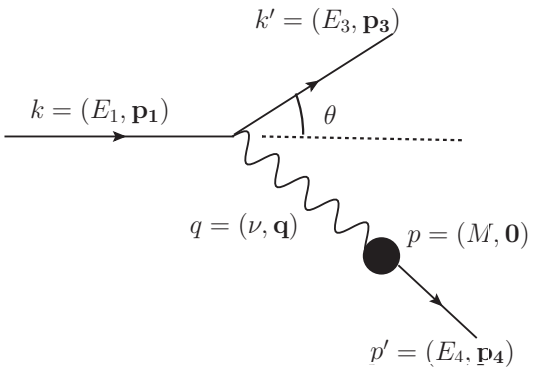

Figure 1.1. Lab frame electron scattering from a stationary target.

Figure 1.1 shows the most basic scattering process, elastic lepton - lepton scattering. At leading order in α, the scattering occurs through the exchange of a single virtual photon. Because the fine structure constant of electromagnetism is so small ($\alpha = \frac{e^2}{\hbar c}$ (in cgs units)= $\frac{1}{137.03599911}$ experimentally [8]), first-order perturbation theory in α (Born approximation) is a very good approximation to the real physics process.

According to the Feynman rules for QED, the invariant amplitude for lepton-lepton scattering can be read off from the diagram as,

$$-iM = \bar{u}(k')(ig_e\gamma^\mu)u(k)\left(-i\frac{g_{\mu\nu}}{q^2}\right)\bar{u}(p')(-ig_e\gamma^\nu)u(p). \tag{1.2.3}$$

In Equation (1.2.3), $u(k)$ and $\bar{u}(k')$ are the solutions to the momentum space Dirac equation $(\gamma^\mu p_\mu - mc)u = 0$ for incoming and outgoing particles. The quantity $q^2 = (k-k')^2 = (p'-p)^2$ is the four-momentum transfer squared and also the invariant mass of the virtual photon. Each vertex adds a vertex factor, $ig_e\gamma^\mu$, with g_e representing the coupling strength of the vertex, here the charge of the electron, $g_e = e$. The photon propagator, $-i\frac{g_{\mu\nu}}{q^2}$ is sandwiched between them. Squaring the invariant amplitude $-iM$, one can obtain:

$$\mid M \mid^2 = \frac{e^4}{(k-k')^2}[\bar{u}(k')\gamma^\mu u(k)][\bar{u}(p')\gamma_\nu u(p)][\bar{u}(k')\gamma^\mu u(k)]^*[\bar{u}(p')\gamma^\nu u(p)]^*. \tag{1.2.4}$$

However, because of the lack of knowledge of the spin degrees of freedom, the average of the all-spin states of $\mid M \mid^2$, $\mid \bar{M} \mid^2$ was calculated by averaging over initial spins and summing over final spins to find the *unpolarized* scattering amplitude of the process. In parallel, the invariant amplitude square, $\mid \bar{M} \mid^2$ for lepton-nucleon scattering can be written in different form as,

$$|\bar{M}|^2 = \frac{e^4}{q^4}L_e^{\mu\nu}L_{\mu\nu}^{target}, \tag{1.2.5}$$

introducing the new quantities L, which are the leptonic and hadronic tensors. The leptonic tensor expression is defined in [6] as:

$$L_e^{\mu\nu} = \frac{1}{2}Tr((\not{k}' + m)\gamma^\mu(\not{k} + m)\gamma^\nu) = 2(k'^\mu k^\nu + k'^\nu k^\mu - (k'.k - m^2)g^{\mu\nu}), \quad (1.2.6)$$

which gives information about the lepton arm of the scattering process. The hadronic tensor, $L_{\mu\nu}^{target}$ gives information about the hadron arm of the scattering process which is particular to each nucleon type. However, for lepton-lepton scattering, the hadronic tensor in Equation (1.2.5) should be replaced by the leptonic tensor which is given by Equation (1.2.6). Therefore, by substituting the leptonic tensor, Equation (1.2.6) for both $L_e^{\mu\nu}$ and $L_{\mu\nu}^{target}$ in Equation (1.2.5), and then using the resulting $|\bar{M}|^2$ into Equation (1.2.2), one can calculate the *unpolarized* cross-section of the lepton-lepton scattering.

Similarly, using elastic scattering of a lepton from a point-like spin-1/2, Dirac particle, one can demonstrate the cross-section calculation through the Lorentz invariant matrix element, M. By replacing the $L_{\mu\nu}^{target}$ by the Dirac particle tensor, which is assumed similar to the electron tensor, the following general expression for $\langle \mid \bar{M} \mid^2 \rangle$ is obtained for scattering of e^- of mass m from a Dirac particle of mass M:

$$\langle \mid \bar{M} \mid^2 \rangle = \frac{8e^4}{(k-k')^4}[(k.p)(k'.p')+(k.p')(p.k')-(k.k')M^2-(p.p')m^2+2m^2M^2]. \quad (1.2.7)$$

In the high-energy limit $k \gg m$, the electron mass can effectively be neglected. With the target particle at rest, and using energy-momentum conservation, $k+p = k'+p'$, the invariant matrix element in Equation (1.2.7) can be simplified as,

$$\langle \mid \bar{M} \mid^2 \rangle = \frac{e^4M^2}{E_1E_3\sin^4\theta/2}\left(\cos^2\theta/2 - \frac{q^2}{2M^2}\sin^2\theta/2\right), \quad (1.2.8)$$

and hence the differential cross-section from Equation (1.2.2) can be written as,

$$\frac{d\sigma}{d\Omega} = \frac{\alpha^2}{4E_1^2 \sin^4\theta/2}\frac{E_3}{E_1}\left(\cos^2\theta/2 - \frac{q^2}{2M^2}\sin^2\theta/2\right), \tag{1.2.9}$$

where $\alpha = e^2/\hbar c \approx 1/137$ is the fine structure constant. For the elastic scattering, the quantities E_3 and q^2 are given by,

$$\frac{E_3}{E_1} = \frac{M}{M + E_1(1-\cos\theta)}, \qquad q^2 = -\frac{2ME_1^2(1-\cos\theta)}{M + E_1(1-\cos\theta)} \tag{1.2.10}$$

so that the cross-section depends on only a single independent variable, θ. This seems to be the product of Rutherford-like scattering cross-section with some additional factors. The ratio E_3/E_1 gets close to unity at small scattering angles ($\theta \to 0$) where the target recoil is small. It becomes smaller as θ increases, falling to $E_3/E_1 \approx M/2E_1$ at large scattering angles, $\theta \to \pi$, where the target recoil is a maximum.

The cross-section of Equation (1.2.9) represents electron scattering from a point-like, spin-1/2, Dirac particle. Such a particle would have an intrinsic magnetic moment of magnitude, $\mu = e\hbar/(2Mc)$, *i.e.*, $\mu = 1$ in units of the nuclear magneton $\mu_N = e\hbar/(2Mc)$. If the spin-1/2 target particle is replaced by a spin 0 target particle, the $\sin^2\theta/2$ term in Equation (1.2.9) gets omitted and the cross-section becomes,

$$\left(\frac{d\sigma}{d\Omega}\right)_{Mott} = \frac{\alpha^2}{4E_1^2 \sin^4\theta/2}\frac{E_3}{E_1}\cos^2\theta/2, \tag{1.2.11}$$

known as the *Mott cross-section* with the additional recoil factor E_3/E_1. Since the spin 0 particle has no intrinsic magnetic dipole moment, the $\sin^2\theta/2$ term in Equation (1.2.9) must be due to scattering from the intrinsic magnetic dipole moment of the spin-1/2 target particle. The $\cos^2\theta/2$ term, common to both Equations (1.2.9) and (1.2.11), must be due to scattering from the Dirac particle electric charge.

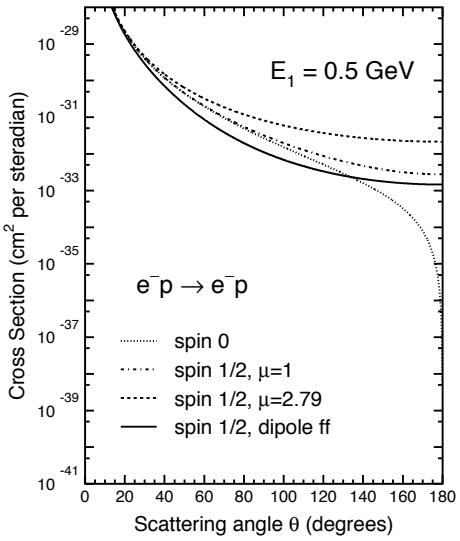

Figure 1.2. Differential cross-section $d\sigma/d\Omega$ for elastic $e^{-}p$ scattering in the lab frame, for electron beam energy of 0.5 GeV, for various assumptions about the spin and structure of the target proton [9].

Examples of the cross-sections $d\sigma/d\Omega$ and $d\sigma/d\Omega_{spin0}$ predicted by Equations (1.2.9) and (1.2.11) for a point-like Dirac target and a point-like spin-0 target are shown in Figure 1.2. For small scattering angles, θ, the spin-0 and spin-1/2 cross-sections are identical. The effect of the magnetic scattering term $(-q^2/2M^2)\sin^2\theta/2$ becomes evident at large scattering angles; the spin-0 cross-section falls to zero as $\theta \to \pi$, while the spin-1/2 cross-section remains finite. The cross-section of the spin-1/2 target with the assumption of the dipole form factor is also shown in Figure 1.2.

1.2.1 Elastic Electron-Proton Scattering

Detailed study of the nucleons is very important to understand the nucleus. In the mid-1950s, a series of experiments led by Robert Hofstadter at Stanford University established electron scattering as a powerful technique for exploring nuclear structure [10–12]. In particular, this work established that the proton has an extended charge distribution and measured its size. One of the main advantages of this technique

is that it can reveal the electromagnetic structure of a nucleon or nucleus. The small cross-sections associated with electromagnetic processes necessitate a very high-luminosity experiment with intense electron beams. Despite this limitation, electron scattering or lepton scattering more generally is a precision probe of nuclear structure.

1.2.1.1 Born Approximation

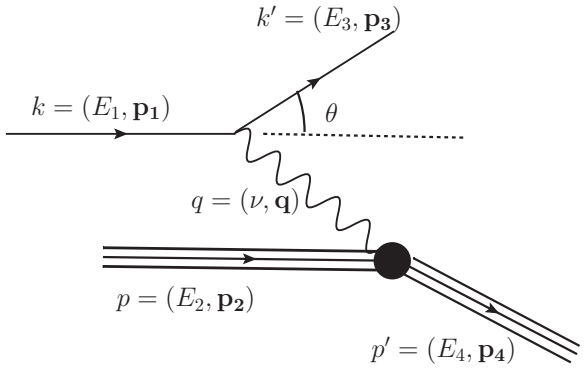

Figure 1.3. Leading order Feynman diagram for elastic electron-proton scattering in the one-photon exchange (Born) approximation.

The basic electron-proton scattering is the elastic scattering in the one-photon exchange (OPE) approximation [7]. That is, in the reaction $e^- + p \rightarrow e^- + p$, the stationary proton is probed by the electron by exchanging only one photon, while the struck nucleon stays in its ground state and the energy and momentum of the electron-nucleon system are conserved. If the proton is a point charge q with Dirac magnetic moment $q\hbar/2Mc$, one would have the same Equation (1.2.9) for the differential cross-section. But, in reality, the proton is not a point charge. It has an internal structure with quarks and gluons. Therefore, modifications are needed to the matrix element accordingly by keeping the electron tensor as is and addressing the proton tensor separately:

$$|\bar{M}|^2 = \frac{e^4}{q^4} L_e^{\mu\nu} W_{\mu\nu}^{proton} \tag{1.2.12}$$

The black solid circle in Figure 1.3 indicates that the QED vertex factor is to be modified to take into account the nucleon's internal electromagnetic structure. By applying the Feynman rules for QED, the invariant amplitude for elastic $e^- N$ scattering can be read from the diagram as,

$$-iM = \bar{u}(k')(ig_e\gamma^\mu)u(k)\left(-i\frac{g_{\mu\nu}}{q^2}\right)\bar{u}(p')(-ig_e\Gamma^\nu)u(p). \tag{1.2.13}$$

Here it is noted that one of the electron vertex factors, γ^μ from the lepton-lepton scattering in Equation (1.2.3), which represents scattering from a spin-1/2 point particle, is replaced by the nucleon vertex factor, or current Γ^ν, which describes a spin-1/2 composite proton. Its magnetic moment is determined by the combined spin and orbital angular momentum of three valence quarks, the surrounding sea of transient quark-antiquark pairs and gluons that fluctuate in and out of existence in the strong color field of the valence quarks. Therefore, the nucleon vertex factor Γ^ν in Equation (1.2.13) can be generalized as,

$$\Gamma_\mu = \gamma_\mu F_1(Q^2) + (iF_2(Q^2) + \tilde{F}_2(Q^2)\gamma_5)\sigma_{\mu\nu}q^\nu + \tilde{F}_3(Q^2)(q_\mu \not{q} - q^2\gamma_\mu)\gamma_5, \tag{1.2.14}$$

by noting that the electromagnetic current is conserved [13]. The objects $F_1, F_2, \tilde{F}_2, \tilde{F}_3$ are called *form factors*. These form factors are Lorentz invariant quantities which are the functions of $Q^2 = -q^2 = (p - p')^2$. Here is the summary of the physics of these form factors.

1.2.1.2 Charge Form Factor, $\mathbf{F}_1$

This form factor is known as the Dirac form factor. First, consider that the initial and final states of the fermion are the same. In this situation, $p = p'$ and $s = s'$. *i.e.*, the momentum transfer 4-vector q vanishes and therefore, $q^2 = 0$. Therefore, the

matrix element of the electromagnetic current operator:

$$< p', s'|j_\mu(x)|p, s >= \frac{e^{-iq\cdot x}}{\sqrt{2E_pV}\sqrt{2E_{p'}V}}\bar{u}_{s'}(p')e\Gamma_\mu(p,p')u_s(p) \tag{1.2.15}$$

become,

$$\begin{aligned} < p, s|j_\mu(x)|p, s > &= \frac{eF_1(0)}{2E_pV}\bar{u}_s(p)\gamma_\mu u_s(p) \\ &= \frac{eF_1(0)p^\mu}{E_pV} \end{aligned} \tag{1.2.16}$$

The normalization of the spinors $\bar{u}_r(p)u_s(p) = -\bar{v}_r(p)v_s(p) = 2m\delta_{rs}$ and the Gordon identity, $m\bar{u}(p)\gamma^\mu u(p) = p^\mu\bar{u}(p)u(p)$ were used. Assuming a purely electric field in which $\mathbf{A} = 0$, and only $A^0 = \phi$ is non-vanishing, the quantity, $p^0 = E_p$.

$$- < j_\mu > A^\mu = -\frac{eF_1(0)\phi}{V}. \tag{1.2.17}$$

The Lagrangian term is $-\rho\phi$, where ρ is the charge density. Thus, here $\rho = eF_1(0)/V$. In a volume V, which conclude that

$$eF_1(0) = Charge\ \ of\ \ the\ \ particle.$$

where $F_1 = Q_c$ is the charge in fundamental unit of e, of the particle whose vertex is being considered. Therefore, $F_1(q^2)$ is often called the *charge form factor*. In a more general form for the photon field A^μ, which is non-vanishing $\mathbf{A}$ and q^2, the matrix element in the Equation (1.2.15) can be rewritten using the Gordon identity as,

$$< p', s'|j_\mu(x)|p, s >= \frac{e^{-iq\cdot x}}{\sqrt{2E_pV}\sqrt{2E_{p'}V}}\frac{eF_1(q^2)}{2m}\bar{u}_{s'}(p')[(p+p')_\mu - i\sigma_{\mu\nu}q^\nu]u_s(p). \tag{1.2.18}$$

In the non-relativistic case, *i.e.*, when $E_p \approx E_{p'} \approx m$, the dominant contribution from $(p+p')_\mu$ in the square bracket reduces to the electric charge, which has been discussed above. The contribution of the other term, $i\sigma_{\mu\nu}q^\nu$ to the matrix element is

obtained by coupling this term to a photon field A^{μ} [13]. By expanding $F_1(q^2)$ of the result in a Taylor series around $q^2 = 0$, and taking the inverse Fourier transform for the first constant term, the matrix element of the operator is given in [13] as,

$$\frac{1}{V}\frac{eF_1(0)}{2m}\sigma \cdot \mathbf{B} = \frac{1}{V}\frac{eQ_c}{2m}\sigma \cdot \mathbf{B}, \tag{1.2.19}$$

where now $\mathbf{B}$ is the magnetic field in co-ordinate space. This is exactly the magnetic moment of a particle in a volume, V,

$$\mu_D = \frac{eQ_c}{2m}\sigma = \frac{eQ_c}{m}\mathbf{S}, \tag{1.2.20}$$

where $\mathbf{S} = \frac{1}{2}\sigma$ is the spin vector of the particle. $\hbar$ = c = 1. This contribution to the magnetic moment, coming from the charge form factor , is called the *Dirac magnetic moment*, μ_D. Usually, the magnetic moment is expressed in terms of the Lande g-factor, which is defined by,

$$\mu = \frac{eQ_c}{2m} g\ \mathbf{S}, \tag{1.2.21}$$

where eQ_c is the charge of the particle and m is its mass. By comparing above Equations (1.2.20) and (1.2.21), it shows that the charge form factor, $F_1(0) = Q_c$ gives the total charge of the particle, resulting in $g = 2$ for the g-factor.

1.2.1.3 Anomalous Magnetic Moment, $\mathbf{F}_2$

This form factor is known as the Pauli form factor. The contribution to the magnetic moment from the Pauli form factor is called the *anomalous magnetic moment*, which is given by μ_A [13]:

$$\mu_A = -eF_2(0)\sigma = -2eF_2(0)\mathbf{S}. \tag{1.2.22}$$

By comparing the above Equations (1.2.21) and (1.2.22), the form factor, F_2 gives a contribution of $-\frac{4m}{Q_c}F_2(0)$ to the g-factor. Therefore, the Lande g-factor for a particle with a charge eQ_c, which is the contribution to the magnetic moment coming from both Dirac and Pauli form factors, is obtained by summing the two contributions:

$$g = 2 - \frac{4m}{Q_c}F_2(0). \tag{1.2.23}$$

For the protons, the contribution from the anomalous magnetic moment is smaller and therefore, $g>0$. However, the uncharged particles such as neutrons also can have magnetic moments. For such particles, the anomalous part of the magnetic moment is larger and therefore, $g<0$.

The g-factor is 2 for Dirac particles (point-like). Having $g-2$ non-zero as in Equation (1.2.23) is due to the anomalous magnetic moment, which arises from the internal structure of the nucleus. This knowledge of the nucleon anomalous magnetic moment was the first hint that it has a substructure, found by Otto Stern's measurement in 1933 [4] as mentioned in Section 1, long before Hofstadter's scattering experiments.

Since a non-zero Electric Dipole Moment, $\tilde{F}_2$, and Anapole Moment, $\tilde{F}_3$ [14, 15] are parity-odd, these form factors can appear only for parity-violating interactions. Because QED is parity invariant, the discussion about these form factors is beyond the scope of this dissertation. More details about $\tilde{F}_2$ and $\tilde{F}_3$ can be found in [13].

1.2.1.4 Elastic Form Factors

The only form factors that appear in pure QED interactions from the expression (1.2.14) are F_1 and F_2. Therefore, the vertex function becomes,

$$\Gamma^\nu = \gamma^\nu F_1(q^2) + i\sigma^{\nu\alpha}\frac{q_\alpha}{2M}F_2(q^2). \tag{1.2.24}$$

These form factors are fundamental properties of the nucleon, representing the effect of its structure on its response to electromagnetic probes such as electrons. As explained in Section 2.1, $F_1(0) = 1$ gives the proton charge in units of e, and $F_2(0)$ gives the anomalous magnetic moment.

By substituting Equation (1.2.24) into Equation (1.2.13) and then using Equation (1.2.2), one can calculate the differential cross-section for unpolarized electron-proton elastic scattering in the lab frame similar to Equation (1.2.9) as,

$$\left(\frac{d\sigma}{d\Omega}\right)_{lab} = \left(\frac{\alpha^2}{4E_1^2 \sin^4 \frac{\theta}{2}}\right) \frac{E_3}{E_1}\left[\left(F_1^2 - \frac{q^2}{4M^2}F_2^2\right)\cos^2\frac{\theta}{2} - \frac{q^2}{2M^2}(F_1 + F_2)^2 \sin^2\frac{\theta}{2}\right]. \tag{1.2.25}$$

Another commonly used choice of the form factors are the linear combinations,

$$\begin{aligned} G_E(q^2) &= F_1(q^2) - \tau F_2(q^2) \\ G_M(q^2) &= F_1(q^2) + F_2(q^2) \\ \tau &= \frac{Q^2}{4M^2} = \frac{-q^2}{4M^2}, \end{aligned} \tag{1.2.26}$$

which are defined in such a way that no interference terms of F_1 and F_2 appear in the cross-section as in Equation (1.2.25). $G_E(q^2)$ and $G_M(q^2)$ are known as Sachs electric and magnetic form factors. The deuteron, as a spin-1 object has one additional form factor: the charge quadruple form factor, G_Q which is related to the deformation of the deuteron from the ground state wave functions.

Then the nucleon vertex factor can be re-expressed in terms of Sachs form factors using Equation (1.2.26) as,

$$\Gamma^\nu = G_M \gamma^\nu + \frac{G_E - G_M}{2M(1+\tau)}(p'^\nu + p^\nu). \tag{1.2.27}$$

The differential cross-section on Equation (1.2.25) for electron-proton elastic scattering in the lab frame can also be redefined in terms of Sachs form factors as,

$$\left(\frac{d\sigma}{d\Omega}\right)_{lab} = \left(\frac{\alpha^2}{4E_1^2 \sin^4 \frac{\theta}{2}}\right) \frac{E_3}{E_1} \cos^2 \frac{\theta}{2} \left(\frac{G_E^2 + \tau G_M^2}{1+\tau} - 2\tau G_M^2 \tan^2 \frac{\theta}{2}\right). \qquad (1.2.28)$$

This is known as the *Rosenbluth formula*. The spatial distributions of charge and magnetization of the proton and neutron are described by the electric (or charge) form factor G_E and the magnetic form factor G_M, respectively, in a particular Lorentz frame, called the Breit (or brick wall) frame, defined by $\mathbf{p}' = -\mathbf{p}$. There is no energy transferred to the proton in this frame, and it behaves as if the electron had bounced off a brick wall. However, this has no physical meaning. In contrast, the recoil of the proton makes it impossible to interpret the Fourier transforms of G_E and G_M as the spatial charge and magnetic moment distributions. In this case, more complicated forms of the form factors have tried using different theoretical models. Kelly [16] has tried to model the charge and magnetization densities at the rest frame.

1.2.1.5 Radiative Corrections

Radiative corrections to the measured cross-section are necessary to obtain the Born-level cross-section which measures the form factors from the Rosenbluth separation technique. The standard radiative corrections are QED and can be determined from the first principles. However, at the higher order radiative correction terms (hard two-photon exchange, etc.), it is not straightforward and model-dependent to a certain extent, because of uncertain hadron structure. Starting from the "recipe" of Mo and Tsai [17] on the point-like nucleons, the radiative correction model was updated in the recent work by Maximin and Tjon [18], including the structure of

the proton by introducing the proton form factors and eliminating some of the soft photon approximations made by [17]. The various radiation correction processes involving the electron and nucleon are shown in the diagrams of Figures 1.4 and 1.5, respectively.

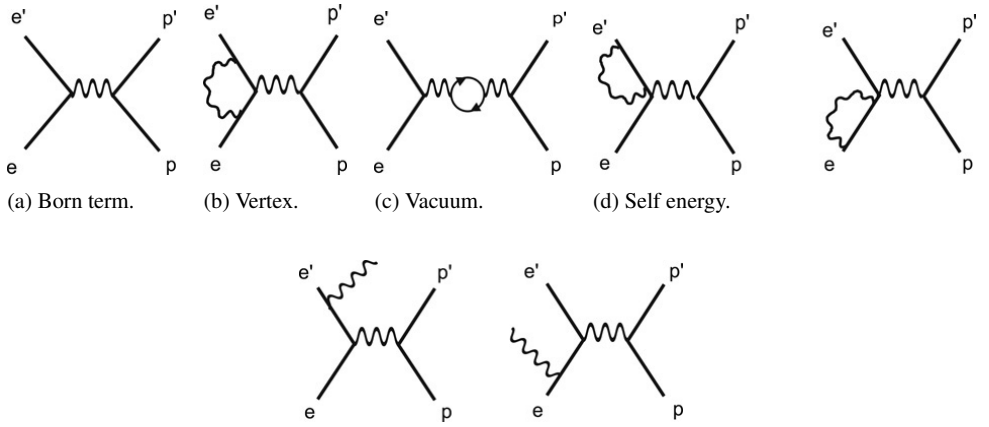

Figure 1.4. Born-term and lowest-order radiative correction graphs for the electron in elastic *ep* scattering [19].

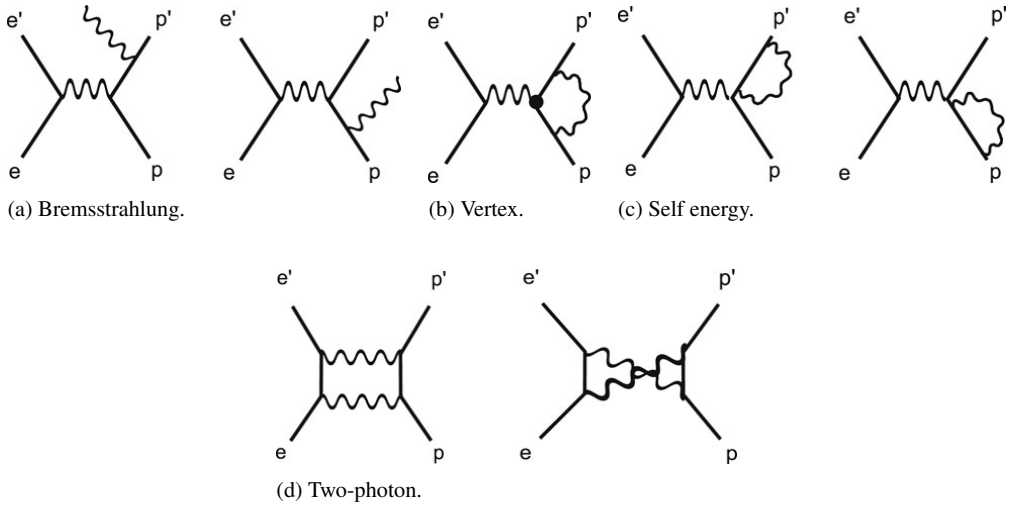

Figure 1.5. The lowest-order radiative correction graphs for the proton in elastic *ep* scattering [19].

At order α^2, the radiative corrections to the electron vertex in elastic *ep* scattering include the radiation of virtual photons, such as vertex corrections (b), one-loop vacuum polarization (c), electron self-energy corrections (d), and the radiation of real photons; *i.e.*, internal Bremsstrahlung (e) as shown in Figure 1.4. Similarly, the proton vertex includes the processes such as internal Bremsstrahlung (a), vertex corrections (b), proton self-energy (c), and two-photon (one soft and one hard photon) exchange (e), which are called Coulomb distortion effects, as shown in Figure 1.5.

The internal Bremsstrahlung is the case in which the incident or scattered electron radiates a real photon in the field of the nucleon participating in the scattering. In addition, there are corrections coming from external Bremsstrahlung, in which the incident and scattered electrons radiate due to interactions with the material, before and after the primary scattering. While the internal Bremsstrahlung correction is coherent with the Born-level scattering amplitude, making the amplitudes interfere, the external Bremsstrahlung correction is incoherent and factorizes from the Born-level process.

The virtual part of the electron radiative correction depends on Q^2. As a factorial correction to the cross-section independent of ϵ, G_E would be corrected by the same factor as G_M, hence G_E/G_M would not be affected. The real part of the radiative correction, Bremsstrahlung corrections, on the other hand, are energy, and, therefore, Q^2 and ϵ dependent. Therefore, these corrections modify the cross-section in an ϵ dependent manner in which the extraction of G_E/G_M is affected. The radiative contributions from the proton vertex that include internal Bremsstrahlung, the virtual part of the proton, as well as the Coulomb distortion effect (two-photon exchange in one soft photon and one hard photon) are relatively small [20], but strongly ϵ dependent. Therefore, in general, the radiative corrections to the cross-section in a Rosenbluth experiment are strongly ϵ-dependent. Typically the radiative corrections change the cross-sections in the range of 10-30%.

1.2.1.6 Two-Photon Exchange (TPE)

Figure 1.6 shows the box and cross-box two-photon exchange diagrams in which both photons are "hard." This process is generally neglected in the standard radiative correction procedure. Since the calculation of the TPE process in elastic eN scattering is sensitive to the structure of the nucleon through the virtual intermediate hadronic state, it is strongly model-dependent and cannot be calculated exactly, in contrast to the case where one of the two photons is "soft," which is part of the standard radiative corrections and is well understood. Higher order corrections to the Born approximation were considered in the past [21, 22], which contributes to the cross-section by order of 1-2 %. However, these estimates give a realistic description of nucleon structure only at low momentum transfers up to $Q^2 \leq 1$ GeV^2, whereas the nucleon structure is largely unknown at the higher values of Q^2. From a general analysis of elastic electron-proton scattering and using the usual definitions,

$$P = \frac{p + p'}{2}, \qquad K = -\frac{k + k'}{2}, \qquad \nu = K \cdot P \tag{1.2.29}$$

$$q = k - k' = p' - p, \qquad Q^2 = -q^2, \tag{1.2.30}$$

for the box diagram of two-(and multi) photon exchange contributions to elastic electron-proton scattering (see Figure 1.6),

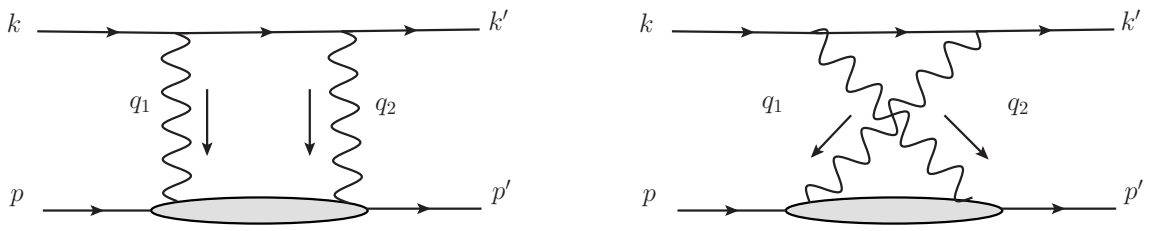

Figure 1.6. Box and crossed-box diagrams for elastic electron-proton scattering in the two-photon exchange [23]. The total four-momentum transfer to the nucleon is $q = k - k' = q_1 + q_2$.

Guichon and Vanderhaeghen [23] have shown that the new nucleon vertex factor Γ^{ν}_{tpe} can be written as,

$$\Gamma^{\nu}_{tpe} = \tilde{G}_M \gamma^{\mu} - \tilde{F}_2 \frac{P^{\mu}}{M} + \tilde{F}_3 \frac{\gamma \cdot K P^{\mu}}{M^2}, \tag{1.2.31}$$

where $\tilde{G}_M,\ \tilde{F}_2,\ \tilde{F}_3$ are complex functions of ν and Q^2. The additional $\tilde{F}_3$ term is generated by the TPE contribution and the Born amplitudes are modified in the presence of TPE as,

$$\tilde{G}_M(\nu, Q^2) = G_M(Q^2) + \delta\tilde{G}_M, \qquad \tilde{G}_E(\nu, Q^2) = G_E(Q^2) + \delta\tilde{G}_E \tag{1.2.32}$$

$$\tilde{F}_2(\nu, Q^2) = F_2(Q^2) + \delta\tilde{F}_2, \qquad \tilde{G}_E(\nu, Q^2) = \tilde{G}_M(\nu, Q^2) - (1+\tau)\tilde{F}_2(\nu, Q^2)$$

$$\tilde{F}_3(\nu, Q^2) = 0 + \delta\tilde{F}_3,$$

giving the new complex amplitudes. In the Born approximation, one obtains,

$$\tilde{G}_M^{Born}(\nu, Q^2) = G_M(Q^2), \qquad \tilde{F}_2^{Born}(\nu, Q^2) = F_2(Q^2), \qquad \tilde{F}_3^{Born}(\nu, Q^2) = 0 \tag{1.2.33}$$

and Equation (1.2.31) reduces to the Born approximation vertex factor given in Equation (1.2.27). Further, using standard techniques, they have derived a generalized formalism for the elastic electron-proton scattering cross-section, in terms of form factors as,

$$\begin{aligned} \frac{\sigma_r}{G_M^2} = 1 + \frac{\epsilon}{\tau}\frac{G_E^2}{G_M^2} + 2Y_M + 2\epsilon\frac{G_E}{\tau G_M}Y_E \\ + 2\epsilon\left(1 + \frac{G_E}{\tau G_M}\right)Y_3 + \wp(e^4), \end{aligned} \tag{1.2.34}$$

$$Y_M \equiv \Re(\delta\tilde{G}_M/G_M) \qquad Y_E \equiv \Re(\delta\tilde{G}_E/G_M), \qquad Y_3 \equiv (\nu/M^2)\Re(\tilde{F}_3/G_M),$$

where $\delta\tilde{G}_M$ and $\delta\tilde{G}_E$ are the modifications to the Born approximation as in Equation (1.2.32). The quantities σ_r is the reduced cross-section, ϵ is the virtual photon polarization parameter, and Y_M, Y_E, Y_3 are the 2γ-amplitudes. As seen in Equation (1.2.34), the TPE contribution to G_E, $\delta\tilde{G}_E$ has an ϵ dependence that has the same sign as the G_E contribution to the cross-section and, in combination with $\delta\tilde{G}_M$, it represents an ϵ-dependent correction to the cross-section.

Similarly, the generalized formalism for elastic positron-proton scattering cross-section in terms of the form factors can be obtained by changing the sign in front of the 2γ-amplitudes in Equation (1.2.34) as,

$$\begin{aligned}\frac{\sigma_r}{G_M^2} = 1 + \frac{\epsilon}{\tau}\frac{G_E^2}{G_M^2} - 2Y_M - 2\epsilon\frac{G_E}{\tau G_M}Y_E \\ - 2\epsilon\left(1 + \frac{G_E}{\tau G_M}\right)Y_3 + \wp(e^4).\end{aligned} \tag{1.2.35}$$

The formalism includes the possibility that the interference of the TPE amplitude with the one-photon exchange amplitude is comparable in size to the G_E^2 term in the unpolarized cross-section at large Q^2. This motivates experimentalists to move forward their work and consider new experiments beyond the Born approximation [24–26].

1.2.2 Inelastic Electron-Proton Scattering

As the energy of the incoming electron is increased, and hence the average value of $|q^2|$ increases, the elastic scattering process $e^-p \to e^-p$ gradually gives way to *inelastic* scattering $e^-p \to e^-X$ where, as a result of the collision, the proton target breaks up into a hadronic system X containing, for example, a proton plus one or more pions. When $|q^2|$ is large ($|q^2| \gg M^2$), *i.e.*, the energy and/or momentum transferred to the proton target via the virtual photon is large, this is termed *deep-inelastic scattering* (DIS).

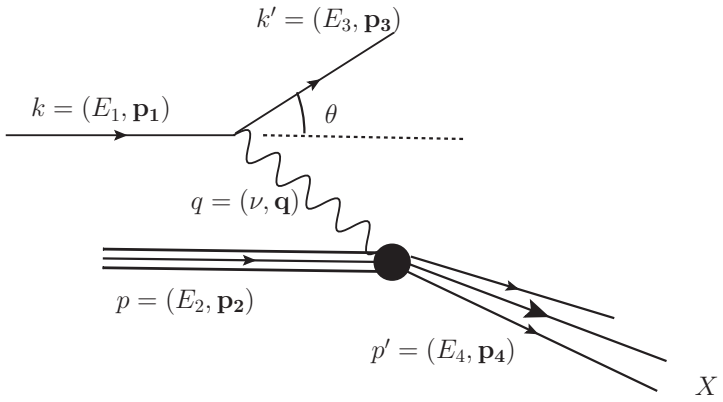

Figure 1.7. Leading order Feynman diagram for inelastic $e^- p \to e^- X$ scattering.

For inelastic scattering, $e^- p \to e^- X$, the invariant mass of the final state hadronic system, W is no longer fixed to be the proton mass M, *i.e.*, the constraint $p_4^2 = M^2$ is no longer valid. Therefore, the invariant mass of the final state W or the "missing mass" in inclusive scattering becomes an important quantity. Unlike elastic scattering, there are two independent variables, q^2 and $\nu = \frac{p \cdot q}{M}$. The invariant mass W of the final hadronic system is related to ν and q^2 by,

$$W^2 = (p+q)^2 = M^2 + 2M\nu + q^2.$$

Since the final state is not a single fermion in inelastic scattering, evaluating the inelastic cross-section in Figure 1.7 has more complex structure than *ep* elastic scattering. The leptonic part and the photon propagator in diagram 1.7 is left unchanged. The proton tensor $W_{\mu\nu}^{proton}$, is now composed of four dimensionless structure functions, two symmetric and two antisymmetric ones [27]. Measuring the experimental cross-sections, one can access different structure functions depending on our control of the spin degrees of freedom [28].

The unpolarized differential cross-section for inelastic electron-proton scattering, $ep \to eX$, neglecting the mass of the electron, is given in [6] as,

$$\frac{d^2\sigma}{dE'd\Omega} \mid_{lab} = \frac{\alpha^2}{4E^2 \sin^4 \frac{\theta}{2}} \left\{ W_2(\nu, q^2) \cos^2 \frac{\theta}{2} + 2W_1(\nu, q^2) \sin^2 \frac{\theta}{2} \right\} \tag{1.2.36}$$

In Figure 1.8, the first peak at W equal to the proton mass, is the elastic peak in which the proton does not get excited. With increasing of q^2 (and hence W), the broader peaks can be seen when the proton is excited to resonant baryon states. When the proton is excited into a Δ state producing an extra π-meson by the $ep \to e\Delta^+ \to ep\pi^0$ or $en\pi^+$ reaction, the invariant mass is $W^2 = M_\Delta^2$ and a peak is shown at the Δ mass at 1232 MeV. When q^2 is very large and hence at lager W, beyond the resonances, the proton starts to break up completely and the complicated multi-particle states with large invariant mass result in a smooth distribution in W.

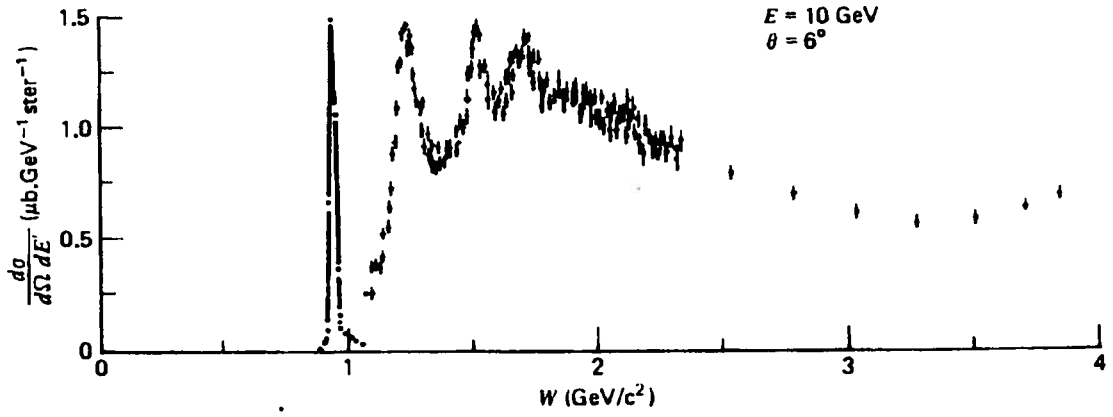

Figure 1.8. The $ep \to eX$ cross-section as a function of the missing mass W. Data are from SLAC E61 [29]. The elastic peak is reduced by large scaler to put on the same scale with the rest.

SECTION 2

OVERVIEW OF EXPERIMENTAL DATA

2.1 Electromagnetic Form Factor Measurements

The form factor measurements became very important in order to understand the structure of the nucleus. In the last few decades with technological improvements, more and more experiments and new experimental methods have been conducted. In the following Sections 2.1.1, 2.1.2.1 and 2.1.2.2, the experimental methods of measuring the elastic proton form factor ratio, G_E/G_M will be briefly discussed. Existing proton and neutron form factor data will also be presented and discussed.

2.1.1 Elastic e-N Scattering : Rosenbluth Cross-Section

In the one-photon exchange (OPE) approximation, the form factors, G_E and G_M are experimentally accessible through the elastic $e^- N$ scattering cross-sections given by Equation (1.2.28), which is known as the *Rosenbluth Formula* [30]. The pioneering measurements were done more than fifty years ago at SLAC [12]. The $e^- p \to e^- p$ cross-section Equation (1.2.28) represents scattering from a composite, spin-$\frac{1}{2}$, proton. In this form, it is clear that the cross-section is the product of the Mott cross-section, which is scattering of spin-$\frac{1}{2}$ electrons from point-like, spinless charged particles, and a "structure" factor determined by the form factors. Mott cross-section is shown in Equation (1.2.11) with an additional recoiling factor, E_3/E_1. By defining the "reduced" cross-section σ_r,

$$\sigma_r = \frac{d\sigma/d\Omega}{d\sigma/d\Omega_{Mott}} = \frac{G_E^2(Q^2) + \tau G_M^2(Q^2)}{1+\tau} + 2\tau G_M^2(Q^2) \tan^2 \frac{\theta}{2} \tag{2.1.1}$$

$$\epsilon = \left[1 + 2(1+\tau)\tan^2\frac{\theta}{2}\right]^{-1} \tag{2.1.2}$$

$$(1+\tau)\epsilon\sigma_r = \epsilon G_E^2 + \tau G_M^2. \tag{2.1.3}$$

It is clear from Equation (2.1.3) that the form factors can be extracted separately by measuring the electron-nucleon elastic scattering cross-section at fixed τ (by varying the incoming beam energy, E and the scattered electron energy, E_3) and varying the scattering angle θ. A fit of σ_r vs ϵ yields a straight line with slope proportional to G_E^2 and intercept proportional to G_M^2. This procedure is called the *Rosenbluth separation technique* or L/T separation. L/T refers to the separation between longitudinally and transversely polarized (virtual) photons, with the degree of longitudinal polarization of the virtual photon characterized by ϵ. However, the factor, $\tau = \frac{Q^2}{4M_N^2}$ (with M_N the nucleon mass) increases with Q^2 and eventually makes a separation of the two terms difficult.

Because the physical nucleon is a composite object with a rich substructure, in the non-relativistic limit of $Q^2 \ll M^2$, the long-wavelength virtual photon has insufficient resolution to be sensitive to this detailed structure. The nucleon should behave like a point particle with charge ze ($z = 1$ for the proton or 0 for the neutron) and magnetic moment $e(z+k)/2M_N$, where k is the anomalous magnetic moment. In this limit, the four-momentum transfer $q = (E_1 - E_3, \mathbf{q})$ becomes approximately a pure three-momentum transfer: $q \approx (0, \mathbf{q})$ so that the reaction can be viewed as scattering of the electron by the static charge distribution of a stationary nucleon. In other words, at low Q^2, three-vector $\mathbf{q^2} \cong Q^2$ and the Rosenbluth formula, Equation (2.1.1), becomes,

$$\frac{d\sigma/d\Omega}{d\sigma/d\Omega_{Mott}} = G_E^2(\mathbf{q^2}) + 2\tau G_M^2(\mathbf{q^2})\tan^2\frac{\theta}{2}, \tag{2.1.4}$$

where $G_E(\mathbf{q}^2)$ and $G_M(\mathbf{q}^2)$ now depend only on the three-momentum squared, $\mathbf{q^2}$. Comparing with the original point-like cross-section of Equation (1.2.9), it seems that,

at low Q^2, the $\cos^2\theta/2$ term associated with scattering from the electric charge of the target is multiplied by a factor $G_E(\mathbf{q})^2$, while the $\sin^2(\theta/2)$ term associated with scattering from its magnetic moment is multiplied by a factor $G_M(\mathbf{q})^2$. The electric form factor dominates the cross-section in this limit, since the G_M^2 term in the cross-section is multiplied by τ, which is small at smaller Q^2. Therefore, neglecting the G_M^2 term, the Rosenbluth formula (2.1.4) can be further simplified to,

$$\frac{d\sigma/d\Omega}{d\sigma/d\Omega_{Mott}} = (G_E(\mathbf{q}^2))^2. \tag{2.1.5}$$

Comparing the cross-section ratio at low Q^2, Equation (2.1.5), of electron scattering from a static charge distribution to the electron scattering from a point charge (see [6], Equation (8.1)), it is confirmed that the static charge distribution, $G_E(\mathbf{q^2})$ is related to the Fourier transform of the proton's charge distribution $\rho(\mathbf{x})$.

$$G_E(Q^2) \cong G_E(\mathbf{q^2}) = \int \rho(\mathbf{x}) e^{i\mathbf{q}\cdot\mathbf{x}}\, d^3\mathbf{x}. \tag{2.1.6}$$

Expanding the exponential in powers of $\mathbf{q}$ for a spherically symmetric charge distribution, $\rho = \rho(r \equiv |\mathbf{x}|)$, this becomes

$$\begin{aligned} G_E(\mathbf{q^2}) &= \int_0^\infty \rho(r) r^2\, dr \int_0^\pi \sin\theta\, d\theta \left(1 + i|\mathbf{q}| r\cos\theta - \frac{1}{2}\mathbf{q}^2 r^2 \cos^2\theta + ...\right) \\ G_E(\mathbf{q^2}) &= 1 - \frac{1}{6}\mathbf{q}^2 \int |\mathbf{x}|^2 \rho(|\mathbf{x}|)\, d^3\mathbf{x} + ... \\ &= 1 - \frac{1}{6}\mathbf{q}^2 \left\langle r^2 \right\rangle + ... \end{aligned} \tag{2.1.7}$$

meaning that, at leading order in $\mathbf{q}^2$, the electric form factor simply measures the r.m.s. charge radius of the nucleon. From the above equation,

$$\left\langle r^2 \right\rangle = -6 \frac{dG_E}{dQ^2}|_{Q^2=0} \tag{2.1.8}$$

i.e., in electron scattering, the root-mean-square radius, r is defined in terms of the slope of the electric form factor at $Q^2 = 0$. Similarly, Equation (2.1.4) shows that in the non-relativistic limit, the magnetic form factor $G_M(q^2)$ can also be interpreted as the Fourier transform of the nucleon's magnetic moment distribution $\mu(\mathbf{x})$,

$$G_M(q^2) \cong G_M(\mathbf{q^2}) = \int \mu(\mathbf{x}) e^{i\mathbf{q}\cdot\mathbf{x}}\, d^3\mathbf{x}. \tag{2.1.9}$$

In the limit of $Q^2 = 0$, Equations (2.1.6) and (2.1.9) show that $G_E(0)$ is the total charge measured in units of $+e$ (+1 for protons and 0 for neutrons) and $G_M(0)$ is the magnetic moment measured in units of the nuclear magneton $\mu_N \equiv e\hbar/2M_p$ (+2.79 for protons and -1.91 for neutrons).

2.1.2 Double-Polarization Observables

Since the magnetic moment of the electron interacts with the magnetic moment distribution of the nucleon in the scattering process, it is useful to know how the reaction depends on the initial and final spin orientations of both the electron and the nucleon. As it turns out, the spin dependence of the scattering amplitude gives rise to a set of polarization observables directly related to the form factors. These observables can be used as an alternative or a complement to cross-section measurements in determining the form factors.

It was pointed out already in 1968 by Akhiezer and Rekalo [31] that the best way to obtain the proton charge form factor is with polarization experiments, especially by measuring the polarization of the recoil proton. Using the cross-section method at large Q^2 makes the separation of the charge form factor difficult because the contribution from the τG_M^2 term in the cross-section Equation (2.1.3) increases with Q^2 and becomes dominated by G_M. In a further paper in 1974, Akhiezer and Rekalo [32] discussed the interest of measuring an interference term of the form $G_E G_M$ by

measuring the transverse component of the recoil proton polarization in the $\vec{e}p \to e\vec{p}$ reaction at large Q^2, to obtain G_E in the presence of a dominating G_M. In 1969, Dombey [33] also discussed the possibility of measuring polarization observables in elastic scattering with a polarized lepton on a polarized target. Furthermore, in 1982, Arnold, Carlson and Gross [34] emphasized that the best way to measure the electric form factor of the neutron would be to use the ${}^2H(\vec{e}, e'\vec{n})p$ reaction. Below is a brief discussion of both methods, the recoil-polarization method and the polarized target, to measure the elastic nucleon form factors highlighting their advantages and dis-advantages.

2.1.2.1 Polarization-Transfer Technique

The development of polarized beams, targets and recoil polarimeters in the 1990's enabled access to the form factor ratio G_E/G_M through a spin correlation in double-polarization experiments. With the high-intensity polarized beams, investigations of the elastic scattering dependence on the initial and/or final spin orientation of the electron and the nucleon were started. If the electron beam is longitudinally polarized, and the nucleon target unpolarized, the scattering can transfer some polarization to the recoiling nucleon, which can then be measured with a suitable technique. This class of experiments is called polarization-transfer, or recoil-polarization.

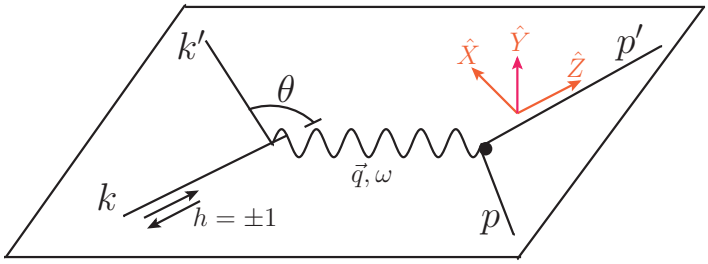

Figure 2.1. Kinematical variables for polarization-transfer from a longitudinally polarized electron to a proton with exchange of a virtual photon.

Figure 2.1 shows the kinematical variables for the polarization-transfer from a longitudinally polarized electron to a struck proton in the one-photon exchange approximation. The electron vertex in Figure 2.1 can be described by basic Quantum Electrodynamics (QED) rules that involve the electron current tensor, $L^{\mu\nu}$, and the proton vertex can be described by QCD and hadron electrodynamics involving the hadronic current $j^{\mu} = \chi'^{\dagger}\Gamma_{\mu}\chi$. Decomposing the contraction $L_{\mu\nu}W^{\mu\nu}$ into unpolarized and polarized (proportional to $\langle\sigma_x\rangle$, $\langle\sigma_y\rangle$ and $\langle\sigma_z\rangle$) terms,

$$L_{\mu\nu}W^{\mu\nu} = L_{\mu\nu}W^{\mu\nu}_{unpol} + L_{\mu\nu}W^{\mu\nu}_{\langle\sigma_x\rangle} + L_{\mu\nu}W^{\mu\nu}_{\langle\sigma_y\rangle} + L_{\mu\nu}W^{\mu\nu}_{\langle\sigma_z\rangle}, \tag{2.1.10}$$

where, σ_x, σ_y and σ_z are the Pauli matrices, the first term reproduces the unpolarized amplitude equal to Equation (1.2.28) relevant to the unpolarized nucleon tensor, $W^{(0)}_{\mu\nu}$ up to a factor of two. The missing factor of two comes from the sum over final proton spin states. Then, the polarization components are defined by the ratio of the different polarized components, transverse (t), normal (n) and longitudinal (l), over the unpolarized term (1.2.28),

$$P_t \equiv \frac{L^e_{\mu\nu}W^{\mu\nu}_x}{L^e_{\mu\nu}W^{\mu\nu}_{unpol}}, \qquad P_n \equiv \frac{L^e_{\mu\nu}W^{\mu\nu}_y}{L^e_{\mu\nu}W^{\mu\nu}_{unpol}}, \qquad P_l \equiv \frac{L^e_{\mu\nu}W^{\mu\nu}_z}{L^e_{\mu\nu}W^{\mu\nu}_{unpol}}, \tag{2.1.11}$$

where, transverse, normal, and longitudinal describes a scattered proton with positive helicity state along the x, y and z-axes, respectively. The x direction is defined as the in-plane transverse coordinate and the y direction is defined as normal to the scattering plane. The z direction is defined as the momentum transfer. Then the polarization components P_t, P_n and P_l are obtained in terms of the electric G_E, and magnetic, G_M form factors [32, 34],

$$I_0 P_t = -2\sqrt{\tau(1+\tau)}G_E G_M \tan\frac{\theta}{2}, \tag{2.1.12}$$

$$I_0 P_n = 0 \tag{2.1.13}$$

$$I_0 P_l = \frac{1}{M}(E_1 + E_3)\sqrt{\tau(1+\tau)} G_M^2 \tan^2\frac{\theta}{2}, \tag{2.1.14}$$

where I_0 is given by:

$$I_0 = G_E^2(Q^2) + \frac{\tau}{\epsilon} G_M^2(Q^2). \tag{2.1.15}$$

Equations (2.1.12) and (2.1.14) show that there are only two non-zero polarization components, transverse and longitudinal, which are proportional to $G_E G_M$ and G_M^2, respectively. The ratio G_E/G_M then can be obtained directly from the ratio of the two polarization components P_t and P_l as follows:

$$\frac{G_E}{G_M} = -\frac{P_t}{P_l}\frac{(E_1 + E_3)}{2M}\tan\frac{\theta}{2}. \tag{2.1.16}$$

In terms of ϵ, the ratio of G_E/G_M is given by,

$$\frac{G_E}{G_M} = -\sqrt{\frac{\tau(1+\epsilon)}{2\epsilon}}\frac{P_t}{P_l} \tag{2.1.17}$$

$$\epsilon = \frac{1}{1 + 2(1+\tau)\tan^2\frac{\theta}{2}} \Rightarrow \tan\frac{\theta}{2} = \sqrt{\frac{1-\epsilon}{2\epsilon(1+\tau)}}.$$

Equation (2.1.16) makes clear that this method offers several experimental advantages over the Rosenbluth separation:

- For a given θ, only a single measurement is necessary, if the polarimeter can measure both components at the same time. This greatly reduces the systematic errors associated with changing angle and beam energy.

- If both polarization components are simultaneously measured, the knowledge of the beam polarization and the analyzing power of the polarimeter is not needed to extract the ratio, G_E/G_M.

In addition, the polarization-transfer method allows for high luminosity by using high-power liquid hydrogen targets to reach high Q^2.

2.1.2.2 Double-spin Asymmetry

The second class of double-polarization experiments is *double-spin Asymmetries*. Instead of measuring the transferred polarization to an unpolarized target, one can measure the cross-section asymmetry between even and odd combinations of beam and target spins (++,- -) vs. (+-,-+) in elastic scattering of a longitudinally polarized electron off a polarized nucleon target. It was pointed out by Dombey [33] that the form factors can be extracted using this technique without measuring the polarization of the outgoing particles. In the one-photon exchange approximation, following the approach of Donnelly and Raskin [35], the elastic eN (N=p or n) cross-section can be written as a sum of an unpolarized part and a polarized part; the latter is non-zero only if the electron beam is longitudinally polarized.

$$\sigma^{pol} = \Sigma + h\triangle \tag{2.1.18}$$

where Σ is the elastic unpolarized cross-section given by Equation (1.2.28), h is the electron beam helicity, and $\triangle$ is the polarized part of the cross-section with two terms , θ^* and ϕ^*, describing the direction of the target polarization relative to the momentum transfer. The expression for $\triangle$ is given in [35] as,

$$\begin{aligned}\triangle = -2\sigma_{Mott}\tan(\theta/2)\sqrt{\frac{\tau}{1+\tau}}\Big\{ &\sqrt{\tau[1+(1+\tau)\tan^2(\theta/2)]}\cos\theta^* G_M^2 \\ &+ \sin\theta^*\cos\phi^* G_E G_M \Big\}.\end{aligned} \tag{2.1.19}$$

Where θ^* and ϕ^* are the polar and azimuthal laboratory angles of the target polarization vector with $\vec{q}$ in the $\vec{u_z}$ direction and $\vec{u_y}$ normal to the electron scattering

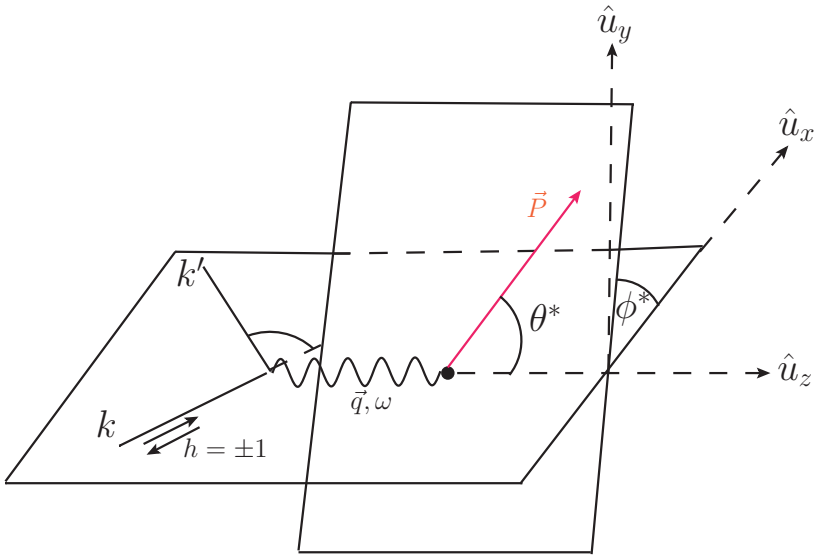

Figure 2.2. Polarized electron scattering from a polarized target.

plane, as shown in Figure 2.2. The physical asymmetry A is then defined as,

$$A = \frac{\sigma_+ - \sigma_-}{\sigma_+ + \sigma_-} = \frac{\triangle}{\Sigma}. \tag{2.1.20}$$

Where σ_+ is the cross-section at the even combination of beam and target spins, (++,- -) and σ_- is that of the odd combination of (+-,-+).

For a polarized target, the measured asymmetry, A_{raw}, is related to the physical asymmetry, A, by

$$A_{raw} = P_B P_T A \tag{2.1.21}$$

where P_B and P_T are electron beam and target polarizations, respectively. By inserting Equations (2.1.19) and (1.2.28) into Equation (2.1.20), one can obtain the expression for the physical asymmetry:

$$A = -\frac{2\sqrt{\tau(1+\tau)}\tan(\theta/2)}{G_E^2 + \frac{\tau}{\epsilon}G_M^2}\Big[\sin\theta^*\cos\phi^* G_E G_M + \sqrt{\tau[1+(1+\tau)\tan^2(\theta/2)]}\cos\theta^* G_M^2\Big]. \tag{2.1.22}$$

It is evident from Equation (2.1.22) that to extract G_E, the target polarization in the laboratory frame must be perpendicular with respect to the momentum transfer vector $\vec{q}$ within the reaction plane, *i.e.*, $\theta^* = \pi/2$ and $\phi^* = 0^0$ or 180^0. For these conditions, the asymmetry A in equation (2.1.22) simplifies to:

$$A_{perp} = \frac{-2\sqrt{\tau(1+\tau)}\tan(\theta/2)\frac{G_E}{G_M}}{\left(\frac{G_E}{G_M}\right)^2 + \frac{\tau}{\epsilon}}. \tag{2.1.23}$$

The asymmetry, A_{perp} is proportional to G_E/G_M. But with $G_E \ll G_M$, the term $(G_E/G_M)^2$ gets smaller and the denominator becomes constant.

In practice, the second term in Equation (2.1.22) is not strictly zero due to the finite acceptance of the detectors. But these effects are small and depend on kinematics only in first order and can be corrected for, so that the ratio G_E/G_M is not affected directly. The discussion described above is only applicable to a free nucleon. Corrections are required if nuclear targets, like ^2H or ^3He, are used instead in quasi-elastic scattering to obtain the form factors. However, in contrast to the polarization-transfer method, the luminosity with a polarized target is generally limited. Therefore, double-spin asymmetry is a suitable method to reach only moderately high Q^2.

2.2 Overview of World Data

2.2.1 Proton Data

Significant advances in experiment and theory have been made over the last decade. This section presents a compilation of previous experimental data on nucleon form factors from Hofstadter's experiments to the present day.

For relatively low Q^2 values up to about 1-2 GeV^2, it is found that the Q^2 dependence of the electric and magnetic form factors of the proton, and the magnetic form

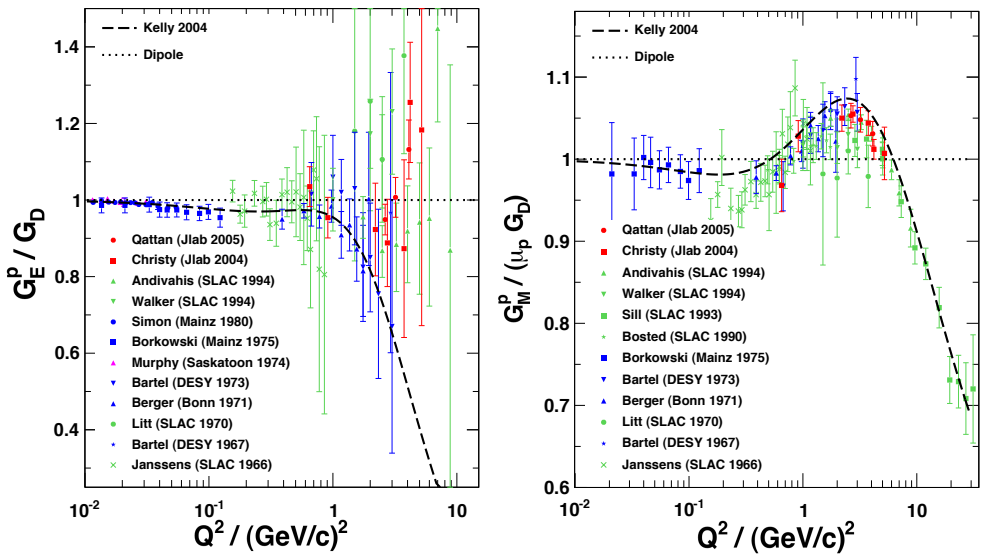

Figure 2.3. *Left*: Proton electric form factor G_E^p from Rosenbluth separation [36–45] and forward-angle measurements [46, 47] normalized to the dipole form factor $G_D = (1 + Q^2/0.71)^{-2}$. *Right*: Proton magnetic form factor G_M^p from Rosenbluth separation [36–45], backward-angle [48], and high-Q^2 cross-section measurements [49].

factor of the neutron, are well described by the dipole parameterization G_D,

$$G_D(Q^2) = \left(1 + \frac{Q^2}{0.71^2}\right)^{-2}. \tag{2.2.1}$$

$$G_E^p = G_D, \quad G_M^p = \mu_p G_D, \quad G_M^n = \mu_n G_D.$$

Figure 2.3 (*left*) and (*right*) plots show the existing data on electric and magnetic proton form factors normalized to the dipole form factor G_D from unpolarized measurements using the Rosenbluth method [36–49], along with a recent form factor parameterization [50]. However, at higher Q^2, the electric form factor is not well known from the Rosenbluth separation. Recalling the Rosenbluth separation method (2.1.3) for the elastic electron-proton scattering cross-section in the Born approximation, it clearly shows that the sensitivity of the total cross-section to G_E^p at higher Q^2 is very low compared to τG_M^p.

In contrast, the double-polarization experiments, Equations (2.1.16) and (2.1.23) allow a precise determination of the proton electric form factor to higher Q^2 than is generally possible with Rosenbluth separations where the magnetic form factor completely dominates the cross-section. The world data of the proton form factor ratio $\mu_p G_E^p/G_M^p$ from double-polarization experiments with polarized target [51, 52], recoil-polarization at Jefferson Lab/Hall A at high Q^2 [53–58] and low Q^2 [59–64], at MAMI [65, 66], and at MIT-Bates [67, 68], are shown in Figure 2.4 along with those obtained from Rosenbluth-separated form factors [36–45]. The polarization-transfer experiments at high Q^2 [53–58] performed with high precision shows a strong decline starting around $Q^2 = 2$ GeV^2 and deviating from the empirical scaling law $\mu_p G_E^p/G_M^p \cong 1$ as suggested by the Rosenbluth data. Thus, the recoil-polarization data are inconsistent with the Rosenbluth data at high Q^2. This "crisis" has generated confusion and doubt about the whole methodology of lepton scattering experiments.

Furthermore, the precise information on the proton charge radius determined from the cross-section method (2.1.8) is also questioned. Having a 7σ discrepancy between the proton charge radius determined from the muonic hydrogen lamb shift [69] and the electron-proton scattering [70, 71] made scientists believe that the possible issues of the proton structure and hence the fitting procedures to the form factors. This doubt about the form factors motivates both experimentalists and theorists to investigate any form factor structure beyond the dipole form.

As the starting point of investigating the form factor discrepancy, it is worth re-mentioning the radiative corrections. As discussed in Section 1.2.1.5, the radiative corrections to the cross-section is typically in the range of 10%-30% in a Rosenbluth experiment which are strongly ϵ-dependent. Therefore, the slope of the Rosenbluth plot can change dramatically in going from uncorrected to corrected cross-sections. The radiative correction contributions arise from the proton vertex that include internal Bremsstrahlung; the virtual part of the proton as well as the Coulomb distortion

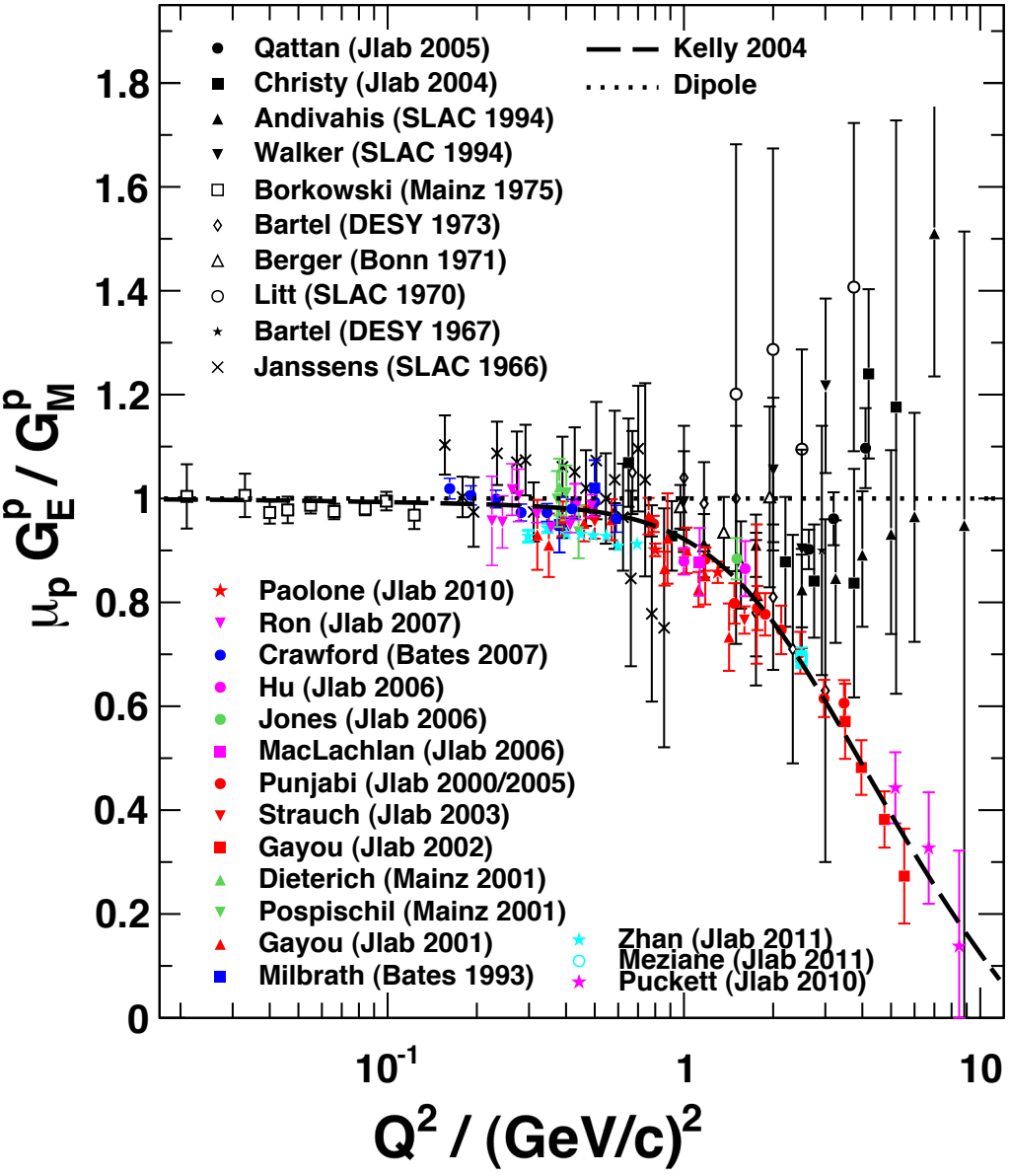

Figure 2.4. Proton electric to magnetic form factor ratio from Rosenbluth-separated cross-sections (*black symbols*) [36–45] and from double-polarization experiments (colored symbols) [51–68]. Theoretical model by Kelly [50] is also shown.

effect are relatively small [20], but strongly ϵ dependent, which reduces $\mu G_E/G_M$ by about 0.05 for Q^2>1 (GeV/c)^2, whereas the effect is gradually reduced at smaller Q^2. The accuracy of G_E^2 determined in a Rosenbluth separation experiment at high Q^2 strongly depends on the accuracy of the radiative corrections [19]. Although it reduces the cross-section, its magnitude is not enough to explain the discrepancy between the Rosenbluth and polarization methods.

In response to the surprising results [53–58], a new high-precision Rosenbluth separation experiment [36] was conducted to determine whether a problem existed with earlier cross-section-based experiments in this Q^2 region that could be revealed by a more precise experiment. This "super-Rosenbluth" experiment was different from previous Rosenbluth separation experiments in that the scattered proton in an elastic *ep* scattering was detected instead of the scattered electron. This cross-section measurement has several advantages over detecting the scattered electrons:

- The ϵ dependence of the proton cross-section $d\sigma/d\Omega_p$ is much weaker than the ϵ dependence of the electron cross-section $d\sigma/d\Omega_e$.
- The proton momentum is constant at fixed Q^2, whereas the electron momentum varies strongly with ϵ.
- The ϵ-dependence of radiative corrections to the cross-section is smaller when the proton is detected.
- The ϵ-dependence of the effect of offsets in beam energy and/or scattering angle on the extracted cross-section is smaller when the proton is detected.

The new method greatly reduced the systematic uncertainties in a Rosenbluth separation experiment relative to experiments in which the electron is detected, allowing a more precise separation of G_E^2 and G_M^2. The results of [36] were consistent with previous Rosenbluth separation experiments, establishing an even stronger disagreement between the cross-section and polarization data at high Q^2. Furthermore,

a followup of Super-Rosenbluth, E05-017, has been carried out in Hall C, Jefferson Lab and the analysis is underway with a Q^2 reach up to 5.5 $(\mathrm{GeV/c})^2$.

This renewed interest in nucleon form factors and intense experimental and theoretical efforts to understand the discrepancy in terms of physics beyond the Born approximation and the standard radiative correction procedures upon which most of the published cross-section data are based. One of the possible explanations to solve the puzzle is using the Two-Photon Exchange (TPE) effect. This effect is generally thought to affect the cross-section in a strongly ϵ-dependent way by, at most, several percent. Several independent studies have been done [23, 72–80] to examine the TPE effects on G_E/G_M. These studies address the intermediate hadron state between the two-photon vertices by exploring states of the intermediate nucleon beyond the ground state, using different approaches to the model of the nucleon. These models were able to reproduce the main features of the form factor distributions while differing at a more detailed level over a large Q^2 range. Guichon and Vanderhaeghen [23] derived the general formalism for the polarization-transfer components as well, including the TPE effect in addition to the formalism for the scattering cross-sections shown in Equation (1.2.34). Including TPE corrections, the polarization-transfer ratio can be written as [23],

$$-\sqrt{\frac{\tau(1+\epsilon)}{2\epsilon}}\frac{P_t}{P_l} = \frac{G_E}{G_M} + Y_E - \frac{G_E}{G_M}Y_M + \left(1 - \frac{2\epsilon}{1+\epsilon}\frac{G_E}{G_M}\right)Y_3 + \wp(e^4). \qquad (2.2.2)$$

Recalling Equation (1.2.34),

$$\frac{\sigma_r}{G_M^2} = 1 + \frac{\epsilon}{\tau}\frac{G_E^2}{G_M^2} + 2Y_M + 2\epsilon\frac{G_E}{\tau G_M}Y_E + 2\epsilon\left(1 + \frac{G_E}{\tau G_M}\right)Y_3 + \wp(e^4).$$

From Equations (2.2.2) and (1.2.34) , they show the ϵ-dependence of the three 2γ-amplitudes, Y_M, Y_E, and Y_3 on the unpolarized cross-section and the polarization-transfer components. It seems that the real part of the TPE amplitude, $\Re(\delta\tilde{G}_M)$

and $\Re(\delta\tilde{G}_E)$ modifies both the unpolarized cross-section and the polarization-transfer components via the two-photon amplitudes, Y_M and Y_E, respectively. As mentioned in Section 1.2.1.6, the combination of positive $\delta\tilde{G}_M$ and positive $\delta\tilde{G}_E$ corrections to the elastic cross-section is large enough to affect the extracted value of G_E. Therefore, the extracted G_E/G_M for the Rosenbluth technique is reduced. In contrast, the polarization method (Equation (2.2.2)) gets affected in a different way. The 2γ-amplitudes Y_E and Y_3 to P_t/P_l have equal magnitudes and of opposite signs, confirming the cancelation of the corrections. Therefore, the effect of the TPE contribution on polarization-transfer components is small, though the size of the contribution changes with ϵ.

With the theoretical explanation of the TPE contribution on Rosenbluth and polarization data, physicists started to investigate beyond the Born approximation. J. Arrington *et al.* [81] has applied the TPE corrections to the existing Rosenbluth data which caused a significant slope as shown in Figure 2.5.

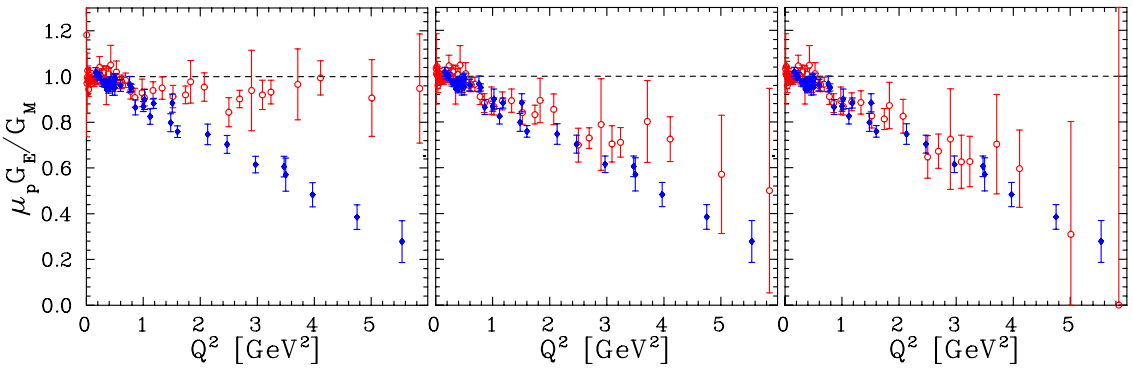

Figure 2.5. Comparison of the polarization measurements (filled diamonds) and LT separations (open circles) with no TPE corrections (left), TPE corrections from Ref. [82] (center), and with the additional high-Q^2 correction applied in Ref. [81] (right).

The corrected results are clearly in better agreement with the polarization data. In particular, the corrections have the proper sign and magnitude to resolve a large part of the discrepancy between the Rosenbluth and polarization techniques.

However, the theoretical evidence is not enough to understand the effect. Several experiments have being performed since the 1960s using unpolarized *ep* scattering of positron-proton and electron-proton taking the advantage of opposite sign for positron and electron scattering for the interference between OPE and TPE as in Equations 1.2.34 and 1.2.35. By taking the ϵ dependence of the ratio of cross-sections, R at fixed Q^2,

$$R = \frac{\sigma_{e+}}{\sigma_{e-}} \cong \frac{(A_{1\gamma} + A_{2\gamma})^2}{(A_{1\gamma} - A_{2\gamma})^2} = 1 + 4\Re\left(\frac{A_{2\gamma}}{A_{1\gamma}}\right) \tag{2.2.3}$$

and measuring the deviation of the ratio of cross-sections R from 1, the magnitude of the TPE correction can be determined. In the last few years, there were three new experiments, using an internal target in a positron/electron storage ring (the VEPP-3 ring) in Novosibirsk [24], using a mixed beam of e^+ and e^-, in Hall B, Jefferson Lab [25] and OLYMPUS experiment at DESY using the DORIS lepton storage ring [26], to compare e^+p and e^-p scattering with the advantage of high intensity e^+ and e^- beams.

Additional experiments will address the discrepancy of the Rosenbluth and polarization data with Rosenbluth-type measurements [83], and single-spin asymmetries [84–89] with a transversely polarized target [84] or a transversely polarized beam [85–89]. New recoil-polarization experiments at Jefferson Lab have extended the Q^2 range up to 9 $(\mathrm{GeV/c})^2$ with a new recoil polarimeter [53, 54] and will extend it up to 15 $(\mathrm{GeV/c})^2$ after the 12 GeV upgrade [90–92]. At low Q^2, new unpolarized measurements [70] and additional polarized measurements are underway [93] .

Due to the enhanced sensitivity to G_E at high Q^2 and the relatively low importance of radiative corrections and TPE effect, the polarization methods make the superior technique to measure both electric and magnetic form factors at high-momentum

transfers. Measurement of the beam-target asymmetry in the elastic *ep* scattering is a polarization method which offers an independent technique to determine G_E/G_M ratio. The latest result from this technique was published by M.K. Jones *et al.* [52] at Q^2 equal to 1.5 $(\mathrm{GeV/c})^2$. Having the same measurement at higher values of Q^2 is very important to understand the discrepancy between the Rosenbluth and polarization-transfer technique. Because the sensitivity of the beam-target asymmetry to TPE effect is the same as in the recoil-polarization, this method is expected to have consistent results with the recoil-polarization method. Having different systematic errors when compared to either the Rosenbluth method or polarization-transfer technique, by measuring G_E/G_M by this technique, the discovery of unknown or underestimated systematic errors in the previous measurement techniques is possible. The analysis of this dissertation contributes G_E/G_M ratio measurements at higher Q^2 extending the results of [52] using this technique, double-spin asymmetry.

2.2.2 Neutron Data

Due to the absence of a pure neutron target, the neutron form factors are not as well known as the proton form factors. They have been measured in both cross-section and polarization experiments on deuterium, ^2H and ^3He.

Extraction of the free neutron elastic form factors from electron scattering experiments on these nuclei requires theoretical models to correct for the binding of the neutrons in a nucleus. Figure 2.6 shows the world data collection of the neutron electric form factor G_E^n. The Rosenbluth separation method at low Q^2 [94] does not allow one to obtain any finite values for G_E^n due to the smallness of it relative to G_M^n (due to z=0, one has G_E^n=0 for $Q^2 \to 0$). A more precise distribution of G_E^n has been obtained by extracting G_E^n from the available experimental data of the deuteron quadrupole form factor $G_Q(Q^2)$ [95]. In the 1990's, double-polarization experiments became possible for quasi-elastic exclusive ($\vec{e}$, e'n) scattering off polarized

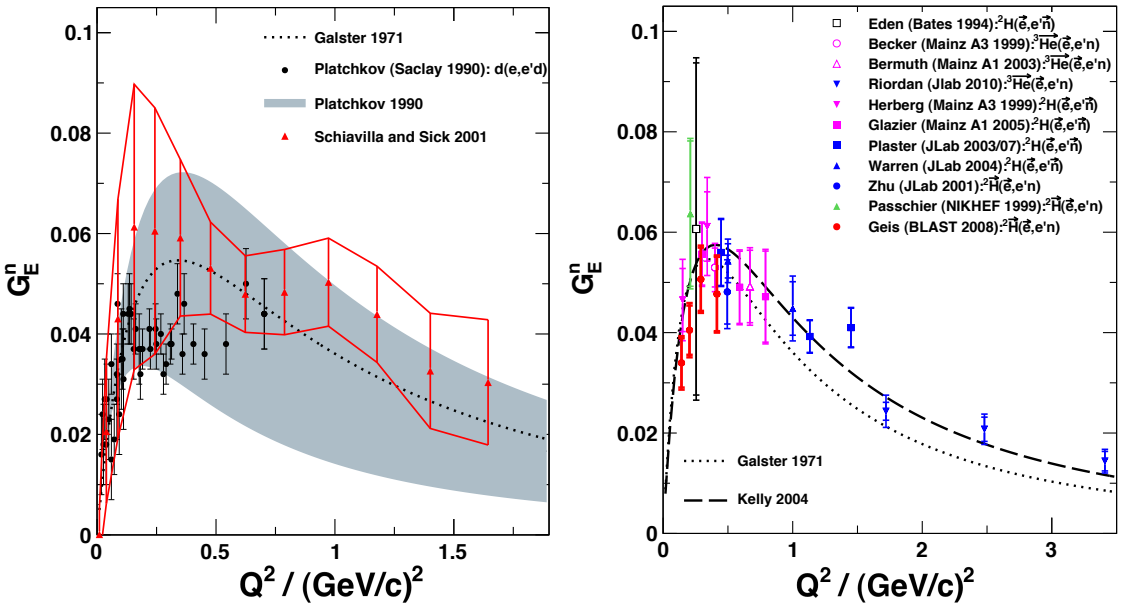

Figure 2.6. *Left*: Neutron electric form factor G_E^n extracted from unpolarized [94] and tensor-polarized [95] elastic electron-deuteron scattering. *Right*: Neutron electric form factor G_E^n from double-polarization observables in quasi-elastic scattering from $^2\vec{H}$ [96–105] and $^3\vec{H}e$ [82, 106–109].

$^2\vec{H}$ and polarized $^3\vec{H}e$ and for measurements of polarization-transfer to the neutron with ^2H. Published results for G_E^n from double-polarization data [82, 96–109] with neutron recoil-polarization [96–101], polarized $^2\vec{H}$ target [102–105], and polarized $^3\vec{H}e$ target [82, 106–109] are shown in the right plot of Figure 2.6. All of the double-polarization experiments measure the ratio G_E^n/G_M^n, and a parameterization for G_M^n [110] has been used to extract G_E^n. Additional data with polarized $^3\vec{H}e$ have been taken at MAMI [111,112] and further experiments [113,114] have been approved to be run at Jefferson Lab after the 12 GeV upgrade to extend Q^2 up to $\simeq$10 (GeV/c)^2.

The neutron magnetic form factor, G_M^n, was first been determined by measuring the unpolarized quasi-elastic deuteron cross-sections of $^2H(e,e'n)$ and subtracting the proton single-arm cross-sections [115–118]. However, the experiments [119–123] developed a more precise technique by measuring the quasi-elastic exclusive cross-sections for the reactions $^2H(e,e'n)$ and $^2H(e,e'p)$ simultaneously, in which theo-

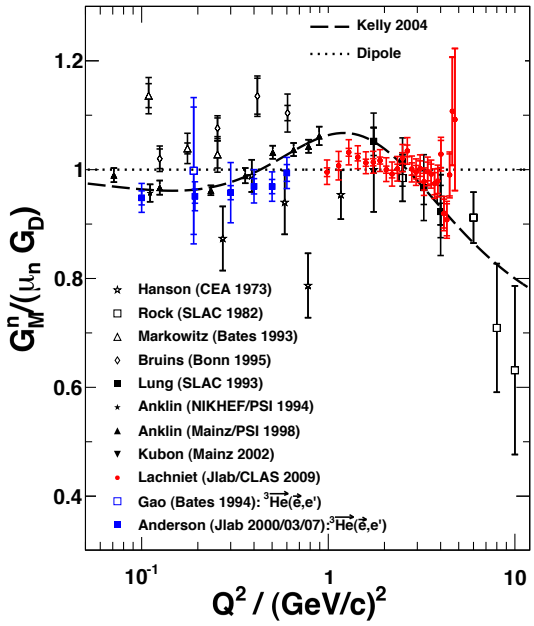

Figure 2.7. Neutron magnetic form factor ratio normalized to the dipole form factor $G_D = (1 + Q^2/0.71)^{-2}$ from quasi-elastic inclusive and exclusive electron-deuteron cross-section measurements [115–118], the cross-section ratio measurements of $d(e, e'n)/d(e, e'p)$ [119–123], and from beam-target asymmetries with polarized ^3He [124–127].

retical uncertainties partially cancel to determine G_M^n. The target spin aligned to the momentum transfer probes G_M^n through the spin dependence of the quasi-elastic cross-section [124–127]. As a different approach, the experiments [128, 129] were conducted using the vector-polarized deuterium as simultaneously polarized proton and neutron targets with aligned spins. The ratio of perpendicular and parallel components of the inclusive beam-target asymmetry for the $^2\vec{H}(\vec{e}, e')$ reaction shows a leading dependence of G_M^n. The most recent data from CLAS at Jefferson Lab, based on the $^2H(e, e'n)/^2H(e, e'p)$ cross-section ratio method, have provided the largest and the most precise data set at high Q^2 [119]. Figure 2.7 shows the published data for G_M^n [115–127]. Another two approved "ratio method" experiments [130, 131] extending the Q^2 region up to ≈ 14 (GeV/c)^2 will run at Jefferson Lab after the 12 GeV upgrade. A detailed discussion of the technical and theoretical challenges involved in measuring the neutron form factors can be found in the review [19].

2.3 Theoretical Interpretation of Nucleon Electromagnetic Form Factors

This section presents an overview of the theoretical understanding of the nucleon electromagnetic form factors with an emphasis on high-momentum transfer, Q^2. Many theoretical attempts have been made to understand the nucleon form factors. Despite their approximations and limitations, some of these non-perturbative methods reveal some insight into the nucleon structure.

2.3.1 Charge and Magnetic Distributions

As discussed in Section 1.2.1.4, in non-relativistic approximation, G_E and G_M are the Fourier transforms of the charge and magnetic moment densities of the nucleon in the Breit frame. However, this interpretation has no physical meaning. Considering only $Q^2 = 0$, in which recoil of the nucleon is negligible and the electron is scattered from a static charge distribution, the Breit frame coincides with the lab frame and the form factor interpretation to the charge and magnetic moment distribution become valid. However, for the Fourier transformation all values of Q^2 have to be considered to derive the spatial distribution. Kelly [16] has derived a theoretical model relating the Sachs form factors to the rest frame charge and magnetic moment densities taking relativity into account. However, this is strictly model-dependent since the Lorentz boost for a composite object such as proton depends on the interactions among the constituent quarks. The most important feature of the proton density from this model is the broader shape of the charge density relative to the magnetic moment density, reflecting the precise recoil-polarization data in which G_E^p falls faster than G_M^p at large Q^2.

2.3.2 Vector Meson Dominance (VMD)

The earliest model to explain the features of the nucleon form factors, such as its dipole behavior, was vector meson dominance (VMD). In this model, the photon couples to the nucleon through the exchange of the three lightest vector mesons, ρ (770), ω (782) and ϕ (1020) which have the same quantum numbers as the photon. In elastic electron-nucleon scattering, the form factors at low Q^2 are dominated by these vector mesons. Within such VMD models, the dipole behavior of the nucleon form factors is identified as the combination of two nearby vector meson poles. The first VMD fit was performed by Iachello *et al.* [132] and a linear decrease of the proton $\mu_p G_E^p/G_M^p$ ratio has been predicted for Q^2>1 (GeV/c)^2, which is in agreement with the result from the polarization-transfer technique. In this model, only three adjustable parameters were used to fit the form factor data available at that time. Gari and Krumpelmann [133] extended the model to conform with pQCD scaling at larger Q^2 with a smooth transition from VMD picture hold at low Q^2. Thereafter, many extended VMD fits have been obtained which provided a good parameterization of nucleon electromagnetic form factors [134–137]. Most of these models involve a number of adjustable parameters to be fitted to experimental data which were described in the form factor data with a reasonable accuracy. Although VMD of the form factor behavior is only expected to hold for relatively low Q^2, the fit results from models incorporating the transition to pQCD at high Q^2.

2.3.3 Constituent Quark Model (CQM)

To understand the structure of the nucleons in terms of quark and gluon degrees of freedom, constituent quark models were developed. This treats baryons as bound states of three quarks moving in a confining potential. In the non-relativistic constituent quark models, quarks are treated as massive particles. The Isgur-Karl model [138] is an example, in which the quarks are confined by a long-range harmonic

oscillator potential supplemented by a short-range one-gluon-exchange quark-quark interaction.

The nucleon is light enough that its internal structure needs to be treated relativistically following the prescriptions by Dirac [139]. This is even more valid since the quarks are much lighter than the nucleon. Although these calculations correctly describe the form factor behavior at larger Q^2, effective degrees of freedom, such as a pion cloud and a finite size of the constituent quarks were introduced to correctly describe the behavior at lower Q^2.

However, constituent quark models do not satisfy the symmetry properties of the QCD Lagrangian, such as chiral symmetry. In the limit of exactly massless u and d quarks, the QCD Lagrangian exhibits chiral symmetry, and the quark chirality is conserved. In reality, the lightest mesons (pions) appear as the Goldstone bosons of the broken chiral symmetry of the QCD Lagrangian. The non-zero masses of the pions observed in nature are required through the chiral symmetry breaking of the non-zero u and d quark masses. Therefore, as the lightest hadron, the pion plays an important role in the structure of the nucleon. Miller [140] added the effects of the pion cloud of the nucleon to the relativistic constituent quark model (rCQM) of the Light-Front Cloudy Bag Model [141] which involves relativistic pion-nucleon form factors. The pion cloud effects within this model made large contributions at low Q^2, particularly for the neutron electric form factor, which is not well reproduced by the rCQM alone. In contrast, quarks are found to dominate at large Q^2.

2.3.4 Form Factors and Perturbative QCD

The theory of the strong interaction, QCD is important in the nucleon form factors with its property of the asymptotic freedom. At higher energies, the probed distance is small; this is where the quarks are asymptotically free, the force between quarks becomes weak, and perturbative QCD applies. Therefore, at higher Q^2, quarks and

gluons play a dominant role in the form factors in which the perturbative QCD (pQCD) makes a prediction about the behavior of those. In pQCD, the quarks interact via single-gluon exchange to leading order in α_s which does not happen in elastic scattering. Elastic scattering takes place at higher Q^2 when the quark is struck by a virtual photon and the struck quark shares the transferred momentum among the two other valance quarks, such that the three quarks remain collinear after the collision. Therefore, at very high Q^2 corresponding to very short distances, elastic scattering cannot occur without a minimum of two hard gluon exchanges sharing the transferred momentum among the three quarks. If one of the exchange gluons among three valence quarks is "soft," then the struck quark fails to share the momentum transfer among the other two quarks and moves rapidly away from the original three-quark center of mass, leading to inelastic scattering. Therefore, the transition from nucleon+meson degrees of freedom to quark+gluon degrees of freedom (pQCD) must happen at higher Q^2.

The nucleon form factors in the high Q^2 in terms of the momentum fractions of the quarks in the initial and final nucleons, including the leading asymptotic Q^2 dependence of the form factor has been derived in [142]. This leads to the prediction of $Q^2F_2/F_1 \rightarrow$ constant, which implies that the ratio G_E^p/G_M^p becomes constant. These predictions are different from the polarization-transfer measurements, where the ratio G_E^p/G_M^p shows roughly a linear decrease with Q^2 and points toward a zero-crossing at some larger Q^2.

Because the current quark mass in the nucleon is negligible in comparison to the mass of the nucleon and Q^2, Belitsky *et al.* [143] have shown that the discrepancy between the high-Q^2 data and pQCD scaling is due to the dominant mechanism for nucleon spin flip in QCD, which is due to the quark orbital angular momentum. Furthermore, they have derived the asymptotic Q^2 dependence of the Pauli form factor in terms of the orbital angular momentum of the quarks. In contrast to pQCD,

in this calculation, the quark transverse momenta were considered non-negligible to allow for orbital angular momentum of the constituents. This consideration leads to a modified scaling behavior for the ratio F_2/F_1 at large Q^2. The recoil-polarization data for F_2^p/F_1^p are compatible with such a scaling for the entire Q^2 range of the data.

2.3.5 Form Factors and Generalized Parton Distributions

Generalized Parton Distributions (GPDs) are the theoretical framework accessed in hard exclusive reactions such as Deeply Virtual Compton Scattering (DVCS) and hard exclusive meson production to understand the quark structure of the nucleon. These processes allow one to remove a quark from the initial nucleon and implement another in the final nucleon. The amplitudes of these processes can be factorized into quark-level sub-processes which can be calculated by GPDs. They contain process-independent nucleon structure information. These GPD functions are characterized as vector, tensor, axial vector and pseudoscaler transition amplitudes. They address the new information about the nucleon structure which cannot be obtained from inclusive reactions such as deep inelastic scattering (DIS). The predictions for the nucleon form factors are derived using a model for the GPDs by Guidal *et al.* [144]. This model achieves a very good agreement with experimental data for all four nucleon form factors in the entire Q^2 range. Because vector and tensor GPDs can be related to the total angular momentum carried by the quark in the nucleon, the behavior of the ratio F_2^p/F_1^p determines the behavior of the GPD, allowing an evaluation of Ji's angular momentum sum rules [145]. These sum rules relate the quark's longitudinal momentum fraction of GPDs to the total angular momentum carried by quarks in the nucleon. GPDs provide the information about the spin structure of the nucleon.

The two-dimensional Fourier transform of vector GPD yields the transverse quark density in the infinite momentum frame as a function of longitudinal momentum fraction. By integrating overall the longitudinal momentum fraction and summing

overall quark flavors, one can obtain the model-independent transverse charge density [146] of the nucleon, which is equal to the two-dimensional Fourier transform of the Dirac form factor F_1.

2.3.6 Dyson-Schwinger Equations (DSEs)

A complementary framework for studying the form factors is via Dyson-Schwinger equations (DSEs) [147, 148]. The investigation of hadron structure in the Dyson-Schwinger approach proceeds for baryons via the covariant Faddeev Equation [149, 150]. This approach provides access to all momentum scales and all quark masses, which is in good agreement in form factor results with the experimental data above $Q^2 \simeq 2$ (GeV/c)^2. However, at low Q^2, pion-cloud effects are not included and therefore, the charge radii and magnetic moments underestimate the data and the enhanced low Q^2 structure in the neutron's electric form factor is absent. Zero-crossing of the form factor ratio G_E^p/G_M^p can occur with the Faddeev approach as well. From the correlations in the Faddeev amplitude between the up, down and strange quarks regime, it has been seen that the orbital angular momentum contributes one-third to the nucleon spin, and this contribution slowly decreases with rising current-quark mass.

Quark-diquark model studies also found a zero-crossing, where its location depends on the model parameters in the calculation [151, 152]. The overall agreement between the [150] and those obtained in the quark-diquark model provides further evidence for the quark-diquark structure of the nucleon.

2.3.7 Lattice QCD

All theories described until now are at least to some extent parametrizations. They used models constructed to focus on selected aspects of QCD. Only lattice gauge theory can provide an *ab initio* calculation. One of the most advanced lat-

tice calculations of electromagnetic form factors has been performed by the QCDSF Collaboration [153]. This limits the calculations to the quenched approximation (in which sea-quark contributions are neglected), to a box size of 1.6 fm and to a pion mass of 650 MeV. Ashley *et al.* [154] have extrapolated the results of these calculations to the chiral limit, using chiral coefficients appropriate to full QCD. But the agreement with the data is poorer than that of any of the other calculations.

Unquenched lattice QCD results from LHPC Collaboration [155] for the nucleon electromagnetic form factors performed for one lattice spacing of a a$\simeq$0.125 fm, and for pion mass in the range m_π=360-775 MeV. This shows that the Q^2 dependence of Dirac isovector form factor F_1^V at the smallest m_π of around 360 MeV in qualitative agreement with the data and the isovector ratio F_2^V/F_1^V approaches the experimental result when decreasing m_π. The results at the lowest pion masses with higher statistics are needed to provide a powerful test of experimental electromagnetic form factor data.

Since the pion cloud calculation of the nucleon form factors are more relevant to the behavior of the nucleon form factors at low momentum transfers, it is not discussed in this dissertation. An extensive discussion of the theoretical model explanation on the form factors can be found in the review paper [19].

To summarize, the preceding chapters motivated the use of elastic electron-nucleon scattering to study the structure of the nucleon. The methods to obtain scattering cross-section, polarization-transfer observables and beam-target asymmetry in polarized target experiments in terms of electric (G_E) and magnetic (G_M) form factors which fully characterize the effect of the nucleon's electromagnetic structure on the reaction, were discussed and an overview of the available data was given. The theoretical interpretation of nucleon electromagnetic form factors were also briefly discussed.

SECTION 3

EXPERIMENT SETUP

The main goal of the experiment E03-007, known as the **S**pin **A**symmetries of the **N**ucleon **E**xperiment (**SANE**) was to measure the inclusive spin asymmetries with the target spin aligned parallel and perpendicular to the beam direction (*i.e.*, parallel and perpendicular spin asymmetries) for polarized electron scattering from a polarized proton target. A subset of the data was used to measure the elastic beam-target spin asymmetry from elastic electron-proton scattering. Polarized electrons with energies 4.72 GeV and 5.89 GeV were scattered from the polarized proton target with the spin of the proton aligned nearly perpendicular (80°) to the beam direction. Recoiled protons were detected by the High-Momentum Spectrometer (HMS) at 22.3° and 22.0°, and central momenta of 3.58 GeV/c and 4.17 GeV/c, respectively, for the two different beam energies. Scattered electrons were detected by the Big Electron Telescope Array (BETA) in coincidence with the proton in HMS. In addition to that, single-arm electron scattering data were also taken by detecting the elastically scattered electron in the HMS at a central angle of 15.4° and central momentum of 4.4 GeV/c for an electron beam energy of 5.89 GeV.

The beam polarization was measured by the Hall C Moller polarimeter during the experiment. Polarized protons were obtained by polarizing the frozen NH_3 crystals using Dynamical Nuclear Polarization at 1 K temperature and 5 T external magnetic field. The spin direction of the polarized proton can be aligned parallel (positive polarization) or anti-parallel (negative polarization) to the field direction by changing the induced transition frequency applied by the microwave radiation. Data were taken at both frequencies.

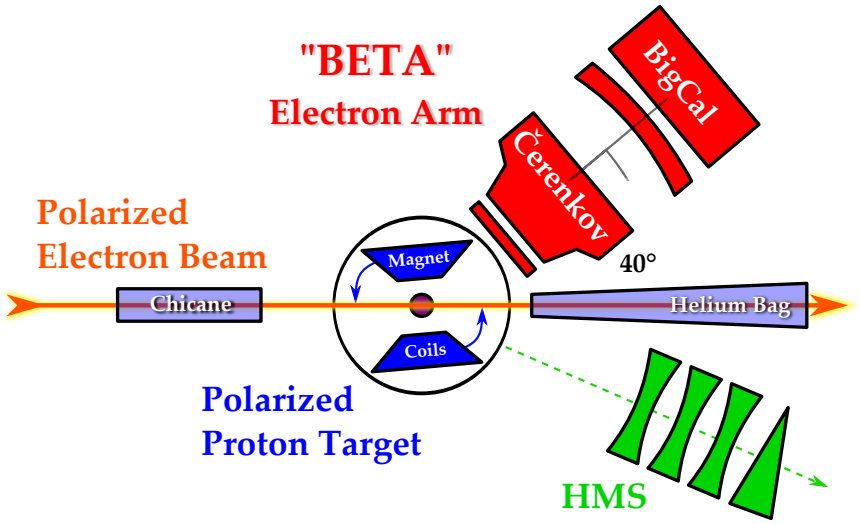

Figure 3.1. Schematic overview of SANE's experimental setup with the electron arm (BETA) at 40° and the proton arm (HMS) [156].

In the following sections, the subcomponents of the polarized electron beam, the detectors and the target, trigger and the data acquisition system (DAQ) will be briefly discussed.

3.1 Polarized Electron Beam

There are many components which are responsible to produce a good polarized electron beam [157]. The polarized electron source and the electron accelerator in Thomas Jefferson National Accelerator Facility (TJNAF) will be briefly discussed in the following sections.

3.1.1 Polarized Electron Source

Depending upon the experiment, the electrons can be generated either in a polarized state from a DC photo-emission gun using a cathode, or in an unpolarized state from a thermionic gun. Polarized electrons are emitted by illuminating a Gallium

Arsenide (GaAs) cathode using a circularly polarized laser light with a frequency equal to the energy of the band gap of the material.

The circularly polarized light, which is directed onto the cathode, is produced by sending the laser light through a Pockels cell, which is an electro-optical crystal that converts linearly polarized light to circularly polarized light. The helicity of the directed light can be varied by changing the voltage of the Pockels cell, which can be used to change the helicity of the emitted electrons. At Jefferson Lab, the Pockels cell reverses the polarization of the laser light between left and right circular polarization at a frequency of 30 Hz. Right-handed polarized light excites electrons from $P_{-3/2}$ and $P_{-1/2}$ valence band states into $S_{1/2}$(-) and (+) conduction band states, respectively, while the left-handed light does the transitions from $P_{3/2}$ and $P_{1/2}$ to $S_{1/2}$(+) and (-). These transitions can be seen in a) of Figure 3.2 with the transitions induced by right-handed circularly polarized light in blue and the transitions induced by left-handed circularly polarized light in red.

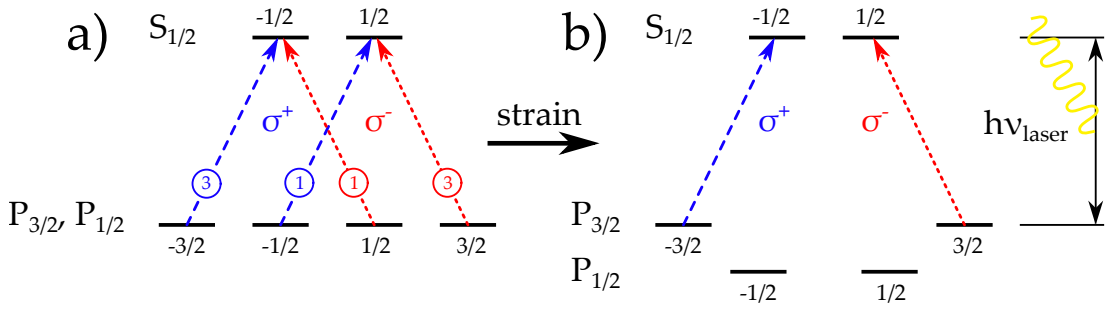

Figure 3.2. Energy levels and laser induced transitions for unstrained and strained doped GaAs [157].

With the $P_{1/2}$ and $P_{3/2}$ energy states being degenerate, theoretically, a pure GaAs induces only about 50 % of the electron beam polarization [157]. However, Jefferson Lab's polarized source uses a superlattice GaAs photocathode, in which the pure GaAs is doped by phosphorous in every other layer. The "superlattice" is generated by

inducing a gap between the $P_{1/2}$ and $P_{3/2}$ energy states which breaks the degeneracy as seen in b) of Figure 3.2. As a result, the source delivers an 85 % polarized electron beam with a quantum efficiency of 1%. Additionally, insertable and rotatable half-wave plates are used by the experiments to passively reverse the polarization of the laser light. Three diode lasers, one for each experimental hall, are used. Each laser is pulsed at a frequency of 499 MHz, and the three are phase shifted relative to each other by 120°. Each laser pulse produces a single bunch of electrons, and the combined train of electron bunches has a frequency of 1497 MHz, equal to the resonant frequency of the RF accelerator cavities in the linear accelerator.

The orientation of the beam polarization is rotated by a Wien filter before injection into the accelerator to optimize the delivery of longitudinal polarization to the experimental halls.

3.1.2 Accelerator

The Continuous Electron Beam Accelerator Facility (CEBAF) is composed of two parallel linear accelerators (north linac and south linac), 9 recirculating arcs of magnets and a 67 MeV injector [158]. Injector energy needs to match with the linac energy. 67 MeV is the energy at the injector in order to get the maximum final beam energy of 6 GeV. The photo-emitted electrons are sent off into the injector by a 100 KV DC electron gun. The photocathode and the electron gun are housed in an ultra-high vacuum enclosure which prevents degradation of the quantum efficiency of the photo cathode by the residual gas. The injector itself accelerates electrons up to 67 MeV before entering into the north linac.

The electron acceleration takes place in superconducting RF-resonant Niobium cavities cooled to well below their transition temperatures by superfluid Helium at $\approx$ 2 K. Cavities are operated by an oscillating electromagnetic field such that the electron bunch always sees a net positive charge in front of its path (Figure 3.3),

which forces the electrons to accelerate continuously throughout the cavity. Eight RF cavities are housed within a cryo module, which is a large cryostat containing all the necessary support structures for the accelerating cavities. The injector consists of $2\frac{1}{4}$ cryo modules.

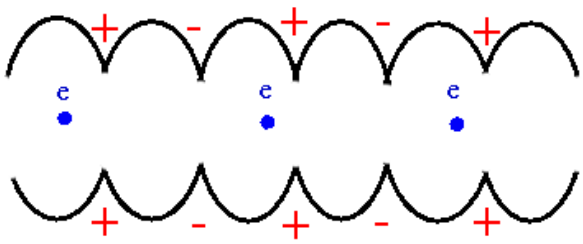

Figure 3.3. Charge distribution in the RF cavities at one instant. When the electron moves forward the oscillating electromagnetic field induces a positive charge in front of the electron thereby accelerating it continuously when it is traveling in the cavity.

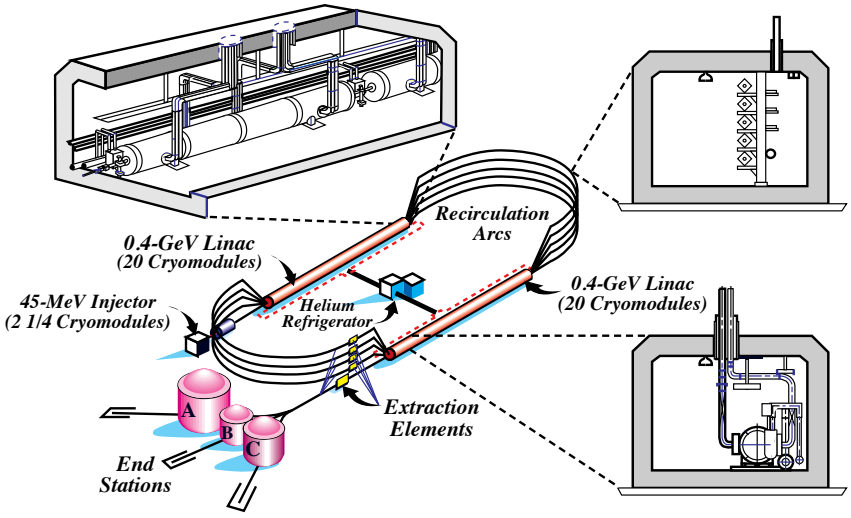

Figure 3.4. Thomas Jefferson National Accelerator Facility (TJNAF) [158].

The two linacs are made of 20 cryo modules each. The layout of the accelerator is shown in Figure 3.4. Each linac accelerates electrons by a maximum of 600 MeV. This amount depends on the desired beam energy of the experiment. Linacs are connected by nine re-circulating arcs, with five at the north and four at the south. With this "race track" design, the electron beam can travel through both linacs up

to five times, giving the maximum energy of approximately 6 GeV before extraction and delivery to the three experimental halls. At any given time, up to five electron beams of different energies are sitting on top of each other in the linac.

At the end of each linac, a series of dipole magnets separate the beam electrons according to their momentum and direct them into one of the re-circulating arcs. The arcs consist of room-temperature magnets, dipoles with different bending fields for steering electrons along a path with the same radius of curvature, and quadruples for focussing. At the exit of each arc is an identical series of magnets with opposite polarity to recombine the electrons from the five-arc beam lines back into a common beam pipe for another pass through the linac.

At the end of the south linac, the beam can be extracted from the main race track to any given hall using RF separator magnets operating at 499 MHz after any number of passes. These extracted beams enter the beam switch yard (BSY) where the beams are directed into the beam line leading to the appropriate experimental hall. This design allows the accelerator to provide different beam energies to the three experimental halls simultaneously. Any given hall can choose a desired number of passes which are multiples of linac energies. This limits the beam energy one can use at the hall. The nominal beam energy is determined from the magnet settings in the arcs or in the experimental hall's beam arcs.

Exploiting the advantage of superconducting RF technology over the normal conducting cavities, CEBAF has the ability to consistently deliver continuous wave (CW) electron beams with high energy, intensity and polarization, which makes it the leading electron scattering facility in the world for nuclear and particle physics experiments.

3.1.3 Standard Hall C Beam Line

The extracted beam from the linac is directed to the experimental halls from the BSY through the arc beam lines. Standard equipments are installed in the beam lines to provide precise information on the energy, position, current and polarization of the beam, which enables the experiments to run successfully. The Hall C arc consists of 8 dipoles, 12 quadrupoles and 8 sextuples which steer and focus the beam. The beam is rastered to increase its spot size, which spreads the heat load over a wider area of the target [159].

Beam Position Measurement

Hall C Beam Position Monitors (BPMs) monitor the beam position continuously. There are three BPMs; each consists of a resonant cavity which contains four antennae, rotated by 45 degrees relative to the vertical and horizontal axes in order to minimize synchrotron radiation damage. These cavities are operated with the frequency equal to that of the accelerator and the Hall C beam. An asymmetry of the amplitudes of the signals coming from the antennae on the opposite side of the beam is proportional to the distance between the beam and the mid-point of the two antennae [160]. Because the slow-raster system rapidly changes the actual beam position on the target during the experiment SANE, the BPM information for a particular event is not the exact beam position on the target for that event. Therefore, no absolute event-by-event beam position was measured. Instead, the relative position to the beam center was measured by recording the raster X and Y amplitudes in an ADC.

Beam Current Measurement

There are three devices used to measure the beam current entering into Hall C. The first two devices are the cylindrical cavities, BCM1 and BCM2, which have been designed to resonate at the same frequency as the accelerator RF [161–163]. These resonances get excited by the beam which is picked up by antennae placed

inside the cavities. The antennae are used to convert the RF power of the excited resonance, which is proportional to the square of the beam current, to an analog voltage signal. Since the cavity's resonance frequency is determined mainly by its size and shape, and since it is temperature dependent, the BCM cavities are kept thermally insulated at a constant temperature of 43.3 °C. The third device used to measure the beam current is a parametric current transformer, called a *Unser monitor* [161]. Because of its gain stability, it is used to calibrate the BCM cavities. For cross-section measurements, careful calibration of the BCMs must be performed periodically in order to minimize the uncertainty on the total charge collected by the experiment. But for the asymmetry measurements, the result does not depend on the total charge delivered to the experiment.

Beam Energy Measurement

The Hall C arc dipole magnets are used as a spectrometer to measure the energy of the electron beam as it enters the hall. Three pairs of high resolution superharps at the entrance, middle and exit of the arc precisely measure the beam positions and angles of the beam. Using the curvature of the beam over its 34.4° deflection by dipoles and the precise knowledge of the arc dipole fields, the energy of the beam can be determined by,

$$E \simeq p = \frac{e}{\theta} \int \vec{B} \cdot \vec{dl} \tag{3.1.1}$$

with electric charge, e, arc bend angle θ , and the magnetic field integrated over the path of the beam.

However, during the experiment SANE, the beam current was low ($\sim$100 nA) and the superharps did not work. Therefore, the less accurate beam position data from the beam position monitors was used. The average beam energy per run for each beam energy for each target field configuration is shown in Table 3.1.

Table 3.1. Table of beam energies averaged per run for each run configuration.

Nominal E (GeV)	Target Field Angle	Average E (MeV)	Standard Deviation
4.7	180°	4736.6617	0.9090
4.7	80°	4728.5463	0.7535
4.7	80°	4729.1416	0.5483
5.9	180°	5895.0354	1.9615
5.9	80°	5892.0832	4.9354

Beam Polarization Measurement

The polarization of the beam at the injector is not the same as the polarization delivered to the experimental halls, because of the precession of the electron spin in the recirculating arcs of the CEBAF accelerator and the Hall C arc owing to its small anomalous magnetic moment. This precession depends on the number of passes through the accelerator, the linac energy, and the Wien filter setting. The Wien filter, which consists of crossed electric and magnetic fields with adjustable strength and orientation, is used to rotate the electron spin at the injector to an initial orientation in order to maximize the delivered longitudinal polarization to one or more experimental halls after precession in the magnetic beam transport elements.

A Mϕller polarimeter was used to measure the polarization of the beam entering Hall C [164]. Using the well-known cross section calculable from QED for the reaction $\vec{e} + \vec{e} \rightarrow e + e$, the polarized cross section $d\sigma\ /d\Omega$ can be written as,

$$\frac{d\sigma}{d\Omega} = \frac{d\sigma_0}{d\Omega}\left[1 + P_t^{\parallel} P_b^{\parallel} A_{zz}(\theta)\right] \tag{3.1.2}$$

$$\frac{d\sigma_0}{d\Omega} = \left[\frac{\alpha(4 - \sin^2\theta)}{2m_e\gamma \sin^2\theta}\right]^2, \qquad A_{zz}(\theta) = -\sin^2\theta \frac{(8 - \sin^2\theta)}{(4 - \sin^2\theta)^2}$$

for the scattering angle θ [164], where $\frac{d\sigma_0}{d\Omega}$ is the unpolarized cross section, $A_{zz}(\theta)$ is the analyzing power, $P_t^{\parallel}$ is the polarization of the electron target parallel to the beam axis, and $P_b^{\parallel}$ is the beam polarization. Then the asymmetry of the cross sections for

beam and target spins parallel and anti-parallel is,

$$\epsilon = \frac{d\sigma^{\uparrow\uparrow} - d\sigma^{\uparrow\downarrow}}{d\sigma^{\uparrow\uparrow} + d\sigma^{\uparrow\downarrow}} = A_{zz}(\theta) P_t^{\parallel} P_b^{\parallel}. \tag{3.1.3}$$

This measurement is done by scattering the electron beam on a pure iron foil polarized by a 4 T superconducting split-coil solenoid. As the analyzing power is maximized for the electrons scattered by 90° in the center of mass frame, pairs of electrons scattered around 90° are detected in coincidence. The coincidence eliminates background from other processes, such as Mott scattering from the iron nuclei. A system of movable collimators allows selection of a narrow range about 90° in the center of mass frame. Figure 3.5 shows a schematic layout of the Hall C Mϕller polarimeter.

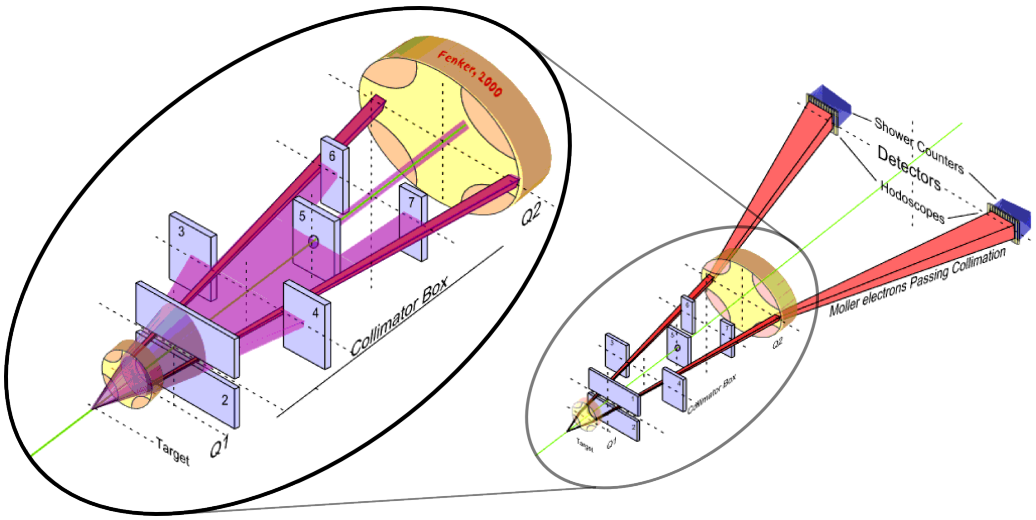

Figure 3.5. Schematic of the Hall C Mϕller polarimeter.

The scattered electrons that pass through the system of quadrupole fields and collimators are detected by two lead-glass shower counters at the end equipped with photomultiplier tubes. For the actual beam polarization measurement, the asymmetry in Equation (3.1.3) is produced by using the coincidence counting rate between these two shower counters at different beam helicities. Since the iron film degrades

the beam, Møller measurements cannot be performed simultaneously with the data taking, but are performed periodically to monitor the beam polarization. Because the precise beam polarization is very important to determine the correct asymmetries, nine Møller measurements, as shown in Table 3.2, were taken during the experiment.

Using the beam energy, Wien angle, quantum efficiency of the superlattice GaAs cathode and half wave plate status recorded by the EPICS system, the beam polarization for each run can be calculated [165–167]. The beam polarization per run averaged over charge accumulated on target during SANE is shown in Figure 3.6.

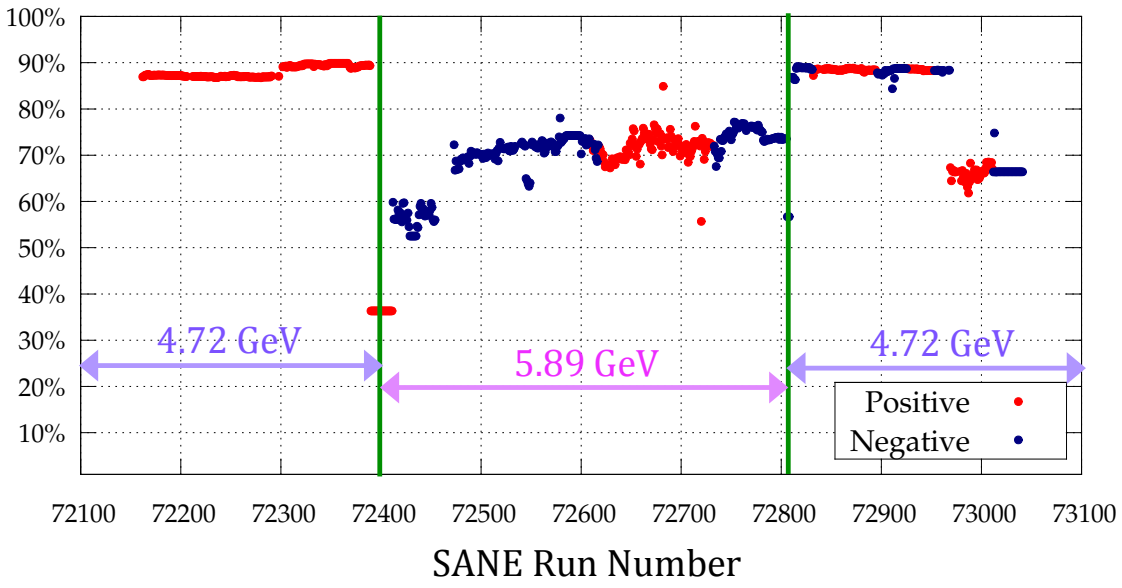

Figure 3.6. Electron beam polarization for each SANE experimental run. The polarizations depend most strongly on the beam energy of the run. The 4.72 GeV beam energy setting allows the polarization around 90%, while for the 5.89 GeV beam energy (in the middle of the experiment), the polarization drops significantly. At end of the experiment, a cryo module failure necessitated 5 accelerator passes to achieve 4.72 GeV and hence the beam polarization was effected. This can be seen around the run numbers 72975-73050.

Table 3.2. Table of SANE Mϕller runs. HWP=Half Wave Plate, QE=Quantum efficiency.

Date	Run	HWP	Wien(°)	Beam E (MeV)	QE(%)	Polarization (%)
1/25	71942	IN	29.99	4730.46	0.1844	87.79 ±1.54
	71943	IN	29.99	4730.48	0.1844	88.21 ±0.98
	71944	IN	29.99	4730.51	0.1844	85.13 ±0.93
	71945	IN	29.99	4730.53	0.1844	87.71 ±0.99
	71946	IN	29.99	4730.53	0.1844	88.24 ±1.01
	71947	IN	29.99	4730.53	0.1844	86.76 ±0.95
	71948	IN	29.99	4730.53	0.1844	87.33 ±1.55
	71949	IN	29.99	4730.52	0.1844	86.58 ±0.99
	71950	IN	29.99	4730.52	0.1844	85.38 ±0.97
	71951	IN	29.99	4730.53	0.1844	86.71 ±0.97
	71952	IN	29.99	4730.49	0.1844	85.64 ±1.05
	71953	IN	29.99	4730.49	0.1844	89.95 ±1.17
	71954	IN	29.99	4730.49	0.1844	86.65 ±1.25
	71956	IN	29.99	4730.50	0.1844	88.32 ±1.09
2/1	72209	IN	29.99	4729.25	0.0888	89.00 ±1.02
	72210	IN	29.99	4729.29	0.0888	87.32 ±1.10
	72211	IN	29.99	4729.28	0.0888	83.45 ±1.04
2/5	72300	IN	29.99	4728.23	0.0708	87.26 ±0.68
	72301	IN	29.99	4728.27	0.0708	85.64 ±0.93
2/11	72465	OUT	29.99	5892.84	0.3124	-61.16 ±1.10
	72466	OUT	29.99	5892.70	0.3124	-60.56 ±1.11
	72467	OUT	19.99	5892.81	0.3124	-72.83 ±1.02
	72468	OUT	19.99	5892.43	0.3124	-72.04 ±0.98
	72469	OUT	19.99	5891.65	0.3124	-75.35 ±0.97
	72470	OUT	22.99	5891.75	0.3124	-71.88 ±1.06
	72471	OUT	22.99	5891.46	0.3124	-70.82 ±1.06
	72472	OUT	22.99	5891.08	0.3124	-70.64 ±2.17
2/14	72537	OUT	22.99	5891.24	0.2790	-73.36 ±1.08
	72538	OUT	22.99	5891.11	0.2790	-73.70 ±1.05
	72539	OUT	22.99	5891.03	0.2790	-72.19 ±1.83
2/24	72767	OUT	13.00	5892.92	0.0830	-75.51 ±1.08
	72768	OUT	13.00	5892.85	0.0830	-76.90 ±1.00
2/28	72839	IN	29.99	4728.95	0.2516	87.63 ±0.96
	72840	IN	29.99	4728.88	0.2516	86.28 ±1.08
3/9	72965	OUT	-18.00	5895.58	0.1635	-90.22 ±1.29
	72966	OUT	-18.00	5894.22	0.1635	-86.81 ±1.27
3/12	72977	OUT	21.19	4736.33	0.1789	65.83 ±0.97
	72978	OUT	21.19	4736.34	0.1789	66.36 ±0.99

Fast-Raster

The electron beam generated at CEBAF is a high-current beam with a very small size (≤ 200 μm). The fast-raster system is designed to increase the effective beam size in order to prevent damage to solid targets and to prevent local boiling in cryogenic targets. This intense heat can even melt the Aluminum windows of the cryostat targets as well as damage the beam dump.

The fast-raster system, 25 meters upstream of the target, consists of two sets of steering magnets [168, 169]. The first set rasters the beam vertically and the second rasters the beam horizontally. Triangular wave forms are used to drive the magnet currents to produce a uniform square beam spot of 1×1 mm^2. Figure 3.7 shows the fast-raster pattern during an example run in SANE.

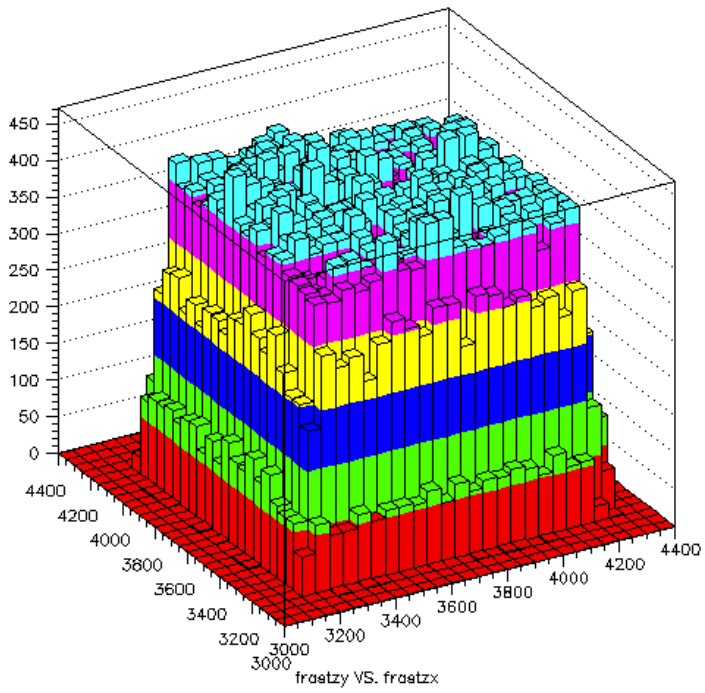

Figure 3.7. Histogram of number of hits in HMS versus the fast-raster position for SANE production run 72790, showing the fast-raster pattern in ADC channels.

3.1.4 SANE Hall C Beam Line

In addition to the standard Hall C beam-line equipment, SANE required extra beam-line equipment to accommodate the UVa polarized target. The slow-raster was added to spread the beam over an even larger area of the target material cup. When the target magnetic field is nearly perpendicular to the beam, the electron beam is deflected down, away from the target center. To counteract this, the beam was sent through a chicane of magnets which bent it down and then back up at the target. Even after the beam passed through the target center, it would continue to bend down, deflecting away from the standard beam dump in the hall. So, a helium-filled bag was used to transport the beam to a temporary beam dump.

Slow-Raster

Due to radiation damage, the polarization of the ammonia target material decreases. Therefore, the beam was rastered a second time to spread it evenly over a larger area. This second raster was circular, unlike the square fast-raster, to match the circular shape of the target cup face [170]. Throughout the experiment, the diameter of the slow-raster was 2 cm. Three wave-form generators were used to drive the slow-raster magnets. While one was creating the amplitude modulation to control the radius of the spiral, the other two generators were used to generate sine waves with a 90° phase difference, creating a circle. This results in the final spiral raster pattern. Figure 3.8 shows an example of the slow-raster pattern for a run in SANE.

Chicane Magnets

The SANE experiment was run with two 5 T target magnetic field configurations. The first one is parallel to the electron beam and therefore the trajectory of the beam is unaffected. The second one, which is relevant to this thesis, is nearly perpendicular (80°) to the electron beam. The trajectory of the standard Hall C electron beam would start to deflect down entering the target magnetic field region, causing the

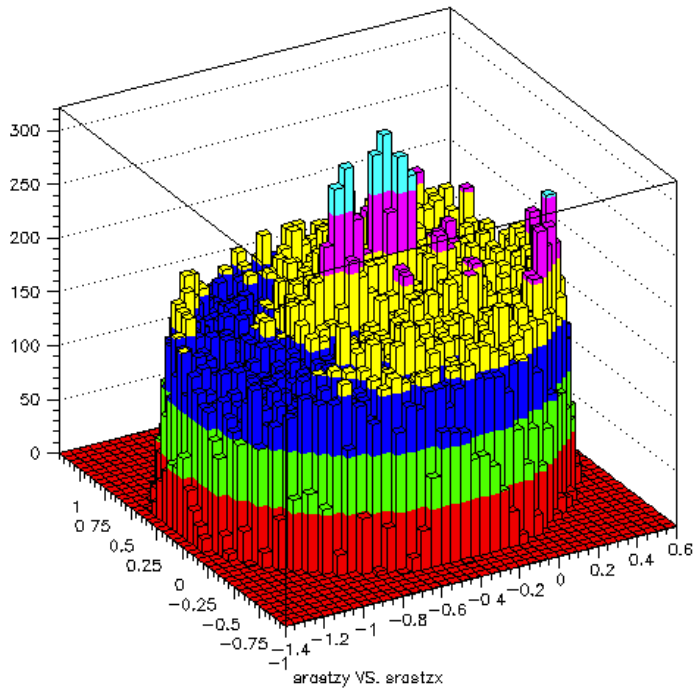

Figure 3.8. Histogram of number of hits in HMS versus the slow-raster position for SANE production run 72790, showing the slow-raster pattern in cm.

beam to miss the center of the target. A chicane magnet was used to counteract this bend of the beam before it reached the target as seen in Figure 3.9.

The chicane consists of two dipole magnets, BE and BZ. While BE bends the incoming beam downwards toward the BZ, BZ bends the beam back up to the target. The magnets were precisely positioned and tuned to allow the beam to reach the center of the target after being bent by the target magnetic field. Table 3.3 shows the integrated $\int B \cdot dl$ of the chicane magnets and the target for the two-beam energy settings used in the perpendicular field configuration.

Table 3.3. Table of chicane parameters for 80° field for both beam energy settings. Integrated Bdl given in units of Tm.

Beam E (GeV)	BE Bend	BZ Bend	Target Bend	BE Bdl	BZ Bdl	Target Bdl
4.7	0.878°	3.637°	2.759°	0.513	1.002	1.521
5.9	0.704°	2.918°	2.214°	0.513	1.002	1.521

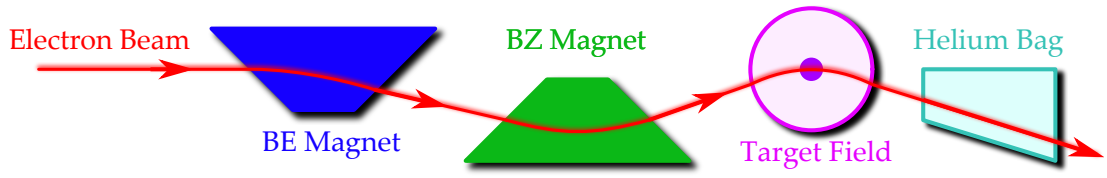

Figure 3.9. Vertical motion of the beam through the chicane magnet setup during the perpendicular target field configuration.

Helium Bag

In Figure 3.9, the electron beam can be seen bending down in the target field region after passing through the target, which is causing it to miss the standard Hall C beam dump. This would cause the beam to interact with air in the hall while it passes through toward the beam dump, by which the ionization would create an unacceptable background with harmful by-products. Therefore, an 80-foot-long helium bag was used as an additional beam line from the scattering chamber to the beam dump. The exit windows were large enough to accept the different beam deflections 2.8° and 2.2° for the different beam energies 4.72 and 5.89 GeV, respectively. This large aperture of the exit volume does not allow evacuation done as for the standard Hall C beam exit pipe. Therefore, helium is used instead of air filling to minimize ionization.

3.2 BigCal Electromagnetic Calorimeter

The electromagnetic calorimeter of the BETA detector package is called *BigCal*, which was assembled by the $GE_p - III$ collaboration [53,54]. It consisted of 1744 type TF1-0 lead-glass bars. 1024 of these were $3.8 \times 3.8 \times 45.0$ cm^3 blocks contributed by the Institute for High Energy Physics (IHEP) in Protvino, Russia, while the remaining 720 were $4.0 \times 4.0 \times 40.0$ cm^3 blocks from the Yerevan Physics Institute in Armenia,

and were previously used to study Real Compton Scattering (RCS) on the proton in Hall A at Jefferson Lab. The Protvino blocks were stacked 32×32 to form the bottom section of BigCal and the RCS blocks were stacked 30×24 on top of these as seen in Figure 3.10.

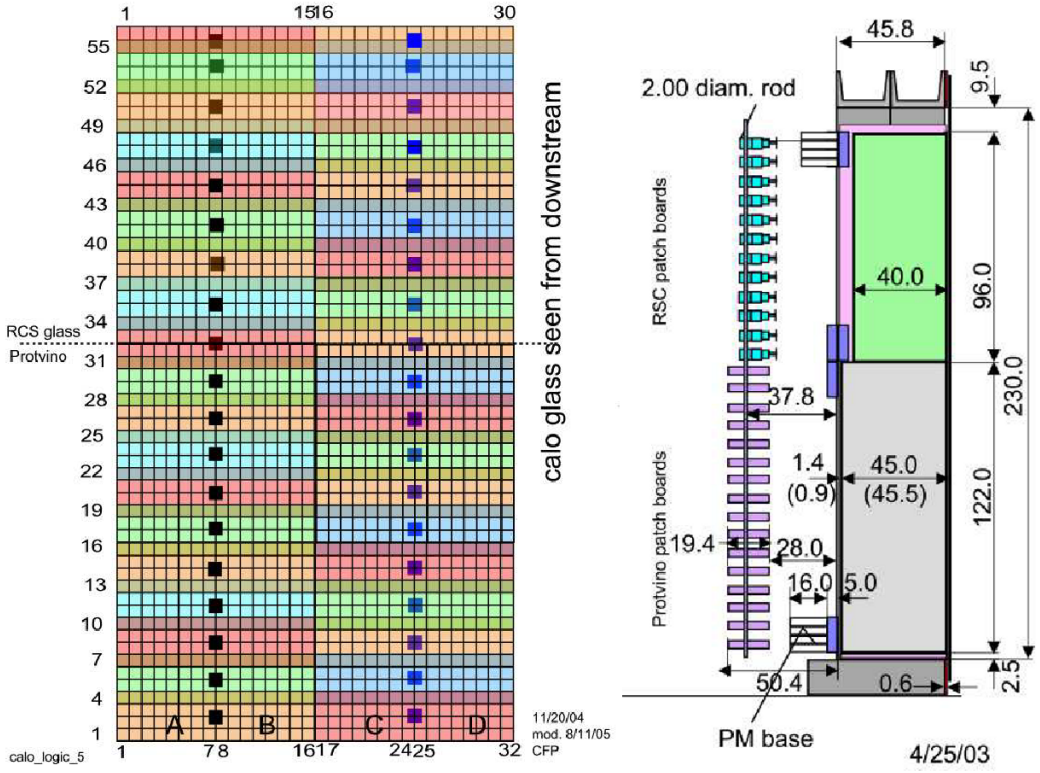

Figure 3.10. *Left*: The face of BigCal showing 1,744 lead-glass blocks, with different colors indicating the groupings of the trigger channels. *Right*: Cutaway view of the calorimeter from the side. Diagrams are from reference [171].

The assembled calorimeter had an area of roughly 122×218 cm^2, making a large solid angle of approximately 0.2 sr with the face of the calorimeter placed 3.50 m from the target cell.

When an energetic electron passes through a given material, it loses energy by radiation producing Bremsstrahlung photons. These high-energy photons convert to e^+e^- pairs, which in turn radiate more photons, and the chain of events leads

to a "shower" of electrons, positrons and photons. The process continues until the energies of the secondary particles fall below 100 MeV, after which they lose energy, predominantly through ionization, and are eventually absorbed. An electromagnetic shower of particles in a calorimeter block is shown in Figure 3.11.

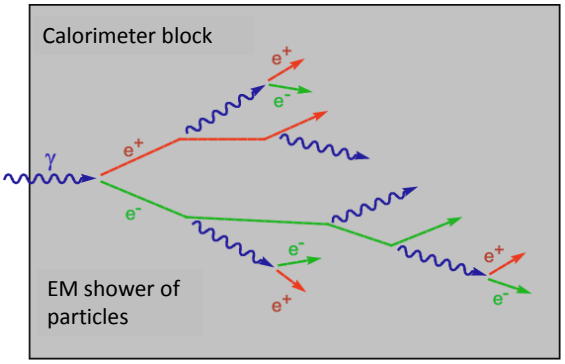

Figure 3.11. Electromagnetic shower of particles in a calorimeter block.

The primary and secondary electrons and positrons move close to the speed of light, and faster than c/n, where n is the index of refraction of the material. Therefore, they emit Cherenkov radiation at optical wave lengths, which can be collected by photomultiplier tubes (PMT) to obtain a measurement of the energy of the incident particles.

Table 3.4. Table of characteristics of TF1-0 lead-glass used for BigCal.

Index of Refraction, n	1.6522
Density, ρ	3.86 g/cm^3
Radiation Length, X_0	2.74 cm
Moliere Radius, R_M	4.70 cm
Critical Energy, E_c	15 MeV

The characteristics of the TF1-0 lead-glass used in BigCal are shown in Table 3.4. It has a high density, ρ, a high index of refraction, n and a relatively short radiation length, X_0 which is the mean distance electrons travel through a given material for an interaction before losing $1/e$ of their energy by bremsstrahlung. The radiation

length, X_0 is expressed by the atomic number, Z and the mass number, A of the material as, $X_0 \approx 180 \cdot A/Z^2$. The thickness of the lead-glass blocks in BigCal is approximately 16 radiation lengths (16.2 for the RCS section, 16.4 for the Protvino section) and this is enough material to fully stop electrons with energies up to 10 GeV. It is also highly transparent, making it an efficient collector of photons emitted by showering particles. Therefore, all scattered electrons in this experiment deposit their full energy in BigCal. The individual lead-glass bars are optically isolated from each other by an aluminized mylar wrapping to ensure that the light radiated in each bar is contained within that bar. Each of the bars is optically coupled to a PMT through a 5 mm thick Si-pad and the whole system is enclosed in a black box to keep the setup light tight. The signal and power cables enter the black box by labyrinth openings. The analog signals come from PMT that are taken through several stages of summing and discriminating to produce final ADC (analog-to-digital converter) and TDC (time-to-digital converter) signals. The wiring of BigCal has been documented in research conducted by Perdrisat and Puckett [171, 172].

The Moliere radius, R_M, is the radius of a cylinder containing on average 90% of the shower's energy deposition, 99% of the shower is contained within 3.5 R_M. Compared with the ~ 4 cm transverse size of the blocks, electron showers are typically spread out in 3×3 to 5×5 block clusters. By calculating the center of gravity of each cluster of signals in a shower, its coordinate can be reconstructed.

In order to perform a coincidence experiment with the proton detected in HMS, the electron detector is required to have a large acceptance to match the electron acceptance to the proton acceptance defined by the HMS collimator. The lead-glass electromagnetic calorimeter, BigCal, provides the needed acceptance with enough energy and angular resolution. Andrew Puckett's theses contains discussion of the background and use of the calorimeter in great detail [173].

3.3 High Momentum Spectrometer, HMS

The primary apparatus for the data of this thesis is based on the superconducting magnetic spectrometer called *High Momentum Spectrometer (HMS)* which has a large solid angle and momentum acceptance, providing the capability of analyzing high momentum particles (up to 7.4 GeV/c). It is located on the right side of the beam line as viewed from upstream of the target (see Figure 3.1). The spectrometer consists of three quadrupole magnets and one dipole magnet in a QQQD configuration together with the detector package. A schematic view of HMS is shown in Figure 3.12.

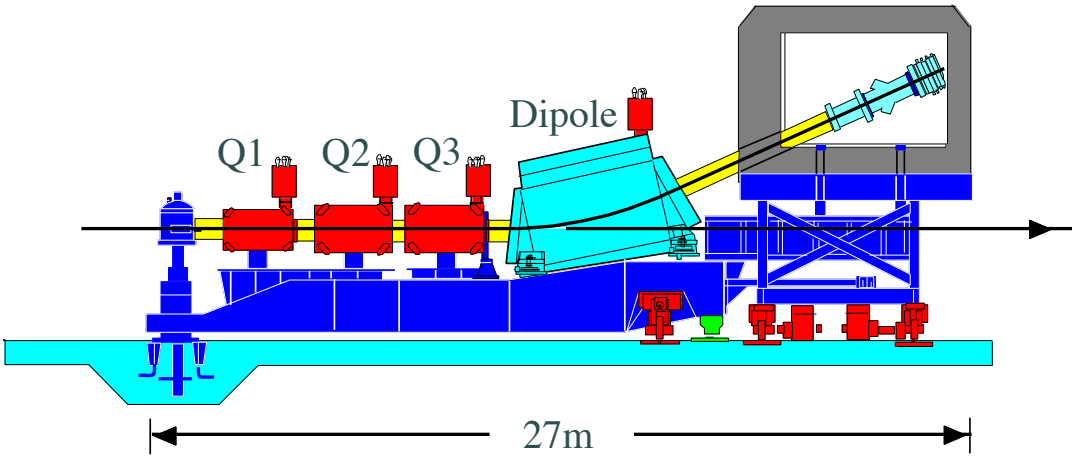

Figure 3.12. Schematic of the HMS spectrometer.

The detector support frame is mounted on a common carriage with the magnets so that it remains stationary with respect to the optical axis. The shielding hut surrounding the detector package is supported on a separate carriage. The entire structure rests on concrete rails so that it can be rotated around the rigid central pivot of the experimental hall.

3.3.1 Magnets

The HMS magnet system consists of three quadrupole magnets which focus charged particle trajectories, and a dipole magnet which deflects the particle trajectories according to their momentum into the detector hut by a 25° vertical bend. The superconducting coils of the magnets are cooled by liquid helium at 4 K temperature supplied by the CEBAF End Station Refrigerator (ESR).

Quadrupoles

The three quadrupole magnets are a cold-iron superconducting design and are named Q_1, Q_2, and Q_3 for the order in which scattered particles from the target pass through them. Q_2 and Q_3 are identical, while Q_1 is somewhat smaller in dimensions. Table 3.5 shows the size and operating parameters of the HMS quadrupoles (the maximum current, I^*_{max} is for 4.0 GeV/c central momentum). The optical axis of each quadrupole was determined using the Cotton-Mouton method [174] and all magnets in the hall are aligned with respect to the optical axis.

Table 3.5. Operating parameters of the HMS quadrupoles.

magnet	effective length, m	inner pole radius, cm	I^*_{max}, A
Q_1	1.89	25.0	580
Q_2	2.155	35.0	440
Q_3	2.186	35.0	220

The initial model used to determine the field settings was generated using the COSY INFINITY program from MSU [175]. The quadrupoles were all field-mapped, and the maps were used to determine the conversion between current and field integral ($\int B \cdot dl$). The focal plane is defined as the surface created by varying the angles of the initial rays, and determining the point where they are focussed by the magnetic system. This refers to the "true" focal plane. However, the nominal focal plane used when analyzing the data is defined to be the plane perpendicular to the central

trajectory, at the position where the central ray intersects the true focal plane. In HMS, the focal plane is located near the center of the two drift chambers. The true focal plane of the spectrometer is actually tilted $\sim 85^\circ$ from the "detector" focal plane.

The HMS magnets are operated in their standard tune: point-to-point tune in which the quadrupoles Q_1 and Q_3 are focusing in the dispersive direction, while Q_2 focuses in the non-dispersive direction. This tune provides a large momentum acceptance, solid angle, and extended target acceptance. The quadrupole fields are regulated by monitoring the current in the magnets and typically, the current is stable at the 10^{-4} level. In order to minimize particle loses and resolution degradation due to multiple scattering, and to provide thermal insulation, the entire magnetic length of the HMS is evacuated from the acceptance-defining collimators to the dipole exit flange which is just upstream of the first detector and the location of the optical focal plane of the spectrometer. Using the coordinates and the in-plane, out-of-plane angles of the trajectories at the focal plane, tracks can be reconstructed to determine the location and direction of the events at the target.

Dipole

The HMS dipole is a superconducting magnet with a 25° vertical bend for the central ray. The gap between its flat poles is 42 cm. The dipole's bending radius is 12.06 m, giving an effective length of 5.26 m for the 25° central bend. The momentum dispersion of HMS is 3.71 cm/% [176] meaning that a 1% deviation of the particle momentum from the central momentum results in a physical displacement of 3.71 cm from the central ray at the focal plane. The dipole is also field-mapped. The dipole field is stable at the 10^{-5} level, which is monitored and regulated with an NMR probe.

Particles of a given momentum entering the dipole at a higher vertical position see a smaller $\int B \cdot dl$ with respect to the central path and thus undergo smaller deflection, while the particles entering the dipole at a lower vertical position undergo a larger deflection.

3.3.2 Collimators

A slit system was installed in front of the first quadrupole, allowing remote insertion and removal of various collimators. There are three HEAVYMET (90% machinable Tungsten with 10% CuNi) collimators with density of 17 g/cm^3. The three collimators are shown in Figure 3.13.

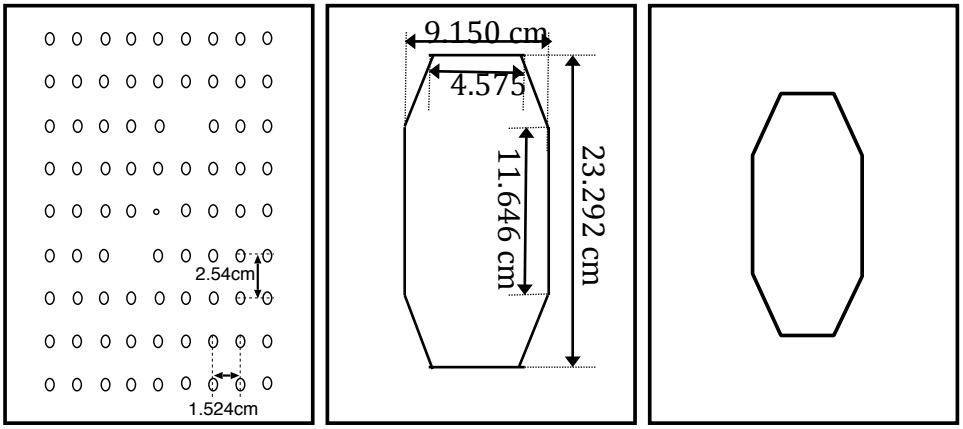

Figure 3.13. *Left*: The HMS sieve slit, *center*: The larger (pion) collimator, *right*: The smaller collimator.

The first collimator, Figure 3.13 (*left*), is a 3.175 cm thick sieve slit used for testing the optical properties of the HMS. It contains a large number of small holes, in which nine rows (columns) in the dispersive (non-dispersive) direction with 0.508 cm in diameter, except for the central sieve hole, which has a smaller diameter of 0.254 cm and is used to determine the HMS angular resolution. The hole spacing is 2.54 cm in the vertical direction and 1.524 cm in the horizontal direction. Two holes are

missing in the sieve slit in order to verify proper left-right and top-bottom directions of the reconstructed angles. The outermost rows of sieve holes are located at ±10.16 cm, corresponding to ±61.2 mrad in the dispersive direction, while the outermost columns of sieve holes are located at ±6.10 cm, corresponding to ±36.7 mrad in the non-dispersive direction at a distance of 166 cm from the target. To use the sieve slit to calibrate the spectrometer optics coefficients, scattered electrons from a series of thin solid foil targets located at a known position along the beam line are measured. The in-plane and out-of-plane angles are geometrically determined by the ray from the thin target foil to the small sieve slit hole and compared with the measured data. SANE has used the optics coefficients calibrated by the previous experiments and Figure 3.14 shows the event reconstruction at the front of the sieve slit. The Y axis represents the vertical position while the X axis represents the horizontal position for each reconstructed event on the sieve slit in HMS coordinate system. Note that there are no sieve holes at the vertical extremes of the HMS acceptance. This means that the optical reconstruction parameters obtained from fitting sieve slit data give relatively poor resolution when extrapolated to the extreme regions of the acceptance not covered by the sieve slit.

Either of two octagonal collimators of different sizes is used to define the solid angle acceptance of the HMS. The large collimator is designed to prevent particle losses over a large momentum bite for a point target, and the small collimator is designed to prevent particle losses for an extended target. For an extended target, a slightly larger range of in-plane angles is accepted since particles coming from anywhere along the target length can pass through the collimator. Both are 6.35 cm thick and have flared holes to match the angular acceptance of the HMS. For the experiment SANE, the larger of the two collimators so-called pion collimator was used. This has an opening of 9.150 cm in the horizontal direction and 23.292 cm in the vertical direction as shown in Figure 3.13 (*center*). At a distance of 166.00 cm

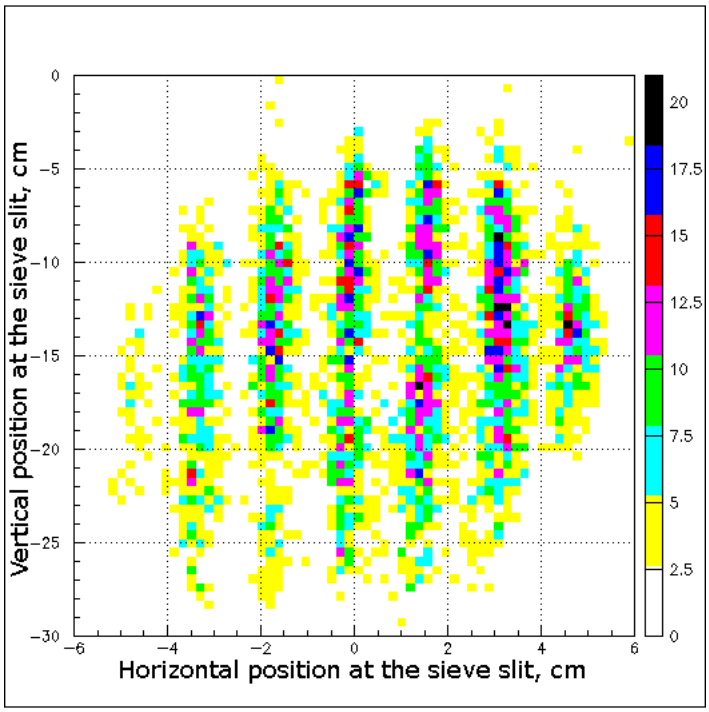

Figure 3.14. HMS reconstruction at the Sieve Slit for the target magnetic field off, run 72088.

from the target, the angular acceptance defined by the collimator is roughly 70 mrad in the out-of-plane angle and 28 mrad in the in-plane angle, giving a solid angle of 6.74 msr.

The HMS was designed to have a maximum central momentum of 7.4 GeV/c. Table 3.6 summarizes the performance characteristics of the HMS in its standard configuration.

3.3.3 Detector Package

The HMS is equipped with a set of detectors to detect and track charged particles scattered from the target. In the standard configuration, the HMS consists of a pair of gas drift chambers (DC1 and DC2), four planes of scintillator hodoscopes (S1X, S1Y, S2X, S2Y), a gas Cherenkov detector, and a lead-glass calorimeter. The

Table 3.6. Acceptance and resolution of HMS in its standard configuration.

Max. central momentum, GeV/c	7.4
Min. central momentum, GeV/c	0.5
Momentum acceptance	±10%
Momentum resolution	<0.1%
Solid angle, msr	6.74
Scattering angle acceptance, mr	±27.5
Out-of-plane angle acceptance, mr	±70
Extended target acceptance, cm	7
Scattering angle resolution, mr	1.0
Out-of-plane angle resolution, mr	2.0

two drift chambers provide the particle tracking information at the focal plane. The scintillator hodoscopes are used for triggering the detector read-out and provide the timing information while the gas Cherenkov detector and the lead-glass calorimeter provide the particle identification. A schematic of the HMS detector package is shown in Figure 3.15. All the detectors except the lead-glass calorimeter are oriented perpendicular to the Z axis which coincides with the central ray. High-voltage power supplies were used to provide voltage for all the detectors. These power supplies are located in the counting house.

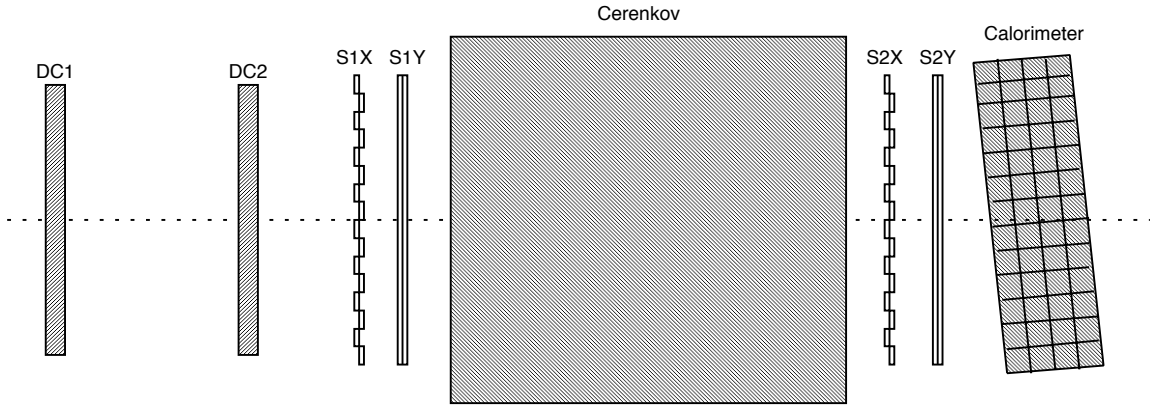

Figure 3.15. A schematic side view of the HMS detector hut.

3.3.3.1 Drift Chambers

Drift chambers are gas-ionization detectors which are used to measure the position and angle of the charged particle trajectories at the focal plane. The HMS consists of two drift chambers which are separated by 81.2 cm [177]. Each drift chamber contains six planes, two measuring X (the dispersive direction), two measuring Y (non-dispersive direction), and two that were rotated $\pm 15^{\circ}$ from the X planes (the U and V planes) in a gas-tight enclosure sealed by thin aluminized mylar windows. The planes were ordered X, Y, U, V, Y', X' as seen by incoming particles, spaced 1.8 cm apart. Figures 3.16 and 3.17 show the front and side views of one of the HMS drift chambers.

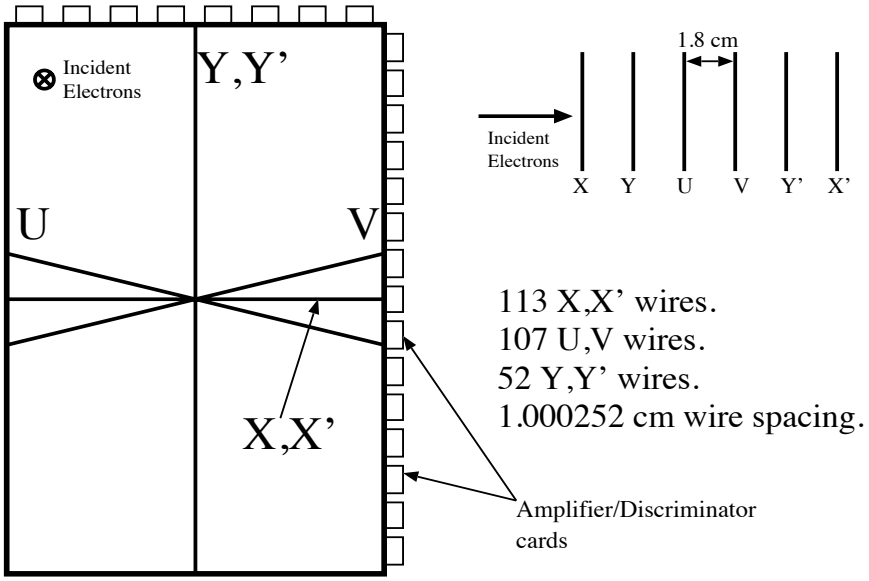

Figure 3.16. Front view of the HMS drift chambers. The read-out cards are shown on the outside of the chamber [177].

Since the U and V wires are much closer to the X, X' wires in their orientation than to the Y, Y' wires, the track position and slope are more precisely determined in the dispersive direction than in the non-dispersive direction. Each active plane contains alternating field and sense wires. The sense wires (anodes) are 25 μm diameter gold-

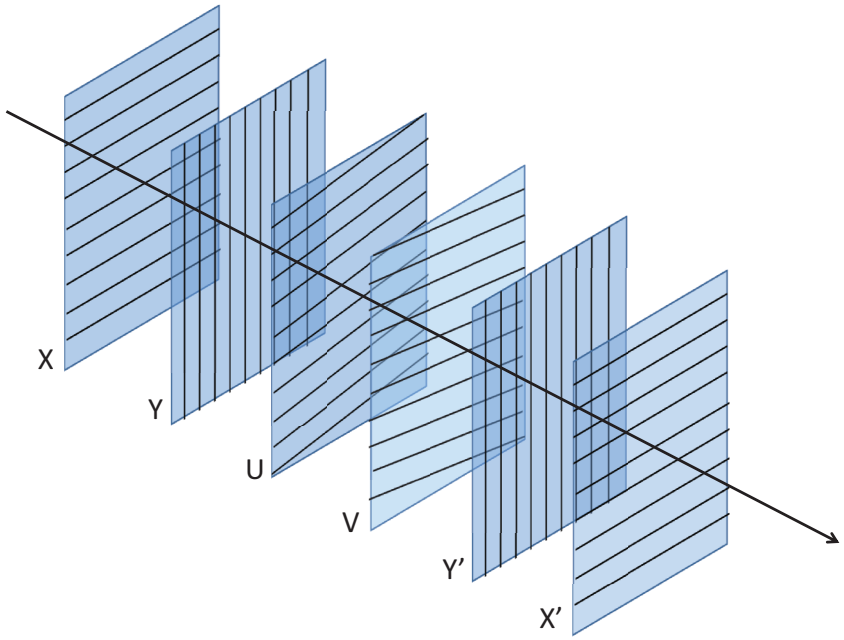

Figure 3.17. Arrangement of the drift chamber planes as seen by the incoming particles.

plated tungsten wires with a spacing of 1 cm, which are kept at positive voltage. The negative field wires (cathodes) are 150 μm gold-plated copper-beryllium wires spaced 0.5 cm to the nearest sense wires. In between the sense and field wire planes are planes of guard wires which define a symmetric "drift cell" around each sense wire by surrounding eight field wires. The negative high voltage applied to each field wire is proportional to the distance from the field wire to the sense wire. This provides an equipotential surface surrounding the sense wire that is nearly circular over the drift cell. This insures that the drift time measured by a sense wire depends only on the distance between that sense wire and the track that caused the ionization.

The gas used by the drift chambers is a 50%/50% argon-ethane mixture (by weight), doped with 1% isopropyl alcohol. There are parallel gas streams to the two chambers while the gas flow is monitored by a mass flow meter. The argon gas in the mixture provides the primary ionization and the ethane gas propagates the avalanche near the sense wire and enhances the drift properties of the mixture. Dur-

ing continuous operation at high particle rates, the gas is capable of forming polymers by recombination of dissociated organic molecules which can accumulate on the anode and cathode wires and degrade the chamber performance. The small amount of alcohol limits this formation and enhances the chamber lifetime. It also reduces chamber noise by molecular absorption.

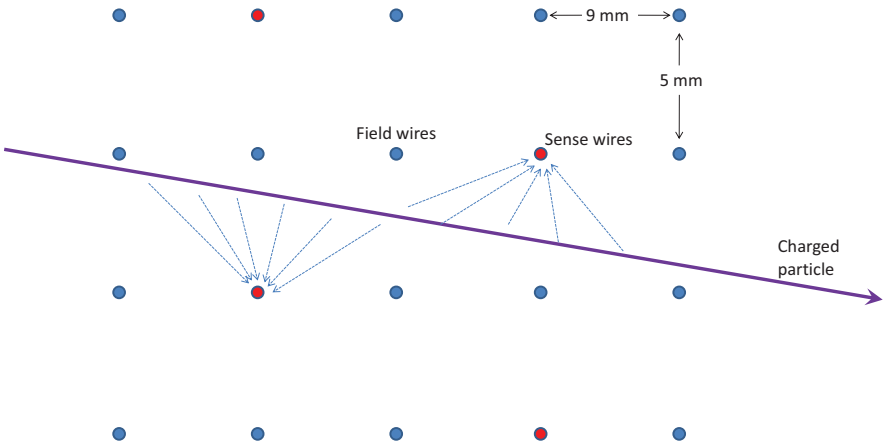

Figure 3.18. A diagram of a drift chamber cell structure representing the sense wires (red dots) and the field wires (blue dots). As the charged particle ionizes the gas in the drift chamber, the electrons are attracted to the sense wire by the electric potential generated by the field wires.

When a charged particle passes through the chamber, the gas becomes ionized, and the liberated electrons are attracted to the nearest sense wire by the electric field maintained by the voltage differential between the sense wire and the field wires (see Figure 3.18). Then an electric signal is induced on the sense wire by these electrons. These signals are amplified and discriminated by the electronic cards attached directly to the chambers. These logic signals are then sent to time-to-digital converters (TDC) located in the back of the detector hut. Fast signals from the HMS hodoscopes generated by a charged particle passing through the hodoscopes triggers the main data acquisition system to read out an event, and a stop signal is sent to the drift chamber TDCs. The hodoscope timing is used to reconstruct the time when the

particle passed through the focal plane. Then, one can determine the time it took for the electrons created by the ionizing particle to "drift" to the wire by taking the time difference between the reconstructed hodoscope time and the signal on the wire. This drift time is converted to a drift distance, which is then added to the wire position in order to get the position of the trajectory when it crossed the wire plane. This allows a determination of the position of the particle with better than 0.5 cm accuracy (half the wire spacing). By measuring the position with all six planes, the X and Y positions of the particle and its trajectory through the chamber can be measured. The large separation in Z between the two chambers provides a precise determination of the angles of charged particle trajectories and hence provides the precise particle track through the detector.

However, multiple scattering of the ionized electrons in the chamber gas, fluctuations of the drift velocity due to the electric field, and uncertainty in the absolute positioning of the wires within the chambers and in the absolute positioning of the chambers themselves relative to the HMS optical axis, contribute to the position resolution of the drift chambers of approximately 280 μm. However, unfortunately, there was a drift chamber gas leak during the SANE experiment and the efficiencies of the drift chambers were reduced dramatically. The drift time-to-drift distance calibration and their performance will be discussed in the next chapter.

3.3.3.2 Hodoscopes

The HMS is equipped with two pairs of scintillator planes which are separated by 2.6 m in Z direction [178]. Each pair consists of X and Y planes. By their fast response time, they provide fast trigger and timing information. The planes are constructed by long narrow strips of scintillators connected to the phototubes on both ends by lucite light guide which couples the flat rectangular shape of the end of the scintillator bar to the circular photo cathode of the PMT (see Figure 3.19). Each strip is 1.0 cm

thick, 8.0 cm wide, and 75 (120.5) cm long for the X (Y) paddles with approximately 0.5 cm overlap between the paddles in order to avoid the gaps between them. The X (Y) planes have 16 (10) elements each, giving each X-Y pair an active area of 120.5 cm by 75.5 cm. The 16 paddles in the X planes are oriented horizontally so that the transverse dimension of the paddle measures the dispersive coordinate by using the dimensions of the paddles. The longitudinal dimension measures the non-dispersive coordinate by using the timing information of a PMT at the opposite ends of each paddle. Similarly, the 10 paddles in the Y plane are oriented vertically so that their transverse dimension measures the non-dispersive coordinate and their longitudinal dimension measures the dispersive coordinate. The coordinate corresponding to the transverse size of the paddles localizes the trajectory of the particles to a square area of 8×8 cm^2, which is useful to support the drift chamber track reconstruction at high particle rates.

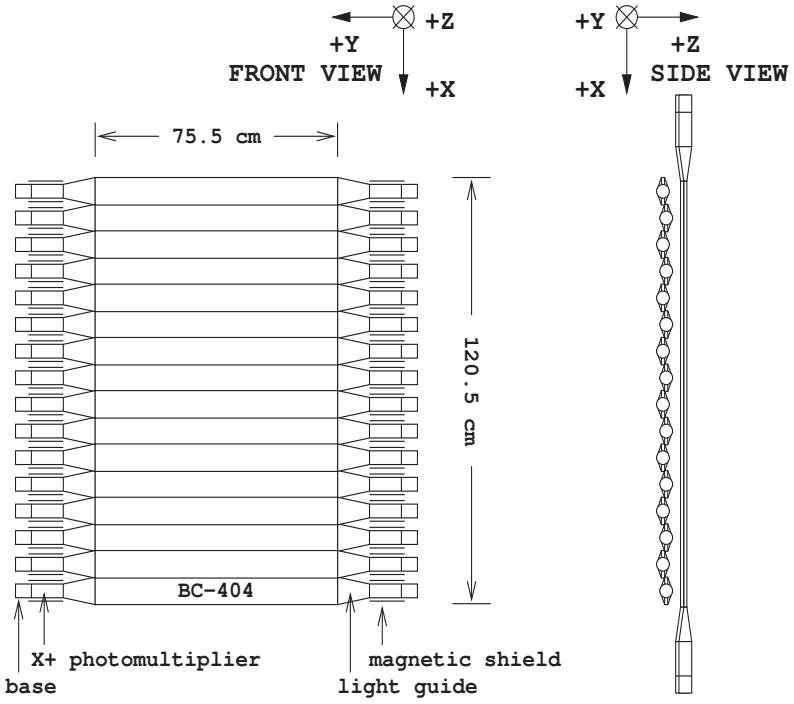

Figure 3.19. HMS hodoscope structure.

All hodoscope PMTs were gain-matched using a ^{60}Co γ-ray source in order to obtain uniform signal, timing and efficiency characteristics. The PMT voltages were adjusted so that the position of the Compton edge in the γ-ray spectrum was constant and large enough to give a high trigger efficiency for photons.

When energetic charged particles are passing through the material, they ionize the atoms in the material and liberate electrons. These electrons excite the molecules in the material which emits optical photons by de-excitation. This light propagates through the scintillator bar and the light guide to the PMTs at the end via total internal reflection, which then convertes to charge and amplifies by the PMTs. The scintillators and the light guides are wrapped in one layer of aluminum foil and one layer of black Tedlar for light-tightness, which completely reflects the scintillation light emitted at the angles larger than its critical angle for internal reflection and makes them also reach the PMTs. The signals from each PMT are sent to ADCs, TDCs and logic modules in the counting house. These logic modules generate the logical OR of all the signals coming from each side of the hodoscope planes. For example, all the signals coming from the right side of the hodoscope plane 1, S1X$_+$ is given by the logical OR of the signals coming from the right side of all of the individual scintillator paddles in plane 1, S1X1$_+$ to S1X16$_+$:

$$S1X_+ \equiv (S1X1_+ \text{ OR } S1X2_+ \text{ OR } \ldots\ldots\ldots\ldots\ldots \text{ OR } S1X16_+)$$

. Similarly, all of the signals coming from the left side of the hodoscope plane 1, S1X$_-$ is given by the logical OR of the signals coming from the left side of all of the individual scintillator paddles in plane 1, S1X1$_-$ to S1X16$_-$

$$S1X_- \equiv (S1X1_- \text{ OR } S1X2_- \text{ OR } \ldots\ldots\ldots\ldots\ldots \text{ OR } S1X16_-)$$

Then these two logic signals from each side are combined as $S1X \equiv$(S1X$_+$ AND S1X_-) indicating whether the S1X plane fired. Similarly, the logic signals S1Y, S2X and S2Y are generated and a new logic signal is generated using these four signals to

indicate that at least three of the four planes are fired. This logic signal (SCIN) is then sent to the main trigger logic and to the scalers to be recorded.

Having more precise timing information from both pairs of hodoscopes, it can be used to determine the time-of-flight information and hence be used for particle identification. However, this is extremely limited at high momenta and particle velocities. Because of the large distance between two scintillator pairs, the trigger formed by the hodoscopes is very restrictive on the angles of tracks coming from the chambers. Acquiring of the coincidence between both pairs decreases the probability of triggers in one pair or the other caused by low-energy background radiation, noise and other background or random signals mixed with good events of real charge particle tracks coming from the target through the HMS and both drift chambers.

3.3.3.3 Gas Cherenkov Detector

Gas Cherenkov detectors are typically used for electron/pion identification and separation. They detect the Cherenkov radiation emitted by the charged particle passing through the detector medium (with index of refraction, n) with velocity β, which is faster than the speed of light in that medium, c/n (where c is the speed of light in vacuum). The light is emitted in a forward-pointing cone with an opening angle, $\cos\theta_c = 1/n\beta$. This light is then reflected from focussing mirrors to PMT tubes. By choosing the medium properly, the threshold velocity ($=c/n$) can be made such that electrons emit Cherenkov radiation and pions do not. For separating pions from electrons in a momentum range 1-4 GeV, the index of refraction of the medium must be very small and therefore, a gas can be used as the Cherenkov medium. The type of gas and operating pressure can be chosen in order to maximize the signal for electrons, while minimizing scintillation and keeping the pion Cherenkov threshold above the spectrometer momentum. Still, a pion can be misidentified as an electron if the pion produces a knock-on electron of sufficient energy to emit Cherenkov light. Because

the total thickness of material that can cause knock-on electrons is dominated by the window and the detector material immediately in front of the Cherenkov detector, a thin entrance window is used to reduce this effect.

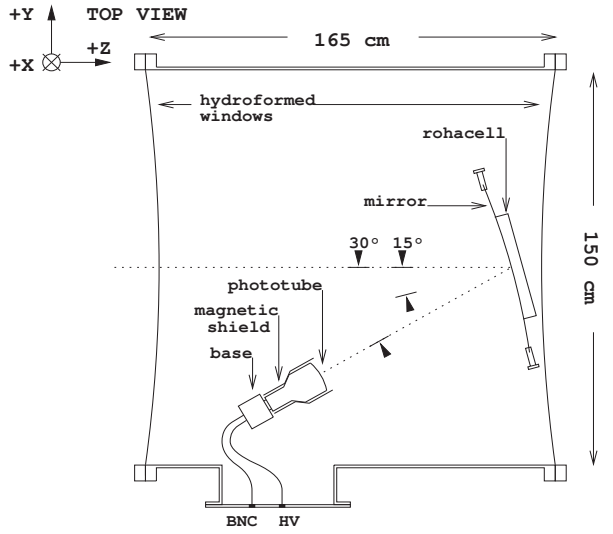

Figure 3.20. HMS Cherenkov detector geometry.

The HMS Cherenkov tank is cylindrical with an inner diameter of $\sim$ 150 cm and a length of $\sim$ 165 cm. Its entrance and exit windows are made of 0.1016 cm Al (0.27 g/cm^2). A pair of front-reflecting spherical mirrors are placed vertically at the far end of the tank at a 15° angle with the effective length (length before the mirrors) of $\sim$ 12$Tedlar$0 cm (see Figure 3.20). The mirrors reflect and focus the Cherenkov light into two PMTs which produce the signals proportional to the number of Cherenkov photons. In addition, the PMT front surfaces are coated with a wavelength-shifting coating in order to improve the PMT quantum efficiency in the ultra-violet wavelengths. The tank is filled with 0.42 atmospheres of C_4F_{10}, giving an index of refraction of 1.0006. This gives a pion threshold of 4 GeV/c and electron threshold of $\sim$ 15 MeV/c. The signals from each PMT are sent to ADCs and TDCs in the counting house to be recorded.

3.3.3.4 Lead-Glass Calorimeter

The HMS lead-glass calorimeter is positioned at the back of the HMS detector hut and is used as a particle identification detector together with the gas Cherenkov detector by measuring the deposited energy of the charged particles. It consists of four layers of 13 stacked 10 cm × 10 cm × 70 cm blocks of lead-glass giving a total of 52 blocks with an active area of 130 cm × 70 cm. Lead-glass has a density of 3.86 g/cm^3 and a radiation length of 2.54 cm, making the entire calorimeter $\sim$ 16 radiation lengths in total thickness. PMT tubes are attached to each block at one end and each block is wrapped with one layer of aluminized mylar (25 μm) and two layers of Tedlar PVF film (38 μm each) to make them light tight. As seen in Figure 3.12, the calorimeter is tilted about 5° with respect to the optical axis to avoid particles from passing in between the blocks. The operating voltages of the PMTs were set to match the gain of the individual blocks.

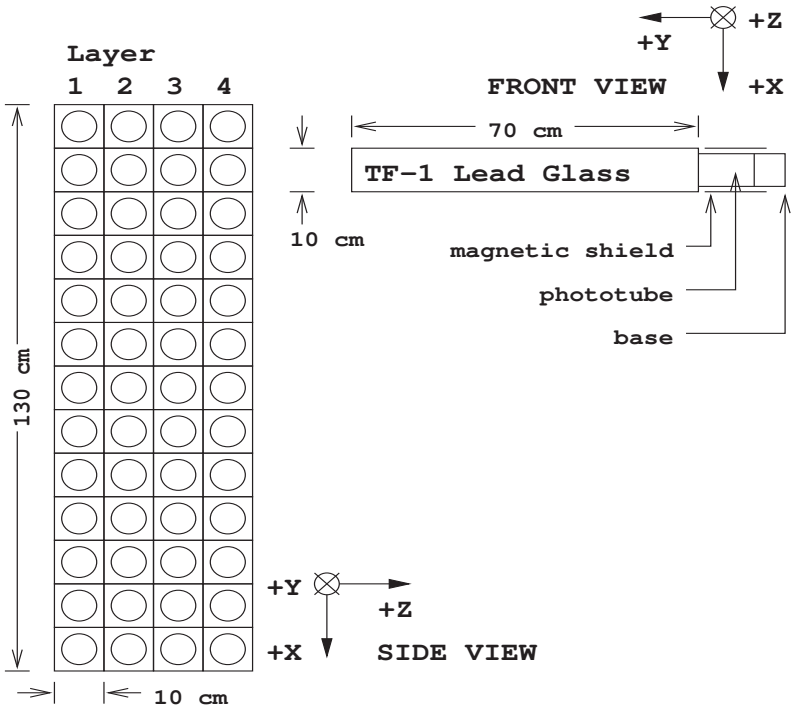

Figure 3.21. Calorimeter detector geometry.

All of the electron energy that strikes the calorimeter is deposited in the calorimeter by producing a shower of particles (e^-, e^+, γ) as described in Section 3.2. An example of an electromagnetic shower of particles in a calorimeter block can be seen in Figure 3.11.

The Cherenkov light produced by the process is detected by a PMT connected to each lead-glass block. The total signal in the PMTs is proportional to the total energy of the initial electron. The calorimeter PMT signals are sent to the read-out electronics in the counting house to the ADC modules. The calorimeter is calibrated for the conversion of the ADC to the energy deposition.

3.4 Target

As a double polarization experiment, SANE requires a polarized nucleon target. Frozen ammonia (NH_3) was utilized as a polarized proton target. In addition to the polarized targets, ^{12}C and CH_2 targets were also used for calibration purposes. The protons in the NH_3 molecules were polarized using Dynamic Nuclear Polarization (DNP) in a 5 T magnetic field at 1 K temperature. The polarization of the target was monitored continuously by a Nuclear Magnetic Resonance (NMR) system. In this section, the principle of DNP, how NMR was used to measure the target polarization, and an overview of the SANE polarized target will be briefly discussed.

3.4.1 Dynamic Nuclear Polarization (DNP)

In DNP, nucleons were polarized by transferring the free electron polarization in the medium to the nucleons which is induced by microwave radiation at high magnetic field and low temperature. When the material is placed in a magnetic field, unpaired electron and nuclear spins tend to align themselves in the direction of the magnetic field due to the interaction between the magnetic moments, $\vec{\mu}$ and the magnetic field,

$\vec{B}$. For an electron, the interaction is given by, $\vec{\mu_e} = g_e \mu_B \vec{S}$, and for a proton, it is given by, $\vec{\mu_p} = g_p \mu_N \vec{S}$, where $\vec{S}$ is the particle spin, μ_B and μ_N are the Bohr and nuclear magnetons, and g is the gyroscopic, *i.e.*, g-factor of the particle, $g_e \sim 2$, $g_p \sim 2 * 2.79 = 5.58$. Further, this interaction creates a set of $2J+1$ energy sublevels via the Zeeman interaction, where J is the total spin of the particle. The polarization describes the alignment of the nuclear spins in the magnetic field for a desired energy sub-level. For a nucleus with total spin J, the nuclear polarization, P_J is given by,

$$P_J = \frac{\Sigma_i J_{z,i} N_i}{J \Sigma_i N_i},$$

where N_i is the total number of nuclei with spin projection along the axis of the magnetic field, which is considered here as along the Z axis. The relative population of spins aligned to anti-aligned in two different energy sublevels for a spin-1/2 system is given by a Boltzmann distribution,

$$\frac{N_\uparrow}{N_\downarrow} = exp\left(\frac{\mu B}{kT}\right),$$

hence, the vector polarization of the spin-1/2 particles is given by,

$$P_{1/2} = \frac{N_\uparrow - N_\downarrow}{N_\uparrow + N_\downarrow} = \tanh\left(\frac{\mu B}{kT}\right),$$

where $\vec{\mu} \cdot \vec{B} = \mu B$ (along $\vec{B}$ direction) is the energy of the Zeeman interaction, k is the Boltzmann constant, and T is the temperature of the medium. According to the above equation, at 2.5 T magnetic field and 1K temperature, the electron polarization reaches about 92%. However, having a much smaller magnetic moment than the electron ($\mu_e \sim 600 \mu_p$), the proton reaches a far lower polarization of about 0.25% at the same magnetic field and temperature conditions [179]. As magnetic

fields far beyond 2.5 T and temperatures far below 1 K are difficult to achieve, DNP is used to increase the nucleon polarizations enormously.

In DNP, microwaves are introduced to the thermal equilibrium polarization method. In addition, the target material has to be doped with paramagnetic impurities in the form of unpaired electrons. The Hamiltonian of such a system of free electrons and a spin-1/2 nucleons placed in a magnetic field is given by,

$$H = H_0 - \vec{\mu_e} \cdot \vec{B} - \vec{\mu_N} \cdot \vec{B} + H_{ss}.$$

The term H_0 is the free Hamiltonian for the electrons and the nucleon. The second (third) term describes the interaction between the electron (nucleon) and the magnetic field. The final term, H_{ss} arises due to dipole-dipole interactions between the electron and the nucleon which has relatively small effect on H_0 compared to the second and third terms. The hyper-fine splitting from spin-spin interactions of the electron and proton in the magnetic field results in four discrete energy levels corresponding to the four permutations of aligned and anti-aligned spins as in Figure 3.22.

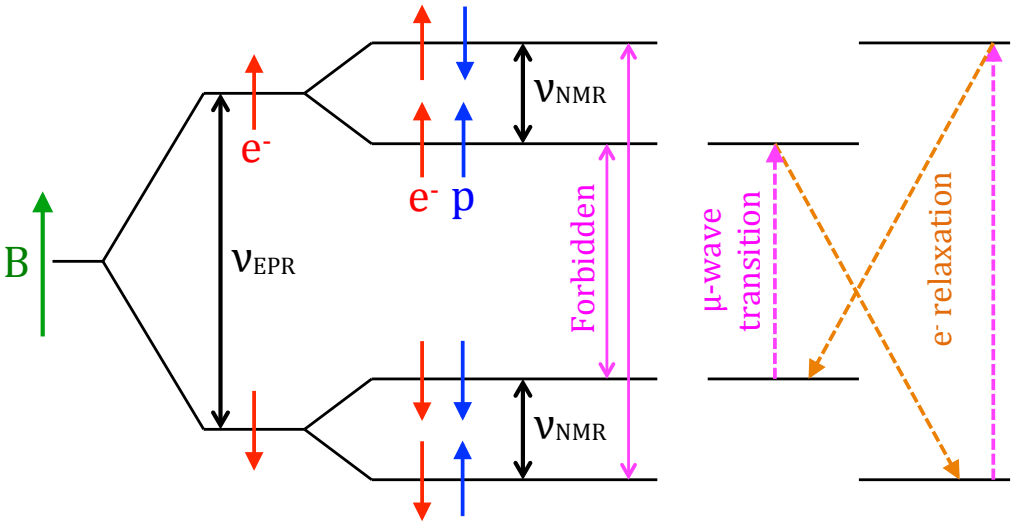

Figure 3.22. The energy level diagram of a spin-1/2 nucleon electron system placed in a magnetic field. Details are given in the text.

These are four states, $|\ -+\rangle$, $|\ --\rangle$, $|\ ++\rangle$, and $|\ +-\rangle$, where the first sign indicates the electron spin direction and the second sign indicates the nucleon spin direction. The transitions $|\ --\rangle \rightarrow |\ +-\rangle$ and $|\ -+\rangle \rightarrow |\ ++\rangle$ are due to electron spins flipped by applying microwaves at the EPR (Electron Paramagnetic Resonance) frequency, ν_{EPR}, which corresponds to the Zeeman energy of the electron's magnetic moment in the given $\vec{B}$ field, $\vec{\mu_e} \cdot \vec{B}$. Similarly, the proton transitions $|\ +-\rangle \rightarrow |\ ++\rangle$ and $|\ --\rangle \rightarrow |\ -+\rangle$ can be carried out by proton spins flipped by microwaves at the NMR (Nuclear Magnetic Resonance) frequency, ν_{NMR}, corresponding to the proton Zeeman energy, $\vec{\mu_p} \cdot \vec{B}$. However, the transitions that require flipping both the electron and the nucleon spins, $|\ --\rangle \rightarrow |\ ++\rangle$ and $|\ -+\rangle \rightarrow |\ +-\rangle$ are forbidden due to the dipole selection rules. But the dipole-dipole interaction, which is much smaller than the Zeeman effect, leads to a slight mixing of the nuclear states. This then allows transitions of the type $|\ --\rangle \rightarrow |\ ++\rangle$ and $|\ -+\rangle \rightarrow |\ +-\rangle$ with a probability much less ($\sim 10^{-4}$) than the allowed transitions.

Thus, the transitions $|\ --\rangle \rightarrow |\ ++\rangle$, from anti-aligned protons to aligned ones leading to *positive polarization*, can be induced with microwaves at $\nu_{\mu-} = \nu_{EPR} - \nu_{NMR}$. Because of the strong interaction with the lattice, the electrons reach thermal equilibrium very rapidly (in 10^{-3} s) by relaxation to the lowest energy state, $|\ ++\rangle \rightarrow |\ -+\rangle$ allowing it to flip the spin of another proton, which continuously drives protons into positive polarization. However, due to the weak coupling to the lattice, the relaxation time of the nucleons is much larger, $\sim 10^3$ s. They instead relax through coupling with the electron spin-spin system via the same transitions induced to polarize the nucleons with microwaves. As these transitions are "forbidden", they are less likely, between 10^4 and 10^6 times smaller than the electron relaxations [180]. This populates one spin state of the nucleons near that of a free electron. In the same manner, aligned protons can be anti-aligned, called *negative polarization*; the transition $|\ -+\rangle \rightarrow |\ +-\rangle$ is induced using microwaves at $\nu_{\mu+} = \nu_{EPR} + \nu_{NMR}$. The

electrons become relaxed by the transition $|+-\rangle \rightarrow |--\rangle$ back to their lowest energy state, allowing them to flip the spin of another proton. In this way both positive and negative polarizations can be achieved with the same magnetic field by altering the microwave frequency.

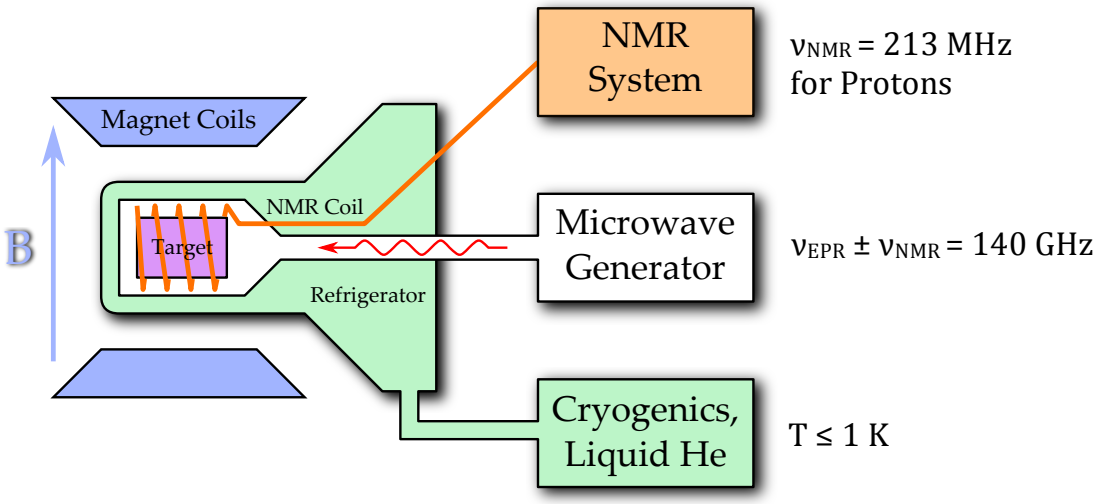

Figure 3.23. Schematic overview of the systems required for Dynamic Nuclear Polarization [156].

Figure 3.23 shows the schematic overview of the systems required for Dynamic Nuclear Polarization. In SANE, the protons in NH_3 were polarized using DNP in a 5 T magnetic field at 1 K temperature. The positive polarization was reached by applying the microwave radiation with a frequency of 140.1 GHz, while the negative polarization was reached by 140.5 GHz.

3.4.2 Monitoring of the Target Polarization

A Nuclear Magnetic Resonance (NMR) system was used to monitor the polarization of the SANE target. As described in the previous section, a particle with total spin, J placed in an external magnetic field $\vec{B}$ results in $2J+1$ energy levels due to Zeeman splitting. In addition, the magnetic field, $\vec{B}$ exerts a torque, $\vec{\Gamma}$ on the particle

magnetic moment, $\vec{\mu}$ in the form of $\vec{\Gamma} = \vec{\mu} \times \vec{B} =\mid \gamma \vec{L} \times \vec{B} \mid$, where γ is the gyromagnetic ratio and L is the angular momentum. This causes the spins of the nucleons to precess about the direction of the applied $\vec{B}$ field. The frequency of this precession, known as the Larmor frequency, is given by $\omega_0 = \gamma \mid \vec{B} \mid$. In the NMR technique an oscillating magnetic field, $\vec{B_1}$ with RF frequency ω is applied perpendicular to the static $\vec{B}$ field with the frequency equal to the particle's Larmor frequency, ω_0 to match the energy difference between the nuclear spin levels. This causes a flip of the nucleon spin as it absorbs or emits energy due to the magnetic susceptibility, $\chi(\omega)$ of the material as a function of RF frequency ω,

$$\chi(\omega) = \chi'(\omega) - i\chi''(\omega),$$

which can be expressed as the difference of a dispersive term $\chi'(\omega)$ and an absorption term $\chi''(\omega)$. For a given spin type, the absorption portion of the magnetic susceptibility integrated over the frequency is proportional to the polarization of the material [181],

$$P = K \int \chi''(\omega) d\omega \tag{3.4.1}$$

with a constant K containing information on spin species, spin density, gyromagnetic ratio and other NMR system quantities. This absorptive signal can be measured using an inductor, called an NMR coil embedded in the target material sample. The oscillating magnetic field $\vec{B_1}$ with a radio frequency near to the Larmor frequency was applied to this NMR coil to flip the spin of the nucleon. In turn, this changes the susceptibility of the material surrounding the coils, which creates an inductance,

$$L_C(\omega) = L_0[1 + 4\pi\eta\chi(\omega)], \tag{3.4.2}$$

where L_0 is the coil inductance for unpolarized material, and η is the coil filling factor, a function of the coupling of the coil to the material. The coil's impedance is then,

$$\begin{aligned} Z_C &= r_C + i\omega L_C(\omega) \\ &= r_C + i\omega L_0[1 + 4\pi\eta\chi'(\omega) + i4\pi\eta\chi''(\omega)] \\ &= r_C - 4\pi\omega L_0\eta\chi''(\omega) + i[\omega L_0(1 + 4\pi\eta\chi'(\omega))] \end{aligned} \tag{3.4.3}$$

for a coil resistance r_C. The real part of this measurement gives the absorption component of the magnetic susceptibility and thus a measurement proportional to the polarization.

To measure the real portion of the NMR coil's impedance over frequency, called *Q-curve*, an LCR circuit called *Q-meter*, developed by the University of Liverpool [182] was used. A schematic of such a Q-meter and the NMR system used during SANE is shown in Figure 3.24.

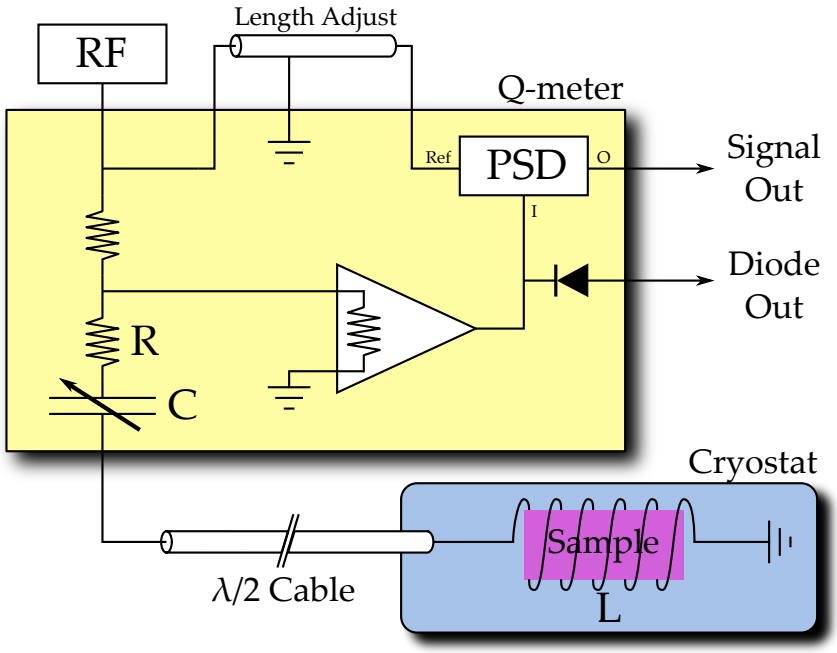

Figure 3.24. Diagram of Q Meter circuit with LCR components and target material inside the inductor coil [156].

Inductance (and impedance) of the NMR coil changes when the surrounding material absorbs or emits energy and thus changes the voltage of the LCR circuit. This circuit was tuned to the Larmor frequency of the particle, which for a proton in a 5 T magnetic field is 213 MHz. For negative polarizations in the target material, as the spin absorbs energy from RF to flip from aligned to anti-aligned, the impedance is increased above the Larmor frequency of the particle. For positive polarizations, spin emits energy while flipping from anti-aligned to aligned and the impedance is decreased below the Larmor frequency. The Q-curve is produced by the output of the Q-meter, given by the impedance plotted against the RF frequency. Integration of this Q-curve over the frequency gives a measurement proportional to the material's polarization after subtracting out the background signal. The background Q-curve is produced with unpolarized target material which depends on many quantities of the system.

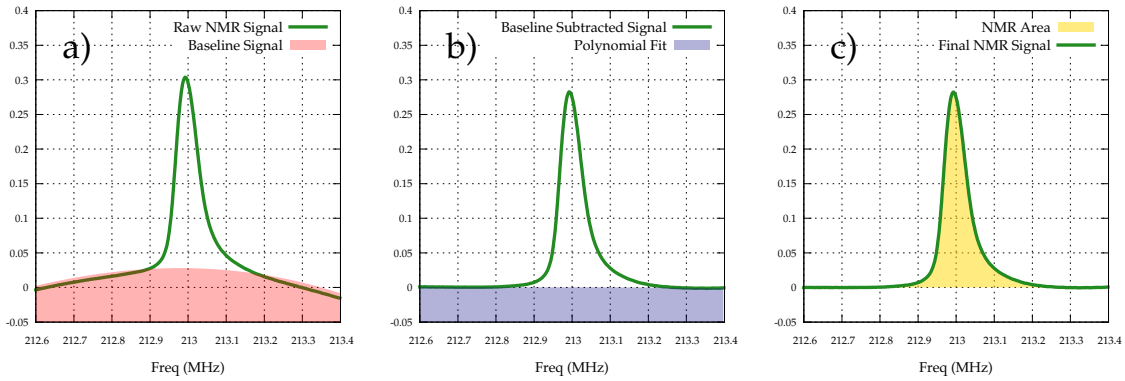

Figure 3.25. Steps on NMR signal analysis [156]. (explained in the text)

An example of NMR signal from negatively polarized NH_3 is shown in Figure 3.25. The background signal is subtracted from the signal as in a) of Figure 3.25. Then, a polynomial fit is performed on the wings of the remaining signal to remove any residual background and isolate the area of the Q-curve which is due to the polarization of the material as in b) of Figure 3.25. The final signal after subtracting this polynomial

fit can be integrated to determine the material's polarization in arbitrary units as in *c*) of Figure 3.25. However, this polarization needs to be calibrated to get the true polarization. The proportionality constant, called *calibration constant*, can be determined by measuring the area of Q-curve for a known polarization. Since the polarization at thermal equilibrium, P_{TE}, is a known quantity at a given temperature, T,

$$P_{TE} = \tanh\left(\frac{\mu B}{KT}\right),$$

the system allows to relax into the thermal equilibrium and then measure the Q-curve. The calibration constant formed by this Q-curve area allows the correction of the Q-curve area for the absolute polarization of the material. The final polarizations, which include the calibrations from the thermal equilibrium measurements and other corrections have been obtained by re-integrating the recorded NMR signals. These analyses are done by the SANE collaborator James D. Maxwell and more details can be found in [156].

3.4.3 Polarized Target Material

Choosing $^{14}NH_3$ as the polarizable proton target material has several advantages compared to lithium hydride (^{7}LiH and ^{6}LiH) which is the other commonly used irradiation doping DNP target material. Its higher maximum achievable polarization (>90% at 1 K and 5 T), the high rate at which it reaches the maximum polarization (<30 minutes), its higher resistance to radiation damage caused by an experimental beam and the high percentage of polarizable nucleons for scatterings, its dilution factor, the ratio of free, polarizable protons to total nucleons in the material, which is roughly 17.6% protons for $^{14}NH_3$, are the crucial properties. Butanol, on the other hand, is also used as a polarized proton target. However, it needs to be chemically

doped and its high ability to sustain radiation damage makes it a disadvantage in use with a high-luminosity electron beam [179].

SANE used ammonia crystals made by freezing the gaseous ammonia in a sealed aluminum cylinder in a bath of liquid nitrogen and crushed to form irregular beads of a size of about 2 mm. The small size and shape of the beads prevents overheating of the target due to the electron beam and provides a high packing fraction of the material. The packing fraction is the ratio of the volume taken by the ammonia to the target cup volume, which is determined by comparing measured and simulated yields. In order to form the free, unpaired electrons to use in DNP, ammonia beads were ionized to knock out an atomic hydrogen from NH_3 molecules to form $N\dot{H}_2$ paramagnetic centers. This process has been done at Medical Industrial Radiation Facility (MIRF) in Maryland using a 19 MeV electron beam with the material in a 87 K liquid Argon bath (LAr_2) and irradiating the material with $\sim 10^{17} e^-/\text{cm}^2$. This production of radicals turns the colorless frozen ammonia beads into a pale violet. By keeping the material at 77 K in liquid nitrogen, these radicals can remain in the material from months to years.

3.4.4 SANE Target System

SANE used the University of Virginia polarized target. This replaced the standard Hall C target housing called *scattering chamber*. The UVa target system also has cutouts for the two spectrometers, HMS and BETA, large enough to cover the full angular acceptances for both in-plane and out-of-plane angles. In addition, there are entrance and exit openings for the electron beam. The beam line connects directly to the entrance opening of the target system so that the beam does not pass through any other material before the target. The system is mounted to the same fixed pivot which used to mount the scattering chamber in the hall. The top of the system contains the cryo target plumbings and lifting mechanism of the solid target insert.

The solid target insert can be lifted out of the target system, keeping the system sealed off so that it can then be replaced or repaired without breaking the system's operating conditions. An overview of the target system is shown in Figure 3.26.

The target system consisted of several subsystems:

- A superconducting Helmholtz pair of magnets, which provided a 5 T magnetic field to the target. The magnets were kept at a temperature of 4 K through a liquid helium reservoir. The reservoir is insulated by a 77 K liquid nitrogen, LN_2 shield.

- A target insert. The targets were placed with the target insert in the uniform field region of the magnet in the refrigerator. This is roughly 2 m long, providing the room for four target materials, in 2.5 cm diameter target cups. Figure 3.27 shows a photograph of the bottom of the target insert. Two target cups were filled with the crystalized NH_3 beads for the main experiment. One is for a carbon disk used for tuning of simulations and the other one is for a titanium cross-hair which is used to monitor the beam position on the target cup. During the calibration data collection at the beginning of SANE, the NH_3 targets were replaced by crystalized CH_2 beads. Further, the insert was equipped with thermocouples, platinum resistors, and carbon-glass resistors in order to measure the precise temperature of the target materials required for anneals. Heater wires were run to the bottom of the two NH_3 target cups to provide the heat needed to perform anneals. The insert guided all the cables down to the target area. It was raised and lowered by a hydraulic lift to position the correct target cup to the beam.

- A liquid helium evaporation refrigerator system to keep the target material at 1 K temperature. The refrigerator was fed by the liquid helium reservoir which was used to cool the superconducting magnets.

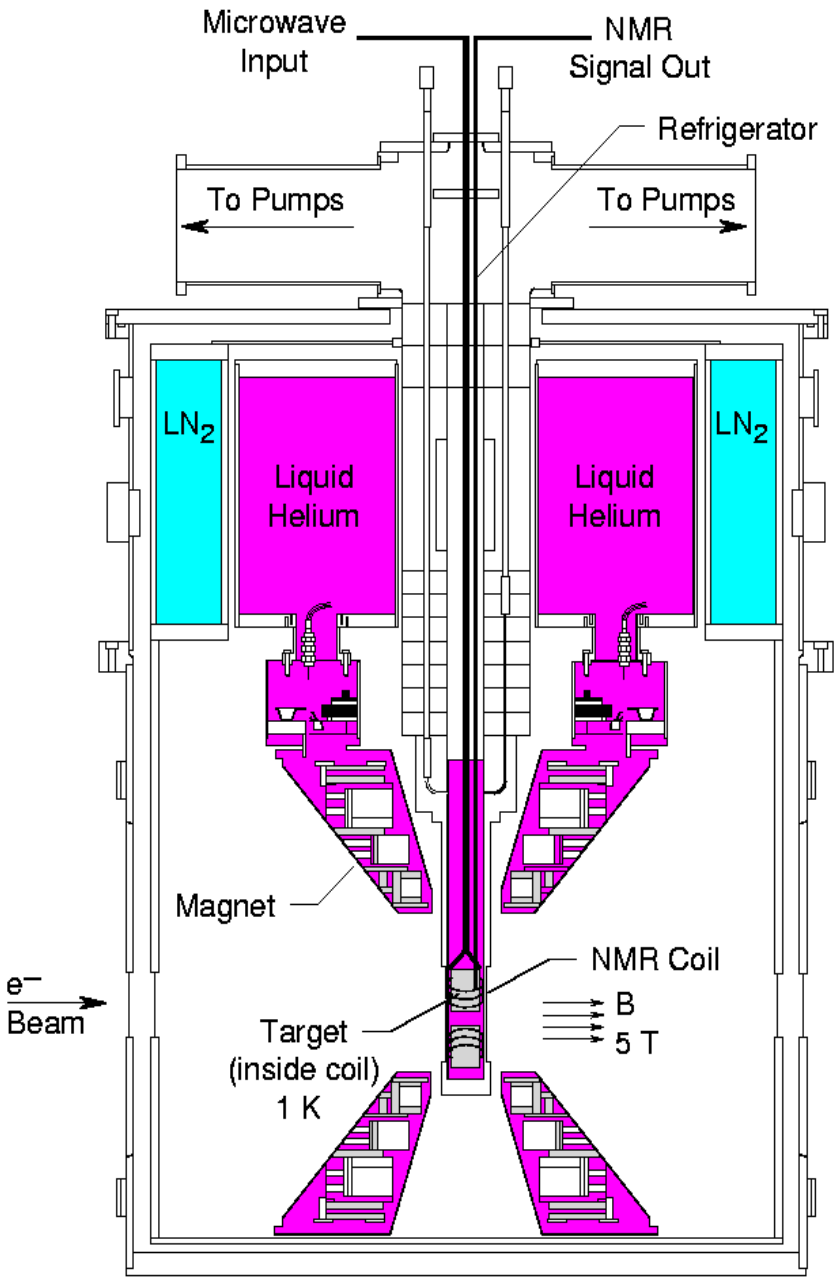

Figure 3.26. Schematic overview of the UVa polarized target used in SANE [156].

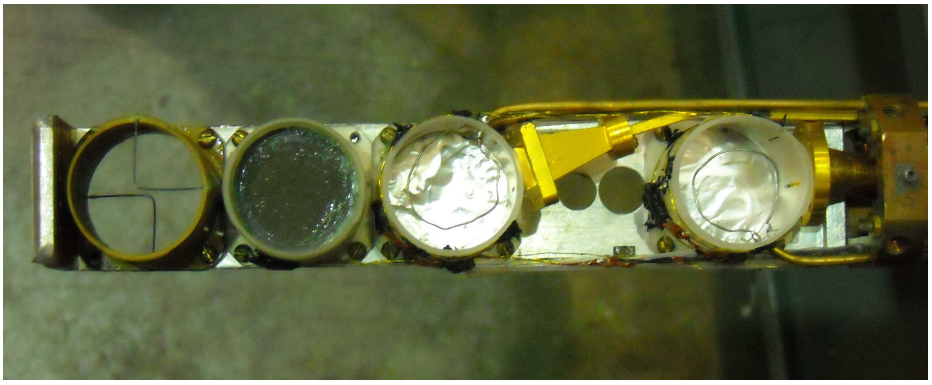

Figure 3.27. A photograph of bottom of the SANE target insert. *From left to right*: A titanium cross-hair, a carbon disk, and two NH_3 target cups [156].

- A NMR system. The NMR system provided an online target polarization and recorded the operating conditions. The microwave horns were trained on each NH_3 target cup to provide the microwave radiation required for target DNP, and the NMR coils were embedded into the two NH_3 target cups to measure the target polarizations. Microwaves were provided by the Extended Interaction Oscillator (EIO).

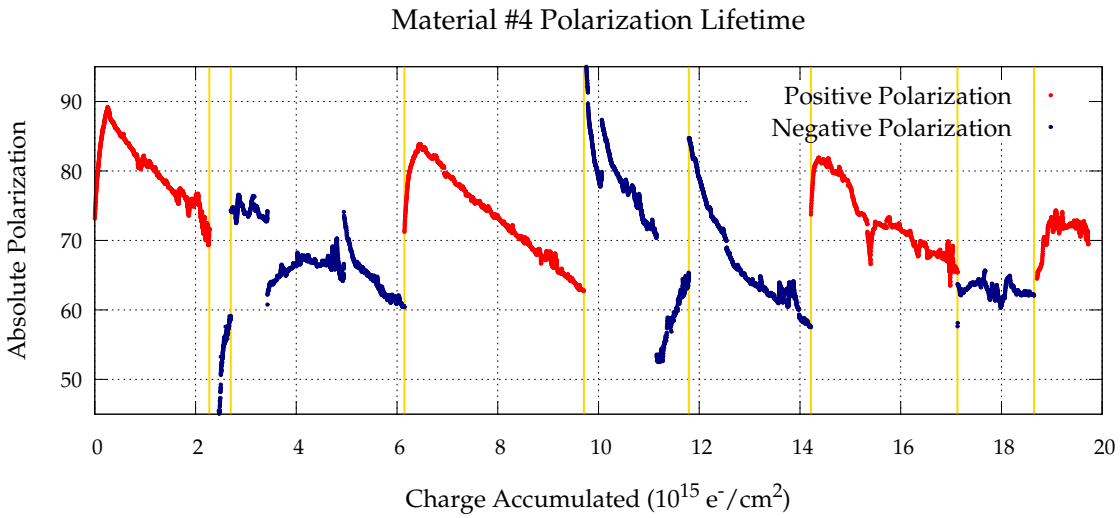

Figure 3.28. Offline polarization of the target material sample #4 versus total charge accumulated showing the positive target polarization (red), negative target polarization (blue) and anneals of the material (vertical gold bars).

Absolute polarization of a DNP polarized NH_3 sample versus accumulated beam charge on target is shown in Figure 3.28 [156]. The polarization of the irradiated ammonia in an experimental beam follows three basic stages:

1. The exponential decay of polarization due to radiation damage of the material.

The high-energy electron beam from the CEBAF accelerator starts to ionize the target material, creating more $N\dot{H}_2$ paramagnetic centers. These excess free electrons in the system allows more relaxation paths through the forbidden transitions, which leads to a higher proton relaxation rate, causing an imbalance between the electron and proton relaxation times. This reduces the DNP efficiency and creates the exponential decay of the polarization over time. During SANE, this dropped the polarization from 80% to 60% in 8 hours of 100 nA beam current exposure on $^{14}NH_3$. These polarization decays are shown in Figure 3.28 with positive polarizations in red and negative polarizations in blue.

2. The immediate reduction of DNP efficiency and hence the target polarization due to the target heating.

The CEBAF electron beam of 100 nA produces roughly 300 mW of heat while passing through the target. This heat load cannot be entirely absorbed by the cryogenic systems maintaining the target material temperature. Therefore, the target temperature increases and the maximum polarization of the material becomes limited by the thermal equilibrium polarization of the electron spins which depends on the material's temperature. This is clearly visible in the target polarization plots shortly after beam trips, where the polarization rises up due to removal of the heat load. When the beam returns, the polarization starts to drop again, generally producing many small spikes of polarization over time, which results in a $\sim 5\%$ of overall polarization reduction. These small spikes can be seen on the positive and negative

polarization decays in Figure 3.28 together with a large rise at $10{\cdot}10^{15}e^{-}/\mathrm{cm}^2$ due to the beam drop.

3. The rapid decrease of the polarization after repeated anneals indicates the end of the material's useful life.

The process, called "annealing," allows the recombination of paramagnetic centers to restore the polarization. The target is removed from the beam and the polarizing microwave radiation, and the temperature of the target material is increased. During SANE, anneals were done using a coiled heater wire at the bottom of the target insert. The current through the wire heats helium in the target volume, which convectively heats the material to 70-100 K for 10 to 60 minutes. But removing too many radicals causes polarization loss due to less DNP efficiency. In Figure 3.28, anneals are shown by the vertical gold bars.

Although anneals recover the polarization of the target material, the material still has a limited lifetime of total accumulated radiation dose. After successive cycles of irradiation dose in the experimental beam, followed by polarization recovery via anneals, the rate of the polarization decay due to radiation damage is increased. (see Figure 3.28 at total charge accumulated between 19 to $20{\cdot}(10^{15}e^{-}/\mathrm{cm}^2)$). This is thought to be due to creation of different free radicals such as hydrazine, N_2H_4, which are formed from $N\dot{H}_2$ when the material is heated during an anneal. At this point, the target material reaches the end of its useful lifetime and needs to be replaced for experiment continuation.

In addition to these three major facts, the spontaneous polarization drops at 3 and $11{\cdot}(10^{15}e^{-}/\mathrm{cm}^2)$ in Figure 3.28 are due to the loss of liquid helium in the refrigerator. This increases the target temperature and hence the polarization drops.

Figure 3.29 shows the charge averaged polarizations for each run of the SANE experiment [156]. These data are summarized in Table 3.7.

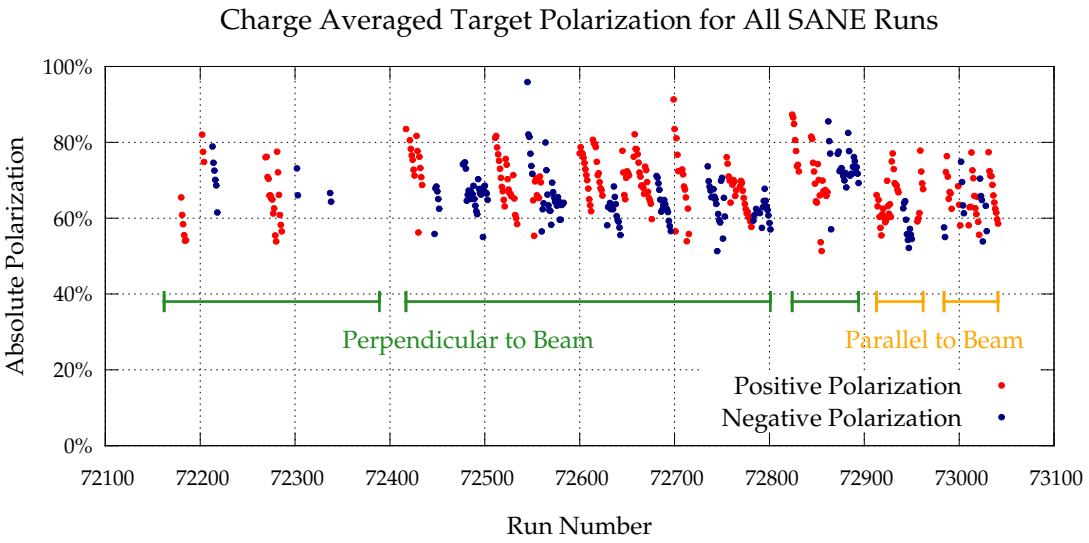

Figure 3.29. Offline target polarizations for all SANE runs, showing the positive target polarization (red) and negative target polarization (blue) for the two different target magnetic field configurations, perpendicular (horizontal green bar) and parallel (horizontal gold bar).

Table 3.7. Table of absolute, charge-averaged final polarizations averaged for all runs of each target magnetic field configuration of SANE.

B Field Orientation	Beam Energy Setting	Absolute polarization
Perpendicular	5.9 GeV	69%
	4.7 GeV	66%
Parallel	5.9 GeV	66%
	4.7 GeV	68%
Entire Experiment		68%

3.5 Trigger and Data Acquisition

A key element in an experiment is the event trigger. The net rate of particles entering the spectrometer can be quite large and one needs to discriminate real events from the many background events that pass through the detectors. When a charged particle passes through the detectors, it produces trigger signals. A certain logical combination of these signals is used to produce a pre-trigger for the event read-out. Both BETA and HMS have their own event-selection criteria and once fulfilled, a so-called singles pre-trigger is formed. In coincidence mode, pre-triggers from both HMS and BETA that arrive within a certain timing window are accepted.

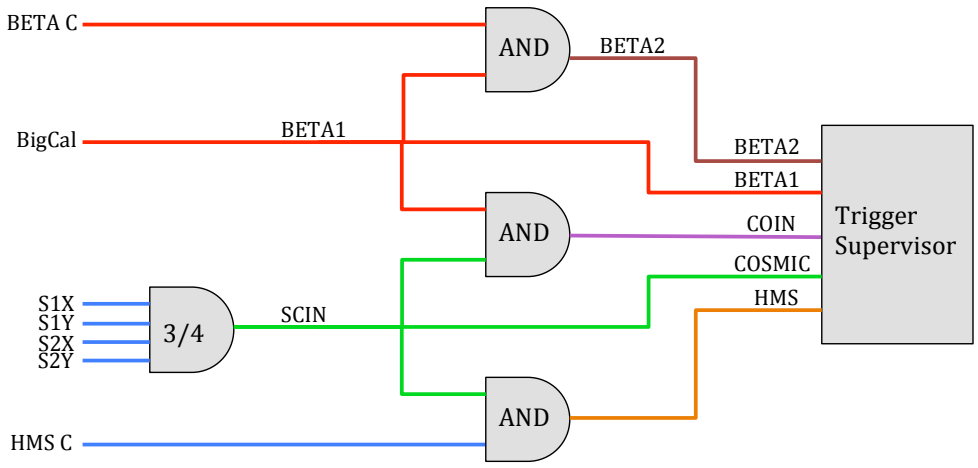

Figure 3.30. Schematic showing the five types of triggers used by the experiment.

During the experiment SANE, five different trigger types were defined for production data-taking, including four single-arm triggers (BETA1, BETA2, HMS and COSMIC), and one coincidence trigger (COIN) as shown in Figure 3.30. One of the two BETA single-arm triggers was BETA1, which was produced by using the BigCal trigger. The second BETA signal, BETA2 is produced by the "AND" logic signal of both BigCal and BETA Cherenkov triggers, which was not used for the COIN trigger. For the HMS single-arm data, HMS electron trigger (HMS) was produced by requir-

ing a Cherenkov signal (HMS C) and the Hodoscope trigger (SCIN). SCIN trigger is produced if 3/4 hodoscope planes are fired; see the section of 3.3.3.2. For coincidence data-taking, the protons detected by HMS in coincidence with electrons in BigCal were acquired with the coincidence trigger (COIN). It was defined by the HMS hodoscope trigger (SCIN) together with the BETA electron trigger, BETA1. In addition to the COIN trigger, part of the coincidence data was collected using a "COSMIC" trigger, which used only HMS hodoscope trigger, SCIN. It detects everything that produces hits in BETA, under the condition that the HMS hodoscope trigger was fired. This made it possible to count the accidental background in BETA within the accepted HMS scintillator timing window. However, the elastic event-selection criteria could remove much of these backgrounds. The BigCal single-arm triggers were always highly pre-scaled because their raw particle rate was very high. The triggers formed by the HMS side and COIN were always read out with a pre-scale factor of 1, meaning all the events were recorded to disk.

The pre-triggers were coordinated by a Trigger Supervisor (TS), which received trigger information from all detectors. The trigger supervisor accepts the trigger if it is not busy reading the previous event, and a signal is sent to generate gates for ADCs and to start signals for TDCs. For every run, the first 1000 triggers were generated for pedestals. The Data Acquisition (DAQ) system records the read-outs from the ADCs. Then the physics events are read by the DAQ. The data-acquisition system is handled by CODA (Cebaf Online Data Acquisition) [183] in three types:

- The ADCs and TDCs from each detector for each event.
- Scaler information, which has read every two seconds.
- The information from the EPICS database, which contains the slow-control parameters like magnet settings, beam position, target temperature and pressure.

From there, the data is copied to long-term tape storage.

SECTION 4

DATA ANALYSIS

The analysis of the data consisted of four major steps. The first step was reconstruction of the individual events by decoding the raw data received from HMS and BETA and determination of the particle trajectories, momenta and the positions of the scattered particles at the interaction vertex. The second step was to calibrate the detectors in order to get the physics meaning of timing, positioning and energy recorded by each detector. Elastic and inelastic event separation was the third step, which involved studying kinematic correlations of elastic electron-proton scattering, the target magnetic field and also correcting the data with target and beam offsets determined by comparing with the Monte Carlo simulation. The fourth step was to calculate the raw and physics asymmetries and their errors and then to extract the form factor ratio for both single-arm and coincidence data.

In this chapter, these four steps are discussed in detail.

4.1 Event Reconstruction

Once the raw signals were recorded by the Data Acquisition System (DAQ), transforming them into particle tracks, particle identification and time-of-flight information are the crucial parts. This task is performed by standard Hall C analysis code, the replay ENGINE. A separate stand-alone FORTRAN code then continues with the physics analysis, including calculating the track-reconstructed quantities such as scattering angles and the positions at the target, as well as the physics quantities such as invariant mass, W, and the momentum transfer squared, Q^2. Furthermore, ENGINE keeps track of various scaler quantities such as charge, current and tracking

efficiencies for each experiment run separately. The output of the data was in three forms:

- Scaler files which contain all the scaler quantities for each run.
- PAW [184] HBOOK files containing the standard set of histograms which are used to check the detector performances and monitor the hardware.
- PAW Ntuple files containing the event-by-event information for each run. This information consists of detector quantities and, track quantities such as trajectory and position at the focal plane of the spectrometer and at the target. These Ntuples are the main output used in the final physics analysis.

The determination of the particle trajectory and momentum at the target was done mainly by two major steps. The first step was to find the trajectory at the detector focal plane and, the second step was to reconstruct the trajectory back to the interaction vertex. The first part was done using the two HMS drift chambers. The drift chamber hits were used to identify clusters of hits (space points) which required at least four out of six planes in each chamber to have a "hit." A straight line fit to these hits in each space point, called a "stub," is a small track. A total of 2^6 stubs per space point can be generated for all left-right combinations for the wires that are fired by the charged particle. The stub with the lowest χ^2 was selected as the best stub for each space point. After all of the best stubs were selected for all of the space points separately for the two chambers, the tracking algorithm fits all the combinations of particular space points belonging to the best stubs between two chambers to form a straight line segment through both chambers. The minimization of χ^2 requires that the resulting track is consistent with the best stubs in each chamber. The fit track is then extrapolated to the detector focal plane, which is approximately half way between the two chambers, and the focal-plane quantities, X_{fp}, Y_{fp}, X'_{fp} and Y'_{fp}, of the particle track at the focal plane were determined. By convention, X_{fp} is the

position in the dispersive direction (pointing vertically downwards in the spectrometer coordinate system) while Y_{fp} is the position in the non-dispersive direction (pointing left to smaller angles). The quantities X'_{fp} $(= \frac{dX_{fp}}{dZ})$ and $Y'_{fp}(= \frac{dY_{fp}}{dZ})$ are the slopes of the tracks at the focal plane. The Z direction of the spectrometer coordinate system is parallel to the central ray.

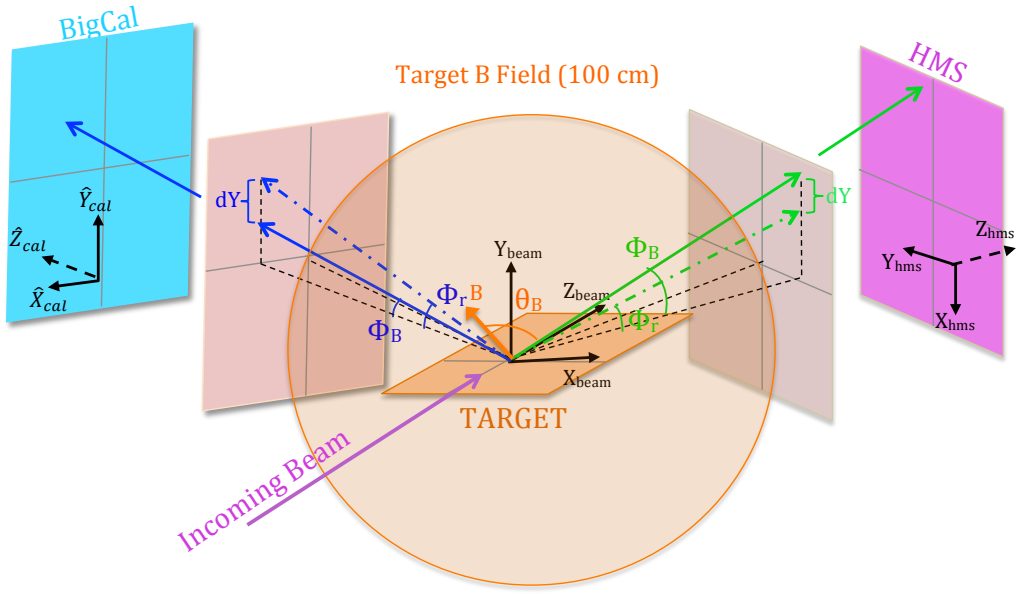

Figure 4.1. Diagram showing the bent particle path due to the target magnetic field and its straight-line projection from the target together with the magnetic field representation at the target. The HMS, BigCal and the beam coordinate systems are also shown.

These focal-plane track quantities are determined using the drift chamber. The position of the particle as it passes perpendicularly through each plane of the drift chamber can be determined from the drift time of each particle to the fired wire and the wire position. The drift times of the particle to each wire of a plane can be measured by taking the time difference between the particle passing through the focal plane (as determined by the HMS hodoscopes discussed in Section 4.2.1) and the signal generated at each fired wire by the passing particle.

The particles scattered off from the target are transported through the HMS magnets to the focal plane. The particle trajectories are characterized at the target by the HMS reconstructed position ($Z_{tar} = 0$, X_{tar}, Y_{tar}), angles (X'_{tar}, Y'_{tar}) and the fractional momentum deviation from the spectrometer central momentum, P_0 , $\delta = (P - P_0)/P_0$. The coordinates X_{tar} and Y_{tar} are in the HMS coordinate system as shown in Figure 4.1 pointing toward X_{hms} and Y_{hms}, respectively. The angle $X'_{tar}(= \frac{dX_{tar}}{dZ})$ is the out-of-plane scattering angle at the target and $Y'_{tar}(= \frac{dY_{tar}}{dZ})$ is the in-plane scattering angle relative to the central ray. Note that the "tar" coordinates are in the HMS spectrometer coordinate system (X_{hms}, Y_{hms}, Z_{hms}).

These reconstructed coordinates $(X_{tar}, Y_{tar}, X'_{tar}, Y'_{tar}, \delta)$ at the target have a one-to-one correspondence with the focal plane coordinates $(X_{fp}, Y_{fp}, X'_{fp}, Y'_{fp})$ if the vertical position of the particle track at the target, X_{tar}, is assumed to be zero. The target coordinates can then be reconstructed using the focal-plane coordinates and the matrix transformation:

$$X^i_{tar} = \sum_{j,k,l,m} M^i_{jklm} (X_{fp})^j (X'_{fp})^k (Y_{fp})^l (Y'_{fp})^m \tag{4.1.1}$$

with the constraints of $j + k + l + m \leq N$ where N is the order of the expansion and i goes from 1 to 4, which is defined by X'_{tar}, Y_{tar}, Y'_{tar} and δ. The reconstruction coefficients M^i_{jklm} are determined by a fit using an iterative process starting with a COSY INFINITY model [185] of the spectrometer optics. By a series of dedicated optics runs using a sieve slit collimator and thin multi-foil targets, the spectrometer reconstruction coefficients can be calibrated. The assumption of $X_{tar} = 0$ is corrected for by studying the slow-raster X position, X_{raster}.

4.1.1 Target Magnetic Field

With the polarized target experiments, the reconstruction methodology in HMS is modified from the ordinary one. In this case, there is an extra magnetic field around the target which is used to polarize the target. This magnetic field deflects both beam and scattered particles. The chicane magnets used on the beam line compensate for this extra magnetic field around the target and direct the electron beam to the target center. However, the scattered particles are deflected before they are transported through the HMS magnets. Therefore, an additional particle transport through the target magnetic field has been added to the existing HMS particle-tracking algorithm. The SANE target magnetic field is assumed to be cylindrical around the target with a dependence only on the radius and position along the axis. The field strength decreases with radius and has non-negligible strength up to 100 cm from the target center. The standard Hall C HMS reconstruction matrix elements are defined to reconstruct the particle tracks from the focal plane to the interaction vertex for unpolarized targets without an additional target magnetic field. Using the same reconstruction matrix elements for the polarized target experiment mistracks the particles because the particle starting point at the focal plane is now different from the unpolarized case due to the extra deflection. However, the target magnetic field integral is much smaller than that of the HMS dipole magnetic field. Therefore, SANE used a separate transport system for the particles going through the target magnetic field region in addition to the existing HMS transport system. Further, because SANE used a 2×2 cm beam rastering system, the reconstruction matrix element coefficients of this additional transport system were included with the slow raster X and Y positions as well.

The angular deflection for a particle with charge, e and momentum, P passing through a magnetic field, B is,

$$\Delta\Phi = \frac{e}{P}\int B \cdot dl, \tag{4.1.2}$$

which can be determined for each momentum using the target magnetic field map provided by the manufacturer. The out-of-plane angle deflection is, $\Delta\Phi = \phi_B - \phi_r$, where ϕ_r is the projected out-of-plane angle for the case of no magnetic field, and ϕ_B is the observed out-of-plane angle with magnetic field. This angle deflection causes the vertical position difference, dY in the field-free region as shown in Figure 4.1. This dY modifies the particle track while keeping the standard Hall C reconstruction matrix elements the same.

First, the particle tracks are reconstructed by the HMS reconstruction coefficients to the target center, assuming no target magnetic field. Then, by knowing the target coordinates, $X_{raster}, Y_{tar}, X'_{tar}, Y'_{tar}$, the particle is projected back to the field-free region at Z=100 cm from the target center, which is determined by the target at Z=0. The particle's new coordinates, X, Y, X', Y' at Z=100 cm, are then transported back to the target at Z=0 through the target magnetic field, determining the track X position, X_{tar}. A corrected X_{tar} position is calculated by adding the difference by the raster position. The new reconstructed target coordinates calculated with the corrected X_{tar} are projected back to the field-free region and transported to the target through the target magnetic field. Projecting the new coordinates forward to the field-free region at Z=100 cm, transporting them backward to the target at Z=0 and correcting the X_{tar}, were iterated continuously until the difference between X_{tar} and X_{raster} is less than 1 mm. Once the iteration is completed with this requirement, the particle reconstruction procedure continues with the next event. In this manner, the

new target coordinates for each event are reconstructed, including the target magnetic field effects.

4.2 HMS Detector Calibrations

Calibrations have to be performed in order to get the timing information from individual scintillator elements, to determine the gain parameters of the calorimeter and Cherenkov PMTs, and to convert the drift chamber TDC values to drift distances. The drift chambers, hodoscopes and calorimeter have more complicated calibration procedures. For the gas Cherenkov, for each PMT, the gain parameter representing the number of ADC channels per photoelectron, is determined by finding the one-photoelectron peak in the ADC spectrum. The calibration procedure of all of the HMS detectors is presented in detail in Sections 4.2.1, 4.2.2, 4.2.3, 4.2.4.

4.2.1 Hodoscope Calibration

The main purpose of the HMS hodoscopes was to determine the start time for drift chambers, which is the time when the particle passed through the HMS focal plane. There are a number of corrections to be applied in order to reconstruct the timing of the event using the raw ADC and TDC information [186]. First, the raw TDC value is converted to time in nanoseconds with the conversion factor of 25.9 ps per TDC count, which was determined at the initial commissioning of the HMS [178]. Hence, the "raw" time is given by $t_{raw} = 25.9\ ps \times TDC$ for each TDC bin.

The next correction to the scintillator time is to subtract the zero offset, a determined for each channel in order to account for the variations in cable delay between channels. During the calibration procedure, one of the PMTs is arbitrarily chosen to have zero offset and determines the time of each scintillator hit relative to the time

on the arbitrary PMT, which defines the start time for the drift chamber hits. All the other PMTs were calibrated relative to this reference PMT.

The next correction to the timing signal is to correct for the light-propagation time in the scintillator bar. The point where the particle passed through the scintillator paddle is determined from drift-chamber tracking information. The path length of light in each scintillator bar (in cm) is defined as the distance from the PMT to this DC-determined paddle position which is p (max. 30 cm). Then the time correction is given by p/b, where b is the effective speed of light in the scintillator bar in units of cm/ns. The maximum time correction should be $30/1.4 = 21$ cm/ns for the scintillator material with a refractive index of 1.4. Because the light has an internal reflection in the bar, the actual value of the effective speed can be less than 21 cm/ns.

The final correction for the scintillator time is the *pulse-height correction* or *time-walk correction*, using the pedestal subtracted ADC value for a particular PMT. Since the PMT signals are leading-edge discriminated at fixed threshold, larger signals will exceed the threshold and start the TDC earlier than smaller signals. Therefore, the correction to the time for the pulse height is made of the form $d/\sqrt{ADC}$, where d is determined for each PMT in the calibration procedure.

The time corrections described above can be written as,

$$t_{corr} = t_{raw} - a - p/b - d/\sqrt{ADC}.$$

The goal of the hodoscope calibration is then to determine the above three parameters (zero offset a, time-walk correction coefficient d, and effective propagation speed b). The standard HMS time-of-flight calibration code written by P. Bosted [186] was used to obtain the best set of parameters. This code fits all three parameters for all PMTs simultaneously, for a total of 156 parameters. The calibration code runs

separately from the replay ENGINE and requires a special parameter file defining several start values.

After the initial calibration was done using a good run with at least 500,000 electron events and 50 ns time periods, additional iterations with 10 ns and 3 ns time intervals were performed in order to avoid a bias due to accidental hits. The calibrations were checked by looking at the reconstructed velocity $\beta = v/c$, where v is the particle velocity and c is the speed of light. Figure 4.2 shows the velocity spectrum of β for both electrons (using the experiment run 72994) and protons (using the experiment run 72878) for which the tracking selection criteria for each track are used. The code checks for a hit on each scintillator paddle.

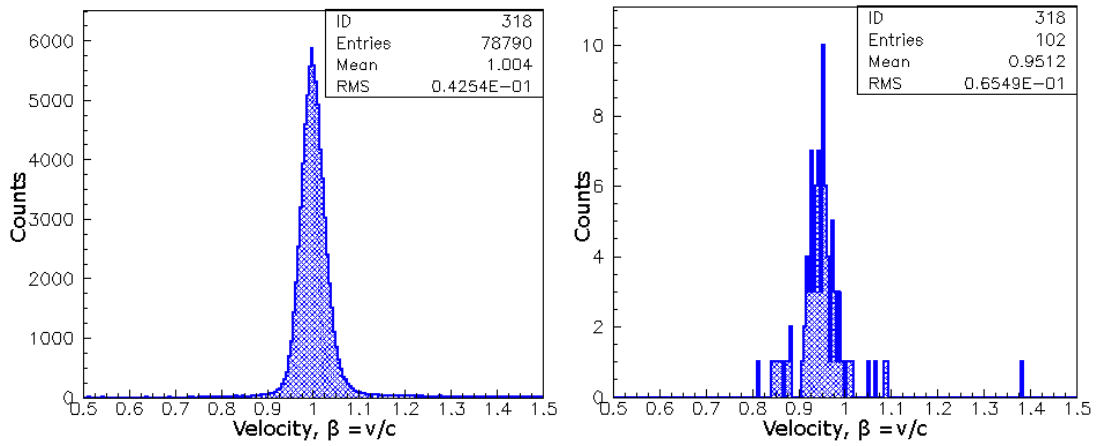

Figure 4.2. The reconstructed β spectrum with the tracking selection criteria on all scintillator hits. *Left*: A nice narrow peak centered on 1 for electrons. *Right*: Velocity β as calculated from the momentum, P of the particle for hadrons, which is centered at 0.938 for protons.

The calibration parameters depend on the PMT high voltages (HV). Therefore, each time when the HV is changed, the calibration needs to be repeated. Because we used the same HV during SANE, only one calibration was enough. Taking the average time difference between the two hodoscope sets, $S1$ and $S2$ (two planes on

each), the velocity of the particle can be calculated and hence used as the particle identification to distinguish the particles between electron, proton, pion and kaon.

4.2.2 Drift Chamber Calibration

Drift chambers are used to determine the particle tracks. When a particle traverses the drift chamber, a list of hits along with a TDC value for each hit is produced. Using the hodoscopes to determine the time when the particle passed through the focal plane, the drift chamber TDC value can be converted into a drift time. In order to determine the drift distance, which is the distance between the particle track and the fired wire, a time-to-distance map is generated. This is done by processing the TDC values from all hits on a given plane for a large number of events. This gives the drift-time distribution, $F(t)$. The drift distance, $D(t)$ is then calculated from,

$$D(t) = D_{max} \frac{\int_{t_{min}}^{t} F(t')dt'}{\int_{t_{min}}^{t_{max}} F(t')dt'},$$

assuming the drift position distribution is uniform for all wires after averaging over all cells. The distance D_{max} is the maximum possible distance which is 1/2 of the wire spacing (0.5 cm); the time limits t_{max}, t_{min} define the range of times included in the fit. The time t is the time value converted from the TDC. Separate time-to-distance maps are generated for each plane of the chambers. Figure 4.3 shows the measured drift-time distribution for the plane $X1$ (*left*) along with the calculated drift distance (*right*) using the measured drift time.

The drift chamber efficiency for electrons as a function of the focal-plane coordinate X_{fp}, (vertically pointing down in the HMS coordinate system) was calculated using the hodoscopes hits. For each scintillator X paddle ($X = 1$ to 16), the number of hits with the full number of HMS Cherenkov photo electrons, $N_{cer}>0.5$ and good velocity from the hodoscope, $0.7<\beta<1.3$ were recorded as the *good scintillator hits*.

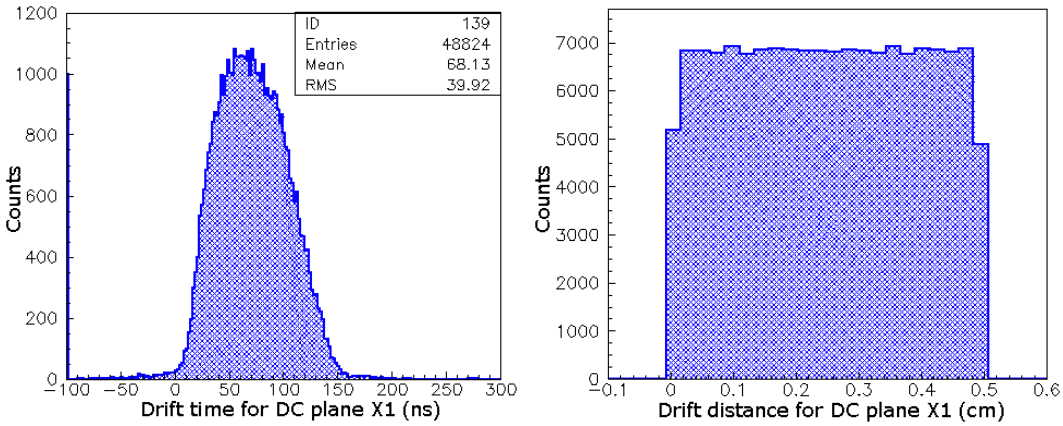

Figure 4.3. *Left*: The measured drift-time distribution for the plane $X1$. *Right*: The drift distance calculated using the measured drift time after the drift chamber calibration.

Then the ratio of the number of events with a good drift chamber track in the focal plane to all *good scintillator hits* was calculated. In this manner, the DC tracking efficiency as a function of the scintillator paddles was obtained, and by converting the paddle number to the vertical position from the known geometry, the tracking efficiency as a function of the focal plane vertical position, X_{fp}, is determined. Figure 4.4 shows the DC tracking efficiency as a function of the focal plane X_{fp} for the C run 72782. The drift chamber showed dramatic efficiency degrading with the particle's vertical position, *i.e.*, with the particle relative momentum δ.

The reason for the efficiency degrading over time during SANE was assumed to be due to the drift chamber gas leak. Therefore, different time-to-distance maps were generated for runs taken at different time periods. In Table 4.1, different run periods are shown with a Carbon run used to generate the time-to-distance map within that range of runs. The reason why it was required to generate separate maps within the particular run period is also shown. The DC calibration procedure has been documented by P. Bosted [186].

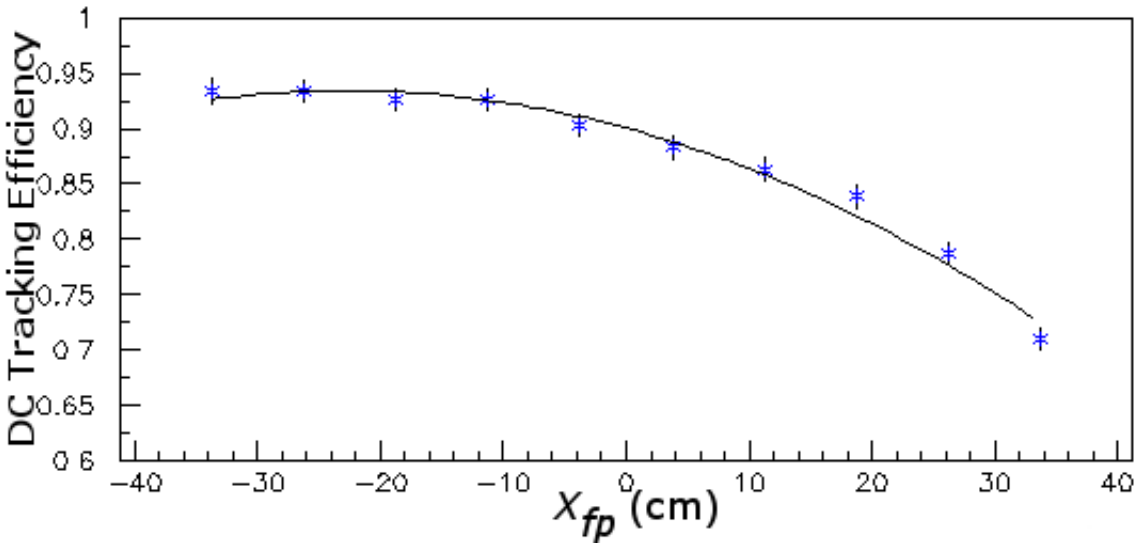

Figure 4.4. DC tracking efficiency as a function of the focal plane coordinate X_{fp} for the C run 72782.

Table 4.1. Table of run period, carbon run used to generate the time-to-distance map within that run period, and the reason why it was needed to generate different maps for each run period.

The run period	C run	Reason to change the drift maps
72478-72652	72505	Re-established the DC gas flow
72653-72781	72678	Control run
72782-72862	72835	Control run
72863-72926	72909	Used a new Ar bottle
72927-72962	72940	Changed the DC1 gas flow rates from 100 cm^3/min to 400 cm^3/min keeping the DC 2 rate at 600 cm^3/min
72963-72992	72973	Changed the DC1 filter and the DC gas flow rates. DC 1 from 400 cm^3/min to 450 cm^3/min and DC 2 from 600 cm^3/min to 450 cm^3/min
72993-72999	73026	Changed DC Argon bottle

4.2.3 Cherenkov Calibration

The Cherenkov light reflected from the two mirrors in the HMS Cherenkov detector tank is collected by the two PMTs which encoded in the ADC spectrum. The Cherenkov calibration is performed by identifying the location of the single-photo-electron peak in the ADC distribution. Figure 4.5 illustrates the ADC histograms (*left*) and the number of photo-electron histograms (*right*) for both top and bottom mirrors. Data are taken from the electron run 72375.

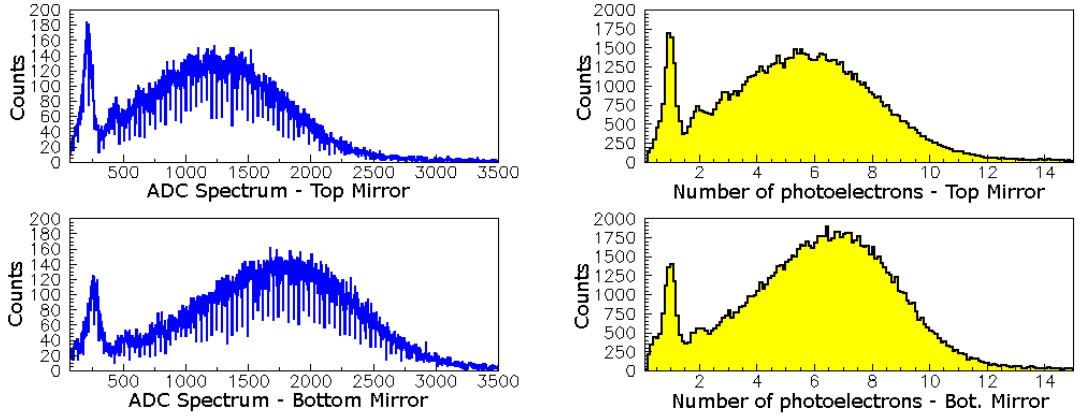

Figure 4.5. *Left*: The ADC histograms for the top (top plot) and bottom (bottom plot) mirrors. *Right*: The number of photo-electron histograms (calibrated) on the same mirrors.

In Figure 4.5 (*left*), the single-photo-electron peak is clearly visible at ADC channel 219 (267) while the two-photo-electron peak appears in the proper place near channel 438 (534) for the top (bottom) mirror. The ADC channels at the single photo-electron peaks are saved as the calibration constants for the top mirror as 1/219 and that for the bottom mirror as 1/267 in a separate parameter file to be used for further data analysis. The calibration constants depend on the PMT high voltages. Each time when PMT high voltage is changed, a new Cherenkov PMT calibration is needed. The calibrated signals from each PMT are summed to get the

total number of photo electrons produced per event. Figure 4.6 (*left*) presents an example of the full Cherenkov response for the electron run 72782. This average signal is approximately 6 photo electrons per event. For particle identification, electrons are identified from the number of total photoelectrons >2, while for protons the number of total photo electrons is <2.

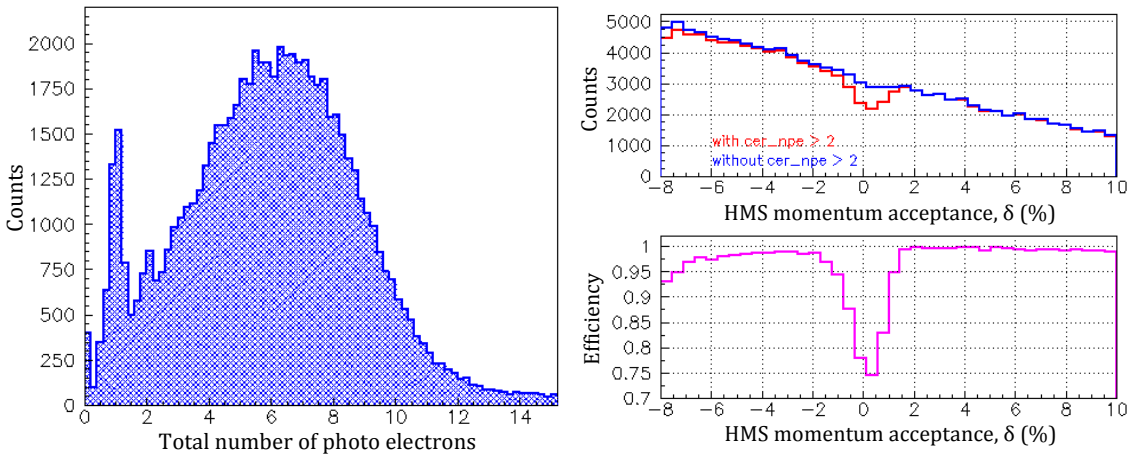

Figure 4.6. *Left:* an example of a full Cherenkov response for the electron run 72782. *Right:* the inefficiency of the Cherenkov as a function of δ for the same run 72782.

However, because the two mirrors are aligned vertically, there is an inefficiency at the central region where the two mirrors meet each other. This inefficiency for electrons is determined by calculating the ratio of yields with a cut of Cherenkov photo electrons > 2 to Cherenkov photo electrons > 0 as a function of momentum acceptance of the HMS, δ. As seen in Figure 4.6 (*right*), the Cherenkov cut of 2 photo electrons causes an inefficiency up to 20% in the central region of the δ spectrum. This inefficiency is applied in Monte Carlo simulation as a function of δ in order to correct the Monte Carlo yields.

4.2.4 Lead-Glass Calorimeter Calibration

The lead-glass electromagnetic calorimeter measures the energy deposited by a charged particle. The Cherenkov light produced by the charged particle is collected by PMTs which are connected to the end of the lead glass bars. The PMT signal is proportional to the total energy deposited in each bar which read as ADC channels by electronics. In order to correct for the gain differences between the lead glass modules and to define a coefficient to transform the ADC amplitude to the energy deposition for each shower counter block, the calibration is performed. The relationship between the energy of the electron as determined from the track reconstruction, E_i and the calibration coefficient, C_i for the i-th block, can be constructed using the ADC amplitude, A_i and the pedestal in the particular ADC channel, P_i as follows:

$$E_i = C_i(A_i - P_i).$$

for the good electron events selected using the Cherenkov detector. In order to minimize the difference between the energy sum from all blocks and the true energy, E_e^n of the electron, the χ^2 minimization procedure,

$$\chi^2 = \sum_{n=1}^{N} \left(\sum_{i \epsilon M^n} C_i \cdot (A_i^n - P_i) - E_e^n \right)^2 = \chi^2_{min}$$

is performed and the final coefficients for each block were calculated, where, N is the number of events, i is the number of blocks, and M^n is the set of block numbers in the cluster. After all the calorimeter blocks are calibrated (total of $13 \times 17 = 78$), the energy deposition, E, is calculated by summing over all blocks involved n a cluster:

$$E = \sum_{i \epsilon M^n} E_i.$$

The obtained resolution has been $\Delta E/E = 6 - 8\%/\sqrt{E}$ for HMS (E in GeV).

Because the experiment used the same PMT high voltages on each PMT for the whole run period, a single set of calibration constants was generated and used for all runs. The histogram of the ratio of the total energy deposited by the negative particles (electrons and pions) in the calorimeter to the detected energy is shown in Figure 4.7 (blue) plotted from the electron run 71392.

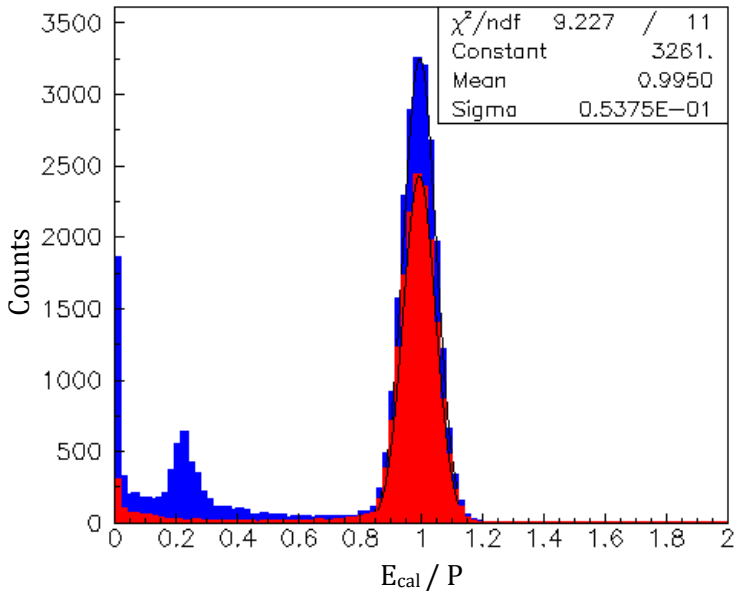

Figure 4.7. The HMS shower counter spectrum after applying the PID cut of Cherenkov photo electrons > 2: The ratio of the total energy deposited in the calorimeter, E_{Cal} to the measured energy, P of the particles. The electron peak is at $E_{cal}/P = 1$ and the pion peak is at about 0.25.

The electron peak can be clearly seen at $E_{Cal}/P = 1$. It also shows a clear pion peak. Since the electron and the pion have different energy depositions, they form separate peaks in the plot. Electrons, positrons and photons deposit their entire energy in the calorimeter, giving a ratio of energy detected in the calorimeter to particle momentum determined from tracking close to 1. In contrast, hadrons usually deposit a constant energy per layer due to ionization and produce little or no Cherenkov light (depending on their momentum and refraction index of the lead glass). At HMS kinematics, pions deposit a constant energy of approximately $200 -$

300 MeV in the calorimeter blocks. So the pion signal appears at ~ 0.25 GeV/P_π in the energy fraction distribution. However, the neutral pions produced from negative π^- in secondary $\pi^- p \to \pi^0 n$ reactions can decay to e^+e^- pairs via $\pi^0 \to 2\gamma \to e^+ + e^-$ at the lead glass blocks and deposit the full energy of the neutral pion. This leads to a high-energy tail for the pion toward the electron peak and may misidentify the pion-generated electrons as good electrons.

A small peak at 0 in the energy fraction distribution is due to misidentified tracks. If the drift chamber does not identify the electron tracks correctly, the calorimeter clusters we are looking for projected by the drift chambers do not have any energy deposited. This gives the deposited energy near zero. The actual track deposits its energy somewhere else in the calorimeter.

The Figure 4.7 (red) shows the same E_{cal}/P spectrum after applying the Cherenkov cut of Cherenkov photo electrons > 2, which cleans almost all pions. Therefore, for particle identification, using the selection cuts on the energy fraction, E_{Cal}/P together with the Cherenkov cut allows one to distinguish electrons from pions. SANE used E_{Cal}/P>0.7 to extract the electrons.

4.3 BigCal Calibration

As the first step toward the BigCal calibration, the high voltages supplied to the PMTs were adjusted so that each ADC channel corresponds to 1 MeV. This was done using cosmic rays before the experiment started taking data. The rest of the calibration procedure was continued in parallel with data-taking, using a large number of π^0 events produced in the target. These neutral pions decay very rapidly into two photons with a 98.82% probability and a mean lifetime of 8.4×10^{-17} s [187]. These photons deposit their full energy in the calorimeter, forming two separated *clusters* in BigCal.

The particle shower in the calorimeter, as discussed in Section 4.2.4, deposits its energy in several blocks surrounding the point where the primary particle enters the calorimeter. In order to determine the energy and the position of this incident particle, this set of blocks called a *cluster* is identified by the highest ADC value from the BigCal phototubes for a given event. Starting with the block with the highest energy, the neighboring blocks, whose energy exceed a threshold of 10 MeV, are added to the first block making the cluster of blocks. This process continues to grow the cluster by adding blocks whose energy exceeded the threshold until the maximum number of 25 blocks in a 5×5 grid is reached. Once the highest energy cluster is completed, the second highest energy cluster is generated by adding the neighboring blocks to the second highest energy block until all the energy threshold exceeding blocks have been added. This process continues until all the clusters are identified. The energy of each cluster, E_c can be defined as,

$$E_c = \sum_i C_i A_i,$$

where A_i is the ADC value of the block i of the cluster, and C_i is the calibration constant for that block. The calibration started with rough values for C_i assuming each ADC channel corresponds to 1 MeV. The goal of the calibration is to determine an accurate value C_i for each block of BigCal.

The position of the particle entering the calorimeter, *the average position*, is determined by calculating the energy-weighted average of the block positions in the cluster as,

$$\begin{aligned} x_{clust} &= \langle x \rangle = \sum_i \frac{C_i A_i}{E_c} \cdot x_i \\ y_{clust} &= \langle y \rangle = \sum_i \frac{C_i A_i}{E_c} \cdot y_i, \end{aligned} \tag{4.3.1}$$

where x_i and y_i are the individual block coordinates at the BigCal face for a given cluster.

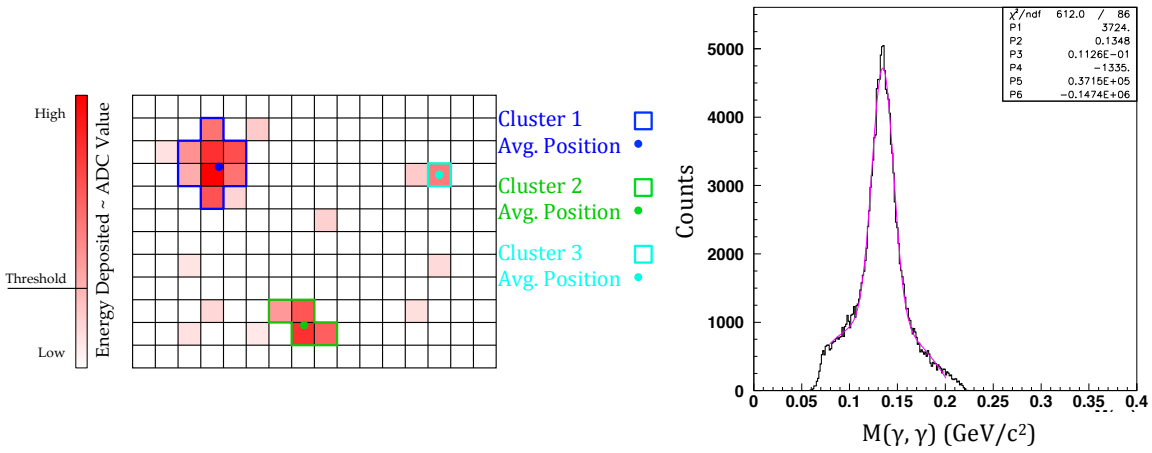

Figure 4.8. *Left*: Diagram showing an example of clustering for a set of calorimeter blocks including energy-averaged cluster positions. *Right*: The plot of π^0 mass reconstructed after calibration of calorimeter blocks (by H. Baghdasaryan from reference [188].

Once the clusters and their positions on the calorimeter are identified, the calibration constant, C_i can be adjusted using the reconstructed π^0 mass. For the π^0 events detected by the calorimeter, there are two separated clusters of energy E_1 and E_2 with energy-averaged positions (x_1, y_1) and (x_2, y_2). Some of these π^0 photons convert to electron-positron pairs even before reaching BigCal. These electron-positron pairs also deposit their energy in BigCal. However, these e^+e^- pairs are directed mostly back-to-back and deposit their energy in the calorimeter in two clusters with a higher distance between them. Therefore, by choosing the clusters between 20 and 80 cm apart, the energy depositions due to electron-positron pairs are removed. Then the invariant mass of the π^0 can be determined by,

$$m_{\pi^0}^2 = 2E_1E_2(1-\cos\alpha), \qquad \cos\alpha = \frac{x_1x_2 + y_1y_2 + z^2}{(x_1^2+y_1^2+z^2)(x_2^2+y_2^2+z^2)}, \tag{4.3.2}$$

where α is the angle of separation of the two photons, *i.e.*, the angle between the two trajectories from the target to each cluster position. The variable, z, is the distance from the target to the calorimeter face. The calibration is performed by

histogramming the π^0 mass and checking the peak position of the mass distribution for the block with the highest signal. Dividing this invariant mass by the known π^0 mass of $m_{\pi^0} = 134.9\ \mathrm{MeV/c^2}$, this histogram should show a peak at 1. If not, dividing the calibration constant, C_i by the peak value of the mass distribution and squaring gives the new calibration constant for the particular block. This calibration process continues for all of the calorimeter blocks. Once the new constants were determined, the verification process started again by producing the invariant mass distribution and checking the peak value of the distribution for each block. This process iterates until the normalized peak value of the invariant mass becomes 1 for all the blocks, and then the calibration constants, C_i for all the blocks are determined. Figure 4.8 (*right*) shows the π^0 mass reconstructed after calibration of a subset of calorimeter blocks.

The newly determined calibration constants need some angle correction as well. So far, all the particles have assumed that start showering at the face of the calorimeter blocks and have a measured z position (needed for Equation 4.3.2) from the target to the face of the calorimeter. But the depth in the calorimeter block at which the particle shower starts can vary with the energy of the incident particle. The z position should be measured from the target to the real cluster positions which are inside the blocks. A particle that starts showering deeper inside the calorimeter block has a smaller angle to the beam axis than one that starts showering closer to the face of the blocks. Therefore, the angle α between the two photon clusters is different and needs to be corrected. This correction was done by a neural network [189]. In the neural network, a set of inputs is transformed to a set of outputs via a number of steps to reproduce the specific results. The SANE neural network had 27 inputs, two for the x-y coordinates of the maximum energy block, and 25 for the energy deposited on the neighboring blocks, which is the maximum number of blocks in the cluster. Three outputs, x, y coordinates of the new cluster center and the cluster

energy were generated. Because this method gives a better accuracy and better resolution, the energy and the coordinates determined from this method were used to reconstruct the π^0 mass for each block that once has the maximum energy entry and hence to determine the calibration constant, C_i. The calibration was performed by SANE collaborator H. Baghdasaryan. Then the BigCal hit positions of the scattered electrons (X_{clust}, Y_{clust}) were determined using the energy-weighted average of the block positions in the cluster.

4.4 Elastic Event Selection

A subset of SANE data was used to measure the beam-target asymmetry from elastic electron-proton scattering. Polarized electrons with energies 4.72 GeV and 5.89 GeV were scattered from the polarized proton target with the spin of the proton aligned nearly perpendicular (80°) to the beam direction. Single-arm electron scattering data were taken by detecting the elastically scattered electrons in the HMS spectrometer at a central angle of 15.4° and 4.4 GeV/c HMS central momentum for an electron beam energy of 5.89 GeV. In separate runs, coincidence *ep* elastic data were taken in which recoiled protons were detected by HMS at 22.3° and 22.0°, and central momenta of 3.58 GeV/c and 4.17 GeV/c, respectively, for the two different beam energies of 4.72 GeV and 5.89 GeV in coincidence with the scattered electrons detected in BETA at a central angle of 40.0°. The summarized HMS elastic kinematics are shown in Table 4.2.

After the reconstruction of each event and the detector calibrations were complete, the elastic and inelastic event separation was the next task in the data analysis. This was done separately for the two data sets.

Table 4.2. Summarized HMS elastic kinematics for both single-arm and coincidence data.

Spectrometer Mode	Coincidence	Coincidence	single-arm
HMS detects	Proton	Proton	Electrons
HMS polarity	+	+	-
Beam energy E (GeV)	4.72	5.89	5.89
HMS central momentum P_{HMS} (GeV/c)	3.58	4.17	4.40
HMS central angle θ_{HMS} (Deg)	22.3	22.0	15.40
Q^2 (GeV/c)^2	5.17	6.26	2.20
Elastic events	231	1200	3×10^4

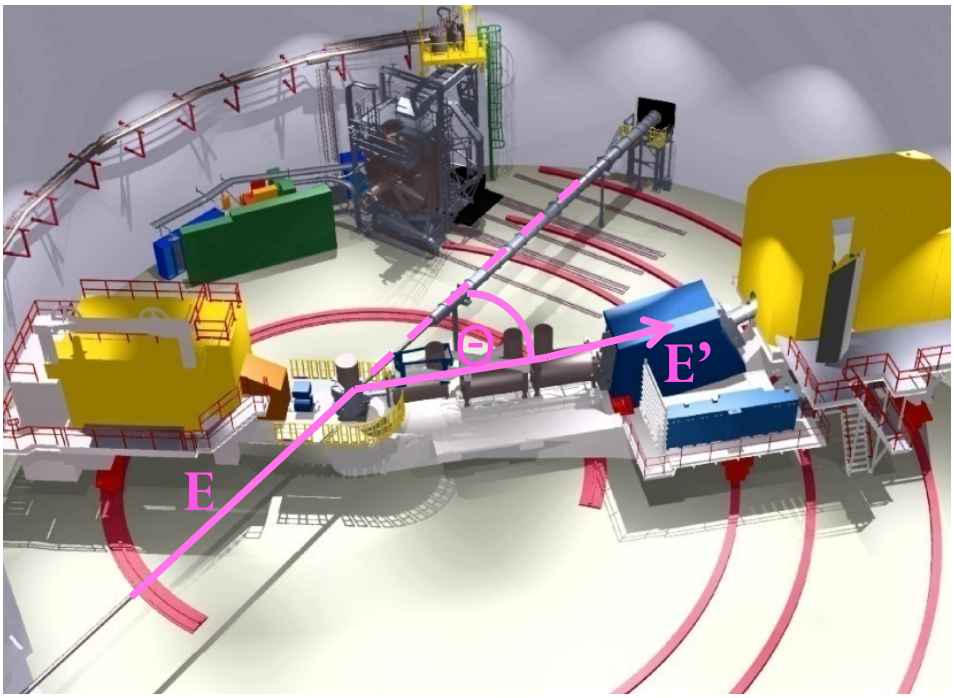

Figure 4.9. The schematic diagram of the detector setup during the single-arm data collection for SANE.

4.4.1 Single-Arm Electron Scattering Data

Figure 4.9 shows the schematic diagram of the detector setup during the single-arm data collection. The scattered electron energy, E', and the scattered electron angle, θ, are measured by the HMS spectrometer for the incoming beam energy, E. A range of experiment runs, 72783-72801 was considered.

4.4.1.1 Kinematic Correlation

By knowing two kinematic variables, the rest of the elastic kinematics can be determined by using the elastic kinematic correlations. In general, for inclusive scatterings, the beam energy E, the scattered energy E' and the scattering angle θ can be used to calculate the four-momentum transfer squared as,

$$Q^2 = 4EE' \sin^2\left(\frac{\theta}{2}\right)$$

and the $\gamma^* + p$ invariant mass squared, W^2 as,

$$W^2 = M^2 - Q^2 + 2M(E - E').$$

Observation of elastic events is very basic because the invariant mass of the elastic events should be at the proton rest mass of 0.938 GeV. But the experimental data comes with a significant inelastic background from N, He and Al walls. Therefore, separating the elastic events from quasi-elastic and inelastic background plays a very important role in the single-arm data analysis.

4.4.1.2 Particle Identification (PID) Cuts

Identification of electrons in HMS is straightforward and is done mainly with the PID and momentum acceptance cuts. By using the Cherenkov cut of, N_{cer}>2 and calorimeter cut of E_{Cal}/P>0.7, (PID cuts), the background due to π^- particles is

suppressed. The quantitie, N_{cer} is the number of photoelectrons for the Cherenkov counter and E_{Cal} is the deposited energy in the HMS calorimeter. The HMS spectrometer measures the momentum of the detected electron, P. Figure 4.10 shows the number of Cherenkov photo electrons versus calorimeter energy to illustrate the separation of pions and electrons.

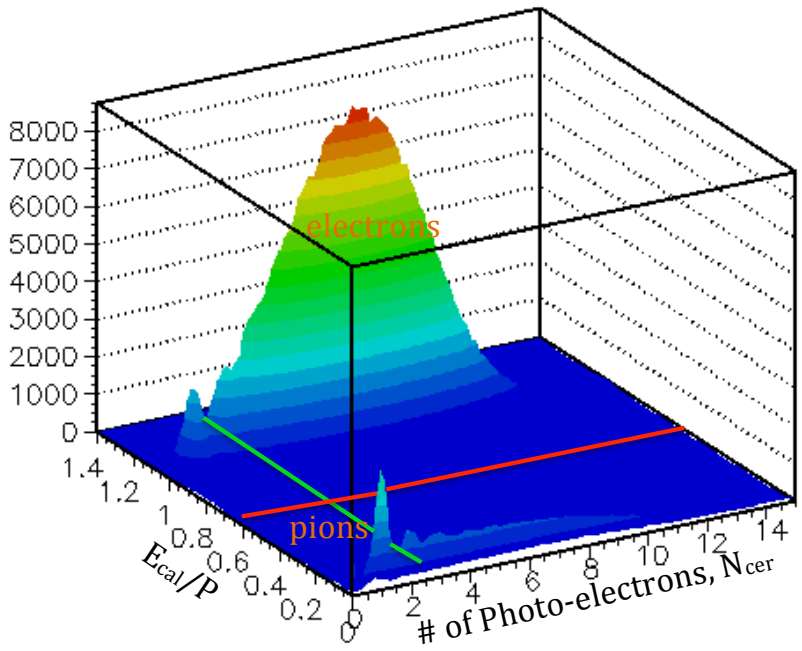

Figure 4.10. Cherenkov photo electrons and calorimeter energy regions for both pions and electrons. The red (green) line indicate the calorimeter (Cherenkov) cut used to separate electrons.

4.4.1.3 The Relative Momentum Acceptance (δ)

An acceptance cut on the momentum relative to the central momentum has been applied to the data in addition to the PID cuts. This eliminates events that are outside of the spectrometer acceptance, but end up in the detectors after multiple scattering in the magnets or exit windows. Also, this cut eliminates events where the acceptance is not well determined. The relative momentum is defined as, $\delta = \frac{P-P_c}{P_c} = \frac{\delta P}{P}$, which is well determined in the region of -8 %$<\delta<10$ %, where P_c is the central momentum

of HMS. Figure 4.11 (*left*) shows δ of the total single-arm electron data as a function of invariant mass, W. It shows that the elastic events are mostly populating an even higher region of the δ acceptance, 10 %<δ<12 %, where the reconstruction matrix elements are not well known.

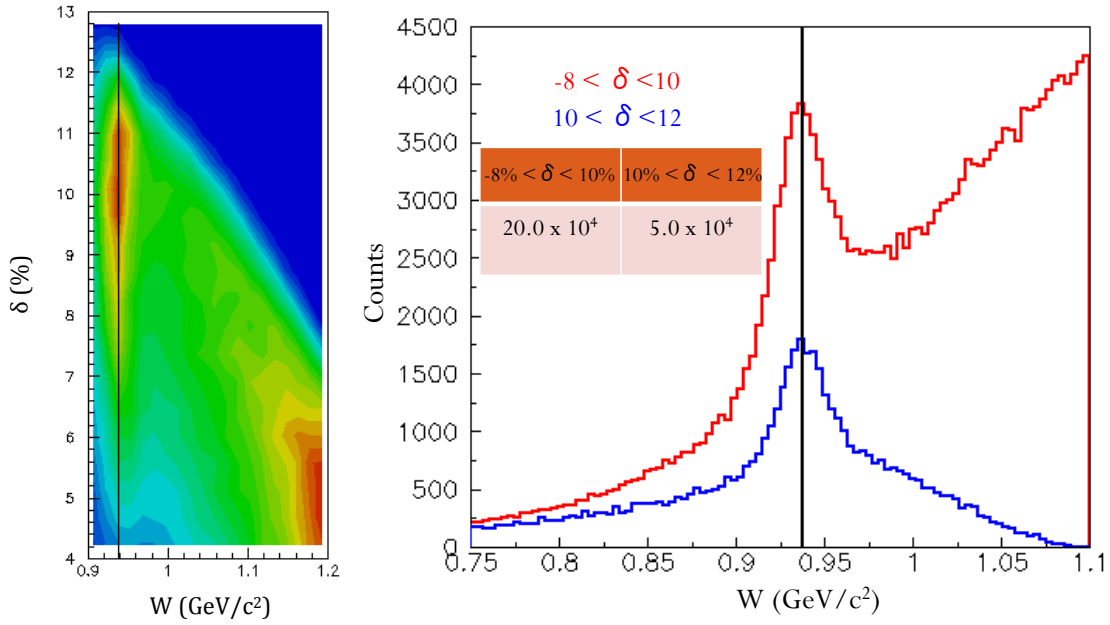

Figure 4.11. *Left:* The momentum acceptance of the total single-arm electron data as a function of invariant mass. *Right:* The raw yield after applying PID cuts as a function of the invariant mass, W for two different δ regions.

Figure 4.11 (*right*) shows the total raw yield as a function of the invariant mass, W after applying PID cuts. The elastic yield would be extracted after subtracting the inelastic background from the raw data. However, the data in the higher δ region were analyzed separately so that the systematic uncertainty from the HMS optics can be determined and included in the final results. Therefore, two δ intervals of the elastic data were used separately in addition to the PID cuts to extract the elastic events.

4.4.2 Coincidence Data

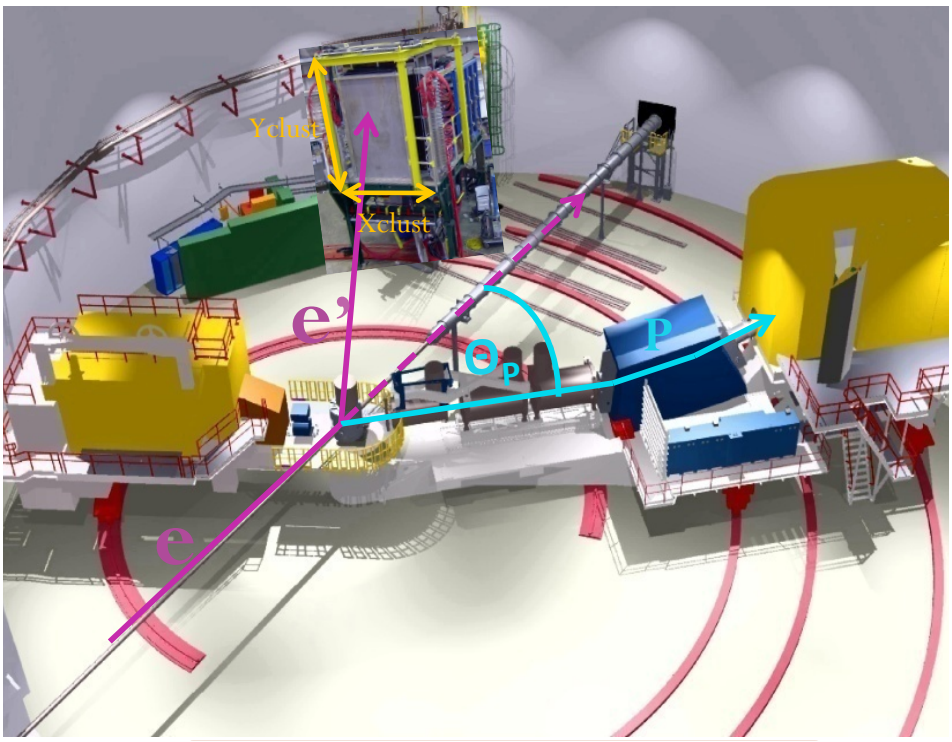

Figure 4.12. Schematic diagram of the detector setup during the coincidence data collection for SANE.

Figure 4.12 shows the schematic diagram of the detector setup during the coincidence data collection for SANE. Although it is possible to separate elastic and inelastic events from the reconstructed proton momentum, P_p and the proton scattering angle, θ_p, the overlap between elastic and inelastic scattering within the resolution of HMS makes the separation less clean. Therefore, by detecting the scattered electron in coincidence with the proton in HMS, the cleanest possible separation can be achieved. A series of experiment runs, 72515-72781 and 72845-72894 were considered at two-beam energies of 5.895 GeV and 4.720 GeV, respectively.

4.4.2.1 Proton θ_p-P_p Kinematic Correlation

Based on energy and momentum conservation for electron-proton elastic scattering, the proton scattering angle, θ_p and the reconstructed proton momentum, P_p can be related for a given electron beam energy, E by,

$$P_p(\theta_p) = \frac{2M_pE(E+M_p)\cos\theta_p}{M_p^2 + 2M_pE + E^2\sin^2\theta_p}, \tag{4.4.1}$$

where M_p is the rest mass of the proton. The difference between the proton momentum measured by HMS, P and the momentum predicted by the scattered proton angle, P_p, using Equation (4.4.1), can be used to define the relative momentum difference, $\Delta_p = \frac{P-P_p(\theta_p)}{P_c} \times 100$, which is expressed as a percentage of the HMS central momentum, P_c. Elastic events were centered at $\Delta_p = 0$. Figure 4.13 shows the Δ_p spectrum for the two different kinematic settings.

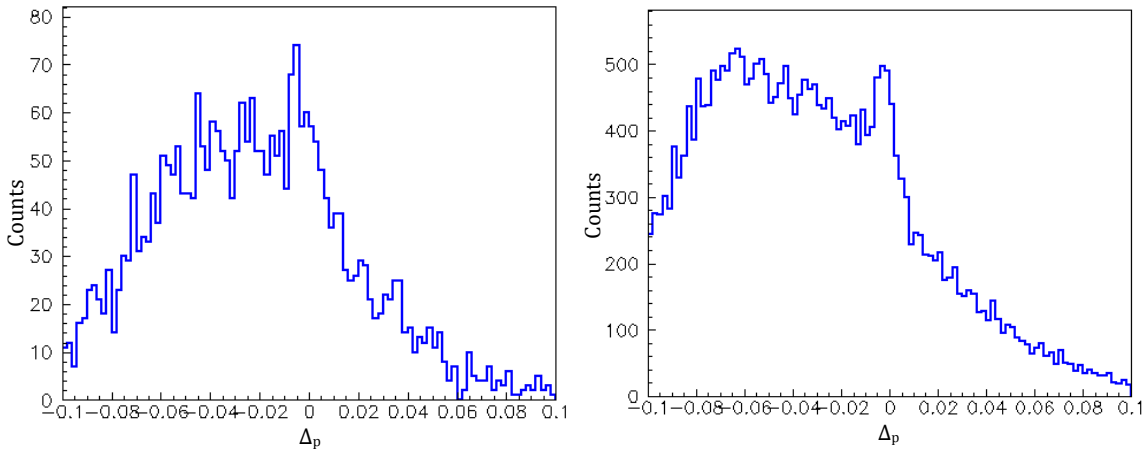

Figure 4.13. Δ_p spectrum for $Q^2 = 5.17$ (GeV/c)^2 (*left*) and $Q^2 = 6.26$ (GeV/c)^2 (*right*). (Any coincidence cuts are not applied yet.)

For both settings, the elastic peak is visible together with a significant background increasing to the left side of the peak, which has lower momentum than the expected momentum for elastic scattering. These protons are primarily from the neutral pion photo production reaction $\gamma + p \rightarrow \pi^0 + p$, which is similar to elastic ep scattering.

The bremsstrahlung photons, radiated by the electron beam with energy near to the beam energy, interact with the proton target and the resulting proton is detected by the HMS. The produced π^0 decays immediately to two photons, $\pi^0 \rightarrow \gamma + \gamma$, with some probability for one or both photons to hit BigCal with enough energy to pass the BigCal trigger threshold. Because both the electron and photon-induced showers give identical signals in BigCal, the only way to distinguish them is the position of the detected particle in the BigCal. Due to the random angular distribution of the neutral pion decay photons, they do not have the kinematic correlation between the particle detected in the BigCal and the proton in HMS as in the elastic case, which makes this method a very powerful way to remove the inelastic π^0 backgrounds. The reaction of Compton scattering, $\gamma + p \rightarrow \gamma p$ also contributes to the background, which has, however, a much smaller cross-section compared to the pion photo production and is, hence, neglectable [190].

4.4.2.2 Electron-Proton Kinematic Correlation

The scattered electron angle, θ_e can be calculated using the measured proton momentum in HMS, P_p as in Equation (4.4.2) using the elastic kinematics,

$$\theta_e = \sin^{-1}\left(2\sqrt{\frac{2M_p(E-E_3)}{4EE_3}}\right). \tag{4.4.2}$$

The scattered electron energy, $E_3 = E - E_p + M_p$ and the proton energy, E_p are given by $\sqrt{P_p^2 + M_P^2}$. The transverse coordinates of the interaction vertex, X_{beam} and Y_{beam} are given by the slow raster X, Y signals and the Z_{beam} coordinate is given in terms of Y_{tar} and Y'_{tar} reconstructed by HMS as,

$$Z_{beam} = Y_{tar}\left(\frac{\cos\theta_{hms}}{\tan(\theta_{hms} - Y'_{tar})} + \sin\theta_{hms}\right),$$

where θ_{hms} is the central angle of the HMS. The X_{beam} (Y_{beam}) coordinate axis points beam right (vertically up) while Y_{tar} and Y'_{tar} are the horizontal coordinate and the in-plane angle at the target in the HMS coordinate system as shown in Figure 4.1. The HMS azimuthal-angle is centered at $\phi_p = -\frac{\pi}{2}$, and BigCal is centered at $\phi_e = \frac{\pi}{2}$. The azimuthal-angle of the electron determined by the co-planarity is, $\phi_e = \phi_p + \pi$. The unit vectors of the orthonormal basis along the electron trajectory in the BETA coordinate system is,

$$\hat{X}_{cal} = \sin\theta_e \sin\phi_e$$

$$\hat{Y}_{cal} = -\sin\theta_e \cos\phi_e$$

$$\hat{Z}_{cal} = \cos\theta_e.$$

The coordinates measured at BigCal are parallel to its surface, with $+X_{cal}$ pointing in the direction of increasing θ_e, and $+Y_{cal}$ pointing vertically upward. By calculating the distance where the electron trajectory intersects the surface of BigCal, S_0,

$$S_0 = \frac{R_{cal} - X_{beam}\sin\theta_e - Z_{beam}\cos\theta_e}{\hat{X}_{cal}\sin\theta_e + \hat{Z}_{cal}\cos\theta_e}$$

where R_{cal}=335 cm is the distance from the target to the center of BigCal, the coordinates of the electron at point S_0 along its trajectory are defined as,

$$X(S_0) = X_{beam} + S_0\hat{X}_{cal}$$

$$Y(S_0) = Y_{beam} + S_0\hat{Y}_{cal}$$

$$Z(S_0) = Z_{beam} + S_0\hat{Z}_{cal}.$$

The expected coordinates from the proton kinematics (X_{HMS}, Y_{HMS}) can then be calculated as,

$$X_{HMS} = X(S_0)\cos\theta_e - Z(S_0)\sin\theta_e$$

$$Y_{HMS} = Y(S_0).$$

The scattering angles can be calculated as,

$$\phi_{BETA} = \frac{Y_{HMS}}{R_{cal}}, \qquad \theta_{BETA} = \frac{X_{HMS}}{R_{cal}}.$$

However, SANE uses a polarized target with a strong magnet which deflects the outgoing particles by the amount of dY as seen in Figure 4.1. The target magnetic field effects are accounted for the particle track reconstruction by HMS as explained in Section 4.1.1. For the coincidence data, the electron deflections at BigCal, dY are determined using the same target field subroutines. As in Equation 4.1.2, the deflected angle, $\Delta\phi$, results in a vertical position difference of the electrons in BigCal. Prediction of this deflection is started with the scattered electron with energy E' from the interaction vertex of,

$$\begin{aligned} Y_{BETA} &= -Y_{beam} \\ X_{BETA} &= X_{beam}\cos\theta_e - Z_{beam}\sin\theta_e \\ Z_{BETA} &= X_{beam}\sin\theta_e + Z_{beam}\cos\theta_e \end{aligned}$$

with in-plane and out-of plane angles,

$$\begin{aligned} \phi_{BETA} &= -(Y_{HMS} - Y_{BETA})/(R_{cal} - Z_{BETA}) \\ \theta_{BETA} &= (X_{HMS} - X_{BETA})/(R_{cal} - Z_{BETA}) \end{aligned}$$

in the BETA coordinate system. The electron is then considered to pass through the target magnetic field step-by-step, each time calculating the vertical position and angle using the target magnetic field map. This results in the predicted electron coordinates, (X_{HMS}, Y_{HMS}) at BigCal, including the target magnetic field deflection corrections.

4.4.2.3 Elastic Event Selection Cuts

Another selection criteria to extract the good elastic events is by comparing the detected electron position at BigCal (X_{clust}, Y_{clust}) to the expected position (X_{HMS}, Y_{HMS}) calculated from elastic kinematics of the proton detected in HMS. The difference between each pair of coordinates is defined as $\Delta X = X_{HMS} - X_{clust}$ and $\Delta Y = Y_{HMS} - Y_{clust}$. Elastic events should be at $(\Delta X, \Delta Y) = (0, 0)$ as shown in Figure 4.14.

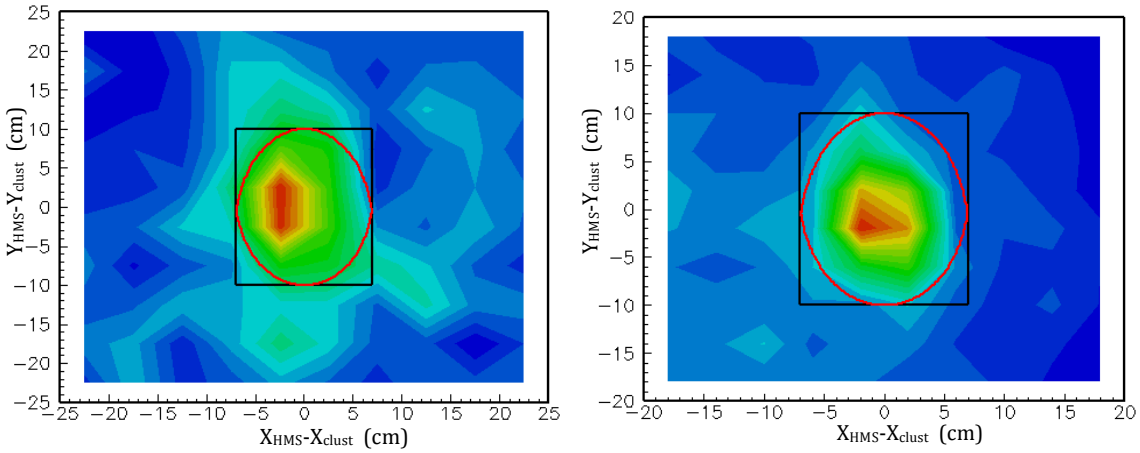

Figure 4.14. Elliptical cut (red) with $(X_{cut}, Y_{cut}) = (7, 10)$ *cm* applied to the ΔY vs ΔX spectra at $Q^2 = 5.17$ (GeV/c)^2 (*left*) and $Q^2 = 6.26$ (GeV/c)^2 (*right*) with no Δ_p cuts applied.

Therefore, in order to get a clean sample of elastic events, cuts have been applied to three variables which are:

- The relative proton momentum difference, Δ_p.
- The horizontal position difference, ΔX.
- The vertical position difference, ΔY.

Applying an elliptical cut to the ΔX and ΔY distributions,

$$\sqrt{\left(\frac{\Delta X}{X_{cut}}\right)^2 + \left(\frac{\Delta Y}{Y_{cut}}\right)^2} \leq 1.$$

achieves a better background suppression than using the cuts on ΔX and ΔY separately, because the shape of the cut matches the shape of the elastic peak in two-dimensional phase space, $(\Delta X, \Delta Y)$. Compared to the rectangular cut (black), an elliptical cut (red) rejects events at the corners of the rectangle where the signal-to-background ratio is lower, leading to a cleaner sample of events. Figure 4.14 shows an elliptical cut with $(X_{cut}, Y_{cut}) = (7, 10)$ cm applied to the ΔY vs ΔX spectra at both $Q^2 = 5.17$ (GeV/c)^2 and $Q^2 = 6.26$ (GeV/c)^2. The Δ_p spectrum of all events after applying the elliptical cut is shown in Figure 4.15 in which a much cleaner selection of elastic events is achieved than compared to Figure 4.13.

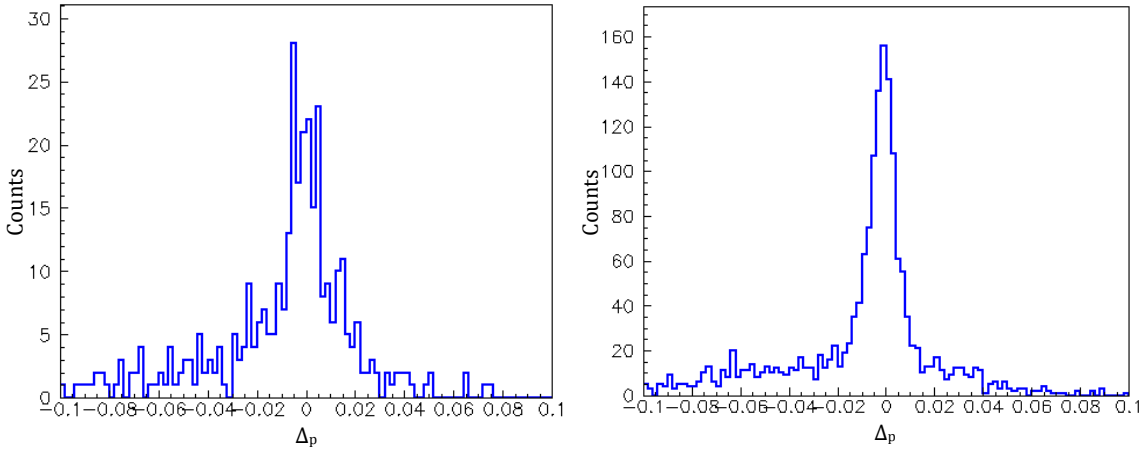

Figure 4.15. Δ_p spectra of all events after applying the elliptical cut at $Q^2 = 5.17$ (GeV/c)^2 (*left*) and $Q^2 = 6.26$ (GeV/c)^2 (*right*).

Even after applying an elliptical cut, there is a tail at negative values of Δ_p which implies that still there are some events passing the elliptical cut coming from inelastic reactions such as π^0 photo-production. In order to suppress these inelastic events, a cut around the elastic peak in Δ_p of $\pm 3\sigma$ is applied. Figure 4.16 shows the ΔX

and ΔY spectra after applying the $\pm 3\sigma$ cut (red) around the elastic peak in the Δ_p spectrum for $Q^2 = 6.26$ (GeV/c)^2. Compared to the same ΔX and ΔY spectra before applying the Δ_p cut (blue) shown in the same Figure, the new ΔX and ΔY distributions are much cleaner.

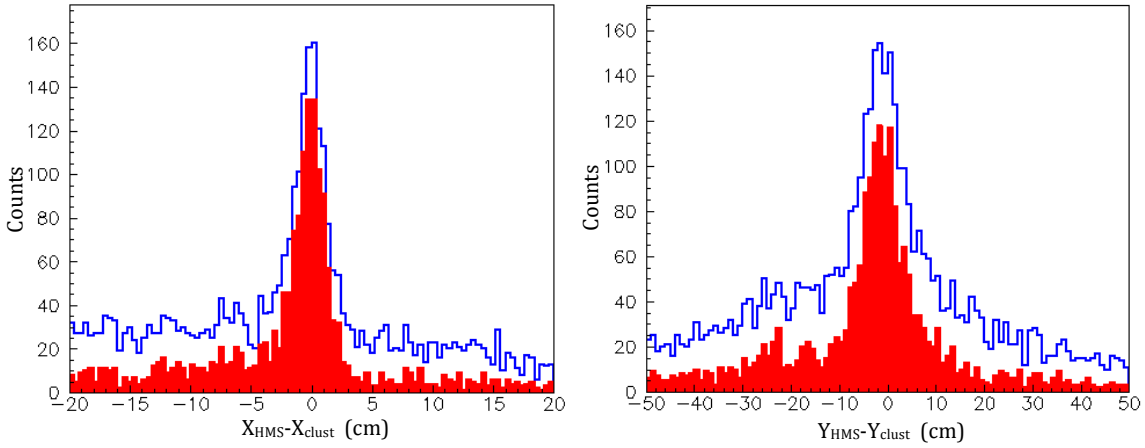

Figure 4.16. ΔX and ΔY spectra after applying the $\pm 3\sigma$ cut of ± 0.02 around the elastic peak (red) in the Δ_p spectrum for $Q^2 = 6.26$ (GeV/c)^2, compared to before applying the Δ_p cut (blue).

4.5 Monte Carlo Simulation

Simulations play a very important role in order to understand the experimental data. The SANE simulation includes details about all detectors, consisting of the physical parameters of the detectors and the materials the particles pass through. To have a better match with the resolution of data, the effects of multiple scattering in the target and the spectrometer were also simulated for both incoming and outgoing particles. The energy loss at the target was also included. After applying radiative corrections and accounting for inefficiencies, the simulated yields are compared with the experimental data. In this way, any unknown problems on the experimental data can be determined. Because the simulation includes all known physics processes when the particle passes through the materials, any differences between the data and the

simulated yields are used to identify the problems and hence to either correct them in the data or to account for them in the simulation.

For the single-arm data collection during SANE, the HMS spectrometer detected the scattered electrons from the NH_3 target and recorded the scattering angle, θ_e and the scattered momentum, P. A single-arm Monte Carlo simulation constructed by M. Eric Christy was used to weight the electron data. The standard Hall C Monte Carlo, SIMC was used for the comparison with the coincidence data. In contrast to the single-arm HMS Monte Carlo, SIMC contains all detector (HMS, SOS, BETA, etc.) Monte Carlos. It is carried out separately for the lepton arm and the hadron arm, in the same way as the single-arm Monte Carlo. SANE used BETA as the electron arm and HMS as the proton arm in coincidence data collection. In addition to the NH_3 data, the scattered electrons from the C target were generated in both single-arm and coincidence settings for the detailed understanding of the data in the inelastic region. Both simulations were modified to use the target magnetic field because the original versions were for unpolarized targets only. In general, both simulations work as follows:

For a given event, initial parameters such as X, Y, Z coordinates and the electron/proton azimuthal and polar scattering angles, as well as the momentum, are generated at the target center. The initial limits for these parameters, initially larger than the physical acceptance of the spectrometer, are set by the user. In SIMC, these initial kinematic generation limits are given for both the electron and the proton, while in the single-arm simulation, the parameters are given for the electron. For the elastic case, only one set of angles is generated. The remaining kinematic variables are calculated. The starting positions, X and Y, of the electron/proton beam at the target is rastered with a uniform sinusoidal raster of 2.00 cm diameter. Table 4.3

shows all the initial parameters except for target parameters for both the proton arm (HMS) and the electron arm (BETA) together with the single-arm Monte Carlo. The particles generated with the initial parameters at the target center are then propagated through the target, checking for possible energy loss and multiple scattering.

Table 4.3. The initial parameters for both proton arm (HMS) and electron arm (BETA) together with the single-arm Monte Carlo parameters.

	HMS_{proton}	$BETA_{electron}$	$HMS_{electron}$
P_c (GeV/c)	4.174	2.559	4.394
θ_c $(deg.)$	22.0	40.0	15.41
δ (%)	$-15<\delta<15$	$-20<\delta<20$	$-15<\delta<15$
Y'_{tar} $(mrad)$	$-250<Y'_{tar}<250$	$-120<Y'_{tar}<120$	$-150<Y'_{tar}<150$
X'_{tar} $(mrad)$	$-200<X'_{tar}<200$	$-240<X'_{tar}<240$	$-200<X'_{tar}<200$

4.5.1 Transport Through the Target Magnetic Field

The standard Hall C COSY INFINITY model generates the particle tracks without a target magnetic field. The generated events at the target center are passed through the target and are then transported through the HMS magnets to the detector hut. However, SANE used a polarized NH_3 target. The magnetic field which is used to polarize the target is directed 80° left to the beam axis and has a cylindrical volume of about 100 cm in diameter around the target. Therefore, the generated electrons from the target bend downward, deviating from a linear trajectory from the target to the HMS collimators, which are located at beam right. The generated protons bend upward in the SIMC simulation. The simulation was modified to account for this deflection, using the same target magnetic field map which is used for the reconstruction of the measured data.

First, the particles are tracked through the target magnetic field up to the edge of the field-free region, beginning at 100 cm from the target center. Then, taking these positions and angles, (X, Y, X', Y') as the starting point, the trajectory is

projected back to the target at $Z = 0$. The projection gives new coordinates at the target, ($X_{new} = X - ZX'$, $Y_{new} = Y - ZY'$, $Z = 0$). Then the particles starting with these new coordinates, (X_{new}, Y_{new}, $Z = 0$) with the same angles of X', and Y' are tracked to the HMS collimator and then through the HMS magnets. As they travel through the magnets, the magnetic optics determine the event trajectory using a matrix calculated with the COSY INFINITY model [191], which agreed well with the HMS optics. This has been done step-by-step through the different apertures in the quadrupoles and dipole. Once the particle track has passed through all the apertures, it enters the detector hut and strikes the detectors. The detector dimensions of the drift chambers and hodoscopes were included in the simulation. So all of the particles were checked so that they would physically hit the detectors. If so, by taking the coordinates at the focal plane, the tracks are then reconstructed back to the target providing reconstructed target coordinates and angles. This was done in the same way as was done by the analyzer discussed in Section 4.1.

For the electron arm in the coincidence simulation, which is the BETA detector, only the electron position at BigCal has been considered. This way, the predicted and measured X and Y positions were simulated. The target magnetic field map was used to calculate the electron's deflection angle and then to track it using the field integral $\int B \cdot dl$. Although the carbon target is not polarized, the target magnetic field was there while taking the C data. So these scattered electrons were affected the same way as the electrons scattered from polarized NH_3 when passing through the target magnetic field to the HMS spectrometer.

4.5.2 Target Parameters

For the single-arm data-to-simulation comparison, both NH_3 and C targets were used. In order to simulate NH_3 in a liquid He bath, N, H and He were generated separately. These contributions were weighted by each target density in the target

cup using the known packing fraction of NH_3. (packing fraction will be discussed in detail in Section 4.5.5.1.) Because the target ladder is immersed in the liquid He bath at the center of the target chamber, the incoming electron beam has to penetrate about a 0.5 cm thick He volume. Data for these front and back He were also generated. Further, the aluminum contributions arising from the target cup lids, the 4 K shields, and the evaporation refrigerator's tailpiece were also generated.

For the carbon target, some data were taken with no He in the evaporation refrigerator. In that case, only the C and the Al backgrounds coming from the 4 K shields and the evaporation refrigerator's tailpiece were simulated. Because a small carbon disk of ~ 0.7 cm thick has been used, carbon does not have any background contributions from the target cup lid nor from front and back He, in contrast to the NH_3 target. However, for the carbon data taken with liquid He in the refrigerator, the He contributions at the target (with a 3 cm thickness of the target cup minus 0.7 cm carbon thickness) as well as the front and back He bath penetrates were generated in addition to the same aluminum background which C has without He.

For all these targets, the effective density of the targets, the thickness of the targets, the Z position of the target measured from the target center, and the one radiation length of the target material were given by the user as inputs. For the coincidence data, only the H target is simulated in addition to the carbon target. The target input data are shown in Table 4.4 assuming the packing fraction of NH_3 is 56 %. In contrast to the different target inputs, all other initial inputs were the same for the same kinematics for all targets. After generating all of the sub-targets, for example H, N, He, Al for the NH_3 target, they were summed together in accordance with their weight-scaling factor. These scaling factors were determined by calculating the luminosity for each target relevant to the total charge of the particular data run and the phase-space factor. The total charge, Q, was measured for each data run and the simulation needs to be scaled by this measured charge. The luminosity of the

Table 4.4. Target data input information.

Target Type	Effective density (g/cm^3)	Thickness (cm)	Z position (cm)	X_0 (cm)
H	0.0861	3.00	0.15	732.17189
N	0.4020	3.00	0.15	94.5025
He	0.0634	3.00	0.15	1487.7287
Liquid He front	0.1450	0.5	-1.60	650.4966
Liquid He back	0.1450	0.5	1.90	650.4966
C (No He in the cup)	2.20	0.684	0.30	19.41
Liquid He with C	0.1450	2.316	0.15	650.4966
Target cup lid-Front	2.736	0.00381	-1.35	8.7756
Target cup lid-Back	2.736	0.00381	1.65	8.7756
4 K shield - Front	2.736	0.00254	-3.80	8.7756
4 K shield - Back	2.736	0.00254	3.80	8.7756
fridge's tailpiece -Front	2.736	0.01016	-2.05	8.7756
fridge's tailpiece -Back	2.736	0.01016	2.35	8.7756

data can be calculated as,

$$L = \left(\frac{Q \times 10^{-6} C}{1.602 \times 10^{-19} C/electron} \right) \cdot \left(\frac{\rho t N_A}{M} \right),$$

where ρ is the target density in g/cm^3, t is the target thickness in cm, N_A is Avogadro's number, M is the target mass in amu, and Q is the charge in μC read from the scaler files. The phase-space factor for the MC yield is,

$$\delta P = 4 \times dX' \times dY' \times \frac{dE'}{1000} \qquad (rad^2 MeV),$$

where dX', dY' are the total out-of-plane and in-plane angles and dE' is the total energy range. Then the weighting scaling factor for each sub-target was calculated as,

$$f = \frac{L \times \delta P}{N_{gen}} \cdot \frac{1}{1000}.$$

The weight scaling factors for each target contribution for C with no He and C with He targets were also calculated in the same manner. The yields for the coincidence

simulation were also scaled by the measured charge. The simulation assumes that all of the detectors and electronics work perfectly, which is not true in reality. Therefore, the MC yields must be corrected for the detector inefficiencies and dead times such as computer dead time, electronic dead time, etc. Further, the MC/SIMC yields are modified by the radiative effects.

4.5.3 Radiative Effects

For each successful event reconstructed to the target, a weight is calculated which consists of a model cross-section modified by the radiative effects. The model cross-sections were determined using the most recent cross-section parametrization, F1F209 by M. Eric Christy and P. Bosted [192] and the electric and magnetic form factors were calculated using a parametrization to the world data by J. Arrington [193]. The uncertainty on cross-sections due to the radiative effects was estimated to be 1% according to the radiative effect studies done at SLAC [194]. The radiative effects calculated using the radiative correction codes, originally written by S. Dasu using Tsai's formula [17] and modified by P. Bosted were used for each input kinematics table. The input kinematic tables were generated for each beam energy, which include $\pm 8^{\circ}$ range of scattering angle, θ around the HMS central angle, θ_c in 0.1° intervals. For each θ value, the scattering momentum, P is varied by $\pm 15\%$ about the HMS central momentum, P_c in 0.01 GeV intervals. The output table gives the model cross-sections modified by radiative effects together with the beam energy, E, scattered particle momentum, P, and the scattered particle angle, θ.

However, NH_3 target, C target and $C+He$ configurations consist of several target materials for which the radiative effects and cross-sections are different. Therefore, the radiative effect tables were generated separately for each sub-target material using common input parameters. A packing fraction of 56% was assumed for the NH_3 target. Table 4.5 shows the kinematics used to create the radiation tables.

For each simulated successful event, by knowing its scattering angle and the reconstructed scattering momentum, the radiated cross-section can be determined from the table by interpolation or extrapolation within its kinematic range. The simulated yields are weighted by this radiated model cross-section separately for each target material.

Table 4.5. Kinematics used to create the radiated cross-section tables for different target types.

	NH_3	C	C+He
E	5.895	5.895	5.895
θ_c	15.41	15.41	15.41
θ	7.41-23.41	7.41-23.41	7.41-23.41
P_c	4.4	4.4	3.10
P	3.74-5.06	3.74-5.06	2.635-3.565

In contrast to the single-arm MC, the radiative effects calculation to the model cross-section is implemented in SIMC codes so that it is not needed to calculate the radiated cross-section tables separately and to do interpolating/extrapolating.

4.5.4 MC Comparison with C Data

The plot in Figure 4.17 shows the comparison of data to Monte Carlo yields for the reconstructed quantities for the C target for run 72782. The data were collected with no He in the evaporation refrigerator. Therefore, only 4 K shields and the evaporation refrigerator's tailpiece contribute to the background. Nominal cuts in the reconstructed spectrometer variables are applied on both data and simulated yields. The HMS acceptance and PID cuts applied to the data as well as to the MC yields are given in Table 4.6. The reconstructed variables, Y_{tar} and X'_{tar} show a shift between data and MC, while Y'_{tar} has a discrepancy at the higher edge of the in-plane angle acceptance. The momentum fraction, $\delta = \frac{\delta P}{P}$ shows a dip at $\frac{\delta P}{P} = 0$ on data, which MC does not show.

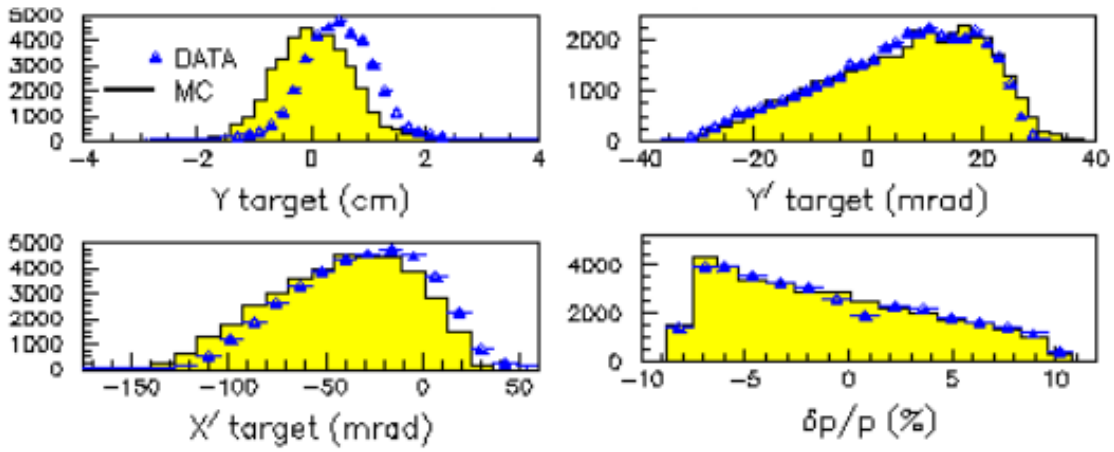

Figure 4.17. Data to MC comparison for HMS reconstruction quantities for the C run 72782.

Table 4.6. HMS acceptance and PID cuts applied to both data and simulated yields.

Acceptance Cuts
$-50<Y'_{tar}<50$ (mrad)
$-200<X'_{tar}<200$ (mrad)
$-0.05<(\theta-\theta_c)<0.10$ (mrad)
$-8\%<\delta<10\%$
PID cuts
$N_{cer}>2$
$E_{cal}/P>0.7$

4.5.4.1 Efficiency Corrections

As mentioned in Section 4.2.3, the Cherenkov detector has an inefficiency of about 20% in the central region of the δ spectrum. In the plot of reconstructed δ in Figure 4.17, the dip in the data at $\delta = 0$ is caused by this inefficiency. Applying the inefficiency as a function of δ to the simulated yields creates the same dip at the same δ, resulting in a better agreement with the data. Since this inefficiency is due to the vertical space between two mirrors, it is constant over the duration of the experiment. Therefore, the inefficiency calculated from the C run 72782 (shown in Figure 4.6: *right*) was used for all C and NH_3 Monte Carlo simulations.

The drift chamber tracking efficiency also degraded as a function of the vertical focal plane coordinate, X_{fp} as discussed in Section 4.2.2. The Monte Carlo simulated yields were normalized with this tracking efficiency as well to get better agreement with the data. For the elastic data, both the C run (72782) and NH_3 runs (72790 and 72795) which were used to compare with MC were in the same kinematic regions. Therefore, the drift chamber efficiencies were calculated using run 72782 as shown in Figure 4.4 were used to correct both C and NH_3 MC yields.

4.5.4.2 Position Offsets (Beam Offsets)

The incoming electron beam was rastered circularly with a radius of 1 cm. So, for each event, the reconstructed target X and Y positions are not well known. No absolute event-by-event beam position was measured. The relative X and Y positions to the beam center were measured by recording the X and Y raster amplitudes in an ADC. The Monte Carlo simulation was used to define the central beam X and Y positions on the target. Figure 4.17 shows the data to MC comparison for the reconstructed target variables using the C target. The horizontal position denoted as "Y target" $= Y_{tar}$ shows a shift between data and MC. Meanwhile, the reconstructed target in-plane angle, "Y' target" $= Y'_{tar}$ also shows a difference at the acceptance

edges. The HMS dipole does not affect the horizontal position or in-plane angle. Therefore, introducing a horizontal offset in X direction to the generated X position of the simulation can shift the reconstructed X position. By adjusting this X offset until the horizontal "Y target" and the target in-plane angle, "Y' target" acceptance of the MC match with the data, the beam X offset on the target, is identified.

Similarly, the reconstructed out-of-plane angle, "X' target"$= X'_{tar}$ at the target also shows a shift between data and MC. Because the X'_{tar} has a first-order dependence on the Y position at the target in the reconstruction matrix elements, using the incorrect raster Y position at the target can cause such a type of shift. Therefore, the generated Y position of the particles at the target was changed by introducing an offset until the reconstructed out-of-plane angle of the data and MC agreed with each other. Figure 4.18 shows the reconstructed distributions of Y, Y', X' and δ after using the X and Y offsets determined by the simulation for C run 72782. The simulation yields are corrected with the Cherenkov and drift chamber efficiencies. The comparison between data and MC for the detected angle relative to the HMS central angle, $\theta - \theta_c$, the invariant mass squared, W^2, the ratios of data to MC for $\theta - \theta_c$ and $\delta p/p$ are also shown in Figure 4.18.

Beam X and Y offsets were checked for both C and NH_3 data following the same procedure and the offsets were the same. The X offset was found to be 0.4 cm; the Y offset was 0.1 cm. An MC scale factor of 0.93 shown in the plot $\theta - \theta_c$ of Figure 4.18 results from the data for the MC-to-data ratio in the δ region of $-8\%<\delta<10\%$. This shows how well the C cross-section model agrees with the data. The C cross-section model is well tested with world data and since the cross-section for N is similar to that for C, normalizing the N yields by this C data-to-MC ratio of 0.93 is one further correction to the N cross-section. Therefore, the NH_3 simulation yields are re-normalized by 0.93.

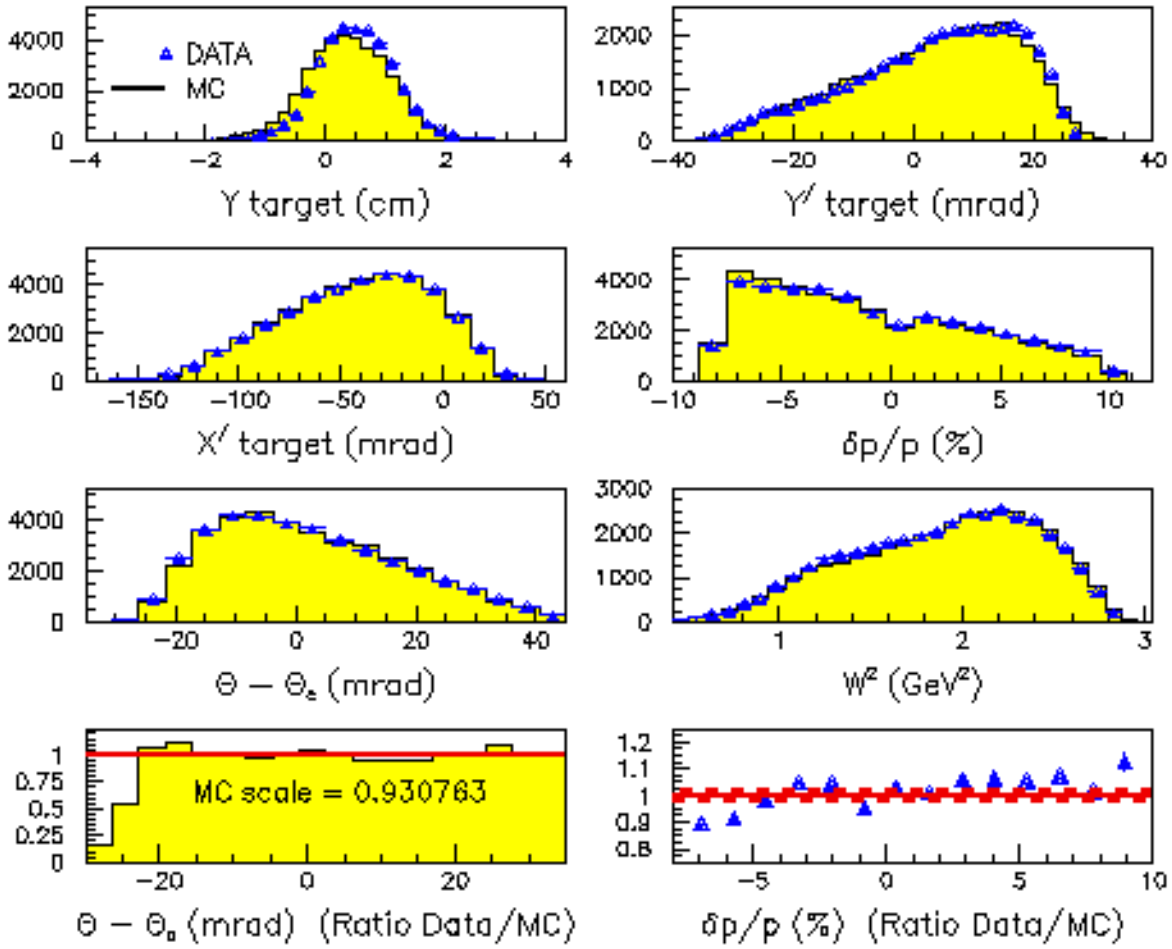

Figure 4.18. Data to MC comparison of reconstructed quantities by HMS with X and Y offsets (X offset=0.4 cm and Y offset = 0.1 cm) from data for the C run 72782. The simulation yields are corrected with the Cherenkov and drift chamber efficiencies.

4.5.4.3 C Cross-Section Shape Correction

Because the elastic peak is located at the higher δ region as seen in Figure 4.11 (*left*), the comparison for elastic data to the Monte Carlo simulation was considered for two different δ regions $-8\%<\delta<10\%$ and $10\%<\delta<12\%$ separately as mentioned in Section 4.4.1.3. A small shift of 0.012 GeV/c^2 of the invariant mass, W was applied to the Monte Carlo yields at the elastic peak for the δ region $-8\%<\delta<10\%$ to have a better match with the data for NH_3 run 72790. The cross-section shape of the C yields after applying the same W shift of 0.012 GeV/c^2 was also tested. Because the elastic peak in the δ region of $10\%<\delta<12\%$ matched better with the data for run 72790 without using any W shift, no W shift applied to these data. Figure 4.19 shows the ratio of C data to simulated yields as a function of invariant mass, W for the two δ regions.

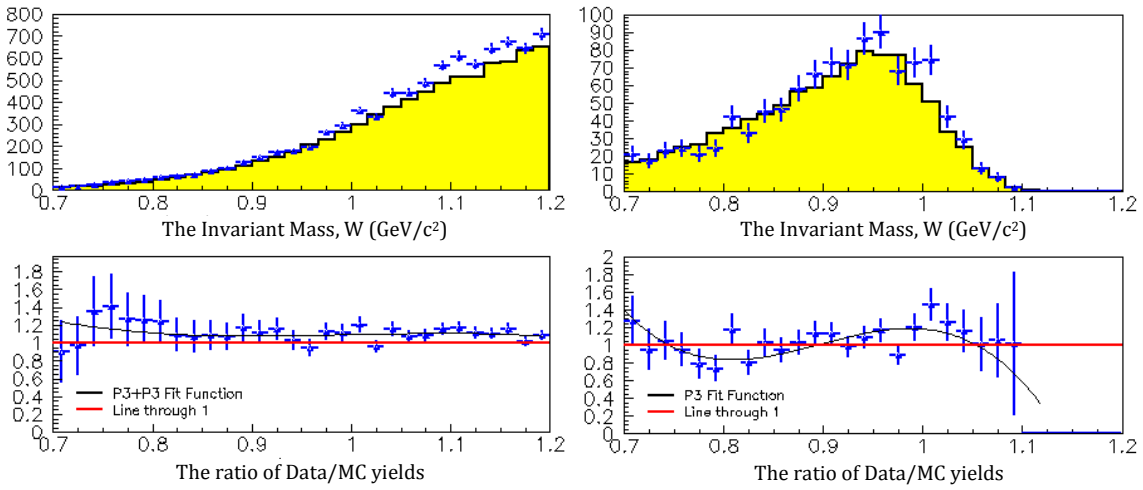

Figure 4.19. The ratio of C data to simulated yields as a function of invariant mass, W for the two δ regions, $-8\%<\delta<10\%$ (*left*) and $10\%<\delta<12\%$ (*right*). Only the MC yields on $-8\%<\delta<10\%$ used the W shift of 0.012 GeV/c^2. The polynomial fits (black) on the ratios are also shown in the plots.

The polynomial fits shown in the plots were used to correct the Monte Carlo yields for the C target, as well as the same fit functions were used to correct all of the background yields in the NH_3 target. In this way, the N, He and Al cross-sections get additional corrections determined by the C cross-section as a function of W. This correction is applied only for the elastic region of $0.7<W<1.1$ GeV/c^2.

4.5.5 MC Comparison with Single-Arm NH_3 Data

Figure 4.20 shows the data to Monte Carlo simulation yield comparison for the reconstructed HMS quantities for NH_3 run 72790. These data were taken with the same kinematics as the C run 72782. The same beam X and Y position offsets as well as the same Cherenkov and drift chamber efficiencies were used on the simulation yields as in run 72782. The C cross-section shape corrections discussed in Section 4.5.4.3 are not applied here.

The X position offset determined by using the Monte Carlo simulation as discussed in Section 4.5.4.2 was re-checked by looking at the correlation between the reconstructed target out-of-plane angle, X'_{tar} and the invariant mass, W. In MC, events are generated at a given X position and then reconstructed back to the same position. However, in the data, the actual X position is not known and the events are reconstructed to target X position. If the reconstructed position is not the same as the start position of the particle, the data will show a correlation between the X'_{tar} and W as in Figure 4.21 (*left*). This correlation can be reproduced by the Monte Carlo simulation as well as by reconstructing the particle to a different horizontal position X than from where it was generated as shown in Figure 4.21 (*right*).

Therefore, reproducing this X'_{tar} vs W correlation in MC generates confidence that the same correlation seen in data are due to the reconstruction of the particle track to the incorrect horizontal target position X. This is a very good method to re-check the target X position for the polarized target experiments.

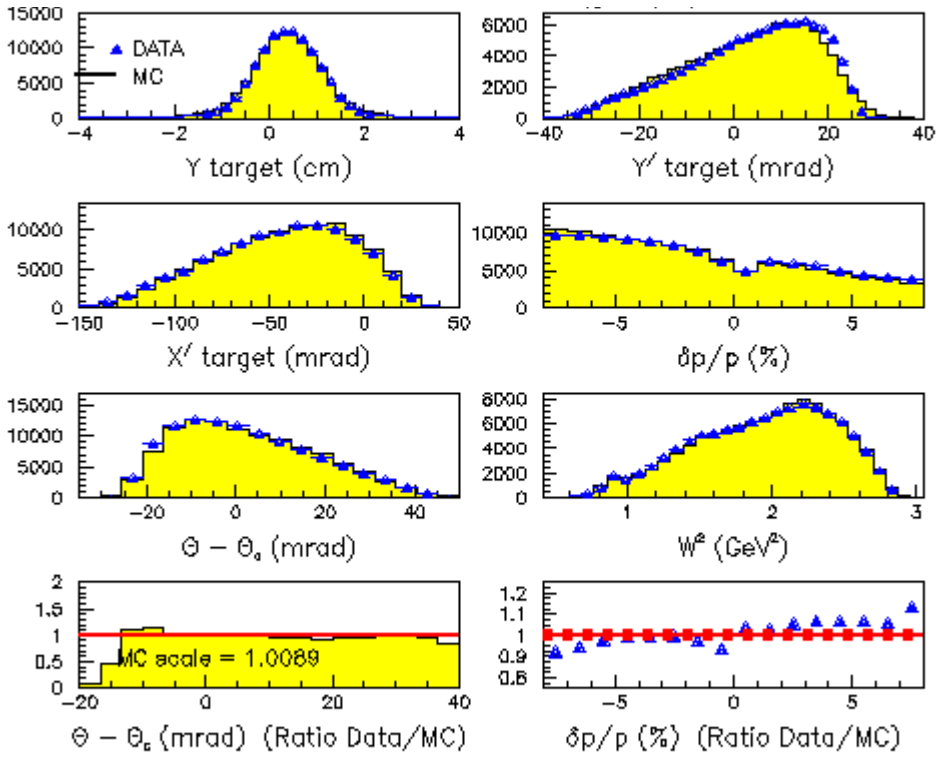

Figure 4.20. After using the same beam X and Y position offsets as well as the same Cherenkov and drift chamber efficiencies as the C run 72782, the data to Monte Carlo comparison for the reconstructed HMS quantities for the NH_3 target 72790 is shown.

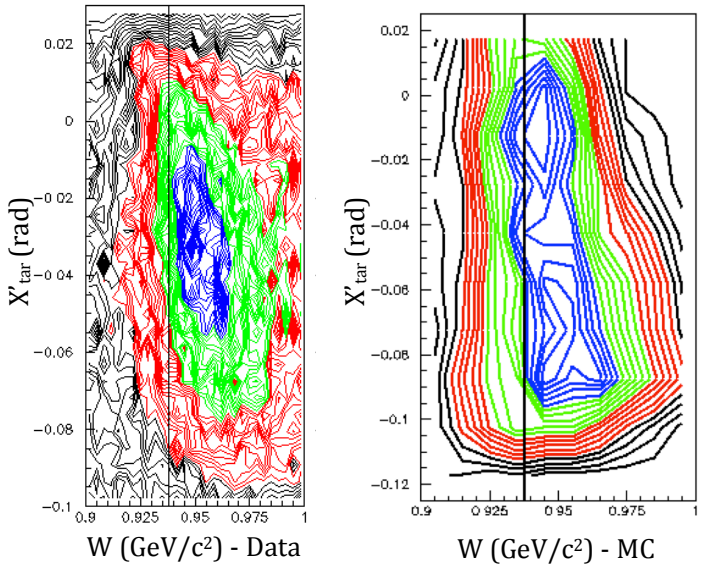

Figure 4.21. The X'_{tar} vs W correlation for the data (*left*) and for MC (*right*).

4.5.5.1 Packing Fraction

SANE utilized ammonia crystals with a density of 0.8670 g/cm^3 as the polarized target. These crystals do not fill the target cup perfectly. The packing fraction is the ratio of the volume taken by this ammonia to the target cup volume. This is determined by comparing the NH_3 data to Monte Carlo simulation. The individual densities of H and N in the target cup are extracted from the density of NH_3. The new effective densities were calculated by accounting for the packing fraction. The effective density of He in the target cup is also calculated by taking the packing fraction into account. When the packing fraction changes, then the effective density of H, N and He in the target cup changes as follows:

The H atomic density in the total density of NH_3 is $0.8670 \times \frac{3}{17}$ g/cm^3 = 0.153 g/cm^3. So the remainder is the atomic density of the N, which is $0.8670 \times \frac{14}{17}$ g/cm^3 = 0.714 g/cm^3. If one assumes that the NH_3 crystals were packed in the target cup with the packing fraction, *f*, then the total H effective density in the target cup is determined as $0.153 \times \frac{f}{100}$ g/cm^3, and the total N effective density in the target cup is $0.714 \times \frac{f}{100}$ g/cm^3. If the fraction of NH_3 in the target cup is only *f*, then the rest of $(1 - \frac{f}{100})$ is liquid He. The density of liquid He used by SANE is 0.1450 g/cm^3. Therefore, the effective density of He in the target cup is determined as $0.1450 \times (1 - \frac{f}{100})$ g/cm^3.

In this way, the effective densities of all the targets were calculated by assuming one packing fraction. Then the simulation of each target type is generated and added all together by their weighting factors as discussed in Section 4.5.2. The ratio of data to Monte Carlo yields in the $\delta = \delta p/p$ spectrum for the momentum acceptance $-8\% < \delta < 10\%$ (seen in Figure 4.22 (*left*)) were determined and the procedure was continued assuming three different packing fractions, 50%, 60% and 70%. Figure

4.22 (*right*) shows the ratio of data to MC yields for the three packing fractions using the "bottom" target data (72790). The NH_3 yields were normalized by the ratio of data to MC yields of C as discussed in Section 4.5.4.2. The data related to Figure 4.22 (*right*) are shown in Table 4.7.

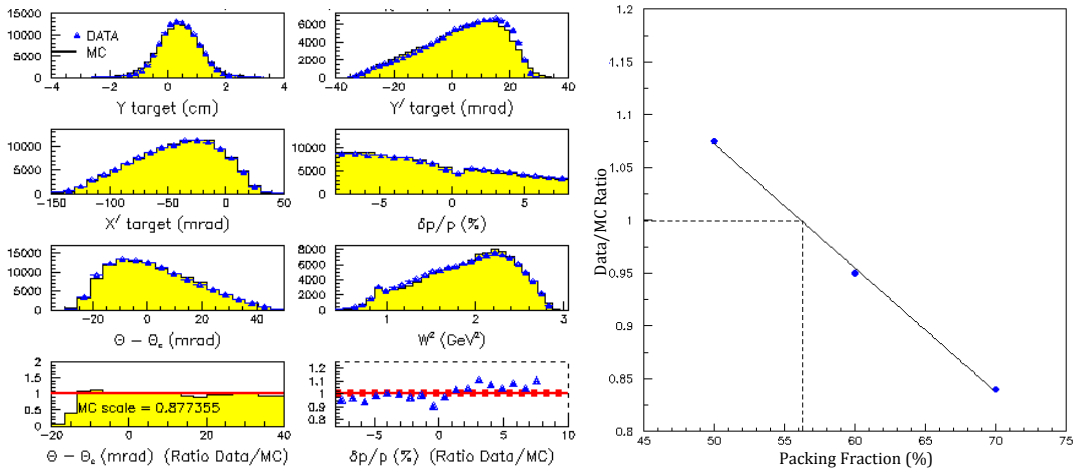

Figure 4.22. The reconstructed target quantities including δ spectrum for the momentum acceptance $-8\%<\delta<10\%$ for the packing fraction of 60% using run 72790 (*left*) and the ratio of data to MC yields for the three different packing fractions 50%, 60% and 70% (*right*).

Table 4.7. Table of the ratio of data to MC yields for three different packing fractions 50%, 60% and 70% using the "bottom" target data (72790).

Packing Fractions (%)	50	60	70
Data/MC Ratio	1.0	0.88	0.78
Data/MC Ratio/0.93	1.075	0.95	0.84

By taking the packing fraction, which gives a ratio of data to MC yield of 1 as shown in Figure 4.22 (*right*), the packing fraction of the NH_3 crystals in the "bottom" target cup is estimated as 56%. During the experiment, several target loads were used and each load had different packing fractions. Because both "top" and "bottom" NH_3 targets (one target load in each) were used for the single-arm electron data, the packing fractions have determined for the two-target cups separately. The packing

fraction for the "top" target using the run 72795 was determined as 58%. The target data inputs in Table 4.4 were calculated for the packing fraction of 56%, which is determined for the "bottom" target using run 72790. Figure 4.20 shows a comparison of reconstructed HMS quantities with the data for run 72790, assuming a new packing fraction of 56%.

The simulated target contributions at the elastic peak compared to the data for the NH_3 run 72795 at both δ regions are shown in Figure 4.23. The W shift of 0.007 GeV/c^2 and the C cross-section shape corrections mentioned in Section 4.5.4.3 were also applied.

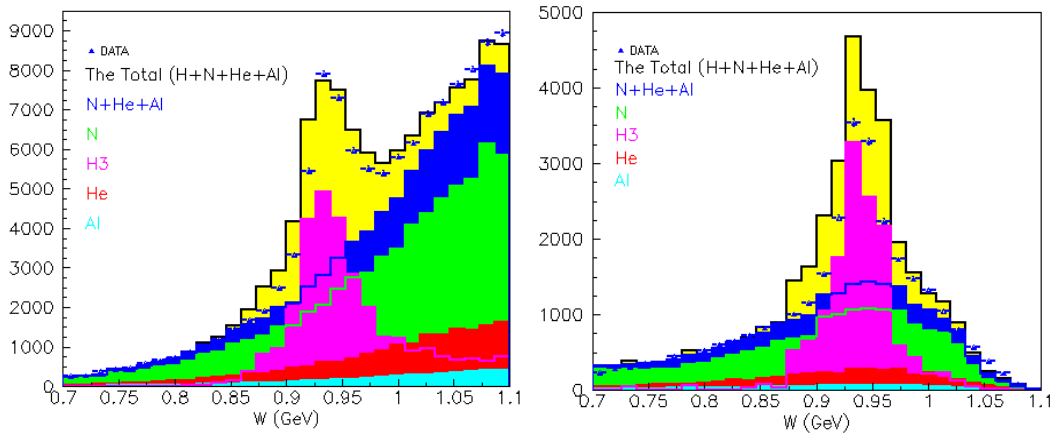

Figure 4.23. The simulated target contributions at the elastic peak compared to the data at both δ regions, $-8\%<\delta<10\%$ (*left*) and $10\%<\delta<12\%$ (*right*) for the experiment run 72795. Different colors show different target type contributions.

4.5.6 MC Comparison with Coincidence NH_3 Data

The SIMC yields-to-data comparison for the coincidence runs is shown in Figure 4.24. All the coincidence runs with beam energy 5.895 GeV are considered. The same elastic cuts defined in Section 4.4.2.3 were used. The shift between the data and MC of the HMS reconstructed Y_{tar} and the Δ_p can be seen.

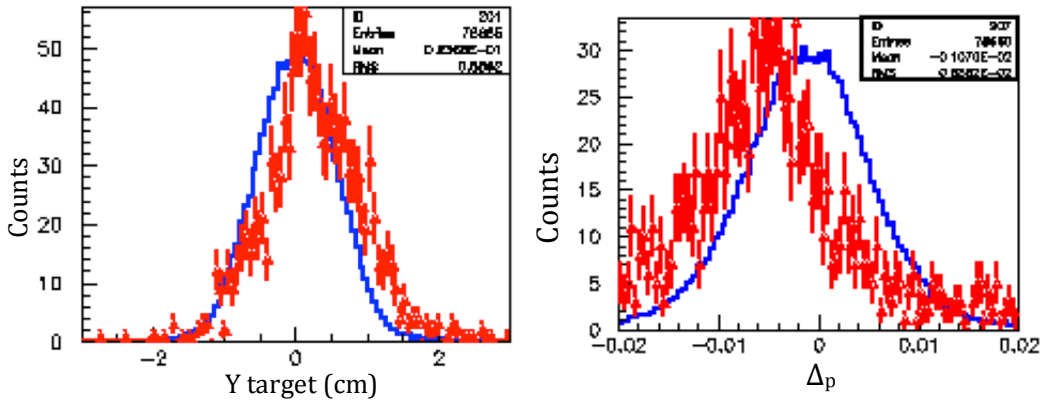

Figure 4.24. Data (red) to SIMC (blue) comparison for the HMS quantity, Y target (*left*) and coincidence quantity, Δp (*right*) for the beam energy 5.895 GeV before correcting for the beam X and Y position offsets.

The beam X position offset for these data was determined by using the proton arm reconstructed quantity, Y_{tar} in the same way as the single-arm MC. The Y offset was determined by looking at the data-to-SIMC comparison of the Δ_p spectrum. The same procedure was followed for both beam energies 5.895 GeV and 4.73 GeV. Figure 4.25 shows the data-to-SIMC comparison for the HMS (*left*) and coincidence (*right*) quantities after correcting for the X and Y offsets on data for the beam energy 5.895 GeV. SIMC yields were also corrected by the Cherenkov and DC efficiencies. Further, both MC and SIMC yields were corrected by the computer lifetime read from the scaler files. Table 4.8 shows the X and Y offsets determined by MC/SIMC for both single-arm and coincidence data.

Table 4.8. The X and Y offsets determined by MC/SIMC for both single-arm and coincidence data.

	X offset (cm)	Y offset (cm)
Single-arm data	0.4	0.1
Coincidence data		
4.730 GeV/c^2	0.3	0.10
5.895 GeV/c^2	0.3	-0.15

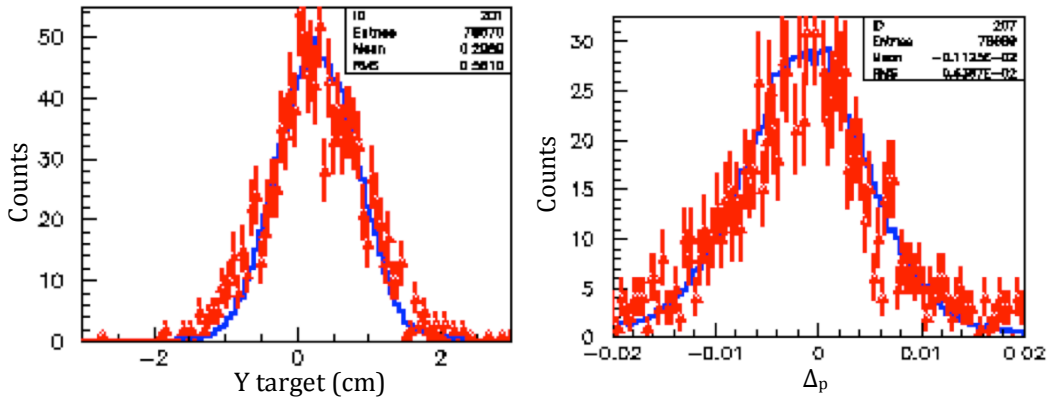

Figure 4.25. Data (red) to SIMC (blue) comparison for the HMS quantity, Y target (*left*) and coincidence quantity, Δp (*right*) after correcting the X and Y offsets for the data determined by the simulation for the beam energy 5.895 GeV.

4.6 Correlation Corrections

After selecting the good elastic events, the correlation of reconstructed out-of-plane angle, X'_{tar} with the invariant mass, W as seen on Figure 4.26 (*left*) showed a problem in the single-arm data, which needed to be corrected. Because the reconstructed out-of-plane angle at the target, X'_{tar} has a first-order dependence on the Y position at the target in the reconstruction matrix element, the vertical beam position deviation from the target center, Y_{off}, can have an effect on the reconstructed X'_{tar}. This causes a correlation of X'_{tar} with the invariant mass, W as seen in Figure 4.26 (*left*).

Similarly, a correlation of the HMS quantities X'_{tar} vs Δ_p and a correlation on the BETA quantities, ΔY vs Y_{clust} were also observed in the coincidence data, as seen in Figure 4.26 (*right*).

Since all of these correlations are related to the vertical position or angle, a correction of azimuthal-angle due to the target magnetic field was considered the best explanation. Subsequently, all these correlations were analyzed with an azimuthal-angle correction using the Monte Carlo simulation.

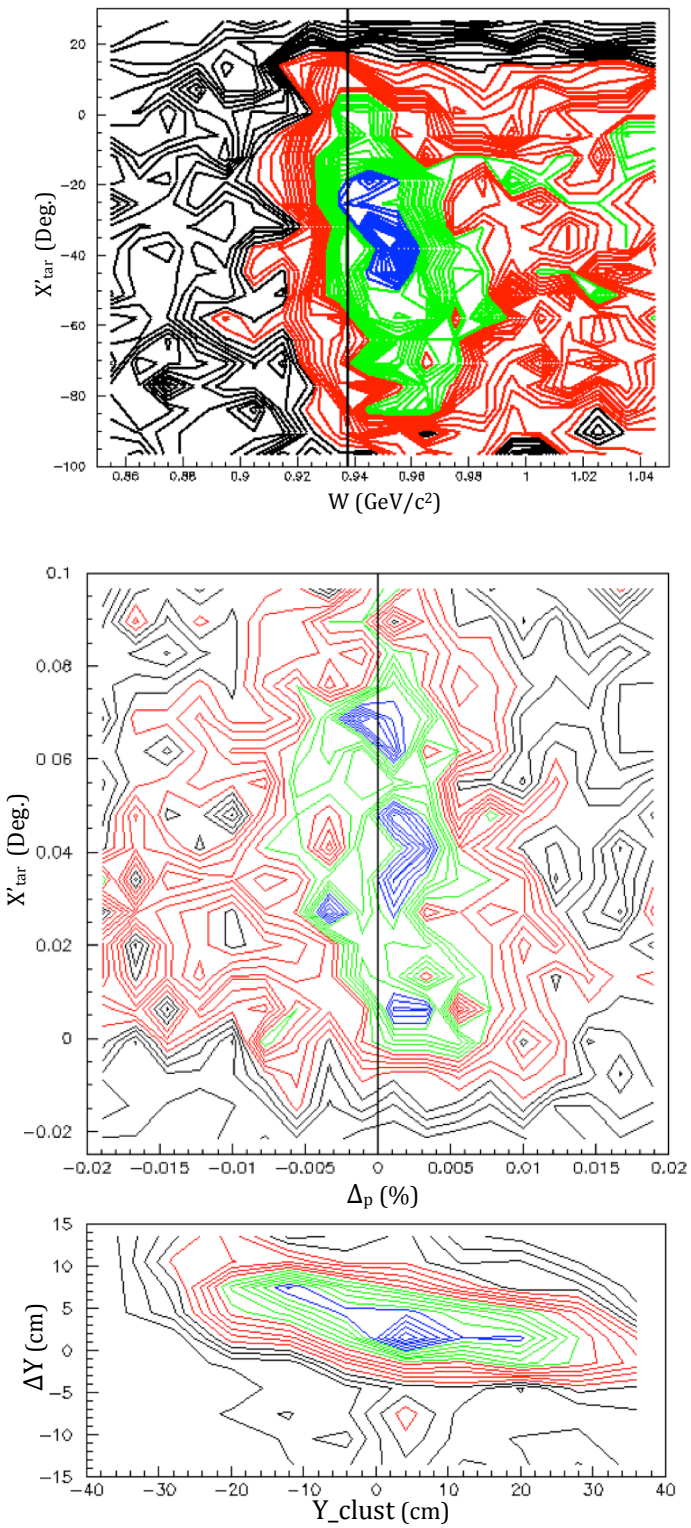

Figure 4.26. The correlation of reconstructed out-of-plane angle, X'_{tar} with the invariant mass, W in single-arm data (*top*) together with the correlation of the HMS quantities X'_{tar} vs Δ_p (*middle*) and a correlation of the BETA quantities, ΔY vs Y_{clust} (*bottom*) in the coincidence data. The variable Δ_p is the relative momentum difference as discussed in Section 4.4.2.1.

4.6.1 Azimuthal-Angle Correction

The target magnetic field has not been mapped in detail. The analysis at first assumed it is cylindrical around the target. All scattered particles would travel the same radial distance through the field, exposed to the same field integral $\int B \cdot dl$. But in reality, the target magnetic field might not be symmetric around the target and it might have some azimuthal-angle (out-of-plane) dependence. This allows the particles to have different $\int B \cdot dl$, depending on the out-of-plane angle, and therefore, undergo different deflections. The validity of this assumption was checked and confirmed with the Monte Carlo simulation. Two new parameters, $\Delta\phi_0$ and $d\phi_0$ are defined as,

$$\begin{aligned} B_{corr} &= (\theta_{azim} - \Delta\phi_0) \times d\phi_0 \\ B_{scale} &= \frac{B_0}{B_0 + abs(B_{corr})}, \end{aligned} \tag{4.6.1}$$

which shifts the out-of-plane angle of the particle, θ_{azim} by an amount of $\Delta\phi_0$, and a target magnetic field gradient of $d\phi_0$ corrects the magnetic field strength at the new vertical angle of $(\theta_{azim} - \Delta\phi_0)$. B_{scale} is the rescaling factor by which the magnetic field is multiplied after introducing the magnetic field correction, B_{corr}. Then the target magnetic field is modified as,

$$\begin{aligned} B(3) &= B(3) + B_{corr} \\ B(3) &= B(3) \times B_{scale} \\ B(1) &= B(1) - B_{corr} \\ B(1) &= B(1) \times B_{scale}, \end{aligned}$$

where $B(3)$ is the field magnitude along the magnetic field Z direction at 80° to the beam Z axis, and $B(1)$ is the X component of the magnetic field pointing downward. The horizontal component, B(2), is pointing left of the target field Z and is not affected by the field vertical angle. Applying this correction only for the forward

direction of the Monte Carlo simulation, the parameters $\Delta\phi_0$ and $d\phi_0$ were adjusted so that the MC generates the same correlation of X'_{tar} vs W as the data shows.

During the data analysis, particle tracks are reconstructed by assuming we know all of the processes which particles undergo from the scattering at the target to the focal plane through the detectors. Using an azimuthal-angle correction for the forward direction and using the same reconstruction as the data does for the backward direction on MC, is an effort to understand the target magnetic field, the particles have passed through in forward direction during the experiment. Figure 4.27 (*left*) shows the X'_{tar} vs W correlation generated by the simulation at $\Delta\phi_0 = 0.06°$ and $d\phi_0 = -0.6$ T/deg. Once the correct $\Delta\phi_0$ and $d\phi_0$ parameters were determined, the azimuthal-angle correction is used in the reconstruction of the experimental data. Figure 4.27 (*right*) shows the plot of X'_{tar} versus W for data after using the correction, indicating that the correlation has disappeared.

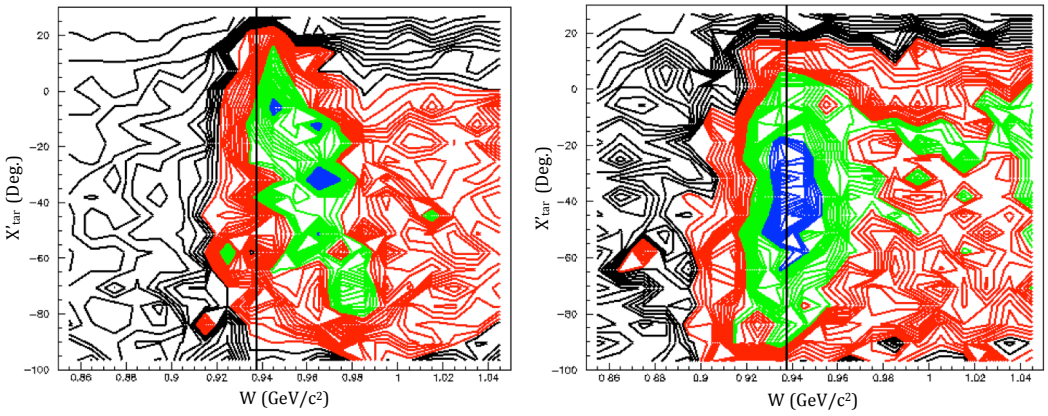

Figure 4.27. Monte Carlo simulated correlation to determine the correction (*left*) and the measured data after using the azimuthal-angle correction (*right*).

For the data taken in coincidence mode, the proton is detected in the HMS at a similar central angle like that of the inclusive electron data. Therefore, assuming the azimuthal-angle correction for HMS in positive polarity is the same as for negative polarity, the correlation of X'_{tar} vs Δ_p was tested in a similar manner with the Monte

Carlo simulation. Figure 4.28 (*left*) shows the simulated correlation after applying the above azimuthal-angle correction only for the forward direction which gives an equivalent correlation as the coincidence data shows in Figure 4.26 (*right-top*). Applying this correction to the reconstructed proton data removes the correlation as shown in Figure 4.28 (*right*). Therefore, the same azimuthal-angle correction from HMS in negative polarity is used for HMS in positive polarity, too.

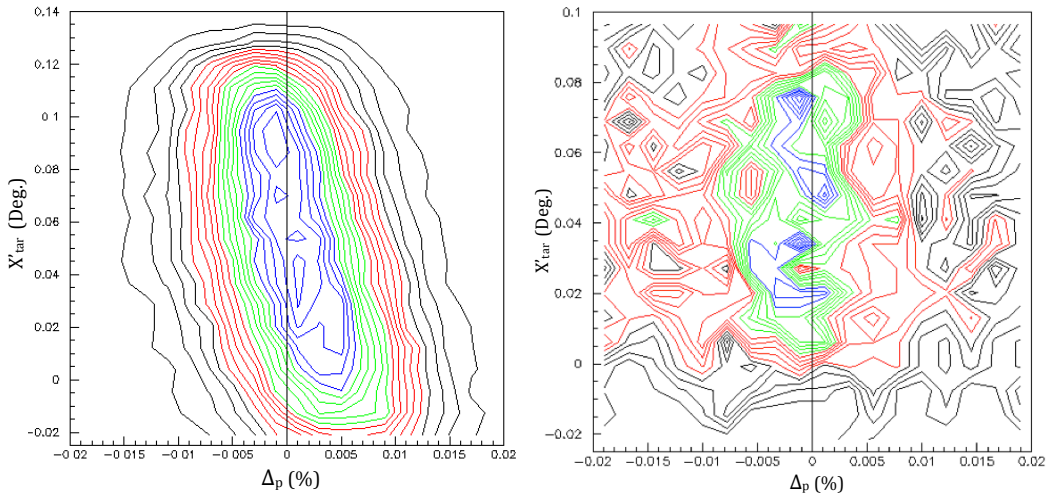

Figure 4.28. The simulated correlation of X'_{tar} vs Δ_p (*left*) after applying the azimuthal-angle correction only for the forward direction and the corrected coincidence data (*right*).

However, scattered electrons were detected by BETA, which is at the central angle of 40° left to the incoming electron beam in coincidence with the proton detected by HMS. These electrons need different $\Delta\phi_0$ and $d\phi_0$ parameters to correct the azimuthal-angle effect of the target magnetic field. These parameters were determined using the same method as for the HMS spectrometer by looking at the correlation of BETA detector quantities, ΔY vs Y_{clust}. From the BETA arm, the only considerations were the measured X and Y, (X_{clust}, Y_{clust}) positions and the predicted X and Y, (X_{HMS}, Y_{HMS}) positions of the electrons at BigCal. Therefore, the azimuthal-angle correction is applied to the predicted values of X and Y. First, both forward and

backward azimuthal-angle corrections on HMS (the proton arm) in the simulation is turned ON and then the $\Delta\phi_0$ and $d\phi_0$ parameters for BETA (the electron arm) are changed until the simulated correlation ΔY versus Y_{clust} becomes the same as for the measured data as in Figure 4.26 (*right-bottom*). The simulated correlation is shown in Figure 4.29 (*top*) and the corrected coincidence data are shown in Figure 4.29 (*bottom*).

The success of this method proves that the azimuthal-angle correction assumption is a good way to correct all of the correlations seen in both single-arm and coincidence data.

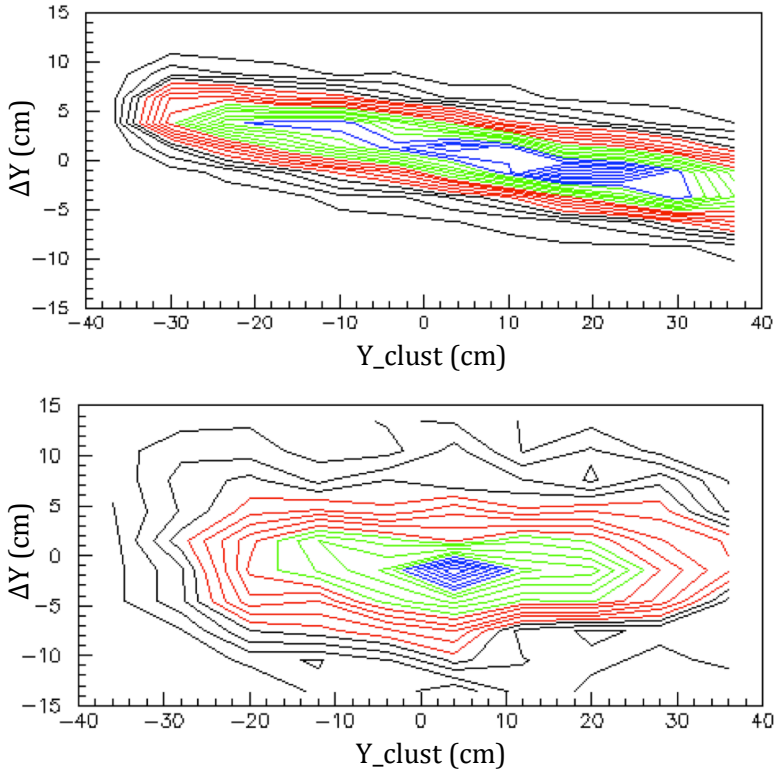

Figure 4.29. The simulated correlation of ΔY vs Y_{clust} after applying the azimuthal-angle correction only for the forward-direction (*top*) and the corrected-coincidence data (*bottom*) at $\Delta\phi_0 = -0.15°$ and $d\phi_0 = -0.4$ T/deg.

4.7 Raw Asymmetry Calculation

To generate experimental asymmetries, first the raw asymmetry is produced using the experimental raw yields. This was done for the single-arm data and the coincidence data separately. Because the single-arm data have much higher statistics compared to the coincidence data, the raw asymmetry for the single-arm data was produced as a function of W. The software loops through all of the events of all of the single-arm electron data runs, and after passing the electron selection cuts defined in Sections 4.4.1.2 and 4.4.1.3, the positive and negative beam helicity were summed separately for each W bin from 0.7 to 1.1 GeV/c^2 in 0.1 GeV/c^2 intervals. Then the measured asymmetry, A_r,

$$A_r = \frac{N_+ - N_-}{N_+ + N_-}$$

is calculated. Here, N_+ and N_- are the positive and negative helicity yields for a given target polarization, which is positive (target polarization is in the same direction as the applied target magnetic field) or negative (target polarization is in the opposite direction as the applied target magnetic field). Because the single-arm elastic data were collected using both *top* and *bottom* NH_3 targets, the raw asymmetries were calculated separately for the two targets. Further, these data were analyzed separately for the two HMS momentum acceptance regions as mentioned in Section 4.4.1.3; the single-arm raw asymmetries were calculated separately for the two δ regions.

In contrast, the coincidence data were taken at higher Q^2 and have low statistics. Therefore, instead of calculating the measured asymmetries as a function of W, all the coincidence runs were separated to a few categories at first, the data taken from top and bottom targets, positive and negative beam and target polarizations for each target cup, and so on. After looping over all of the events within each category and summing all of the positive and negative helicity yields which passed through the coincidence event selection cuts as in Section 4.4.2.3, the raw asymmetry, A_r was

calculated. This was done separately for the two-beam energies. However, all of these helicity yields need to be corrected for the correct accumulated beam charge and lifetimes.

4.7.1 Charge Normalization

Although the helicity flips of the beam polarization provide approximately the same number of electrons to the target for each helicity state, still an unequal number of electrons on the target can introduce a false asymmetry affecting the results. Charge normalization is performed to counteract this effect. Therefore, the charge-normalized raw asymmetry, A_{rc} is calculated as,

$$A_{rc} = \frac{N_+/C_+ - N_-/C_-}{N_+/C_+ + N_-/C_-}$$

for the charge accumulated on the target from the positive and negative helicity states are C_+ and C_- respectively. These C_+ and C_- are read from the helicity scalers in the EPICS data file for each run.

4.7.2 Lifetime Normalization

The trigger supervisor accepts triggers to record events. Then the data acquisition starts recording the events and takes finite time to process it, which keeps the DAQ busy. Triggers accepted by the trigger supervisor during this busy time cannot be recorded and hence these events get lost. The number of events recorded for each helicity state needs to be corrected for the lost events. This is called *dead time correction* [195]. This can be normally done by calculating the computer dead time for each helicity state using the ratio of total accepted trigger events to the total recorded trigger events as recorded by the scalers. But unfortunately, the total recorded positive trigger scaler information was not available during the experiment. It has been

estimated by assuming that the relative dead time for positive and negative polarity has been equal. By fitting the linear correlation of the accepted negative helicity triggers to the total recorded negative helicity triggers that we have from the scaler information, the total recorded positive triggers were determined using the total accepted positive triggers. This was done and implemented for all the data by SANE collaborators H. Baghdasaryan and H. Kang.

The charge and lifetime-corrected raw asymmetries were calculated separately for the two data sets of single-arm and coincidence are shown in Figure 4.30.

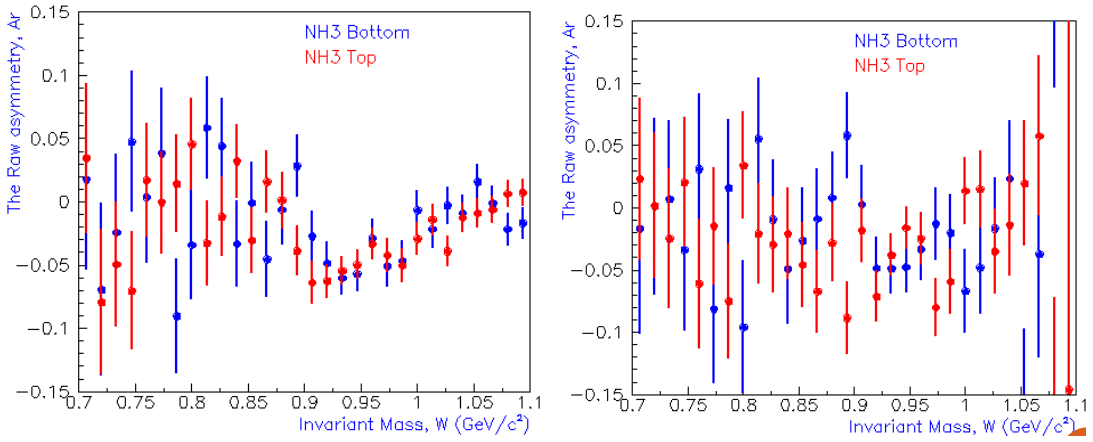

Figure 4.30. The charge and lifetime-corrected raw asymmetries for δ regions of $-8\%<\delta<10\%$ (*left*) and $10\%<\delta<12\%$ (*right*) for all single-arm data for top (red) and bottom (blue) targets.

The raw asymmetries for each category of the coincidence data for both beam energies are shown in Figure 4.31. It shows that all of the data from the beam energy 4.73 GeV fell into only two categories, *i.e.*, positive and negative beam polarization. They all were taken with the bottom target with positive beam polarizations.

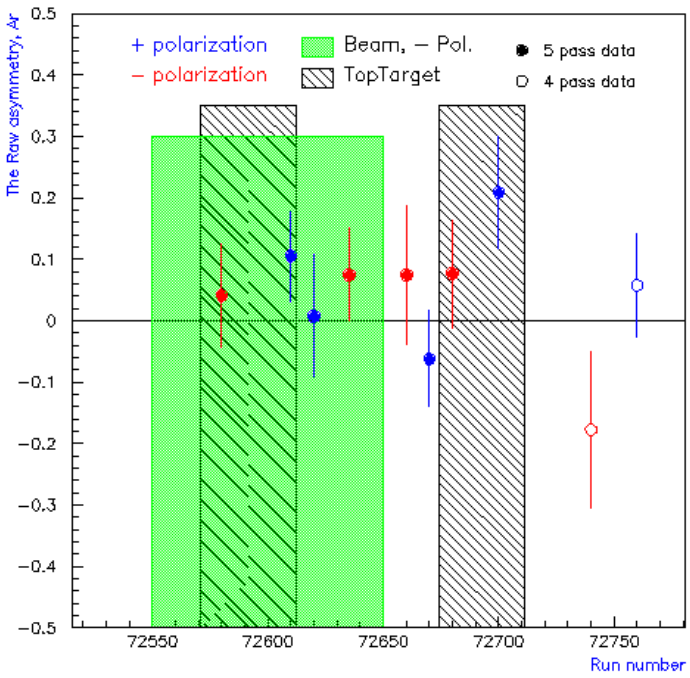

Figure 4.31. The raw asymmetries for each category for the coincidence data. Solid circles show the data from 5.895 GeV beam energy while the empty circles show those at 4.73 GeV beam energy. The X axis shows the run numbers.

4.8 Physics Asymmetry Calculation

After the lifetime and charge normalization have been applied to the raw asymmetries, the physics asymmetry is calculated by,

$$A_p = \frac{A_{rc}}{P_B P_T f} + N_c,$$

where P_B and P_T are the beam and target polarizations, and f is the dilution factor. The N_c term is a correction to the measured asymmetry that eliminates the contribution from quasi-elastic scattering off polarized ^{15}N under the elastic peak. Because SANE used $^{14}NH_3$(ammonia), the correction by N_c for ^{14}N is negligible but of opposite sign as for ^{15}N [52].

Each run is analyzed individually by normalizing the charge-weighted average beam and target polarizations obtained by the Mϕller and target polarization determinations as discussed in Sections 3.1.3 and 3.4.1. Figure 4.32 shows the beam and absolute target polarization reached during the experiment.

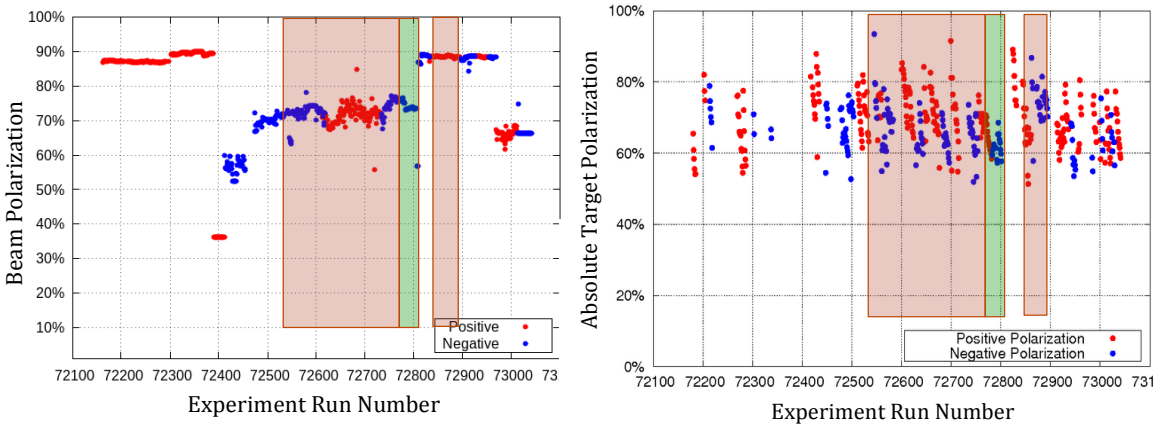

Figure 4.32. The beam polarization (*left*) and the absolute-target polarization (*right*) reached during the experiment. The red box shows the polarizations during the coincidence runs and the green box shows the polarizations during the single-arm electron runs while the red (blue) markers show the positive (negative) polarizations.

Cuts on the beam polarization >60% and the absolute target polarization >55% were applied in the physics asymmetry extraction.

The dilution factor, f is a crucial part in the extraction of the physics asymmetries. The following sections will discuss the determination of f in detail.

4.8.1 Determination of the Dilution Factor

The dilution factor is the ratio of free polarizable protons to the total rates from all other nucleons in the target material. Using polarized NH_3 in a liquid He bath as a polarized proton target, scattering from the unpolarized N, He and Al materials dilutes the $e-p$ scattering asymmetries which require the correction of the dilution

factor to the raw asymmetries. Therefore, the dilution factor can be defined as,

$$f = \frac{Yield_H}{Yield_{(H+N+He+Al)}}.$$

Determination of the dilution factor has been done separately for the single-arm and coincidence data using comparisons of data to simulation yield.

4.8.1.1 Dilution Factor for Single-Arm Data

The single-arm Monte Carlo simulation discussed in Section 4.5.5 was used to determine the dilution factor for the single-arm data. All data were collected using both *top* and *bottom* targets, which have different packing fractions and hence different dilution factors. Two runs, 72790 for the bottom target and 72795 for the top target, were selected to compare with the simulated yields and to determine the dilution factors for the two different target cups. Further, as discussed in Section 4.4.1.3, the data were analyzed separately for the two δ regions for which the dilution factors were also determined for the two δ regions separately. Figure 4.23 shows the Monte Carlo simulated contributions for each target type compared to the total data for two different δ regions separately for the top target using run 72795. Since the total MC and data agree well with each other as shown in the plot, this is the best way to determine the background contributions in the data. The dilution factor has been calculated by taking the ratio of the background subtracted elastic to the total raw yield:

$$f = \frac{Yield_{data} - MC_{(N+He+Al)}}{Yield_{data}}. \tag{4.8.1}$$

Since the low W region is dominated by the unpolarized materials of N, He and Al, the normalization of the MC yields has been done by calculating the scaling factor for the W region of $0.7<W<0.85$ GeV/c^2 using the ratio-of-data to MC yield. Then a polynomial fit of the normalized background (N, He and Al) for the region of

$0.7<W<1.1$ GeV/c^2 is subtracted from total data which includes the contributions from H, N, He and Al, resulting in the free H contribution to the data. The total data and the total simulated MC, the simulated background with the polynomial fit and the background subtracted elastic peak as a function of W for the two δ regions are shown in Figure 4.33. The calculated dilution factor as a function of W is shown in Figure 4.34.

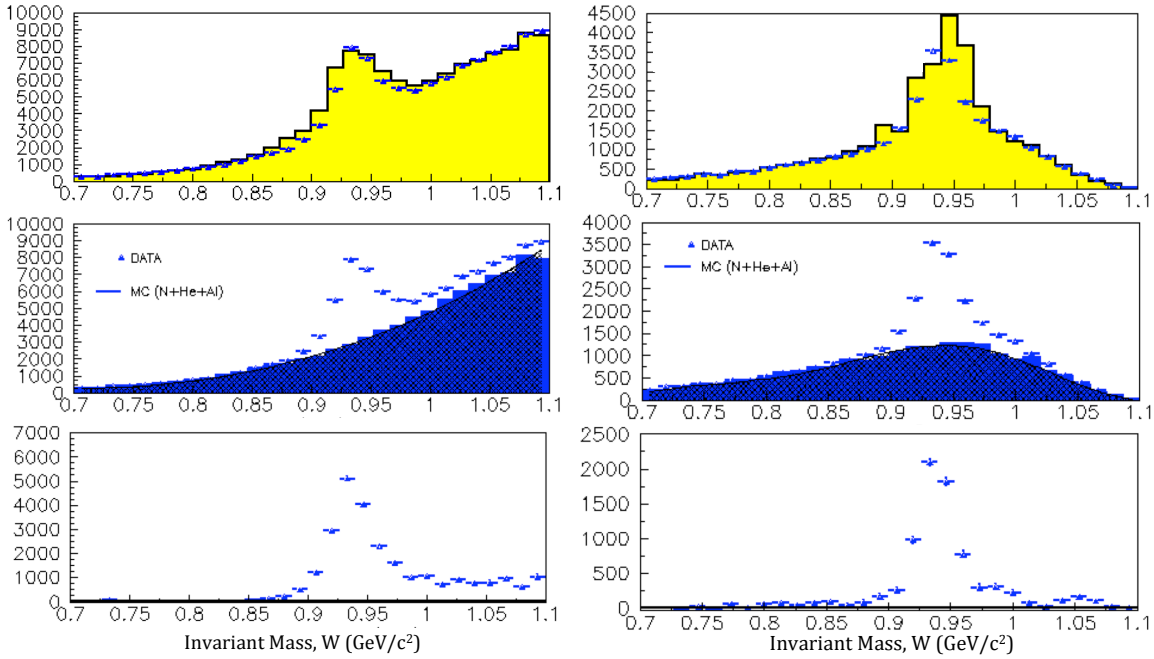

Figure 4.33. The total data and the total simulated MC (*top*), the simulated background with the polynomial fit (*middle*) and the background-subtracted elastic peak (*bottom*) for the two δ regions $-8\%<\delta<10\%$ (*left*) and $10\%<\delta<12\%$ (*right*) for the top target using run 72795.

Similarly, the MC contributions to the total data for different target types are shown in Figure 4.35 for the bottom target using the NH_3 run 72790. Following the same procedure for run 72795 shown above, the dilution factor was also calculated for the bottom target as a function of W. Figure 4.36 shows the relative dilution factors calculated for both *top* and *bottom* targets for the two different δ regions.

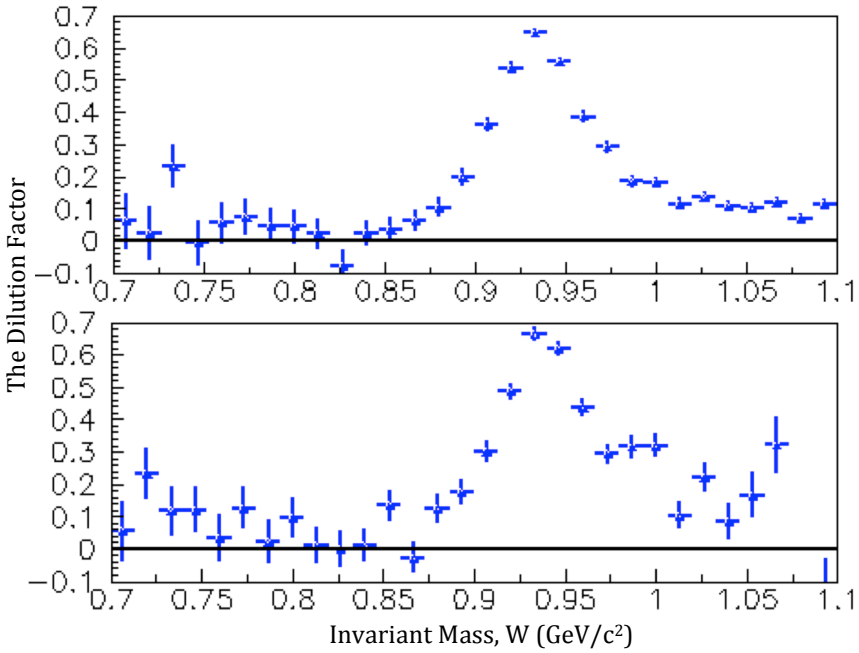

Figure 4.34. The calculated dilution factor for $-8\%<\delta<10\%$ (*top*) and $10\%<\delta<12\%$ (*bottom*) for the top target using run 72795.

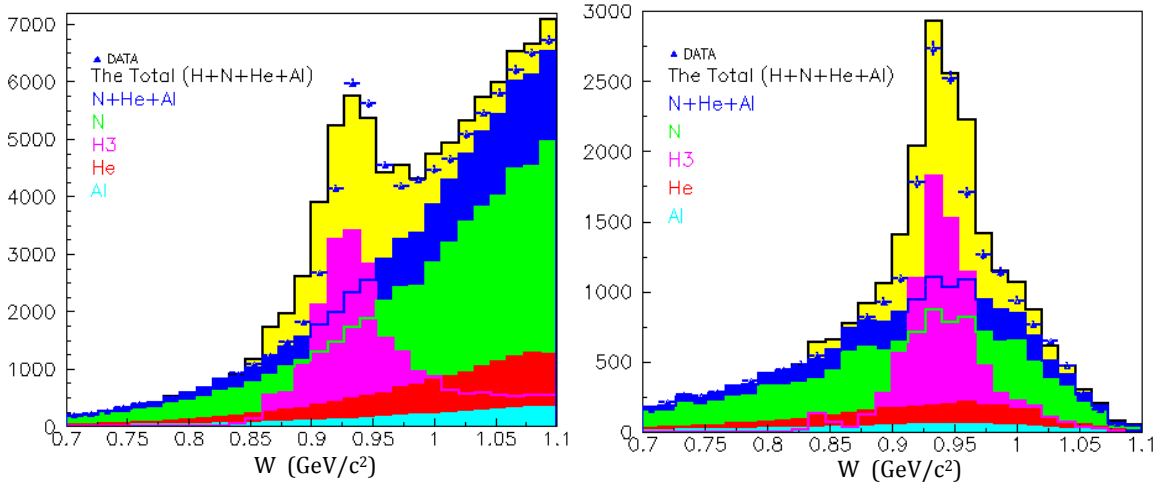

Figure 4.35. The simulated target contributions at the elastic peak compared to the data at both δ regions, $-8\%<\delta<10\%$ (*left*) and $10\%<\delta<12\%$ (*right*) for the bottom target using experiment run 72790. Different colors show different target type contributions.

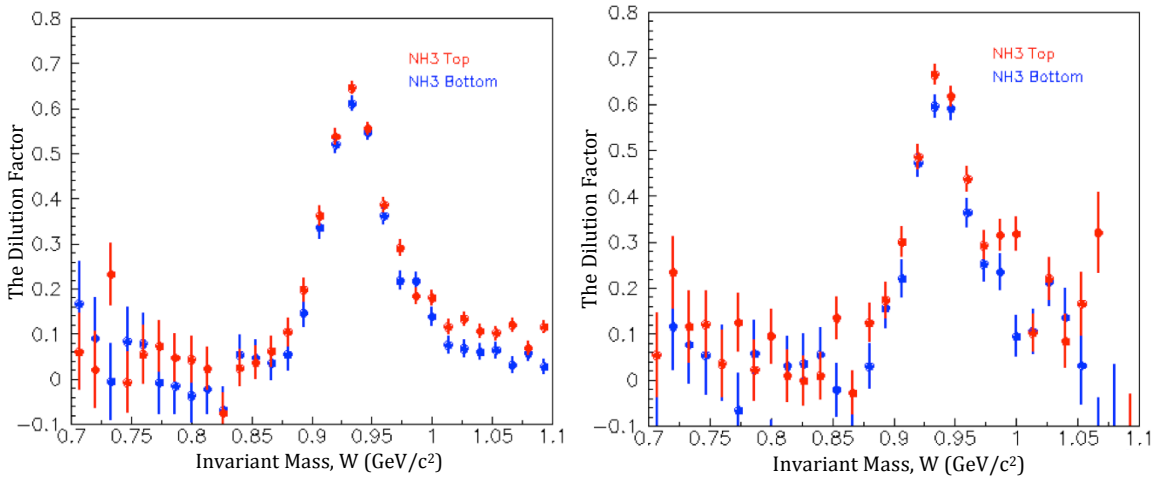

Figure 4.36. The relative dilution factors calculated for both top (*red*) and bottom (*blue*) targets for the two different δ regions $-8\%<\delta<10\%$ (*left*) and $10\%<\delta<12\%$ (*right*).

The total number of elastic events were determined after subtracting the MC background from the data separately for the two different δ regions and were found as $\sim 1.4 \times 10^4$ elastic events for $-8\%<\delta<10\%$ and $\sim 0.5 \times 10^4$ elastic events for $10\%<\delta<12\%$. Therefore, using the higher δ region of $10\%<\delta<12\%$ has gained extra events of about $\sim 40\%$.

The dilution factor is zero and flat for $W<0.85$ GeV/c^2, indicating that the $N + He+Al$ background shape is matched well with data in this region after normalizing all inelastic MC contributions by a constant scaling factor. The dilution factor increases with W and reaches its maximum at the proton mass of 0.938 GeV. It then starts to drop off to nearly a constant value of 0.1 for $W>1.0$ GeV/c^2. The raw asymmetry, A_{rc} calculated for each W bin of a width of 0.13 GeV/c^2 from 0.7 to 1.1 GeV/c^2 were normalized with these dilution factors as a function of W.

Normalizing $A_{rc}/P_B/P_T$ with the dilution factor as a function of W for top and bottom targets separately results in the physics asymmetry, A_p. Figure 4.37 (*left*) shows the top and bottom physics asymmetries for the two different δ regions.

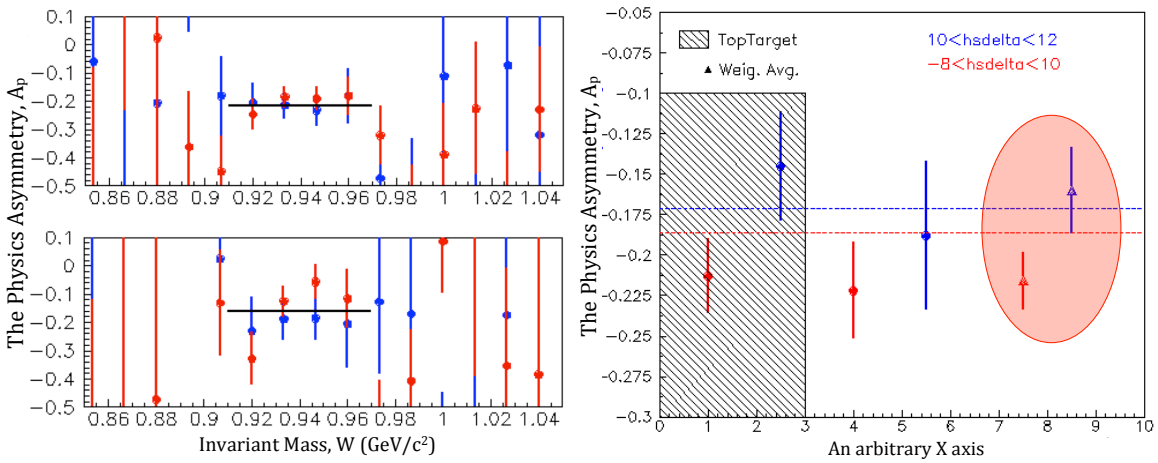

Figure 4.37. (*Left*): The top and bottom target physics asymmetries for the two different delta regions $-8\%<\delta<10\%$ (*top*) and $10\%<\delta<12\%$ (*bottom*). (*Right*): The constant physics asymmetries for both top (inside the hatched box) and bottom (outside the hatched box) targets and the weighted average of it (inside the ellipse) for two different δ regions. The expected physics asymmetries from the known form factor ratio for each Q^2 by Kelly's form factor parametrization [50] are also shown by dashed lines separately for the two different δ regions.

For $W<0.91$ GeV/c^2, the dilution factor f is much smaller with large error bars resulting in the A_p with very large error bars. At $0.91<W<0.97$ GeV/c^2, A_p is constant and the error bars are smaller due to the larger f and smaller error bars on f. For $W>0.97$ GeV/c^2, in the elastic radiative tail, A_p is again resulting in larger error bars. The physics asymmetries and their errors for both targets were determined by using a linear fit in the region of $0.91<W<0.97$ GeV/c^2, where A_p is constant. Then the weighted average physics asymmetry and error were obtained by combining the top and bottom asymmetries for both δ regions; the results are shown in Figure 4.37 (*right*) referring to Table 4.9.

Table 4.9. Physics asymmetries for the top and bottom targets and the weighted average for both δ regions for the single-arm data.

$A_p \pm \Delta A_p$	$-8\%<\delta<10\%$	$10\%<\delta<12\%$
Top Target	-0.213 ± 0.023	-0.145 ± 0.034
Bottom Target	-0.222 ± 0.030	-0.188 ± 0.046
Weighted Average	-0.216 ± 0.018	-0.160 ± 0.027

4.8.1.2 Dilution Factor for Coincidence Data

The dilution factor for the coincidence data were also determined using the data-to-Monte Carlo simulation comparison. The background shape under the elastic peak for the coincidence data was generated using the carbon target. The simulated carbon background was then normalized by the scaling factor determined, using the ratio of data-to-SIMC yields for the region of $0.03<\delta p/p<0.08$ where the data and the simulated carbon background match each other. By adding this normalized carbon background to the SIMC-simulated H, a better match between the total data and SIMC-simulated $H+C$ can be seen in Figure 4.38. Because the coincidence data were taken for two beam energies of 5.89 GeV and 4.73 GeV, this background simulation is done separately for both energies.

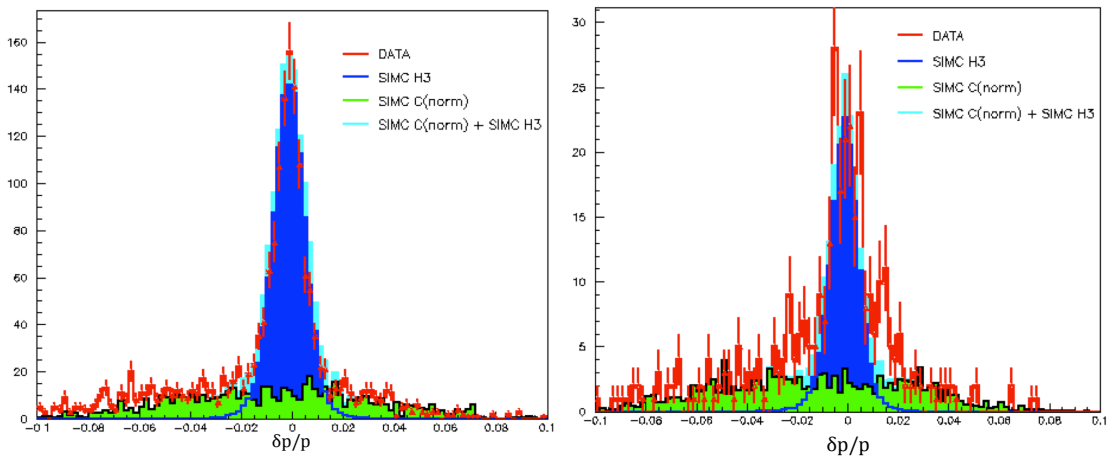

Figure 4.38. The normalized carbon background and H comparison with the coincidence data for the beam energy 5.89 GeV (*left*) and 4.73 GeV (*right*).

Subtracting the normalized carbon background from the experimental data and taking the ratio of the resulting yields to the total data determines the dilution factor as,

$$f = \frac{Yield_{data} - SIMC_{(C)}}{Yield_{data}}. \tag{4.8.2}$$

The coincidence data were also taken using both *top* and *bottom* targets. Therefore, it is needed to determine the dilution factors for the two target cups separately.

However, due to low statistics, it is harder to normalize the raw asymmetry, A_{rc} with the dilution factor bin-by-bin as a function of $\delta p/p$ in a similar way as for the single-arm data discussed in Section 4.8.1.1. Instead, an average dilution factor was calculated using an integration method. Figure 4.39 shows the data and SIMC carbon background used to calculate the dilution factor with the integration method for the top (*left*) and bottom (*right*) targets for the beam energy 5.89 GeV.

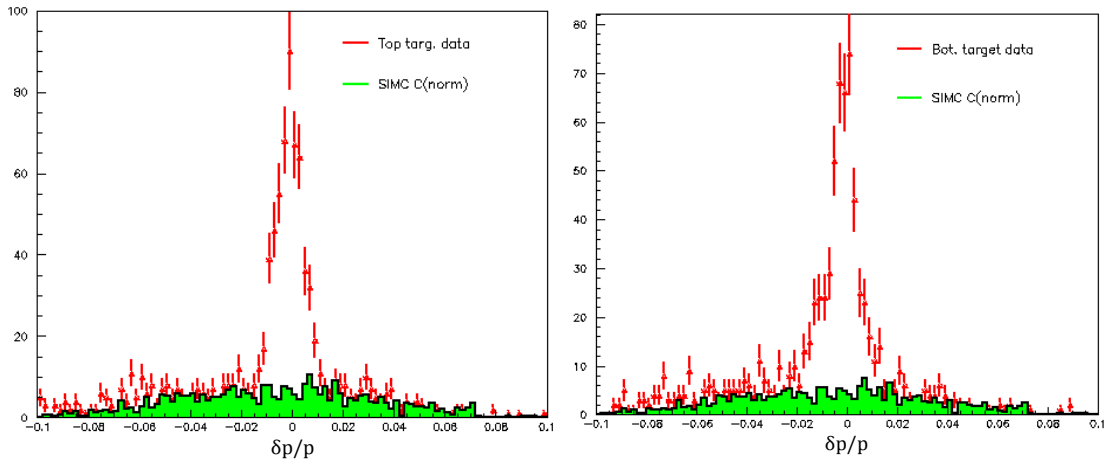

Figure 4.39. The data and SIMC carbon background used to calculate the relative dilution factor using the integration method for the top (*left*) and bottom (*right*) targets for the beam energy 5.89 GeV.

This determines the integrals of both the normalized carbon MC and the measured counts under the elastic peak over the $\delta p/p$ region with a narrower cut of ± 0.02 for both targets. The dilution factor is then calculated using Equation 4.8.2. However, the 4.73 GeV data has much lower statistics than the 5.895 GeV data. Therefore, for

these data, both top and bottom targets were considered as one target. The dilution factors calculated from the integration method for the top and bottom targets for the 5.895 GeV beam energy is determined as 0.785 and 0.830, respectively, while that for the 4.73 GeV beam energy is determined as 0.816.

Then the beam and target polarization normalized raw asymmetries, $A_{rc}/P_B/P_T$ are again normalized with the calculated dilution factors, and the physics asymmetries, A_p were obtained for each category of data. Figure 4.40 shows the extracted physics asymmetries for different categories for both beam energies. The weighted average physics asymmetries and their errors were calculated for the two beam energies as $A = -0.006 \pm 0.077$ for the beam energy of 5.893 GeV, and $A = 0.184 \pm 0.136$ for the beam energy of 4.725 GeV. These results are also shown in the same Figure 4.40.

4.9 Extraction of G_E^p/G_M^p Ratio

The beam-target asymmetry, A_p for elastic electron-proton scattering is directly related to the proton elastic form factor ratio, G_E^p/G_M^p according to Equation 2.1.22. Kinematics variables, a, b and c are introduced to simplify Equation 2.1.22 as,

$$A_p = \frac{-br \sin\theta^* \cos\phi^* - a\cos\theta^*}{r^2 + c}, \tag{4.9.1}$$

where $r = G_E^p/G_M^p$, and θ^* and ϕ^* are the polar and azimuthal-angles between the momentum transfer vector, $\vec{q}$ and the proton's spin vector. The kinematic factors are given by,

$$\begin{aligned} a &= 2\tau \tan\frac{\theta_e}{2}\sqrt{1+\tau+(1+\tau)^2\tan^2\frac{\theta_e}{2}} \\ b &= 2\tan\frac{\theta_e}{2}\sqrt{\tau(1+\tau)} \\ c &= \tau + 2\tau(1+\tau)\tan^2\frac{\theta_e}{2} \end{aligned} \tag{4.9.2}$$

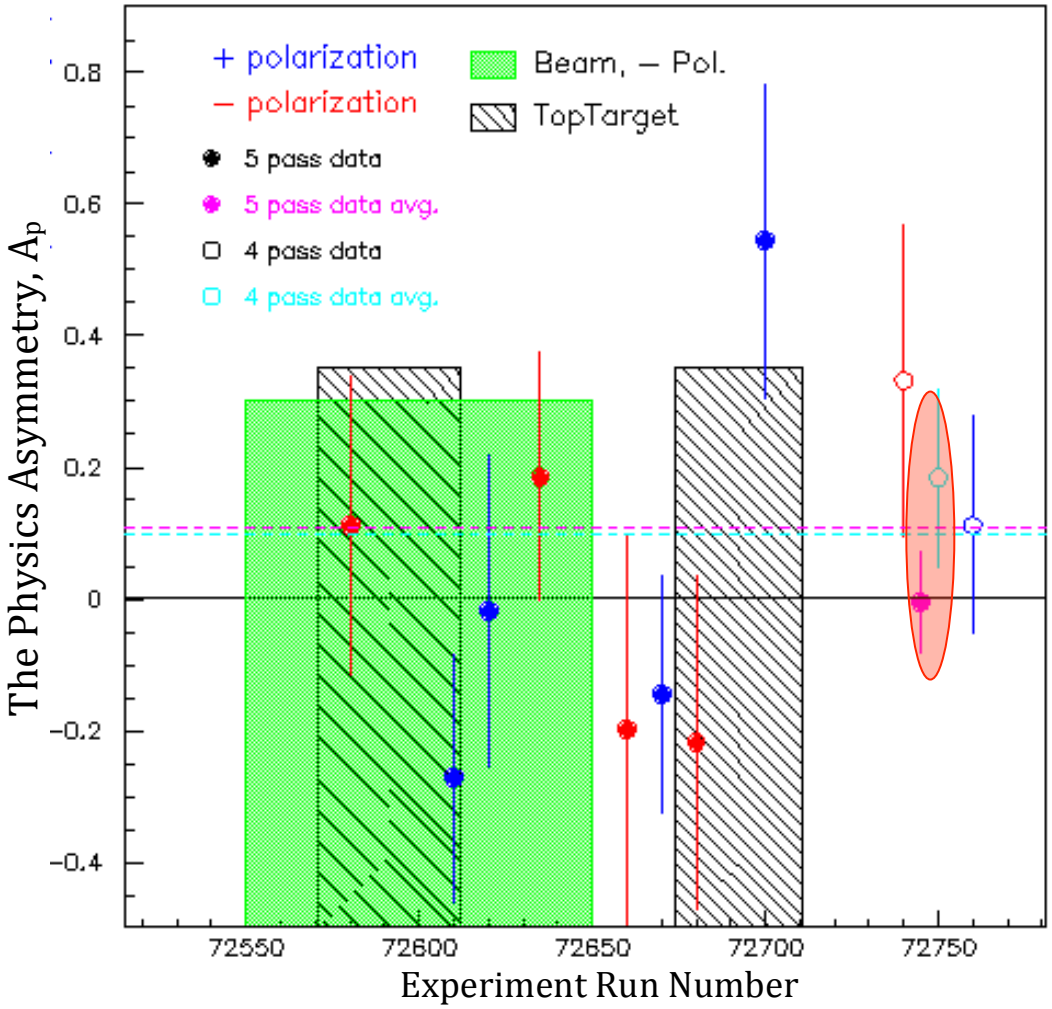

Figure 4.40. The physics asymmetries for each category of the coincidence data. The solid circles show the data from 5.895 GeV beam energy while the empty circles show those at 4.73 GeV beam energy. The X axis shows the run numbers. The weighted average physics asymmetries and their errors for the two beam energies are also shown (inside the brown ellipse). The dashed lines are at the expected values of the physics asymmetries for the two beam energies 4.73 GeV (light blue) and 5.893 GeV (magenta) calculated from the known form factor ratio for each Q^2 by Kelly's form factor parametrization [50].

with $\tau = \frac{Q^2}{4M^2}$.

The four-momentum transfer squared, Q^2 was calculated by using all three elastic electron variables, incoming electron beam energy, E; scattered electron energy, E'; and the scattered electron angle, θ_e. The $Q^2(E, E', \theta_e)$ calculated only from the elastic events were extracted by comparing with the Monte Carlo simulation yields. Figure 4.41 shows the data-to-simulation yield comparison of $Q^2(E, E', \theta_e)$ for two δ regions.

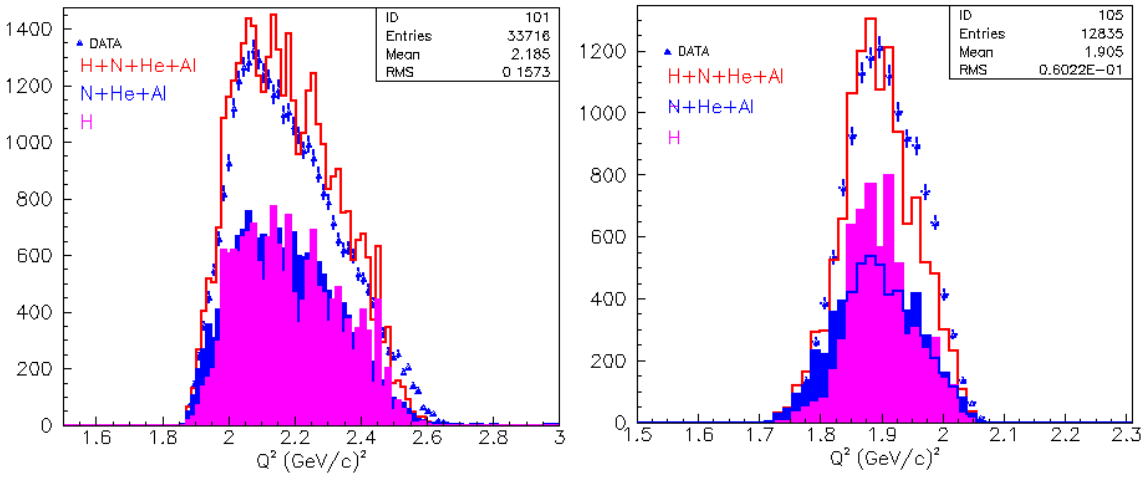

Figure 4.41. The data (blue markers) to Monte Carlo simulation yields (red) comparison of $Q^2(E, E', \theta_e)$ for the two δ regions $-8\%<\delta<10\%$ (*left*) and $10\%<\delta<12\%$ (*right*). The simulated signal H and background (N+He+Al) yields are also shown.

Because the simulated yields and data are matched very well after applying all of the elastic event selection cuts on both data and MC yields, the simulated background yields were subtracted from the data and the resulting Q^2 distribution is shown in Figure 4.42 for both δ regions. The mean values of Q^2 read from Figure 4.42 are $Q^2 = 2.20$ (GeV/c)^2 for the region $-8\%<\delta<10\%$, and $Q^2 = 1.91$ (GeV/c)^2 for the region $10\%<\delta<12\%$.

Using the elastic kinematic relations, E' can be calculated by θ_e and vice-versa. Therefore, $Q^2(E, E')$ and $Q^2(E, \theta_e)$ were also determined in addition to $Q^2(E, E', \theta_e)$ as a cross check. After applying all of the elastic event selection cuts on $Q^2(E, E')$

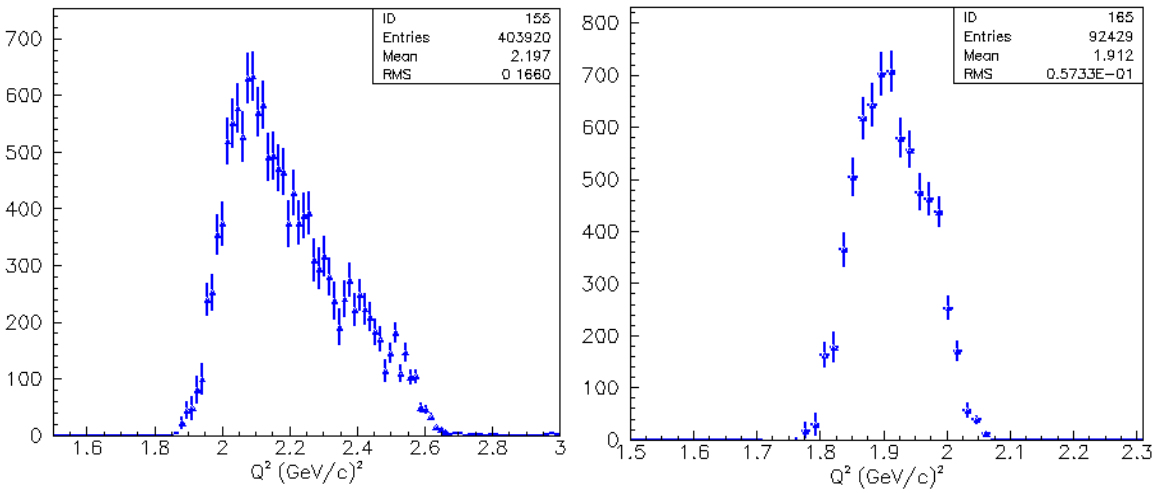

Figure 4.42. The simulated background subtracted $Q^2(E, E', \theta_e)$ distributions for the two δ regions $-8\%<\delta<10\%$ (*left*) and $10\%<\delta<12\%$ (*right*).

and $Q^2(E, \theta_e)$, the mean values were the same as in $Q^2(E, E', \theta_e)$. Therefore, the above mentioned $Q^2(E, E', \theta_e)$ were used for the G_E/G_M extraction.

The mean of the measured electron scattering angle on HMS, θ_e was determined by applying all of the electron selection cuts together with $0.9<W<1.0$ GeV/c^2 for the single-arm data.

The polar and azimuthal-angles, θ^* and ϕ^* are calculated as,

$$\begin{aligned} \theta^* &= \arccos(-\sin\theta_q \cos\phi_e \sin\beta + \cos\theta_q \cos\beta) \\ \phi^* &= -\arctan\left(\frac{\sin\phi_e \sin\beta}{\cos\theta_q \cos\phi_e \sin\beta + \sin\theta_q \cos\beta}\right) + 180^\circ. \end{aligned} \tag{4.9.3}$$

The out-of-plane angle of the scattered electron defined as ϕ_e is further increased by bending downward due to the target magnetic field. The average ϕ_e is estimated by reading the mean value of the measured ϕ_e distribution for the elastic events. The three-momentum transfer vector, $\tilde{\mathbf{q}}$ points at an angle of θ_q, which is the scattered proton angle determined event-by-event by the elastic kinematics of the electron in HMS, and the mean value of θ_q was determined. The angle β is the target magnetic field direction, 80° to the beam Z axis toward the BETA detector package. Then

θ^* and ϕ^* can be calculated using Equation 4.9.3. The proton form factor ratio, $r = G_E^p/G_M^p$ is extracted using the physics asymmetries, A_p for both δ regions for the single-arm data. Equation 4.9.1 has two solutions for G_E^p/G_M^p. The positive value was chosen because the negative value is non physical.

The errors of the form factor ratio G_E^p/G_M^p, Δr were determined by propagating the errors of the physics asymmetry, ΔA_p. The ratios of G_E^p/G_M^p and their errors were obtained for both δ regions separately.

Figure 4.43 shows the predicted A_p for a range of Q^2 values according to the form factor parametrization [50]. Since θ_q varies with Q^2 and hence θ^* varies, the black line is the calculated A_p for known Q^2 with different θ^* calculated according to each Q^2. The different colored lines show the calculated A_p as a function of Q^2 at constant θ^* as shown in the legends. The two black data points are the experimental A_p values for the single-arm data at the two different δ regions. The figure shows that the two data points are consistent with the expected asymmetry A_p within their errors.

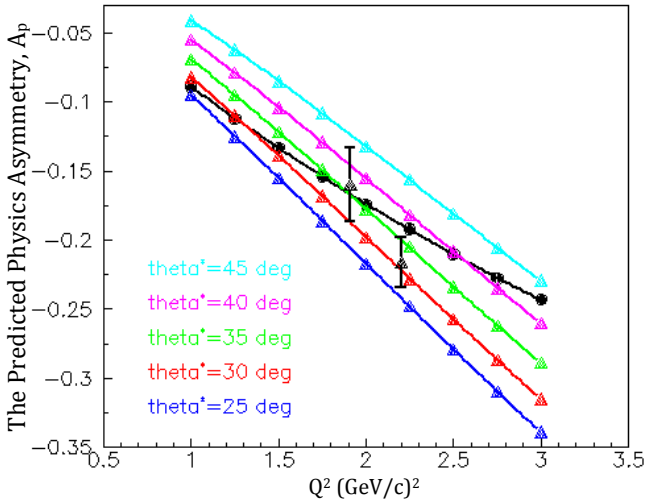

Figure 4.43. The expected physics asymmetry A_p for a range of Q^2 values [50]. The black line is the calculated A_p as a function of Q^2 for different θ^*. Different colored lines show the calculated A_p at constant θ^* as shown in the legends. The two black data points are the experimental A_p values for the single-arm data at the two different δ regions.

For the coincidence data, $Q^2(E, E', \theta_e)$ were determined by taking the mean values after applying all the coincidence event selection cuts on Q^2 for both beam energies. As protons were detected by HMS, the scattered electron angle, θ_e was calculated using elastic kinematics of the protons in HMS. Further, the mean value of θ_q is determined using the detected proton angle from HMS, and the out-of-plane angle of the electron, ϕ_e is determined requiring co-planary, $\phi_e = \phi_q + 180$, where ϕ_q is the mean value of the measured proton out-of-plane angle on HMS. The corresponding polarization angles θ^* and ϕ^* were calculated using Equation 4.9.3 and then G_E^p/G_M^p and its errors were extracted for the two beam energies.

The physics asymmetries A_p, and extracted proton form factor ratios, $r = G_E^p/G_M^p$ together with the experimental parameters for both single-arm and coincidence data are shown in Table 4.10. The extracted $\mu_p r$ ratio for both data sets are shown in Figure 4.44 together with the predicted $\mu_p r$.

Table 4.10. The physics asymmetries, and extracted form factor ratios together with the experimental parameters for both single-arm and coincidence data. The expected ratio $\mu_p r$ from Kelly's form factor parametrization [50] for each Q^2 and the calculated A_p from the above predicted $\mu_p r$ are also shown. The errors ΔA_p and $\Delta(\mu_p r)$ are statistical.

	single-arm		Coincidence	
	$-8\%<\delta<10\%$	$10\%<\delta<12\%$		
E (GeV)	5.895	5.895	5.893	4.725
θ_q (Deg)	44.38	46.50	22.23	22.60
ϕ_q (Deg)	171.80	172.20	188.40	190.90
θ_e (Deg)	15.45	14.92	37.08	43.52
ϕ_e (Deg)	351.80	352.10	8.40	10.95
Q^2 (GeV/c)^2	2.20	1.91	6.19	5.14
θ^* (Deg)	36.31	34.20	101.90	102.10
ϕ^* (Deg)	193.72	193.94	8.40	11.01
$A_p \pm \Delta A_p$	-0.216 ± 0.018	-0.160 ± 0.027	-0.006 ± 0.077	0.184 ± 0.136
$\mu_p r \pm \Delta(\mu_p r)$	0.483 ± 0.211	0.872 ± 0.329	0.937 ± 0.428	-0.052 ± 0.678
predicted $\mu_p r$	0.73	0.78	0.305	0.38
predicted A_p	-0.186	-0.171	0.107	0.097

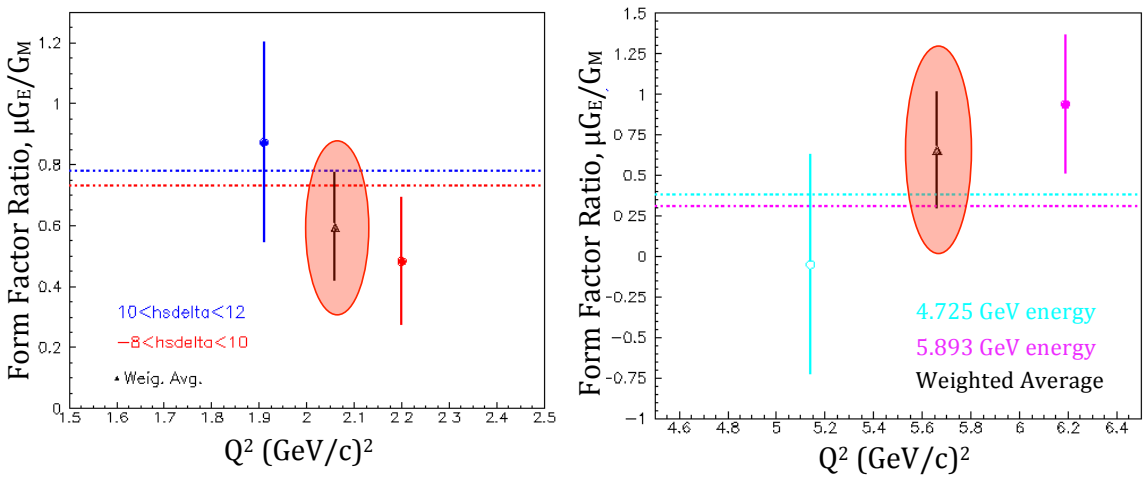

Figure 4.44. The extracted $\mu_p G_E^p/G_M^p$ ratio for the single-arm data (*left*) and for the coincidence data (*right*). The expected $\mu_p G_E^p/G_M^p$ for each data point is shown by the similar color-coded dashed lines [50].

4.10 Systematic Error Estimation

Systematic errors are uncertainties due to the experiment measurements and the experiment instruments. In contrast to the statistical error which fluctuates for each individual measurement independently of others, the systematic error is a constant for the measurements taken under the same conditions. There is no well-defined method to treat or analyze the systematic errors. In this dissertation data analysis, mostly Monte Carlo simulation was used to estimate the systematic uncertainties from different sources.

During SANE elastic data collection, HMS played the main role recording each particle momentum and angle. HMS was placed at a defined central angle and with a defined central momentum. The accuracy of both measurements depends on the accuracy of the instrument used for the measurements. The accuracy of the energy of the incoming beam also depends on the method and the instrument used to measure the beam energy. The errors arising from the kinematic quantities were estimated by varying each quantity (one at a time) by its corresponding uncertainty (0.05% for

the beam energy, 0.1% for the central momenta, and 0.5 mrad for the spectrometer angle) and propagating it to the Monte Carlo extracted G_E^p/G_M^p ratio. The resulting difference in the extracted G_E^p/G_M^p ratio from the value at the nominal kinematics is taken as the uncertainty in the G_E^p/G_M^p ratio due to the uncertainty in that quantity. In general, the uncertainties due to the kinematic variables are less than 1%.

The quantities, θ^* and ϕ^* were calculated using Equation (4.9.3), which shows that both quantities depend on the angles θ_q, β and ϕ_e. Therefore, the errors on these quantities propagate to the errors on θ^* and ϕ^*. Using the Jacobian of the elastic electron-proton reaction,

$$J = \frac{\delta\theta_p}{\delta\theta_e} = \frac{P_e}{P_p}\frac{\sin\theta_e}{\sin\theta_q}, \tag{4.10.1}$$

the error on the θ_q, $\delta\theta_q$ can be determined for the known $\delta\theta_e = 0.5$ mrad, where the angles θ_e and θ_q are the scattered electron and recoiled proton angles, respectively. The scattered electron momentum (=energy) is denoted as P_e, while the recoiled proton momentum is denoted as P_p, which can be calculated for known beam energy E and the scattered electron angle θ_e using the elastic kinematics. Hence, the error on the θ_q, $\delta\theta_q$ propagated from the beam energy E and the scattered electron angle θ_e was determined as 0.03°.

Then the uncertainty on the θ^* and ϕ^* were determined using the uncertainties on the θ_q, $\delta\theta_q = 0.03°$ and the uncertainty on the target magnetic field direction β, $\delta\beta = 0.1°$. As the final step, the uncertainty on the G_E/G_M ratio due to the uncertainty in the θ^* and ϕ^* was determined. Taking the difference between the extracted G_E/G_M ratio from the value at the nominal kinematics and that of after varying each quantity, θ^* and ϕ^* one at a time by its corresponding uncertainty, the error on the G_E/G_M from the error on the θ^* was determined as 0.54%, while that from the ϕ^* was determined as 0.01%

The systematic error on the target polarization is the largest individual contribution to the uncertainty. The accuracy of the target polarization is based on the accuracy of the calibration constants used to produce the polarization from the NMR area. The systematic error is determined by the standard deviation of the individual calibration constants for a given material sample to its mean value and was estimated as 5 % [156].

The error on the beam polarization measurement comes from a global error of the Mϕller measurements and the error due to the fit to these measurements. The beam polarization uncertainty during SANE is measured as 1.5 % [156].

The calculation of the dilution factor, f is another important source of systematic uncertainty in the extraction of the form factor ratio G_E/G_M. For both single-arm and coincidence data sets, the dilution factor has been determined using data-to-Monte Carlo simulated yield comparisons. Therefore, the uncertainty of the dilution factor is based on how well the data match with the simulated yield. Since the simulated yields are based on the packing fraction, the error of 5% (analysis has done by SANE collaborator Hoyoung Kang) in the packing fraction measurement propagates to the dilution factor. Therefore, the new packing fraction of $(pf+5)\%$ is determined by applying the error to the nominal packing fraction, pf determined by the Monte Carlo simulation as discussed in Section 4.5.5.1 as (56+5=61)%. The new dilution factor and hence the new proton form factor ratio, $\mu_p G_E^p/G_M^p$ was calculated for the new packing fraction of 61% and takes the difference with the $\mu_p G_E^p/G_M^p$ calculated from the nominal pf=56%. Hence, the uncertainty on the form factor ratio, $\mu_p G_E^p/G_M^p$ due to the 5% uncertainty on the packing fraction is identified as 1.34%.

Single-arm data used the extended momentum acceptance in the region of $10\%<\delta<12\%$, where the HMS optics are not well tested. Therefore, the reconstruction of the events from this region is not understood well and the uncertainty in the COSY model used to determine these particle tracks is a special source of systematic

uncertainty for the single-arm data. The systematic error due to this higher δ region has been tested with a Monte Carlo simulation. As mentioned in Section 4.5.1, the Monte Carlo checks all of the events at several apertures while they go from target to the detector hut. This process was used to estimate the systematic uncertainty. The number of events failed at each of these apertures were checked for the δ region of $10\%<\delta<12\%$ and found that the biggest loss of events in this δ region is at the HMS vacuum pipe exit. Particles with relatively higher momentum are less bent through the target magnetic field and the HMS dipole field where it is possible to hit the upper edge of the vacuum pipe exit and to not make it to the detector hut. In order to estimate this uncertainty, ± 2 mm offsets were used on the vacuum pipe positions on both vertical and horizontal directions separately, and the effective solid-angle differences between the offsets and those at the nominal vacuum pipe position were determined. Taking the average ratio of these effective solid-angle differences to the nominal solid angle, the uncertainty due to higher momentum electron tracks hitting the edge of the vacuum pipe exit was estimated as 0.68 %. However, during the Dilution factor determination, Monte Carlo simulated C cross-section shape match was done for data in both δ regions. Also, Monte Carlo yields were normalized with the ratio of data to Monte Carlo yields in the region $0.7<W<0.85$ GeV/c^2. Therefore, the uncertainty, 0.68 % that comes from losing events due to higher δ are already accounted in the dilution factors.

Table 4.11 summarizes non-negligible contributions to the systematic uncertainty of the single-arm data. The measurements, the uncertainty of each measurement and the relative systematic uncertainty of the $\mu_p G_E^p/G_M^p$ ratio due to the uncertainty on that measurement are shown. The final relative systematic uncertainty was obtained by summing all the individual contributions quadratically. Summing all the individual contributions of the systematic uncertainties linearly represents the maximum

possible error of the measurement. Therefore, the final relative systematic error on $\mu_p G_E^p/G_M^p$ was estimated as 5.44% while the maximum possible error was estimated as 9.13%. The target, beam polarizations and the packing fraction are the dominant contributions to the systematic uncertainty.

Table 4.11. Systematic uncertainty on each measurement and the relative systematic uncertainty on the $\mu_p G_E^p/G_M^p$ ratio due to the uncertainty on that measurement for the single-arm data. The maximum possible systematic uncertainty obtained by summing all the individual contributions linearly and the final systematic uncertainty obtained by summing all the individual contributions quadratically are also shown.

Measurement	Error	$\Delta\mu_p G_E^p/G_M^p/\mu_p G_E^p/G_M^p$ (%)
E (GeV)	0.003	0.07
E' (GeV)	0.004	0.13
θ_e (mrad)	0.5	0.54
θ^* (mrad)	1.22	0.54
ϕ^* (mrad)	0.3	0.01
P_T (%)	5.0	5.0
P_B (%)	1.5	1.5
Packing Fraction, pf (%)	5	1.34
The maximum possible error		9.13
The final error		5.44

SECTION 5

RESULTS AND DISCUSSION

The SANE elastic data consist of two sets, the single-arm electron and the electron-proton coincidence data. The results for the proton elastic form factor ratio, $\mu_p G_E^p/G_M^p$ determined from both data sets are shown in Table 4.10. Two regions of the HMS momentum acceptance were considered separately for the single-arm data, corresponding to slightly different kinematics. The resulting form factor ratio was determined by extrapolating both measurements to the average Q^2 using the parameterization by Kelly [50], as in Equation (5.0.1) and then taking the weighted average, resulting in $\mu_p G_E^p/G_M^p = 0.605 \pm 0.178$ (only the statistical error is shown) for an average four-momentum transfer squared $Q^2 = 2.06$ (GeV/c)^2,

$$(\mu_p r)_{ext} = (\mu_p r)_{exp} + \left(\frac{\Delta(\mu_p r)}{\Delta Q^2}\right) \cdot \left(\langle Q^2 \rangle - Q^2_{exp}\right). \tag{5.0.1}$$

Where the quantities $(\mu_p r)_{ext}$ is the extrapolated form factor ratio using the parameterization by Kelly [50], $(\mu_p r)_{exp}$ is the form factor ratio from the experiment, $\left(\frac{\Delta(\mu_p r)}{\Delta Q^2}\right)$ is the straight-line gradient to Kelly's parameterization [50], $\langle Q^2 \rangle$ is the average Q^2, and Q^2_{exp} is the experiment Q^2 from data.

Due to the low statistics of the coincidence data, the statistical errors of the $\mu_p G_E^p/G_M^p$ ratios are larger at both beam energies, corresponding to Q^2=5.17 and 6.26 (GeV/c)^2. Therefore, the weighted average $\mu_p G_E^p/G_M^p$ and its error were determined from the measurements extrapolated to the average Q^2 using the parameterization by Kelly [50] as in Equation (5.0.1) for the two energy settings. The resulting form factor ratio is given as $\mu_p G_E^p/G_M^p = 0.672 \pm 0.362$ (only the statistical error is shown) for an average $Q^2 = 5.66$ (GeV/c)^2.

Table 5.1 shows the extracted form factor ratios, $(\mu_p r)_{exp}$ for each Q^2, the extrapolated ratios, $(\mu_p r)_{ext}$ to the average Q^2, Q^2_{Avg} using the parameterization by Kelly [50] together with the weighted average of the extrapolated ratios for both single-arm and coincidence data.

Table 5.1. The extracted form factor ratios for each Q^2, the extrapolated ratios to the average Q^2 using the parameterization by Kelly [50] together with the weighted average of the extrapolated ratios for both single-arm and coincidence data.

	single-arm		Coincidence	
	$-8\%<\delta<10\%$	$10\%<\delta<12\%$		
Q^2 (GeV/c)^2	2.20	1.91	6.19	5.14
$(\mu_p r)_{exp}$	0.483 ± 0.211	0.872 ± 0.329	0.937 ± 0.428	-0.052 ± 0.678
Q^2_{Avg} (GeV/c)^2	2.06		5.66	
$(\mu_p r)_{ext}$	0.506 ± 0.211	0.847 ± 0.329	0.975 ± 0.428	-0.089 ± 0.678
W. Avg. $(\mu_p r)_{ext}$	0.605 ± 0.178		0.672 ± 0.362	

Table 5.2 shows the final $\mu_p G^p_E/G^p_M$ ratios with the statistical and systematic uncertainties together with the average Q^2 values. Because the form factor ratio at higher Q^2 of 5.66 (GeV/c)^2 is largely dominated by the statistical uncertainty, the systematic uncertainty for this measurement was not studied.

Table 5.2. The results of the form factor analysis from the experiment SANE. Both the statistical and systematic uncertainties are shown for the lower Q^2=2.06 (GeV/c)^2 while only the statistical uncertainty is shown for the higher Q^2=5.66 (GeV/c)^2.

Q^2_{Avg} (GeV/c)^2	$\mu_p G^p_E/G^p_M \pm \Delta\mu_p G^p_E/G^p_{M(stat)} \pm \Delta\mu_p G^p_E/G^p_{M(syst)}$
2.06	$0.605 \pm 0.178 \pm 0.033$
5.66	0.672 ± 0.362

Compared to the uncertainty of $\mu_p G^p_E/G^p_M$ from the δ region $-8\%<\delta<10\%$ as shown in Table 4.10, the relative error has decreased from $\sim$44% to $\sim$29%, a relative decrease by 34% as shown in Table 5.2 by taking the weighted average between the two measurements in both δ regions. This improvement is due to an extra 40% events gain by the higher δ region $10\%<\delta<12\%$.

Figure 5.1 shows the form factor measurements from SANE together with the world data as a function of Q^2. The inner-error bar shown at $Q^2 = 2.06$ (GeV/c)^2 is statistical and the outer-error bar is a combination of statistical and systematics. The error bar shown at $Q^2 = 5.66$ (GeV/c)^2 is only statistical. The weighted average data point at $Q^2 = 2.06$ (GeV/c)^2 is very consistent with the existing recoil-polarization measurements, confirming the decrease of $\mu_p G_E^p/G_M^p$ with Q^2. Because in theory, the beam-target asymmetry method is equivalent to the polarization-transfer method, the results are expected to be similar to the polarization-transfer data. The measurement does not reveal any unknown systematic difference from the polarization-transfer method. The obtained accuracy confirms the suitability of using the beam-target asymmetry for determination of the $\mu_p G_E^p/G_M^p$ ratio.

The weighted average data point at higher $Q^2 = 5.66$ (GeV/c)^2 has a larger statistical uncertainty due to the small number of counts which makes it difficult to draw a strong conclusion with respect to a change of the proton form factor ratio with Q^2.

The HMS drift chamber gas leak during the coincidence data-taking resulted in the drift chamber tracking efficiency to decrease from $\sim 98\%$ to the average of $\sim 40\%$. This caused about $\sim 60\%$ inefficiency of the elastic proton detection by HMS. In addition, one of the superconducting Helmholtz coils used to polarize the NH_3 target was damaged during the data-taking, which took about a month to have repaired. This prevented about a one-month period of productive data-taking during the given beam time. Therefore, single-arm data were taken only about ~ 12 hours in total and the coincidence data for elastic kinematics were taken about a week for both beam energies, ~ 14 hours and ~ 155 hours, respectively, for two beam energies 4.72 GeV and 5.89 GeV. Therefore, along with optimum proton detection efficiency in HMS, it should be possible to take at least four times the amount of data in the same time period, which would decrease the error bars on both measurements by a factor of

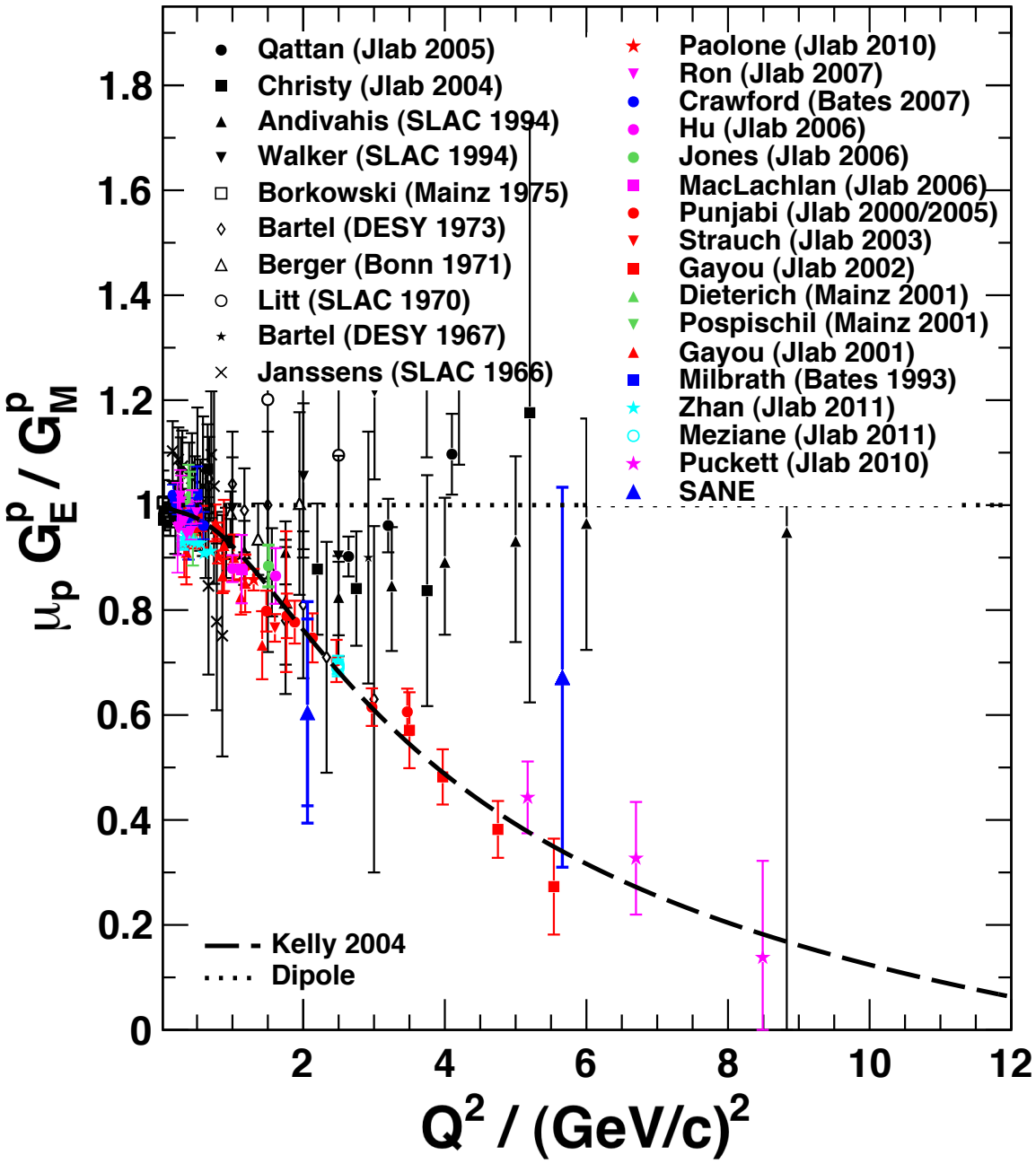

Figure 5.1. The form factor measurements from SANE together with the world data as a function of Q^2. The inner-error bar shown at $Q^2 = 2.06$ (GeV/c)^2 is statistical and the outer-error bar is a combination of statistical and systematics. The error bar shown at $Q^2 = 5.66$ (GeV/c)^2 is only statistical.

two. In addition, the target spin orientation was not optimized for a measurement of G_E/G_M.

Measurement of the beam-target asymmetry in elastic electron-proton scattering offers an independent technique of determining the proton elastic form factor ratio, $\mu_p G_E^p/G_M^p$. The TPE amplitude has a strong ϵ dependence with a large effect on the extraction of the proton form factors from the Rosenbluth separation method. The absence of such a strong dependence for the polarizable observables, the double-spin polarization experiments show a strong validation of the method of measuring the form factor ratio.

The form factor analysis from the experiment SANE extended the proton electric-to-magnetic form factor ratio, $\mu_p G_E^p/G_M^p$ from the double-spin asymmetry up to $Q^2 = 5.66$ (GeV/c)^2. The results at $Q^2 = 2.06$ (GeV/c)^2 are an important test of the reproducibility of the first measurement of the beam-target asymmetry at $Q^2 = 1.5$ (GeV/c)^2 [52]. A measurement with this method at higher Q^2 than the first measurement at $Q^2 = 1.5$ (GeV/c)^2 has been very important to see if this third technique is consistent with the polarization-transfer method as expected, or if it follows the form factor scaling result from the Rosenbluth separation method. The result of this work validates those of the polarization-transfer method and, therefore, strengthens the case for the TPE framework as an explanation for the form factor discrepancy between unpolarized and polarized data.

However, as a byproduct measurement of the SANE experiment, the precision of this result is limited by statistics. It would certainly be possible to improve the precision at high Q^2 with a dedicated experiment.

REFERENCES

[1] H. Geiger and E. Marsden. Proceedings of the Royal Society of London, Series A 82, 495 (1909).

[2] E. Rutherford. Philosophical Magazine, 21, 669-688 (1911).

[3] H. Geiger and E. Marsden. Philosophical Magazine, 25, 148 (1913).

[4] O. Stern. Nature, 132, 169 (1933).

[5] F. R. Wesselmann *et al.* Phys. Rev. Lett. 98, 132003 (2007).

[6] Francis Halzen and Alan D. Martin. Quark and Leptons: An Introductory Course in Modern Particle Physics. John Wiley and Sons, (1984).

[7] Michael E. Peskin and Daniel V. Schroeder. An Introduction to Quantum Field Theory. Westview Press, (1995).

[8] C. Amsler *et al.* (Particle Data Group), "2008 Review of Particle Physics". Phys. Lett. B 667, 1 (2008).

[9] M. Amaryan. Class notes, (2007).

[10] Robert Hofstadter and Robert W. McAllister. American Physical Society, Phys. Rev. 98, 217-218 (1955).

[11] Robert Hofstadter and Robert McAllister. Phys. Rev. 102, 851 (1956).

[12] Robert Hofstadter. Rev. of Mod. Phys. 28(3), 214 (1956).

[13] Amitabha Lahiri and Palash B. Pal. A First Book Of Quantum Field Theory. CRC Press, (2001).

[14] C. M. Maekawa and U. Van Kolck. Phys. Lett. B 478, 73 (2000).

[15] W. H. Hockings and U. Van Kolck. Phys. Lett. B 605, 273-278 (2005).

[16] J. J. Kelly. Phys. Rev. C 66, 065203 (2002).

[17] L. W. Mo and Y. S. Tsai. Rev. Mod. Phys. 41, 205-235 (1969).

[18] L. C. Maximon and J. A. Tjon. Phys. Rev. C 62, 054320 (2000).

[19] C. F. Perdrisat, V. Punjabi, and M. Vanderhaeghen. Prog. Part. Nucl. Phys. 59, 694-764 (2007).

[20] J. Arrington and I. Sick. Phys. Rev. C 70, 028203 (2004).

[21] S. D. Drell and S. Fubini. Phys. Rev. 113, 741 (1959).

[22] G. K. Greenhut. Phys. Rev. 184, 1840 (1969).

[23] P. A. M. Guichon and M. Vanderhaeghen. Phys. Rev. Lett. 91, 142303 (2003).

[24] J. Arrington *et al.* Proposal for an experiment at VEPP-3. Novosibirsk. nucl-ex/0408020, (2004).

[25] J. Arrington *et al.* Proposal E07-005. Jefferson Lab, Hall B, (2004).

[26] D. Hasell, M. Kohl, and R. Milner *et al.* OLYMPUS Proposal at DESY, Germany, (2008).

[27] S. D. Drell and J. D. Walecka. Ann. Phys. 28, 18-33 (1964).

[28] M. Anselmino, A. Efremov, and E. Leader. Physics Reports, 261(1-2), 1-124 (1995).

[29] S. Stein *et al.* Phys. Rev. D 12, 1884 (1975).

[30] M. N. Rosenbluth. Phys. Rev. 79(4), 615 (1950).

[31] A. I. Akhiezer and M. P. Rekalo. Sov. Phys. Doklady Akademii Nauk SSSR. 180, 5, 1081 (1968).

[32] A. I. Akhiezer and M. P. Rekalo. Sov. J. Part. Nucl. 3, 277 (1974).

[33] Norman Dombey. Rev. Mod. Phys. 41, 236 (1969).

[34] Carl E. Carlson, Raymond G. Arnold, and Franz Gross. Phys. Rev. C 23, 363 (1981).

[35] T. W. Donnelly and A. S. Raskin. Ann. of Phys. 169:247, 191:78 (1986).

[36] I. A. Qattan *et al.* Phys. Rev. Lett. 94, 142301 (2005).

[37] M. E. Christy *et al.* Phys. Rev. C 70, 015206 (2004).

[38] L. Andivahis *et al.* Phys. Rev. Lett. D 50, 5491 (1994).

[39] R. C. Walker *et al.* Phys. Rev. Lett. D 49, 5671 (1994).

[40] F. Borkowski *et al.* Nucl. Phys. B 93, 461 (1975).

[41] F. Borkowski *et al.* Nucl. Phys. A 222, 269 (1974).

[42] W. Bartel *et al.* Nucl. Phys. B 58, 429 (1973).

[43] C. Berger *et al.* Phys. Lett. B 35, 87 (1971).

[44] J. Litt *et al.* Phys. Lett. B 31, 40 (1970).

[45] T. Janssens *et al.* Phys. Rev. 142, 922 (1966).

[46] G. G. Simon *et al.* Nucl. Phys. A, 333-381 (1980).

[47] J. J. Murphy, Y. M. Shin, and D. M. Skopik. Phys. Rev. C 9, 2125 (1974).

[48] P. E. Bosted *et al.* Phys. Rev. C 42(1), 38-64 (1990).

[49] A. F. Sill *et al.* Phys. Rev. D 48, 29 (1993).

[50] J. J. Kelly. Phys. Rev. C 70(6), 068202 (2004).

[51] C. B. Crawford *et al.* Phys. Rev. Lett. 98(5), 052301 (2007).

[52] M. K. Jones *et al.* Phys. Rev. C 74(3), 035201 (2006).

[53] M. Meziane *et al.* Phys. Rev. Lett. 106, 132501 (2011).

[54] A. J. R. Puckett *et al.* Phys. Rev. Lett. 104(24), 242301 (2010).

[55] V. Punjabi and C. F. Perdrisat *et al.* Phys. Rev. C 71(5), 069902 (2005).

[56] V. Punjabi and Perdrisat *et al.* Phys. Rev. C 71(5), 055202 (E) (2005).

[57] M. K. Jones *et al.* Phys. Rev. Lett. 84, 1398-1402 (2000) (superseded by [55,56]).

[58] O. Gayou et al. Phys. Rev. Lett. 88, 092301 (2002).

[59] M. Paolone *et al.* Phys. Rev. Lett. 105, 072001 (2010).

[60] G. Ron *et al.* Phys. Rev. Lett. 99, 202002 (2007).

[61] Hu, B., and M. K. Jones *et al.* Phys. Rev. C 73, 064004 (2006).

[62] S. Strauch *et al.* Phys. Rev. Lett. 91, 052301 (2003).

[63] O. Gayou *et al.* Phys. Rev. C 64, 038202 (2001).

[64] G. MacLachlan *et al.* Nucl. Phys. A 764, 261-273 (2006).

[65] T. Pospischil *et al.* Eur. Phys. J. A 12, 125-127 (2001).

[66] S. Dieterich *et al.* Phys. Lett. B 500, 47-52 (2001).

[67] B. D. Milbrath *et al.* Phys. Rev. Lett. 80, 452-455 (1998).

[68] B. D. Milbrath *et al.* Phys. Rev. Lett. 82, 2221 (E) (1999).

[69] R. Pohl *et al.* Nature 466, 213 (2010).

[70] J. C. Bernauer *et al.* Phys. Rev. Lett. 105(24), 242001 (2010).

[71] X. Zhan *et al.* Phys. Lett. B 705, 59-64 (2011).

[72] M. P. Rekalo and Egle Tomasi-Gustafsson. Eur. Phys. J. A 22, 331-336 (2004).

[73] P. G. Blunden, W. Melnitchouk, and J. A. Tjon. Phys. Rev. Lett. 91, 142304 (2003).

[74] P. G. Blunden, W. Melnitchouk, and J. A. Tjon. Phys. Rev. C 72, 034612 (2005).

[75] Y. C. Chen, A. Afanasev, S. J. Brodsky, C. E. Carlson, and M. Vanderhaeghen. Phys. Rev. Lett. 93, 122301 (2004).

[76] A. V. Afanasev, S. J. Brodsky, C. E. Carlson, Yu-Chun Chen, and M. Vanderhaeghen. Phys. Rev. D 72, 013008 (2005).

[77] D. Borisyuk and A. Kobushkin. Phys. Rev. C 74, 065203 (2006).

[78] D. Borisyuk and A. Kobushkin. Phys. Rev. C 78, 025208 (2008).

[79] D. Borisyuk and A. Kobushkin. Phys. Rev. D 79, 034001 (2009).

[80] N. Kivel and M. Vanderhaeghen. Phys. Rev. Lett. 103, 092004 (2009).

[81] J. Arrington, W. Melnitchouk, and J. A. Tjon. Phys. Rev. C 76, 035205 (2007).

[82] S. Riordan *et al.* Phys. Rev. Lett. 105, 262302 (2010).

[83] J. Arrington *et al.* Proposal E05-017. Jefferson Lab, Hall C, (2005).

[84] T. Averett *et al.* Proposal E05-015. Jefferson Lab, Hall A, (2005).

[85] D. Androic *et al.* Phys. Rev. Lett. 107(2), 022501, (2011).

[86] L. Capozza. Eur. Phys. J. A 32, 497-499 (2007).

[87] D. Beck *et al.* (E06-008-G0 Collaboration). Jefferson Lab, Hall C, (2006).

[88] F. E. Maas *et al.* Imaginary Phys. Rev. Lett. 94(8), 082001 (2005).

[89] S. P. Wells *et al.* Phys. Rev. C 63(6), 064001, (2001).

[90] C. Perdrisat *et al.* 12 GeV Proposal PR12-07-109. Jefferson Lab, Hall A, (2007).

[91] S. Gilad *et al.* 12 GeV Proposal PR12-07-108. Jefferson Lab, Hall A, (2007).

[92] E. J. Brash *et al.* 12 GeV Proposal PR12-09-001. Jefferson Lab, Hall C, (2009).

[93] J. Arrington *et al.* 12 GeV Proposal E08-007. Jefferson Lab, Hall A, (2008).

[94] S. Platchkov *et al.* Nucl. Phys. A 510, 740-758 (1990).

[95] R. Schiavilla and I. Sick. Phys. Rev. C 64, 041002 (2001).

[96] B. Plaster *et al.* Phys. Rev. C 73, 025205 (2006).

[97] R. Madey *et al.* Phys. Rev. Lett. 91, 122002 (2003) (superseded by [96]).

[98] D. I. Glazier *et al.* Eur. Phys. J. A 24, 101-109 (2005).

[99] M. Ostrick *et al.* Phys. Rev. Lett. 83, 276-279 (1999).

[100] C. Herberg *et al.* Eur. Phys. J. A5, 131-135 (1999).

[101] T. Eden *et al.* Phys. Rev. C 50, 1749-1753 (1994).

[102] E. Geis *et al.* Phys. Rev. Lett. 101, 042501 (2008).

[103] G. Warren *et al.* Phys. Rev. Lett. 92, 042301 (2004).

[104] H. Zhu *et al.* Phys. Rev. Lett. 87, 081801 (2001).

[105] I. Passchier *et al.* Phys. Rev. Lett. 82, 4988-4991 (1999).

[106] J. Bermuth *et al.* Phys. Lett. B 564, 199-204 (2003).

[107] D. Rohe *et al.* Phys. Rev. Lett. 83, 4257-4260 (1999) (superseded by [106]).

[108] J. Golak *et al.* Phys. Rev. C 63, 034006 (2001) (Applying FSI corrections to [109]).

[109] J. Becker *et al.* Eur. Phys. J. A 6, 329-344 (1999) (without FSI corrections).

[110] J. Friedrich and T. Walcher. Eur. Phys. J. A 17, 607-623 (2003).

[111] Annual Report 2004/2005. Institut fuer Kernphysik, Universitaet Mainz, (2006).

[112] P. Achenbach *et al.* Proposal MAMI-A1-1/05(polarized ^3He), Mainz Microtron, (2005).

[113] B. D. Anderson *et al.* 12 GeV Proposal PR12-11-009 (recoil polarization). Jefferson Lab, Hall C, (2011).

[114] B. Wojtsekhowski *et al.* 12 GeV Proposal PR12-09-016 (polarized He-3), Jefferson Lab, Hall A, (2009).

[115] A. Lung *et al.* Phys. Rev. Lett. 70, 718-721 (1993).

[116] P. Markowitz *et al.* Phys. Rev. C 48, 5-9 (1993).

[117] S. Rock *et al.* Phys. Rev. Lett. 49, 1139 (1982).

[118] K. M. Hanson *et al.* Phys. Rev. D 8, 753-778 (1973).

[119] J. Lachniet *et al.* Phys. Rev. Lett. 102, 192001 (2009).

[120] G. Kubon *et al.* Phys. Lett. B 524, 26-32 (2002).

[121] H. Anklin *et al.* Phys. Lett. B 428, 248-253 (1998).

[122] E. E. W. Bruins *et al.* Phys. Rev. Lett. 75, 21-24 (1995).

[123] H. Anklin *et al.* Phys. Lett. B 336, 313-318 (1994).

[124] B. Anderson *et al.* Phys. Rev. C 75, 034003 (2007).

[125] W. Xu *et al.* Phys. Rev. C 67, 012201 (2003) (supeseded by [124]).

[126] W. Xu *et al.* Phys. Rev. Lett. 85, 2900-2904 (2000) (supeseded by [124]).

[127] H. Gao *et al.* Phys. Rev. C 50, 546-549 (1994).

[128] N. Meitanis. Ph.D. theses, Massachusetts Institute of Technology, (2006).

[129] B. O'Neill. Ph.D. theses, Arizona State University (in preparation).

[130] G. P. Gilfoyle *et al.* 12 GeV Proposal PR12-07-104 (ratio method). Jefferson Lab, Hall B, (2007).

[131] B. Quinn *et al.* 12 GeV Proposal PR12-09-019 (ratio method). Jefferson Lab, Hall A, (2009).

[132] F. Iachello, A.D. Jackson, and A. Lande. Phys. Lett. B 43, 191-196 (1973).

[133] Manfred Gari and W. Krumpelmann. andZ. Phys. A 322, 689-693 (1985).

[134] M. A. Belushkin, H. W. Hammer, and U. G. Meissner. Phys. Rev. C 75, 035202 (2007).

[135] C. Crawford *et al.* Phys. Rev. C 82, 045211 (2010).

[136] I. T. Lorenz *et al.* Eur. Phys. J. A 48, 151 (2012).

[137] Earle L. Lomon and Simone Pacetti. Phys. Rev. D 85, 113004 (2012).

[138] Nathan Isgur and Gabriel Karl. Phys. Rev. D 18, 4187 (1978).

[139] Dirac and A. M. Paul. Rev. Mod. Phys. 21, 392-399 (1949).

[140] G. A. Miller. Phys. Rev. C 66, 032201 (2002).

[141] M. R. Frank, B. K. Jennings, and G. A. Miller. Phys. Rev. C 54, 920-935 (1996).

[142] G. Peter Lepage and Stanley J. Brodsky. Phys. Rev. Lett. 43, 545-549 (1979).

[143] Andrei V. Belitsky, Xiang-dong Ji, and Feng Yuan. Phys. Rev. Lett. 91, 092003 (2003).

[144] M. Guidal, M. V. Polyakov, A. V. Radyushkin, and M. Vanderhaeghen. Phys. Rev. D 72, 054013 (2005).

[145] Xiang-Dong Ji. Phys. Rev. Lett. 78, 610-613 (1997).

[146] Gerald A. Miller. Phys. Rev. Lett. 99, 112001 (2007).

[147] Reinhard Alkofer and Lorenz von Smekal. Phys. Rept. 353, 281 (2001).

[148] Christian S. Fischer. J. Phys. G 32, R253-R291 (2006).

[149] John Arrington, Kees de Jager, and Charles F. Perdrisat. J. Phys. Conf. Ser. 299, 012002 (2011).

[150] I. Aznauryan *et al.* (2009).

[151] I. C. Cloet *et al.* Few Body Syst. 46, 1-36 (2009).

[152] A. Holl *et al.* Nucl. Phys. A 755, 298-302 (2005).

[153] M. Gockeler *et al.* Phys. Rev. D 71, 034508 (2005).

[154] J. D. Ashley *et al.* Eur. Phys. J. A 19, 9-14 (2004).

[155] R. G. Edwards *et al.* PoS LAT2006, 121 (2006).

[156] James D. Maxwell. Probing Proton Spin Structure: A Measurement of g_2 at Four-momentum Transfer of 2 to 6 GeV^2. Ph.D. theses, University of Virginia, (2011).

[157] C. Hernandez-Garcia, M. L. Stutzman, and P. G. O'Shea. Physics Today 61(2), 44-49 (2008).

[158] C. W. Leemann, D. R. Douglas, and G. A. Krafft. Ann. Rev. Nucl. Part. Sci. 51, 413-450 (2001).

[159] C. Yan and R. Carlini. Hall C beamline instrumentation, (1992).

[160] P. Gueye. Technical report, Jefferson Lab, (1992).

[161] K. B. Unser. A. I. P. Conf. Proc. 252, 266 (1992).

[162] G. Niculescu. (Unpublished internal document, Jefferson Lab), (1995).

[163] C. Armstrong. (Unpublished internal document, Jefferson Lab), (1996).

[164] M. Hauger *et al.* Nucl. Instrum. Meth. A 462, 382-392 (2001).

[165] J. M. Grames *et al.* Phys. Rev. ST Accel. Beams 7, 042802 (2004).

[166] B. W. Montague. Phys. Rept. 113, 1-96 (1984).

[167] D. W. Higinbotham. AIP Conf. Proc. 1149, 751-754 (2009).

[168] C. Yan *et al.* Nucl. Instrum. Meth. A 365, 46-48 (1995).

[169] C. Yan, N. Sinkine, and R. Wojcik. Nucl. Instrum. Meth. A 539, 1-15 (2005).

[170] M. Fukuda, S. Okumura, and K. Arakawa. Nucl. Instrum. Meth. A 396, 45-49 (1997).

[171] C. F. Perdrisat. Technical report, Jefferson Lab, Hall C, (2007).

[172] A. Puckett. Technical report, Jefferson Lab, Hall C, (2008).

[173] Andrew J. R. Puckett. Recoil polarization Measurements of the Proton Electromagnetic Form Factor Ratio to High Momentum Transfer. Ph.D. theses, Massachusetts Institute of Technology, (2010).

[174] Joseph K. Cobb and J. J. Muray. Nucl. Instrum. Meth. 46, 99-105 (1967).

[175] M. Berz. COSY Infinity Version 7 Reference Manual, NSCL Technical Report MSUCL-977, Michigan State University, (1995).

[176] L. Tang, C. Yan, and Ed. V. Hungerford. Nucl. Instrum. Meth. A 366, 259 (1995).

[177] O. K. Baker *et al.* Nucl. Instrum. Meth. A 367, 92-95 (1995).

[178] J. Arrington. Ph.D. theses, California Institute of Technology, (1998).

[179] D. G. Crabb and W. Meyer. Ann. Rev. Nucl. Part. Sci. 47, 67-109 (1997).

[180] M. Borghini. Conf. Proc. C680922V4P2, 191-242 (1968).

[181] M. Goldman. Journal of Magnetic Resonance (1969) 17(3), 393-398 (1975).

[182] G. R. Court, D. W. Gifford, P. Harrison, W. G. Heyes, and M. A. Houlden. Nucl. Instrum. Meth. A 324, 433-440 (1993).

[183] CODA-CEBAF Online Data Acquisition User's Manual.

[184] C. Group. PAW (Physics Analysis Workstation) Users Guide. Program Library Q121, CERN.

[185] K. Makino and M. Berz. Nucl. Instrum. Meth. A 427, 338 (1999).

[186] Time of flight scintillator hodoscope calibration. `https://hallcweb.jlab.org/document/howtos/tof_calibration/`, (2009).

[187] K. Nakamura and the Particle Data Group. Journel of physics G:Nuclear and Particle Physics 37(7A), 075021 (2010).

[188] D. Crabb, D. Day, and O. Rondon. A proposal for the renewal of contact no. de-fg02-96er40950, university of virginia.

[189] C. Delaere. class TMultiLayerPerception. `http://root.cern.ch/root/html/TMultiLayerPerception.html`, (2003).

[190] M. A. Shupe *et al.* Phys. Rev. D 19, 1921-1930 (1979).

[191] K. Makino and M. Berz. Nucl. Instrum. Meth. A 427, 338-343 (1999).

[192] M.E. Christy and Peter E. Bosted. Phys. Rev. C 81, 055213 (2010).

[193] J. Arrington. Phys. Rev. C 69, 022201 (2004).

[194] S. Dasu *et al.* Proceedings, 4th Meeting of the Division of Particles and Fields of the APS, 635-638 (1988).

[195] W. R. Leo. Techniques for Nuclear and Particle Physics Experiments. Springer Verlag, (1987).

HABARAKADA LIYANAGE ANUSHA PUSHPAKUMARI

468 Young's Mill Lane, Apt F, Newport News, VA 23602, (757) 2434885, anusha@jlab.org

Education

Doctor of Philosophy (August, 2013), Nuclear Physics, Hampton University, Hampton, VA

Bachelor of Science (April, 2004), Physics, University of Peradeniya, Sri Lanka

Professional Experience

Research Assistant (2006-2013), Hampton University, Hampton, VA

Teaching Assistant (2004-2006), University of Peradeniya, Peradeniya, Sri Lanka

Honors and Awards

Departmental Fellow, full scholarship and stipend, (2006-2013) Hampton University physics Department, Hampton University, Hampton, VA.

First Place, Graduate Student Poster Competition, User Group Meeting, Thomas Jefferson National Accelerator Facility, Newport News, VA, May 2010.

Awarded the visiting scholar award for excellence in scholarship in the natural and computational sciences, 12^{th} Annual Graduate Research Symposium (GRS), The College of William and Mary, Williamsburg, VA, March 2013.

Publications and Presentations

Proton Form Factor Ratio G_E^p/G_M^p at High Q^2 from Double Spin Asymmetry with Polarized Beam and Target, **Poster presentation at the Gorden Research Conference**, New Hampshire, August 2010.

Proton Form Factor Ratio G_E^p/G_M^p from Double Spin Asymmetry with Polarized Beam and Target , **Division of Nuclear Physics meeting of the American Physical Society**, Santa Fe, NM, November 2010.

Measurement of the Proton Form Factor Ratio G_E^p/G_M^p from the Double Spin Asymmetry, **American Physical Society April Meeting**, Anaheim, California, April 2011.

Proton Form Factor Ratio G_E^p/G_M^p from the Double Spin Asymmetry, **Seminar at Thomas Jefferson National Accelerator Facility**, October, 2012.